PHOTOELASTIC PROPERTIES OF OXIDE AND NON-OXIDE GLASSES

by

Justine Galbraith

Submitted in partial fulfillment of the
requirements for the degree of
Doctor of Philosophy

at

Dalhousie University
Halifax, Nova Scotia
December 2014

Table of Contents

List of Tables

List of Figures

Abstract

An unperturbed piece of glass is optically isotropic. Birefringence can be induced by breaking this symmetry, for example by applying a uniaxial stress to the glass. An empirical model exists which predicts when oxide glasses will exhibit positive, negative or zero birefringence under stress. This model has been used to determined new zero-stress optic oxide glass compositions; however, it has not been tested on non-oxide systems, nor does it take into account the wavelength of the incident light.

The stress-optic response in chalcogenide glasses was investigated using stoichiometric GeS_2-P_2S_5 and GeS_2-Sb_2S_3, and non-stoichiometric Ge-P-S. The trends of the stress-optic response in stoichiometric non-oxide glasses correlated well with predictions based on the empirical model for oxide glasses. Small differences between the predictive parameter of the model, $\langle d/N_c \rangle$, were explained by expanding the treatment of metallicity.

The wavelength dependence of the stress-optic coefficient for a large variety of oxide glass formers and modifiers was measured. Glasses composed of positive modifiers (*e.g.* BaO, CaO, Na_2O) exhibited positive dispersion of the stress-optic coefficient, while those with negative modifiers (*e.g.* PbO, SnO) showed negative dispersion. Mixing positive and negative modifiers in a glass resulted in compositions exhibiting wavelength independent stress-optic coefficients.

The photoelastic response of a material can also be described by its elasto-optic tensor (p_{ij}). Isotropic materials have three elasto-optic tensor elements, two of which are independent. These two independent elements were measured for lead and barium borate, phosphate and silicate glasses using Brillouin spectroscopy. Both elements were found to correlate with the empirical parameter $\langle d/N_c \rangle$, while the third dependent element showed no relationship to the empirical model.

Finally, an alternative model of photoelasticity is discussed. The normalized polarizability of a material is found to correlate with both the sign and magnitude of the stress-optic coefficient.

List of Abbreviations and Symbols Used

α, χ	Total polarizability
α_n	Normalized polarizability
α_C	Measure of covalency
β^L, β^T	Longitudinal or transverse part of bond polarizability tensor
Δ	Phase shift of s- and p-polarized light
ϵ	Dielectric constant
$\epsilon_{C,A}$	Intra-atomic matrix elements of the one-electron Hamiltonian
Γ	Correlation term
θ_B	Brewster's angle
λ	Wavelength of light
λ_0	Absorption edge wavelength of a material
Λ	Density dependence of the individual bond polarizability
ν	Poisson ratio
π_{ij}, π_{ijkl}	Piezo-optic tensor element
ρ	Density
σ	Applied stress
χ_b, π	Individual bond polarizability
Ψ	Amplitude ratio of s- and p-polarized light
ω	Frequency of light
$\hbar$	Planck's constant
a, b, c	Parameters of the pseudo-Cauchy fit
A, B, C	Parameters of the Cauchy fit
b	Birefringence

$\mathbf{B}$	Magnetic field
B_{ij}	Inverse dielectric tensor
c	Speed of light in vacuum
C	Stress-optic coefficient
C_{ij}, C_{ijkl}	Elastic tensor element
d	Anion-cation bond length, or thickness of material
$\mathcal{D}_{ij}$	Deformation potential
e	Electron
E	Young's modulus, or band-gap energy, or bond energy
$\mathbf{E}$	Electric field
$\mathcal{E}_0$	Interband energy
$\mathcal{E}_d$	Dispersion energy
f	Oscillator strength
F_B	Buoyancy
$\mathcal{F}$	Interband strength
G	Shear modulus
$\mathcal{H}$	One-electron Hamiltonian
I	Intensity of light
J	Spectral density of scattered light
$\mathbf{k}$	Wavevector
L_1, L_2	Optical deformabilities of atoms' polarizabilities
m	Mass
M	Molar weight, or interatomic matrix element of the one-e Hamiltonian
n	Refractive index
N	Avogadro's number

N_c	Cation coordination number
p_{ij}, p_{ijkl}	Elasto-optic tensor element
$\mathbf{P}$	Polarization
P_0	Power of incident light
q	Charge
$\mathbf{q}$	Wavevector of scattered light
r	Interatomic distance
R, T, A	Reflection, transmission and absorption intensities
R_C, R_A	Ionic radii
R_m	Molar refractivity
s	Applied strain
S	Overlap integral for anion and cation orbitals
S_{ij}, S_{ijkl}	Compliance tensor element
S_0	Oscillator strength
$\mathbf{u}(t)$	Displacement vector
V	Interaction volume
V, H	Vertical or horizonal polarization of light
v_L, v_T	Longitudinal or transverse sound velocity
V_m	Molar volume
W	Weight
x	Molar per cent of additive
X_H	Hydrostatic stress
Z_a	Formal anion valence
z_b	Mean numbers of bonds per molecular unit

DID	Dipole-induced-dipole
EMP	Electron microprobe spectroscopy
FP	Fabry-Perot
IR	Infrared
KK	Kramers-Kronig
LCVR	Liquid crystal variable retarder
RT	Room temperature
TFPI	Tandem Fabry-Perot interferometer
UV	Ultraviolet
vis	Visible

Acknowledgements

There are many people who had a significant impact on my work and on my life, and I would like to thank them.

Throughout my degree, I've worked on some really engaging research topics, but more importantly, I've had the opportunity to work with a truly amazing supervisor. Thank you, Joe Zwanziger.

A lot of my research relied on the contributions from and collaborations with various individuals, and I would like to acknowledge them. Bruce Aitken and Steve Currie prepared glass samples for this work. Jeff Dahn and Robbie Sanderson provided access to and training for the ellipsometer. Leanne Chapman, Jacy Conrad, Victoria Dickinson and Lisa Zhang worked with me for their summer research projects. And the collection of the Brillouin spectra would not have been possible without John Kieffer and Michael Aldridge.

I would also like to thank the faculty and staff at Dalhousie that have been instrumental along the way. I am grateful to Kevin Hewitt and Kimberley Hall for being on my committee. Andy George, Brian Millier, Mike Boutillier, Ulli Werner-Zwanziger, and many others also provided support for this work: thank you. And I'm very appreciative towards both Dalhousie and NSERC for supporting my research financially.

My friends and colleagues have been such an important part of my experience here in Halifax. You are too many to name, but know that the coffee dates, trivia nights, board games, potlucks, parties, shop-talk, and time spent together have all meant a great deal to me. I'm so thankful to my family for all of their love and support.

And to Will Gregory, thank you for everything.

Chapter 1

Introduction

Glass is everywhere. Beyond its common everyday applications, glass also has a wide variety of technological uses. Oxide glasses are often used for optical lenses, projection systems and sealing of electrical devices. Chalcogenide glasses are of interest for optical amplifiers and laser sources. Examining the structure and properties of glasses can help to identify practical technological applications.

The empirical model for photoelasticity proposed by Guignard et al. [1] has been very successful at predicting the sign of the stress-optic coefficient of oxide glasses, as well as new zero-stress optic compositions. However, its predictions are limited to oxide glass compounds, and it does not address the magnitude of the stress-optic response or the wavelength of incident light. The subject of this report is threefold. First, the empirical model is tested using a non-oxide glass systems. Second, the effect of different oxide glass modifiers is related to the dispersion of the stress-optic coefficient in oxide glasses. And third, the complete elasto-optic response of oxide glasses is determined using Brillouin spectroscopy. The main goal of this research is to develop a theory that will predict IR glasses with zero birefringence as well as broadband zero stress-optic oxide glasses. Alternative models of photoelasticity are compared to the empirical model. In this way, a theory that considers not just sign but also magnitude of the stress-optic response in glass is developed.

This thesis is organized into seven parts. Chapter 2 defines the stress-optic response of a glass and describes the widely accepted theories of photoelasticity for oxide glasses. The limited studies on the stress-optic response of chalcogenides are summarized. Theories relating the wavelength of incident light to the stress-optic and elasto-optic coefficients are described. And photoelastic theories that account for all elasto-optic tensor elements are presented.

The theory and measurement techniques for the glass properties (elastic modulus, density, stress-optic and elasto-optic coefficients, and refractive index) are given in

Chapter 3. The principles of ellipsometry and Brillouin scattering and are presented, and the spectroscopic ellipsometer and Fabry-Perot interferometer used to collect data are described.

The results of the investigation on the stress-optic response of sulfide glasses, including discussions of the empirical model and non-stoichiometric glass compositions, are presented in Chapter 4.

The results of the wavelength-dependent stress-optic response of oxide glasses is presented in Chapter 5. A pseudo-Cauchy model is developed to relate the stress-optic coefficient to the incident wavelength.

The individual elasto-optic tensor elements are discussed in Chapter 6. Two of the three tensor elements can be related to the empirical model of photoelasticity. The third elasto-optic coefficient appears to be unrelated to glass composition.

An alternative polarizability model is discussed in Chapter 7. The polarizabilities glass compositions are linearly related to the stress-optic coefficients. An empirical model is suggested which allows predictions of the magnitude of C based on glass composition.

Finally, in Chapter 8, the major results of the thesis are summarized and important future work is presented.

Chapter 2

Background

Glass is an amorphous solid. It exhibits long-range atomic disorder similar to that of a liquid, but the relative positions of those atoms are invariant. Most of the properties of glass, as well as its outward appearance, are solid-like. One of the most referenced theories of glass structure was developed by Zachariasen [2], who argued that since the mechanical properties of glasses are similar to those of crystals, the forces between atoms must be similar as well. The structural building blocks of a glass network – cation polyhedra coordinated by oxygen or another chalcogen – are then hypothesized to be the same or similar to those present in crystals. However, in crystals, these polyhedra have repeating long-range order with different symmetries present depending on the composition. Glasses do not have the same periodicity; the cation polyhedra are randomly oriented in the glass network (pp. 13–59 of [3]).

A wide variety of materials can be made in the glassy state. Soda-lime-silicate glasses made from soda ash (Na_2CO_3), limestone ($CaCO_3$) and silica (SiO_2) are the most commonly used and least expensive commercial glasses. Many oxide glass systems include other silicates, borates and phosphates. Modifiers such as barium oxide, zinc oxide, and magnesium oxide can be added to form new glass families. Moreover, glass can be made from non-oxide materials like fluorides, chlorides and chalcogenides (pp. 1–11 of [3]).

Many properties of glasses show additivity relationships. That is to say the property P can be determined from $P = \sum_i p_i x_i$, where p_i is the value of that property for component i, and x_i is the molar weight of that component in the glass structure. Indeed, the optical properties of glasses are largely dependent on composition. The refractive index (and also density) tends to vary linearly with the components of the glass. The absorption edge wavelength shifts to higher values as heavier additives are incorporated into the glass network. Generally speaking, oxide glasses tend to have smaller indices of refraction and are transparent into the visible range of light.

Chalcogenides, on the other hand, begin to transmit in the near-IR range and have large refractive indices (typically > 2) and low phonon frequencies (typically < 450 cm^{-1}).

Still, while empirical trends are apparent for some properties, there is much left to be understood about the optical response of various glass compositions [4]. In particular, information on the Brillouin scattering of glasses, the wavelength dispersion of the stress-optic response, and the photoelastic properties of non-oxide glasses is sparse. To date, Brillouin measurements of the elasto-optic tensor have focused primarily on silicate glasses; as such, the compositional dependence of p_{ij} is uncertain. We will address this by measuring the complete elasto-optic tensor of silicates, borates, and phosphates. The dispersion of the stress-optic coefficient has also only been measured for a small number of silicate-based glasses, often with many components; the direct effect of modifying the glass network is not well understood. To explore this more closely, the wavelength dependence of the stress-optic coefficient for simple binary and ternary glass systems will be determined. And the stress-optic coefficient has only been measured for a small number of chalcogenide glass systems. We will improve this by comparing stress-induced birefringence to glass structure for both stoichiometric and non-stoichiometric sulfide systems.

2.1 Birefringence in Glasses

An unperturbed piece of glass is optically isotropic; its index of refraction is the same in all directions. When the glass is stressed, however, this symmetry is broken. The indices of refraction along the stress direction (extraordinary axis) and perpendicular to this direction (ordinary plane) are altered from their unstressed values, often by different amounts. This stress-induced change, shown in Figure 2.1, induces birefringence in the glass,

$$b = n_e - n_o. \tag{2.1}$$

Here, n_e is the refractive index measured along the extraordinary axis and n_o is the refractive index in the ordinary plane. For stress loads within the elastic region, the birefringence of a glass is proportional to the applied stress σ:

$$b = C\sigma. \tag{2.2}$$

The constant of proportionality, called the stress-optic coefficient C, is used to characterize the glass. Its unit is Brewsters, where B = TPa^{-1}.

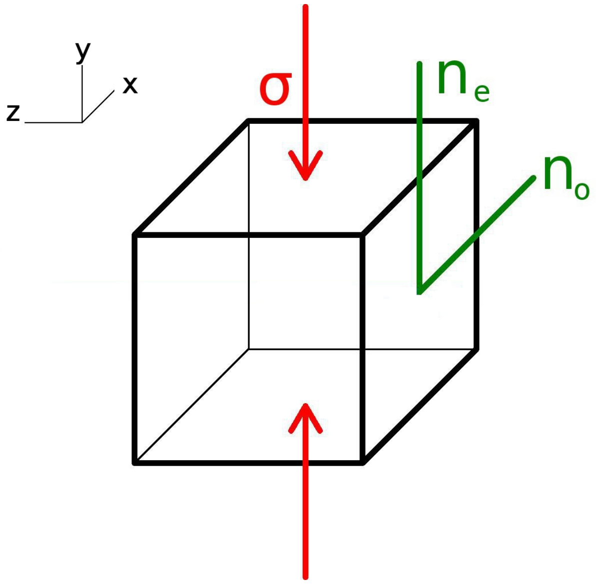

Figure 2.1: Uniaxial stress σ applied to a glass causes a change in the indices of refraction parallel and perpendicular to the stress. This induces birefringence in the glass, $b = n_e - n_o$.

Piezo-optic tensor elements π_{ijrs} and elasto-optic tensor elements p_{ijkl} can also be used to describe the stress-induced birefringence in glass. They are defined as the tensors relating the applied stress or strain with the change in inverse dielectric constant:

$$\Delta B_{ij} = \pi_{ijrs}\sigma_{rs} = p_{ijkl}s_{kl}. \tag{2.3}$$

Here, $B_{ij} = (1/n^2)_{ij} = (1/\epsilon)_{ij}$ is the inverse dielectric tensor, σ_{rs} is the stress tensor, and s_{kl} is the strain tensor [3, 5]. The tensor elements are related by $p_{ijkl} = \pi_{ijrs}C_{rskl}$, where C_{rskl} is the elastic tensor. An abbreviated notation is often used for the subscripts:

$$11 \to 1,\ 22 \to 2,\ 33 \to 3,\ 23 \to 4,\ 13 \to 5,\ 12 \to 6.$$

Due to the isotropy of glass, there are three piezo-optic and elasto-optic tensor elements, but only two are independent. The relationship between the three p_{ij}s or π_{ij}s is

$$\begin{aligned} 2p_{44} &= p_{11} - p_{12}, \\ 2\pi_{44} &= \pi_{11} - \pi_{12}. \end{aligned} \tag{2.4}$$

Using the approximation $n_e \approx n_o \approx n$, *i.e.* the change in refractive index is very small, Equation 2.3 is solved for a uniaxial stress to show that

$$\Delta B_e = \frac{1}{n_e^2} - \frac{1}{n^2} = \frac{n^2 - n_e^2}{n_e^2 n^2} = \frac{(n - n_e)(n + n_e)}{n_e^2 n^2} = \frac{(n - n_e)(2n)}{n^4} = \pi_{33}\sigma_3 = \pi_{11}\sigma_3, \tag{2.5}$$

or

$$(n - n_e) = \frac{n^3}{2}\pi_{11}\sigma_3. \tag{2.6}$$

Likewise, we can show that

$$\Delta B_o = \frac{1}{n_o^2} - \frac{1}{n^2} = \frac{n^2 - n_o^2}{n_o^2 n^2} = \frac{(n - n_o)(n + n_o)}{n_o^2 n^2} = \frac{(n - n_o)(2n)}{n^4} = \pi_{13}\sigma_3 = \pi_{12}\sigma_3, \tag{2.7}$$

or

$$(n - n_o) = \frac{n^3}{2}\pi_{12}\sigma_3. \tag{2.8}$$

Now the birefringence - and thus, the stress-optic coefficient - can be related to the piezo-optical coefficients:

$$b = n_e - n_o = -\frac{n^3}{2}\left(\pi_{11} - \pi_{12}\right)\sigma_3 = C\sigma_3. \tag{2.9}$$

These results are used experimentally to characterize the photoelasticity of a glass sample. The stress-optic coefficient can be related to the shear piezo-optic tensor element by

$$C = -n^3\pi_{44} \tag{2.10}$$

and to the shear elasto-optic tensor element through

$$C = -\frac{n^3}{2G}p_{44}, \tag{2.11}$$

where $G = C_{44}$ is the shear elastic modulus.

Glasses can have positive, negative or zero stress-optic coefficient C depending on their composition. Most common glasses, including silicate, borate, and phosphate families, exhibit positive birefringence. Heavy additives such as lead, bismuth, tin and antimony oxide lower the stress-optic coefficient and can induce negative birefringence with high enough content [1], pp. 478–482 of [3]. One of the first studies on photoelasticity and its dispersion was done by Pockels in the early 1900s [6]. Since that time, many attempts have been made to relate the stress-optic response of a glass to its structure.

2.2 Theories of Photoelasticity: Elasto-Optic Coefficients

It has been a long-standing goal to relate the elasto-optic tensor elements of crystalline and amorphous materials to the properties of that material. Many theories and models have been developed for specific crystalline structures or for simplified amorphous networks, often relating photoelasticity to the polarizability density tensor, the dielectric tensor, and the chemical bonding in the network. Some authors consider both the nearest neighbour effects (often associated with changes in bond or ion polarizabilities), as well as larger effects from induced-dipole fields. Multi-component systems often have complex structures and polarizabilities, which require more detailed theories; many models include a fitting parameter that is determined experimentally to allow for compositional variations. However, there currently exists no widely accepted model which allows for predictive determination of the elasto-optic tensor elements for all glass families.

In the following sections, these previously developed theories and models of elasto-optical properties of materials will be presented and discussed. Particular emphasis will be placed on their successes and failures in predicting p_{ij} and their applicability or extension to glassy networks.

2.2.1 Clausius-Mossotti Model

Perhaps the simplest model for the elasto-optic response of a material is derived from the Clausius-Mossotti relation. This equation relates the dielectric constants (or refractive index) of a material to its polarizability. The relation holds well for isotropic, homogeneous materials such as gases, and can sometimes be applied to other less perfect liquids and solids; see pp. 458–460 of [3], [7].

Typically, the total polarization $\mathbf{P}$ of a material is related to electric field $\mathbf{E}$ as

$$\mathbf{P} = (\epsilon - 1)\epsilon_0 \mathbf{E} = \chi \mathbf{E}, \tag{2.12}$$

where ϵ is the dielectric constant of the material, ϵ_0 is the permittivity of vacuum, and χ represents the total polarizability. Assuming that the total polarization results from a sum of N_L dipoles per unit volume, then

$$\mathbf{P} = N_L \alpha \mathbf{E}', \tag{2.13}$$

where each dipole has mean polarizability α, and $\mathbf{E}'$ is the local electric field on the average dipole. For dense dielectrics (including glass), the local field is the sum of the macroscopic field and a Lorentz field contribution dependent on polarization:

$$\mathbf{E}' = \mathbf{E} + \frac{1}{3\epsilon_0}\mathbf{P}. \tag{2.14}$$

Then, combining Equations 2.12, 2.13 and 2.14 along with $4\pi\epsilon_0 = 1$ gives the Clausius-Mossotti equation:

$$\frac{\epsilon - 1}{\epsilon + 2} = \frac{4\pi N_L \alpha}{3} = \frac{4\pi N \alpha}{3V_m} = \frac{4\pi N \rho \alpha}{3M}, \tag{2.15}$$

where N is Avogadro's number, V_m is the molar mass, M is the weight and ρ is the density of the material. Note that substituting $\epsilon = n^2$ gives the Lorentz-Lorenz equation:

$$\frac{4\pi N \alpha}{3} = V_m \frac{n^2 - 1}{n^2 + 2} = R_m, \tag{2.16}$$

where R_m is called the molar refractivity.

By observing the change in Equation 2.15 with respect to density, and assuming for the perfect, isotropic, homogeneous material that α has no density dependence (or in other words, $d\alpha/d\rho = 0$), the dielectric response of a glass can be related to the elasto-optic tensor elements by

$$3\rho\frac{d\epsilon}{d\rho} = \epsilon^2(p_{11} + 2p_{12}) = (\epsilon - 1)(\epsilon + 2). \tag{2.17}$$

On its own, this model does not fit the experimental results of diverse glass systems. Other models often consider this as one of the terms contributing to the photoelastic response [8–11].

2.2.2 Mueller's Model

Mueller's theory of photoelasticity for amorphous solids incorporates two additional effects to the Lorentz-Lorenz model: changes in the Lorentz-Lorenz forces in the solid (the lattice effect), as well as changes in the mean polarizabilities (the atomic effect) due to strain deformations in the material [8, 9]. The local electric field on an average dipole in a material is given by Equation 2.14; the Lorentz-Lorenz equation is given for multi-atom systems by

$$\frac{n^2 - 1}{n^2 + 2} = \rho \sum \frac{4\pi N \alpha_i}{3M_i}, \tag{2.18}$$

where the sum is over atoms of the type i. However, this equation is valid for homogeneous, isotropic materials. When a small strain z is applied to the material, it will deform the network of atoms. This deformation will change the Lorentz-Lorenz force in a way which depends on the local electric field. If a material is deformed in the z-direction is such that the strain ellipsoid has the axial ratio 1:1:1+z, the components of the local electric field become

$$\begin{aligned} E'_x &= E_x + \frac{P_x}{\epsilon_0}\left(\frac{1}{3}+\frac{2}{15}z\right), \\ E'_y &= E_y + \frac{P_y}{\epsilon_0}\left(\frac{1}{3}+\frac{2}{15}z\right), \\ E'_z &= E_z + \frac{P_z}{\epsilon_0}\left(\frac{1}{3}-\frac{4}{15}z\right). \end{aligned} \tag{2.19}$$

The indices of refraction are found from substituting Equations 2.12 and 2.13 into Equation 2.19:

$$\begin{aligned} n_x^2 - 1 &= \sum \frac{4\pi N\rho\alpha_i}{M_i}\left[1+\left(\frac{1}{3}+\frac{2}{15}z\right)\frac{n_x^2-1}{\epsilon_0}\right], \\ n_y^2 - 1 &= \sum \frac{4\pi N\rho\alpha_i}{M_i}\left[1+\left(\frac{1}{3}+\frac{2}{15}z\right)\frac{n_y^2-1}{\epsilon_0}\right], \\ n_z^2 - 1 &= \sum \frac{4\pi N\rho\alpha_i}{M_i}\left[1+\left(\frac{1}{3}-\frac{4}{15}z\right)\frac{n_z^2-1}{\epsilon_0}\right]. \end{aligned} \tag{2.20}$$

Differentiating these terms about $z = 0$, and considering α to be constant with respect to z, the elasto-optic tensor elements become

$$\begin{aligned} p_{12} &= \frac{1}{3}\frac{(\epsilon-1)(\epsilon+2)}{\epsilon^2} - \frac{2}{15}\frac{(\epsilon-1)^2}{\epsilon^2}, \\ p_{11} &= \frac{1}{3}\frac{(\epsilon-1)(\epsilon+2)}{\epsilon^2} + \frac{4}{15}\frac{(\epsilon-1)^2}{\epsilon^2}. \end{aligned} \tag{2.21}$$

According to Mueller, the first term in Equation 2.21 is due to the change in density with strain; its large magnitude does explain why p_{11} and p_{12} always have positive value. The second term in the equation gives birefringence due to anisotropy of the Lorentz-Lorenz forces. The shear elasto-optic coefficient is then $2p_{44} = p_{11} - p_{12} = (n^2-1)^2/15n^4$. While of the correct order of magnitude, this prediction does not describe the positive and negative stress-optic response of glasses.

Thus Mueller considered a second effect – the change in polarizability of the atoms – to account for the positive and negative birefringence in glasses. Since the photoelastic effect tends to behave linearly, he considered linear response in α with strain:

$$\begin{aligned} \alpha_z &= \alpha(1+\lambda_1 z), \\ \alpha_{x,y} &= \alpha(1+\lambda_2 z). \end{aligned} \tag{2.22}$$

Then the elasto-optic tensor elements become

$$\begin{aligned} p_{12} &= \frac{1}{3}\frac{(\epsilon-1)(\epsilon+2)}{\epsilon^2} - \frac{2}{15}\frac{(\epsilon-1)^2}{\epsilon^2} - \frac{L_2}{3}\frac{(\epsilon-1)(\epsilon+2)}{\epsilon^2}, \\ p_{11} &= \frac{1}{3}\frac{(\epsilon-1)(\epsilon+2)}{\epsilon^2} + \frac{4}{15}\frac{(\epsilon-1)^2}{\epsilon^2} - \frac{L_1}{3}\frac{(\epsilon-1)(\epsilon+2)}{\epsilon^2}, \\ 2p_{44} &= p_{11} - p_{12} = \frac{(L_2-L_1)}{3}\frac{(\epsilon-1)(\epsilon+2)}{\epsilon^2} + \frac{6}{15}\frac{(\epsilon-1)^2}{\epsilon^2}, \end{aligned} \tag{2.23}$$

where L_1 and L_2 are the optical deformabilities of the atoms' polarizabilities, defined by $L_{1,2} = \sum(\lambda_{1,2}N\alpha/M)_i/\sum(N\alpha/M)_i$. Depending on the values of L_1 and L_2, materials can have positive, negative or zero birefringence. Typically the deformabilities are fitted to experimental results, with $0.6 \leq L_1 \leq 1.0$ and $0.1 \leq L_2 \leq 0.3$ depending on glass composition [10].

The elasto-optic tensor element p_{44} given in Equation 2.23 is related to the stress-optic coefficient of a glass. According to Mueller's theory, the lattice term ($\frac{6}{15}\frac{(\epsilon-1)^2}{\epsilon^2}$) will be larger in heavier glasses, since their refractive indices are larger. This theory is often used to relate measured values of C to the structure, arrangement of molecules, and deformations in glass due to stress. However, due to the inclusion of the experimentally determined L_1 and L_1, the predictive power is limited.

2.2.3 Carleton's Model

Carleton's expressions derived for the elasto-optical coefficients [12] are quite similar to Mueller's:

$$\begin{aligned} p_{11} &= \frac{1}{3}\frac{(\epsilon-1)(\epsilon+2)}{\epsilon^2} + \frac{4}{15}\frac{(\epsilon-1)^2}{\epsilon^2} + \frac{14}{15}\frac{(\epsilon-1)^2}{\epsilon^2}\Gamma, \\ p_{12} &= \frac{1}{3}\frac{(\epsilon-1)(\epsilon+2)}{\epsilon^2} - \frac{2}{15}\frac{(\epsilon-1)^2}{\epsilon^2} + \frac{8}{15}\frac{(\epsilon-1)^2}{\epsilon^2}\Gamma, \\ 2p_{44} &= \frac{6}{15}\frac{(\epsilon-1)^2}{\epsilon^2} + \frac{6}{15}\frac{(\epsilon-1)^2}{\epsilon^2}\Gamma, \end{aligned} \tag{2.24}$$

where the correlation term Γ is

$$\Gamma = 3\alpha\int_0^\infty \frac{g_{12}(r)}{r^4}dr, \tag{2.25}$$

and $g_{12}(r)$ is a two-particle correlation function. Carleton developed the strain dependence of the dielectric constant based on the Fixman formulation for ϵ. He defines the correlation term as $\Gamma = (\alpha/\alpha_0)\Gamma_0$, where $\alpha_0 = r_0^3$ and r_0 is the classical molecular radius. The term Γ_0 has values ranging from 0.375 for a highly correlated system to 0.125 for an uncorrelated model.

These equations are sometimes presented as

$$\begin{aligned} p_{11} &= \frac{1}{3}\frac{(\epsilon-1)^2}{\epsilon^2}\left(\frac{3M}{4\pi N\alpha\rho} + \frac{4}{15} - \frac{14}{15}\Gamma\right), \\ p_{12} &= \frac{1}{3}\frac{(\epsilon-1)^2}{\epsilon^2}\left(\frac{3M}{4\pi N\alpha\rho} - \frac{2}{15} - \frac{8}{15}\Gamma\right), \\ 2p_{44} &= \frac{2}{5}\frac{(\epsilon-1)^2}{\epsilon^2}\left(1-\Gamma\right), \end{aligned} \tag{2.26}$$

where $(\epsilon+2)/(\epsilon-1) = 3M/(4\pi N\rho\alpha)$. In this way, it is argued that p_{12} has greater direct density dependence than p_{44} coming from the Lorentz-Lorenz term [10, 13].

2.2.4 Bond-Orbital Model

Bond-orbital models for photoelasticity were developed by Harrison, Biegelsen and Wemple and applied to crystalline solids [14–17]. These model are used to determine the dependence of the dipole moments and dielectric constant on other physical properties, after which the hydrostatic elasto-optic coefficient is found from

$$p_h = \frac{1}{3}\left(p_{11} + 2p_{12}\right) = -\frac{(\epsilon-1)}{3\epsilon^2}\frac{d\ln(\epsilon-1)}{d\ln r}, \tag{2.27}$$

where r is the interatomic distance. Some consideration was given by Wemple to amorphous systems; however, the most thorough application of the model to the photoelastic effect was given by Lines for ionic, covalent and amorphous limits [18]. Lines hypothesized that the optical properties of non-metals depend predominantly on nearest-neighbour environments and bonding characteristics in the material; as such, a bond-orbital theory should do a better job at describing the dielectric response than those focusing on energy band gaps or oscillator strengths. This model also allows both bond-length dependent and independent parameters to be distinguished.

For the derivation, we consider a material with composition C_mA_n, where C denotes the cation and A the anion species. We first assume that there is only one type of cation-anion bond in the system, made up of a linear combination of atomic orbitals $|h_C\rangle$ and $|h_A\rangle$, each unique and specific to the cation or anion. Bonding and antibonding combinations are formed from linear combinations of these atomic orbitals; the normalized bonding orbitals are

$$|b\rangle = u_C|h_C\rangle + u_A|h_A\rangle. \tag{2.28}$$

The equilibrium bond configuration is found by minimizing the bond energy E with respect to the bonding coefficients, where the energy is defined by

$$E = \frac{\langle b|\mathcal{H}|b\rangle}{\langle b|b\rangle} = \frac{u_A^2\epsilon_A + u_c^2\epsilon_C - 2u_Au_CM}{u_A^2 + u_C^2 + 2u_Au_CS}, \tag{2.29}$$

and $\epsilon_{C,A} = \langle h_{C,A}|\mathcal{H}|h_{C,A}\rangle$ are the intra-atomic matrix elements of the one-electron Hamiltonian $\mathcal{H}$. The interatomic matrix element $\langle h_A|\mathcal{H}|h_C\rangle$ is given by $-M$, while S is the overlap integral $\langle h_C|h_A\rangle$. Partially minimizing the energy with respect to u_A and u_C leads to the conditions

$$\begin{pmatrix} E-\epsilon_A & ES+M \\ ES+M & E-\epsilon_C \end{pmatrix} \begin{pmatrix} u_A \\ u_C \end{pmatrix} = 0, \tag{2.30}$$

which is nontrivial when the determinant of the matrix is set to zero, or in other words $(ES+M)^2 = (E-\epsilon_A)(E-\epsilon_C)$. If absolute energies are measured relative to the reference point $\epsilon_A + \epsilon_C = 0$, then the minimum energy occurs at

$$E = \frac{SM}{1-S^2} - \left(\frac{M^2}{(1-S^2)^2} - \frac{\epsilon_A\epsilon_C}{1-S^2}\right)^{1/2}. \tag{2.31}$$

Then, substituting this energy back into the energy matrix, we find the normalization coefficients

$$\begin{aligned} u_C &= \pm\left[\frac{1}{2}\left(\frac{1-S\alpha_C}{1-S^2} - \frac{(1-\alpha_C^2)^{1/2}}{(1-S^2)^{1/2}}\right)\right]^{1/2}, \\ u_A &= \left[\frac{1}{2}\left(\frac{1-S\alpha_C}{1-S^2} + \frac{(1-\alpha_C^2)^{1/2}}{(1-S^2)^{1/2}}\right)\right]^{1/2}, \end{aligned} \tag{2.32}$$

where α_C is a measure of the covalency,

$$\alpha_C = \frac{M}{1-S^2}\left(\frac{M^2}{(1-S^2)^2} - \frac{\epsilon_A\epsilon_C}{1-S^2}\right)^{-1/2}. \tag{2.33}$$

The pure covalent limit is given by $u_C \to u_A$, $r \to 0$ and $\alpha_C \to 1$. The pure ionic limit has $\epsilon_C - \epsilon_A \to \infty$, $\alpha_c \to 0$ and $u_C/u_A < 0$; however, this is impractical for all known chemical bonds. The limit for real ionic systems tends to $u_C = 0$, $u_A = 1$ and $\alpha_C = S$.

The bulk dielectric constant in a material is

$$\epsilon = 1 + \frac{4\pi}{3}\frac{Nz_b\rho}{M}\chi_b, \tag{2.34}$$

where z_b is the mean number of bonds per molecular unit in the structure. The results of the bond-orbital model are used to determine the individual bond polarizability χ_b.

In the presence of an applied electric field, the dipole moment per one-electron e bond is

$$\langle b|ex|b\rangle = p_b = p_b^0 + \chi_b E, \tag{2.35}$$

where x is the distance along the bond measured from the point where $\langle h_C|x|h_A\rangle = 0$. Assuming that x is close to the intersection point of the ionic radii R_A and R_C, the bond dipole moment can be written as

$$\langle b|ex|b\rangle = u_C^2\langle h_c|ex|h_c\rangle + u_A^2\langle h_A|ex|h_A\rangle = -e\gamma_C R_C u_C^2 + e\gamma_A R_A u_A^2, \tag{2.36}$$

where the internuclear bond length is give by $R_C + R_A = d$, and γ_A and γ_C are in general less than 1 (they are 1 exactly for unhybridized atomic orbitals centered at the appropriate atomic nuclei). With the previous definitions for u_C and u_A, the bond dipole moment becomes

$$\langle b|ex|b\rangle = \frac{e}{2}\left[\left(\frac{1-\alpha_C^2}{1-S^2}\right)^{1/2}\left(\frac{\gamma_A R_A + \gamma_C R_C}{R_A + R_C}\right)d + \frac{1 - S\alpha_C}{1-S^2}(\gamma_A R_A - \gamma_C R_C)\right] \tag{2.37}$$

This term must be added to the original one-electron Hamiltonian field. Using the fact that $\langle b|b\rangle \approx 1$, the field can be comprehensively written as

$$\begin{aligned} E = &-\left(\frac{1-\alpha_C^2}{1-S^2}\right)^{1/2}(-\epsilon_A\epsilon_C) - \frac{M}{1-S^2}\left(-S + \alpha_C\right) \\ &- \frac{e}{2}\left(\frac{1-\alpha_C^2}{1-S^2}\right)^{1/2}\left(\frac{\gamma_A R_A + \gamma_C R_C}{R_A + R_C}\right)dE_i - \frac{e}{2}\frac{\gamma_A R_A - \gamma_C R_C}{1-S^2}(1 - S\alpha_C)E_i. \end{aligned} \tag{2.38}$$

At this point, Lines expands $(1-\alpha_C^2)^{1/2}$ as a Taylor series in a local field E_i, and equates this to the individual bond polarizabilities:

$$\chi_b = \frac{e^2\alpha_C^2 f}{2\left(\frac{M^2}{1-S^2} - \epsilon_A\epsilon_C\right)}\left[\frac{\gamma_A R_A + \gamma_C R_C}{R_A + R_C}d - \epsilon_A\epsilon_C S(\gamma_A R_A - \gamma_C R_C)\right]^2, \tag{2.39}$$

where f is the oscillator strength.

The value Lines was primarily interested in measuring is the dimensionless quantity Λ, where

$$1 - \Lambda = \frac{\partial \ln \chi}{\partial \ln \rho} \tag{2.40}$$

and as in previous sections, $\chi = (\epsilon - 1)\epsilon_0$ is the polarizability of the material. The hydrostatic photoelastic coefficient can be written in terms of the volume V or density ρ dependence of the refractive index n or dielectric constant ϵ as

$$p_h = V\left(\frac{\partial n^{-2}}{\partial V}\right) = -\rho\left(\frac{\partial n^{-2}}{\partial \rho}\right) = \frac{\rho}{\epsilon^2}\left(\frac{\partial \epsilon}{\partial \rho}\right). \tag{2.41}$$

Then the parameter Λ can be related to the photoelasticity of the material by

$$1 - \Lambda = \frac{\epsilon^2}{\epsilon - 1} p_h. \tag{2.42}$$

We also note that within the context of the bond-orbital theory, Λ is directly representative of the density dependence of the individual bond polarizability χ_b,

$$\Lambda = -\frac{\partial \ln \chi_b}{\partial \ln \rho}. \tag{2.43}$$

For three-dimensional structures, we can assume $\rho \propto d^{-3}$ to get

$$\Lambda = \frac{d}{3\chi_b}\frac{\partial \chi_b}{\partial d}. \tag{2.44}$$

The term for the individual bond polarizability can be used to predict the value Λ; however, some d-dependence in the parameters S, M, f, $\gamma_{A,C}$, and $R_{A,C}$ has to be assumed. According to Lines, for small variations of d around equilibrium, these dependencies are

$$\begin{aligned} d^{-n} &\propto \frac{M^2}{1 - S^2}, \\ d^m &\propto \frac{e^2 f}{2(1 - S^2)^{1/2}}\left(\frac{\gamma_A R_A + \gamma_C R_C}{R_A + R_C}\right)^2, \\ d^p &\propto \frac{-\epsilon_A \epsilon_C S}{M}\frac{\gamma_A R_A - \gamma_C R_C}{\gamma_A R_A + \gamma_C R_C} = u, \end{aligned} \tag{2.45}$$

and then the value of interest Λ can be written as

$$\Lambda = \frac{2}{3}(1 - n) + n\alpha_c^2 + \frac{m}{3} + \frac{2}{3}\frac{pu}{(1 + u)}. \tag{2.46}$$

To determine some limitations on this equation, Lines turned to experimental results from alkali halides. Here, in the quasi-ionic limit, Λ tends to 0 as $R_A \to R_C$. Also for this group, $\gamma_A = \gamma_C = 1$, so that $u = 0$. These equivalences yield the condition

$$0 = \frac{2}{3}(1-n) + nS^2 + \frac{m}{3}, \tag{2.47}$$

which is assumed to be universal. Thus this result is substituted into the equation for Λ, giving the generalized relationship

$$\Lambda = n(\alpha_c^2 - S^2) + \frac{2}{3}\frac{pu}{(1+u)}. \tag{2.48}$$

According to previous bond-orbital work [17], the measure of covalency can be related to the formal anion valence by $\alpha_C \approx Z_a/4$. For oxides, the value S tends to 1/2 experimentally, and $\gamma_A \approx \gamma_C$, which gives the simplification

$$u = \left(\frac{4 - Z_A}{3Z_A}\right)^{1/2} \left[\frac{R_A - R_C}{R_A + R_C}\right]. \tag{2.49}$$

Then Λ, which itself can be related to the elasto-optical coefficients, can be expressed in terms of dielectric constants, anion-cation bond lengths d and constants of power n and p. It is likely that these powers will depend on glass composition, which limits the predictive power of this model.

2.2.5 Dipole-Induced-Dipole (DID) Theory

Another theory developed to evaluate photoelasticity in isotropic materials predicts that only the refractive index of the material is influential on the elasto-optic coefficients. This theory, initially proposed by Mazzacurati [19] and later compared to experiment by Benassi [20, 21], assumes that the material is made up of individual units with spherical polarizabilities. First, the microscopic polarizability density tensor is used to determine the scattering equations of the material. Then, the dipole-induced-dipole (DID) model is applied to refine the microscopic electric properties and relate them to the photoelasticity.

The spectral density of scattered light can be written

$$J(\mathbf{q},\omega) = I_0 \frac{\omega_I \omega_S^3}{2\pi c^4} \Delta\Omega \int dt e^{i\omega t} \langle [\hat{\mathbf{m}} \cdot \underline{\widetilde{P}}(\mathbf{q},t) \cdot \hat{\mathbf{n}}][\hat{\mathbf{m}} \cdot \underline{\widetilde{P}}(\mathbf{q},0) \cdot \hat{\mathbf{n}}]^* \rangle \tag{2.50}$$

where $\widetilde{P}(\mathbf{q},t)$ is the Fourier transform of the macroscopic polarizability tensor $P(\mathbf{r},t)$,

$$\widetilde{P}_{\alpha\beta}(\mathbf{q},t) = \int d\mathbf{r} e^{-i\mathbf{q}\cdot\mathbf{r}} P_{\alpha\beta}(\mathbf{r},t), \tag{2.51}$$

$\Delta\Omega$ is the solid angle over which light is collected, I_0 is the intensity of incident light, $\hat{\mathbf{m}}$ and $\hat{\mathbf{n}}$ are the polarization unit vectors of the scattered (m) and incoming (n) radiation, $\hbar\omega_I$ and $\hbar\omega_S$ are the energies of incoming and scattered photons, and $\hbar\omega = \hbar\omega_I - \hbar\omega_S$ and $\mathbf{q} = \mathbf{k}_I - \mathbf{k}_S$ are the exchanged energy and wave vector. The values within the $\langle ... \rangle$ symbol are thermally averaged. The intensity of scattered light is then given by

$$I(\mathbf{q}) = \int d\omega J(\mathbf{q},\omega) = I_0 \frac{\omega_I \omega_S^3}{c^4} \Delta\Omega \langle |\hat{\mathbf{m}} \cdot \underline{\widetilde{P}}(\mathbf{q},0) \cdot \hat{\mathbf{n}}|^2 \rangle. \tag{2.52}$$

The macroscopic polarizability can be written in terms of the effective microscopic polarizability tensor of individual units within the dielectric material, $\pi^i_{\alpha\beta}(t)$:

$$\widetilde{P}_{\alpha\beta}(\mathbf{q},t) = \sum_i \pi^i_{\alpha\beta}(t) e^{-i\mathbf{q}\cdot\mathbf{r}^i(t)} \tag{2.53}$$

where i indicates the ith molecule, ion, atom, etc and $\mathbf{r}^i(t)$ is the instantaneous position of the ith unit. (The value π^i is the same as χ_i defined in previous sections, where $P = \pi E$; however, we will continue with the notation of Benassi et al. for this derivation.) For solids, we write $\mathbf{r}^i(t) = \mathbf{x}^i + \mathbf{u}^i(t)$, where $\mathbf{x}^i$ is the equilibrium position of the ith unit, and $\mathbf{u}^i(t)$ is the displacement from equilibrium. If the displacement is much smaller than the nearest-neighbour distance, then we can expand P in terms of $\mathbf{u}^i$:

$$\delta\widetilde{P}_{\alpha\beta}(\mathbf{q},t) = \sum_i \sum_\mu L^i_{\alpha\beta,\mu}(\mathbf{q}) e^{-i\mathbf{q}\cdot\mathbf{x^i}} u^i_\mu(t), \tag{2.54}$$

where here the equilibrium properties of the system are $L^i_{\alpha\beta,\mu}(\mathbf{q}) = -i\pi^i_{\alpha\beta} q_\mu - Q^i_{\alpha\beta,\mu}(\mathbf{q})$, $\pi^i_{\alpha\beta}$ is the equilibrium unit polarizability, and

$$Q^i_{\alpha\beta,\mu}(\mathbf{q}) = \sum_m \left[\frac{\partial \pi^m_{\alpha\beta}}{\partial u^i_\mu}\right]_{eq} e^{i\mathbf{q}\cdot[\mathbf{x}^m - \mathbf{x}^i]}. \tag{2.55}$$

From their normal mode expansion, the displacements can be written

$$u^i_\mu(t) = \sqrt{\frac{\hbar}{2mN}} \sum_{\mathbf{k},\chi} \frac{e_\mu(\mathbf{k},\chi)}{\sqrt{\omega_{\mathbf{k}\chi}}} \hat{A}_{\mathbf{k}\chi}(t) e^{i\mathbf{k}\cdot\mathbf{x}^i}. \tag{2.56}$$

where $\hat{A}_{\mathbf{k}\chi}(t)$ are the phonon field operators with wave vector $\mathbf{k}$ and branch index χ. For isotropic materials like glass, we can assume that the property L^i is site dependent such that it can be written in terms of an average local equilibrium value L, and a small deviation about this value δL:

$$L^i_{\alpha\beta,\mu}(\mathbf{q}) = L_{\alpha\beta,\mu}(\mathbf{q}) + \delta L^i_{\alpha\beta,\mu}(\mathbf{q}), \tag{2.57}$$

where $L_{\alpha\beta,\mu}(\mathbf{q}) = \frac{1}{N}\sum_i L^i_{\alpha\beta,\mu}(\mathbf{q})$. Then the fluctuation of P is given by two terms. The first is crystalline like in nature, with site-averaged quantity L. The second comes from the disordered structure, with deviating δL. This term is incoherent, and does not contribute to the Brillouin peaks. Ignoring the incoherent component, $\delta\widetilde{P}$ becomes

$$\begin{aligned}
\delta\widetilde{P}_{\alpha\beta}(\mathbf{q},t) &= \sqrt{\frac{\hbar}{2mN}}\sum_\mu L_{\alpha\beta,\mu}(\mathbf{q})\sum_{\mathbf{k},\chi}\frac{e_\mu(\mathbf{k},\chi)}{\sqrt{\omega_{\mathbf{k}\chi}}}\hat{A}_{\mathbf{k}\chi}(t)\sum_i e^{i(\mathbf{k}-\mathbf{q})\cdot\mathbf{x^i}} \\
&= \sqrt{\frac{\hbar}{2mN}}\sum_\mu L_{\alpha\beta,\mu}(\mathbf{q})\sum_{\mathbf{k},\chi}\frac{e_\mu(\mathbf{k},\chi)}{\sqrt{\omega_{\mathbf{k}\chi}}}\hat{A}_{\mathbf{k}\chi}(t)N\delta_{\mathbf{kq}} \\
&= \sqrt{\frac{\hbar N}{2m}}\sum_\chi\sum_\mu e_\mu(\mathbf{q},\chi)L_{\alpha\beta,\mu}(\mathbf{q})\frac{\hat{A}_{\mathbf{q}\chi}(t)}{\sqrt{\omega_{\mathbf{q}\chi}}}.
\end{aligned} \tag{2.58}$$

The scattered light intensity can then be determined:

$$I(\mathbf{q}) = I_0 V\rho^2\frac{\omega_I\omega_S^3}{c^4}\Delta\Omega k_B T\sum_\chi\frac{1}{\rho_m v_\chi^2}\left|\frac{1}{|\mathbf{q}|}\sum_\mu \hat{\mathbf{m}}\cdot\underline{L}_\mu(\mathbf{q})e_\mu(\mathbf{q},\chi)\cdot\hat{\mathbf{n}}\right|^2, \tag{2.59}$$

where $\rho = \rho_m/m$ is the number density.

We can relate $L_{\alpha\beta,\mu}$ to the elasto-optic constants by comparing the macroscopic and microscopic polarizability fluctuations. The microscopic polarization is rewritten as

$$\delta\widetilde{P}_{\alpha\beta}(\mathbf{q},t) = \rho\sum_\mu L_{\alpha\beta,\mu}(\mathbf{q})\widetilde{u}_\mu(\mathbf{q},t) \tag{2.60}$$

where $\widetilde{u}_\mu(\mathbf{q},t) = \int d\mathbf{r}e^{-i\mathbf{q}\cdot\mathbf{r}}u_\mu(\mathbf{r},t)$ is the Fourier transform of the displacements. The macroscopic polarizability fluctuation can be obtained from three things: the dielectric tensor:

$$4\pi P_{\alpha\beta}(\mathbf{r},t) = \epsilon_{\alpha\beta}(\mathbf{r},t) - \delta_{\alpha\beta}, \tag{2.61}$$

the definition of elasto-optic constants $P_{\alpha\beta\gamma\delta}$:

$$\delta\epsilon_{\alpha\beta}(\mathbf{r},t) = -\epsilon^2 \sum_{\gamma\delta} P_{\alpha\beta\gamma\delta}\sigma_{\gamma\delta}(\mathbf{r},t) \tag{2.62}$$

and the relation between strain tensor and displacement fields:

$$\sigma_{\gamma\delta} = \frac{1}{2}\left(\frac{\partial u_\gamma(\mathbf{r},t)}{\partial r_\delta} + \frac{\partial u_\delta(\mathbf{r},t)}{\partial r_\gamma}\right). \tag{2.63}$$

Combining these equations yields

$$\delta\widetilde{P}_{\alpha\beta}(\mathbf{q},t) = \frac{-i\epsilon^2}{4\pi}\sum_\mu \widetilde{u}_\mu(\mathbf{q},t)\frac{1}{2}\sum_\gamma q_\gamma(P_{\alpha\beta\gamma\mu} + P_{\alpha\beta\mu\gamma}). \tag{2.64}$$

We can then combine microscopic and macroscopic terms to get

$$L_{\alpha\beta,\mu}(\mathbf{q}) = \frac{-i\epsilon^2}{4\pi\rho}\sum_\gamma q_\gamma \frac{1}{2}(P_{\alpha\beta\gamma\mu} + P_{\alpha\beta\mu\gamma}) \tag{2.65}$$

which, for isotropic solids, simplifies to

$$L_{\alpha\beta,\mu}(\mathbf{q}) = \frac{-i\epsilon^2}{4\pi\rho}|\mathbf{q}|\left(\delta_{\alpha\beta}p_{12}\hat{q}_\mu + (\delta_{\alpha\mu}\hat{q}_\beta + \delta_{\beta\mu}\hat{q}_\alpha)p_{44}\right). \tag{2.66}$$

In order to evaluate $L_{\alpha\beta,\mu}(\mathbf{q})$, the material is considered in its simplest case to be a van der Waals glass, made up of point-polarizable units with polarizability $\alpha\delta_{\alpha\beta}$. The total polarizability is

$$\pi^i_{\alpha\beta}(t) = \alpha\delta_{\alpha\beta} + \alpha\sum_{j\neq i}\sum_\gamma \left[\nabla_\alpha\nabla_\gamma\left(\frac{1}{\mathbf{r}^{ij}(t)}\right)e^{-i\mathbf{k}_I\cdot\mathbf{r}^{ij}(t)}\right]\pi^j_{\gamma\beta}(t). \tag{2.67}$$

Here, we notice that the polarizability of the ith unit is related to that of all other units in the material. The equilibrium polarizability is

$$\pi_{\alpha\beta} = \frac{1}{N}\sum_i \pi^i_{\alpha\beta} = \alpha\delta_{\alpha\beta} + \frac{\alpha}{N}\sum_i\sum_{j\neq i}\sum_\gamma\left[\nabla_\alpha\nabla_\gamma\left(\frac{1}{\mathbf{x}^{ij}(t)}\right)e^{-i\mathbf{k}_I\cdot\mathbf{x}^{ij}(t)}\right]\pi^j_{\gamma\beta}(t). \tag{2.68}$$

We can relate this to the dielectric constant through the equilibrium polarizability density tensor:

$$\epsilon_{\alpha\beta} = 4\pi P^{eq}_{\alpha\beta}(\mathbf{r},t) + \delta_{\alpha\beta} = 4\pi\rho\pi_{\alpha\beta}(\mathbf{k}_I) + \delta_{\alpha\beta}. \tag{2.69}$$

Since in isotropic materials, off-diagonal elements of the equilibrium dielectric tensor are zero, we can write $\epsilon_{\alpha\beta} = \epsilon\delta_{\alpha\beta}$ such that

$$\pi_{\alpha\beta}(\mathbf{k}_I) = \frac{\epsilon - 1}{4\pi\rho}\delta_{\alpha\beta}. \tag{2.70}$$

This can then be used to determine the first term in L:

$$-i\pi_{\alpha\beta}q_\mu = -i\frac{\epsilon - 1}{4\pi\rho}\delta_{\alpha\beta}\hat{q}_\mu|\mathbf{q}|. \tag{2.71}$$

The second term in L can be determined through the value $Q_{\alpha\beta,\mu}(\mathbf{q})$. This is done by evaluating the equilibrium value for $\partial\pi^m_{\alpha\beta}/\partial u^i_\mu$, where $\pi^m_{\alpha\beta}$ is the effective polarizabililty for a van der Waals glass as defined above. The zeroth-order expression for Q is also defined as above, where the j terms tend to equilibrium. By relating the i and j dependent sums in Q to integrals of pair-correlation functions $g(\mathbf{r})$, evaluating these integrals, and simplifying the expression for isotropic conditions, we end with

$$Q_{\alpha\beta,\mu}(\mathbf{q}) = i\frac{4\pi}{5}\rho|\mathbf{q}|\left(\delta_{\alpha\beta}\hat{q}_\mu + \delta_{\alpha\mu}\hat{q}_\beta + \delta_{\beta\mu}\hat{q}_\alpha\right). \tag{2.72}$$

Then, we can substitute this result into the second term of L and use the Lorentz-Lorenz equation to determine the complete expression

$$L_{\alpha\beta,\mu}(\mathbf{q}) = -i\frac{\epsilon - 1}{4\pi\rho}|\mathbf{q}|\left[\delta_{\alpha\beta}\hat{q}_\mu\left(1 + \frac{\epsilon - 1}{5}\right) + \frac{\epsilon - 1}{5}\left(\delta_{\alpha\mu}\hat{q}_\beta + \delta_{\beta\mu}\hat{q}_\alpha\right)\right]. \tag{2.73}$$

This procedure yields the relationships

$$p_{12} = \frac{\epsilon - 1}{\epsilon^2}\left[1 + \frac{\epsilon + 1}{5}\right] \tag{2.74}$$

and

$$p_{44} = \frac{\epsilon - 1}{\epsilon^2}\left[\frac{\epsilon - 1}{5}\right], \tag{2.75}$$

which allows prediction of the elasto-optic tensor elements based on knowledge of the dielectric response in the material.

2.2.6 Discussion of Models and Theories for p_{ijkl}

The Clausius-Mossotti (or Lorentz-Lorenz) model of photoelasticity is derived for ideal, homogeneous isotropic materials. It can be applied to some solids and glasses, but it is not universal. Thus $\epsilon^2(p_{11} + 2p_{12}) = (\epsilon - 1)(\epsilon + 2)$ cannot be universally applied to all glass systems. However, it gets the sign of the response right; p_{11} and p_{12} are found experimentally to be positive, and $\epsilon = n^2$ is always greater than 1. The model also assumes that the change in polarizability with density is zero in glasses. However, following the derivation of Lines, we find that this may not always be the case, which would affect how the elasto-optic coefficients behave with refractive index.

Mueller and Carleton's models are limited in that the experimental photoelastic results must be fitted in order to determine L_1 and L_2 (or Γ). These models are typically used to determine which effects (Lorentz-Lorenz, lattice or atomic) are dominating for a given sample. For example, if p_{44} is negative, the atomic effect must be the primary contributor to photoelasticity, or if p_{12} is large then the lattice effect is dominant. However, the models cannot be used to predict the sign or magnitude of the photoelastic response for new, unmeasured glass systems.

The photoelastic theory derived from Line's bond-orbital model is, again, not predictive. With enough experimental data, the experimental Λ measured from the photoelastic response can be compared to the theoretical value predicted from Equation 2.48. However, a fair number of assumptions must be made in order to determine parameters such as the covalency and the d-dependence of S, M, f, etc. It is interesting that this model includes a dependency on bond length d, which is one of the main parameters in the empirical model.

The model based on DID theory shows inconsistencies between predictions and experimental results, especially in p_{44}. Indeed, the relationship given in Equation 2.75 does not account for the zero and negative stress-optic response that glasses are known to have. The failure of this model is likely due to the assumption of a pure van der Waals glass as the material of interest. This model is a poor fit for real glass systems made up of ionic and covalent bonding environments. The authors suggested improving the predictions by including a bond polarizability model to account for the existence of differently polarizable compounds; however, not much progress was made on this front.

All of the models considered show a dependency on the refractive index of the material. Bond polarizabilities and bond lengths were also considered to be important contributors to p_{ij}. By examining the photoelastic response of positive and negative stress-optic glasses with different glass formers, we aim to identify relevant properties that affect the elasto-optic tensor elements.

2.3 Theories of Photoelasticy: Dispersion of p_{ijkl} in Amorphous and Crystalline Materials

While information on the dispersive nature of the stress-optic coefficient of glasses is limited, there are a few theories concerning the wavelength dependence of the photoelastic response of crystalline and amorphous materials. Due to their anisotropic structures, it is possible to measure most or all independent elasto-optic tensor elements through the stress-induced phase shifts along different symmetry axes. The broadband character of these tensor elements is often determined using ellipsometry; materials such as Si [22, 23], Ge, GaAs, InP, and GaP [24–28], cuprous halides [14], alkali halides [29] and even fused silica [30] have been measured.

Most analysis of the wavelength dependence of p_{ijkl} discusses the energy band structures of crystalline materials. Band gaps can be direct, i.e. occurring at the same wavevector k, or indirect, where the energy gap occurs at different values of k. Calculations of band structures rely on crystal symmetries in the material; as such, the results of previous analyses may not be directly extensible to amorphous glass systems. However, considering these theories could lead to identification of the important properties influencing the dispersive nature of the stress-optic response.

Wemple and DiDomenico considered strain-induced changes to the energy band structures of crystalline materials by approximating the band structure with a simple oscillator model in order to model the elasto-optic tensor [31]. The imaginary part of the dielectric constant, $\epsilon_{2,ij}$ is determined from the band structure and the one-electron wave functions for the material. The real part is determined by the Kramers-Kronig (KK) integral,

$$\epsilon_{1,ij}(\omega) - 1 = \frac{2}{\pi} \int_{\omega_g}^{\infty} \frac{\omega' \epsilon_{2,ij}(\omega')}{(\omega'^2 - \omega^2)} d\omega', \tag{2.76}$$

where ω_g is the absorption threshold frequency. In other words, the dielectric constant is measured in the the transparent region. When strain is applied to the material, the energy band structure will be modified, such that the real part of the dielectric constant becomes

$$\Delta\epsilon_{1,ij}(\omega) = \frac{2}{\pi} \int_{\omega_g'}^{\infty} \frac{\omega' \Delta\epsilon_{2,ij}(\omega')}{(\omega'^2 - \omega^2)} d\omega', \tag{2.77}$$

where the absorption frequency is shifted, $\omega_g' = \omega_g + \Delta\omega_g$. The elasto-optic coefficients are related to this by the change in dielectric constant due to applied strain x,

$$\Delta\epsilon_{1,ij} = -\sum_{k,l} \epsilon_{1,ik} \Delta \left(\frac{1}{\epsilon_1}\right)_{kl} \epsilon_{1,lj} = -\sum_{k,l,m,n} \epsilon_{1,ik}\epsilon_{1,lj} p_{klmn} x_{mn}. \tag{2.78}$$

Instead of calculating the change in the imaginary part of the dielectric constant for all strain components, Wemple and DiDomenico applied simple oscillator approximations to the KK integral. The contributions from the band structure to the real part of the dielectric constant can be modeled for both ionic and covalent crystals with a single-oscillator Sellmeier expression:

$$\epsilon_1(\lambda) = S_0(\lambda_0)^2 \left[1 - \left(\frac{\lambda_0}{\lambda}\right)^2\right]^{-1}, \tag{2.79}$$

where S_0 is the oscillator strength, related to the interband strength ($\mathcal{F} = (hc/e)^2 S_0$) and λ_0 is the oscillator position parameter, related to the interband energy ($\mathcal{E}_0 = (hc)/(e\lambda_0)$). They consider this to be a long-wavelength approximation to the KK integral, which leads to

$$\begin{aligned} (\mathcal{E}_0)^2 &= \left(\frac{\hbar}{e}\right)^2 \int_{\omega_g}^{\infty} \frac{\epsilon_2}{\omega} d\omega \Big/ \int_{\omega_g}^{\infty} \frac{\epsilon_2}{\omega^3} d\omega, \\ \mathcal{F} &= \frac{2}{\pi}\left(\frac{\hbar}{e}\right)^2 \left(\int_{\omega_g}^{\infty} \frac{\epsilon_2}{\omega} d\omega\right)^2 \Big/ \int_{\omega_g}^{\infty} \frac{\epsilon_2}{\omega^3} d\omega. \end{aligned} \tag{2.80}$$

When strain is applied to the crystal, small changes will occur in oscillator position ($\Delta\mathcal{E}_0$) and strength ($\Delta\mathcal{F}$), which can be calculated using the above relations. Then, from the Sellmeier expression, the strain-induced change in the real part of the dielectric constant is

$$\frac{\Delta\epsilon_1}{(\epsilon_1 - 1)^2} = -2\left(\frac{\Delta\mathcal{E}_0}{\mathcal{E}_d}\right)\left(1 + \mathcal{K}_{ij}\left[1 - \left(\frac{\lambda_0}{\lambda}\right)^2\right]\right), \tag{2.81}$$

where

$$\mathcal{K}_{ij} = -\frac{1}{2}\left(\frac{\Delta\mathcal{F}/\mathcal{F}}{\Delta\mathcal{E}_0/\mathcal{E}_0}\right), \tag{2.82}$$

and $\mathcal{E}_d = \mathcal{F}/\mathcal{E}_0$ is the dispersion energy. They introduced a deformation potential $\mathcal{D}_{ij}$, such that $\Delta\mathcal{E}_0 = \sum_{i,j} \mathcal{D}_{ij} x_{ij}$. Assuming that ϵ_1, $\mathcal{E}_0$ and $\mathcal{E}_d$ are approximately isotropic, then

$$\frac{p_{ij}}{(1 - 1/n^2)^2} = \frac{2}{\mathcal{E}_d}\mathcal{D}_{ij}\left(1 + \mathcal{K}_{ij}\left[1 - \left(\frac{\lambda_0}{\lambda}\right)^2\right]\right) \tag{2.83}$$

where $\mathcal{D}_{ij}$ and $\mathcal{K}_{ij}$ can be measured experimentally, expressed in terms of the imaginary part of the dielectric constant and related to the band structure. The value of K_{ij} determines whether the dispersion of p_{ij} is either positive or negative. Wemple and DiDomenico previously found an empirical relationship for the dispersion energy [32]:

$$\mathcal{E}_d = \beta N_c Z_a N_e, \tag{2.84}$$

where N_c is the cation coordination number, Z_a is the formal anion valency, and N_e is the number of valence electrons per anion. Experimentally, β takes on different values for ionic compounds ($\beta_i = 0.26$ eV) and covalent compounds ($\beta_c = 0.39$ eV). The values $\mathcal{E}_d$ and $\mathcal{E}_0$ can also be determined from the dispersion of the refractive index.

Equation 2.83 is thus a two-parameter fit for the elasto-optic dispersion of crystalline materials. Wemple and DiDomenico experimentally determined the values of $\mathcal{D}$ and $\mathcal{K}$ by fitting their dispersive data; they found roughly linear relationships between $n^2 p_{ij}/(n^2-1)^2$ and $1/\lambda^2$ for many materials, though some showed non-linear dispersion throughout the transparent region. They concluded that the presence of excitons also contributes to the dispersion of p_{ij}, and a four-parameter fit is necessary to describe these contributions. Still, while they found parameters with "reasonable" values, there were no obvious correlations between crystal composition, properties and $\mathcal{D}_{ij}$ or $\mathcal{K}_{ij}$.

Cardona et al. took a slightly different approach, considering the electronic band structure of materials when analyzing the piezo-optic response of crystalline materials [33]. The relationship between elasto-optic (p_{ij}) and piezo-optic (π_{ij}) coefficients is $\pi_{ijkl} = p_{ijmn} S_{mnkl}$, or $p_{ijkl} = \pi_{ijmn} C_{mnkl}$, where S and C are the compliance and elastic tensors. The piezo-optic tensor elements of materials are strongly dispersive near their absorption edge, direct edges more so than indirect gaps. For some materials, π_{ij} changes with wavelength such that it reverses sign as the edge is approached; the point where $\pi_{ij} = 0$ is called the 'isotropic point'. Examples of the dispersion of π_{ij} for different crystalline materials are seen in Figure 2.2. GaAs, Ge, GaSb, KBr, KI, KCl, NaCl and CF_2 all have an isotropic point in the transparent wavelength range. This point is attributed to two contributions of opposite sign; one strongly dispersive and due to the absorption edge, and the other, weakly dispersive, from the average of the entire spectrum. The second effect is dominant at low frequencies.

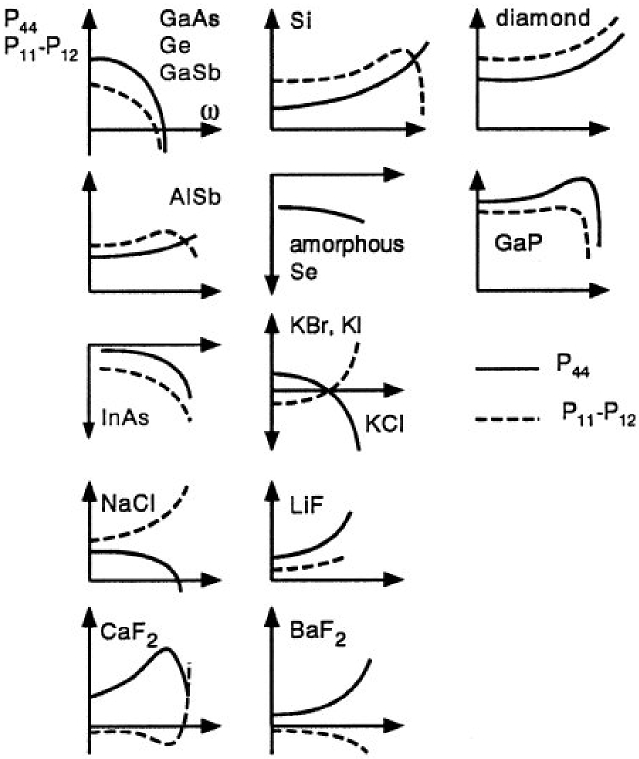

Figure 2.2: Dispersion of piezo-optic coefficients of various crystalline and amorphous materials below the fundamental absorption edge. Figure from [33]. In Cardona's terminology, the piezo-optic coefficients are related to the elasto-optic elements by $P_{ijkl} = \pi_{ijkl} = p_{ijmn}S_{mn}$.

The focus in Cardona's derivation is on electronic contributions to the piezo-optic tensor elements. The band structure of simple materials, such as the zinc-blende crystal Ge, is calculated under strain in order to determine optical properties. Specifically, the contributions of E_0 (region of transparency) and E_1 (outside of transparent region) transitions to π_{ijkl} are considered. The dielectric constant can expressed analytically as a function of these energy gaps, and from this the piezo-optic tensor is calculated. Some of the terms relating the elasto-optic coefficients to the band structure of germanium will be discussed below.

The effect of hydrostatic stress (X_H) on the E_0 direct edge (located at Γ) and its spin-orbit split component $E_0 + \Delta_0$ can be represented by dE_0/dX_H, which for Ge yields the hydrostatic constant

$$(\pi_{11}+2\pi_{12})_{E_0,E_0+\Delta_0}=\frac{1}{2\omega_0}\frac{d\omega_0}{dX_H}P^{-1}\left(G^{(3)}(x)+3F^{(3)}(x)+\frac{1}{2}G^{(3)}(x')+\frac{3}{2}F^{(3)}(x')\right), \tag{2.85}$$

where

$$\begin{aligned}F^{(3)}(x)&=x^{-2}[2-(1+x)^{1/2}-(1-x)^{1/2}],\\ G^{(3)}(x)&=x^{-2}[2-(1+x)^{-1/2}-(1-x)^{-1/2}],\end{aligned} \tag{2.86}$$

with $x=\omega/\omega_0$ and $x'=\omega/(\omega_0+\Delta_0)$. Also, $P=2\pi/a_0$ is the interband matrix element of linear momentum, and a_0 is the lattice constant.

The shear terms of π_{ijkl} coming from E_0 in Ge depend on two effects: the splitting $\delta\omega_0$ of the top valence band Γ_8 by shear stress, and the coupling of Γ_8 with the spin-orbit split state Γ_7. Then

$$\begin{aligned}\pi_{11}-\pi_{12}&=\frac{3}{4}(S_{11}-S_{12})\frac{b}{\omega_0}P^{-1}\left(-G^{(3)}(x)+\frac{4\omega_0}{\Delta_0}\left[F^{(3)}(x)-\left(\frac{\omega_0}{\omega_0+\Delta_0}\right)^{3/2}F^{(3)}(x')\right]\right),\\ \pi_{44}&=\frac{3}{4}S_{44}\frac{d}{2\sqrt{3}\omega_0}P^{-1}\left(-G^{(3)}(x)+\frac{4\omega_0}{\Delta_0}\left[F^{(3)}(x)-\left(\frac{\omega_0}{\omega_0+\Delta_0}\right)^{3/2}F^{(3)}(x')\right]\right),\end{aligned} \tag{2.87}$$

where d and b are “shear deformation potentials”, typically negative values. The $G^{(3)}$ term represents the effect of the band splitting, while the $F^{(3)}$ terms are due to the coupling. The terms P^{-1}, S_{ij}, b and d are approximately equal for most crystalline considered in this study, and a constant term must be added in order to match theory to experiment. Cardona conjectures that for most materials, this positive constant term dominants at low frequencies but with changing wavelength, the dispersive term can overcome the constant, inducing an isotropic point for some materials. However, if ω_0 is small, the shear effects due to the E_0 edge become predominant over the constant term, which results in no isotropic point.

For Cardona's model, the experimentally measured p_{ij} can be compared to the theoretical predictions of Equations 2.85 and 2.87 if the deformation potentials, ω_0 and Δ_0 are known. This is limiting for glass systems, where accurate calculation of the electronic band structure is difficult to obtain.

Kucharczyk also took a single oscillator approach, similar to that of Wemple and DiDomenico, to describe the wavelength dependence of the elasto-optic coefficients

[29]. From a bond polarizability model, the shear tensor element is

$$p_{44} = \frac{8}{n^4 a^3}\left(\beta^T - \beta^L\right), \tag{2.88}$$

where n is the refractive index, a is the lattice constant, and $\beta^{T,L}$ is the transverse or longitudinal part of the bond polarizability tensor. For the alkali halides considered, β^T and β^L were fit using a single oscillator formula,

$$\beta^{T,L} = \frac{A^{T,L}\lambda^2}{\lambda^2 - (\lambda_0^{T,L})^2}, \tag{2.89}$$

with λ in the UV-vis range. This theory has the benefit of simplicity; however, an understanding on the dependence of β on wavelength - namely, prediction of the parameter A - is necessary in order to fully explain the relationship between p_{44} and λ. Still, it is able to account for the so-called "isotropic points" depending on the fitting parameters of the β^T and β^L oscillator formulas.

With an understanding of these theories of dispersion of p_{ij} in crystalline materials, we can identify material properties which could influence the wavelength dependence of C in glasses. In particular, the refractive index, absorption edge and bond polarizabilities of a glass are all likely to contribute to the dispersion of the stress-optic response.

2.4 The Empirical Model of Photoelasticity

An empirical model of photoelasticity in glasses was developed by Guignard and Zwanziger to relate the structure of glass to its stress-optic response [1]. This model focuses on the chemical bonding environment of compounds in the structure rather than lattice and atomic distortions, conjecturing that 'bond metallicity' and coordination number N_c are important in describing the stress-optic response. Bond metallicity correlates well with anion-cation bond length, d [17]. For zero and negative stress-optic glasses, high metallicity is needed for bonds to be distorted along the bonding direction and orthogonal to it. Furthermore, for stress to distort the glass anisotropically, structural anisotropy is required locally. Low coordination numbers allow these distortions, while high coordination numbers prevent them [1]. Thus, this model predicts that glasses with a low d/N_c ratio will have a positive stress-optic coefficient, while glasses with high d/N_c will exhibit negative birefringence.

Table 2.1: Anion-cation bond length d, cation coordination number N_c, ratio d/N_c and sign of the stress optic coefficient C for a variety of glass components. Sources labelled 'calc' determine C from first-principles calculations. Those labelled 'expt' are based on measured values.

compound	d (Å)	N_c	d/N_c (Å)	sign of C	source
Tl_2O	2.517	3	0.84	-	expt [34]
Sb_2O_3	2.022	3	0.67	-	expt [1]
PbO	2.326	4	0.58	-	calc [1], expt [34]
SnO	2.224	4	0.56	-	calc, expt [1]
Bi_2O_3	2.198	4	0.55	-	expt [35]
TeO_2	2.0	4	0.50	+	calc [1]
ZnO	1.988	4	0.50	+	expt [36–38]
PbS	2.967	6	0.49	+	calc [1]
BaO	2.74	6	0.46	+	calc [1], expt [38]
B_2O_3	1.366	3	0.46	+	expt [36]
GeO_2	1.717	4	0.43	+	expt [39]
SiO_2	1.609	4	0.40	+	expt [40]
P_2O_5	1.5	4	0.38	+	expt [34, 38]
MgO	2.1085	6	0.35	+	calc [1], expt [34]
SnO_2	2.055	6	0.34	+	calc [1]

Table 2.1, compiled by Guignard et al. [1], contains the d/N_c ratio and signs of the stress-optic coefficient for various compounds. For the additives that are unable to form a glass on their own, the overall contribution to C in the system was considered. The negative sign is only designated when the addition of a compound to a glass system resulted in a negative coefficient. Glass compounds with $(d/N_c) > 0.5$ Å have a negative stress-optic coefficient, while those with $(d/N_c) \leq 0.5$ Å have positive coefficient. For binary and ternary glasses, the ratio is averaged to derive the expected response. Thus, the composition of a zero stress-optic glass can be predicted using the additivity rule

$$\left\langle \frac{d}{N_c} \right\rangle = \sum_i x_i \left(\frac{d}{N_c} \right)_i \approx 0.5 \text{ Å}, \tag{2.90}$$

where the sum is over all compounds in the glass, x_i is the molar per cent of the ith compound, and $(d/N_c)_i$ is that compound's ratio.

Thus far, the empirical model shows good correlation with known data and it is able to predict glass families with zero birefringence [1, 41–46]. However, it cannot predict the magnitude of the stress-optic coefficient, it does not consider the wavelength dependence of the photoelastic response and it has not been tested on non-oxide glass systems.

2.5 Measured Photoelasticity in Glass Systems

2.5.1 Dispersion of C in Glass

Industrially, a glass with zero stress-optic coefficient across the visible wavelength range is of great interest. However, very few studies on the dispersive nature of birefringence have been performed. The Schott company has performed studies on the wavelength dependence of C for many of their commercially available glasses; Figure 2.3 shows results for glasses in the FK, PK, PSK and SF families. The optical glass SF57 has nearly a zero stress-optic coefficient for all wavelengths in the visible range of light. This is a 'dense flint' glass; the main components of glasses in the SF series are alkaline silicates with $>$ 49% wt. PbO [5]. Most of the glasses in Figure 2.3 see a small increase in the stress-optic coefficient with decreasing wavelength (increasing energy). However, in the glasses SF1, SF14, SF18, SF55 and SF57, C decreases slightly with decreasing λ.

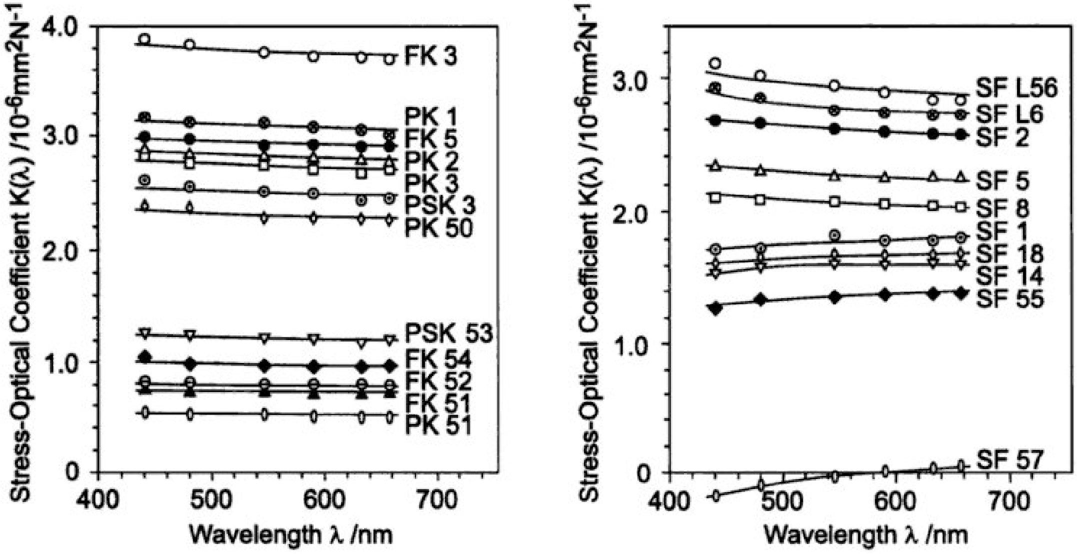

Figure 2.3: Stress-optical coefficient as a function of wavelength for select Schott optical glasses. Image from reference [5].

The dispersion of the birefringence of fused silica has also been examined in detail [40, 47–49]. The wavelength dependence of the stress-optic coefficient is shown in Figure 2.4. Values from Filon and Harris are averaged over multiple trials. The dispersion for wavelengths near the IR edge of the visible spectrum is small. Below 500nm, the stress-optic coefficient begins to quickly increase with decreasing wavelength. Jog derived a dispersion formula to describe the experimental values for $230 \leq \lambda \leq 650$nm for both his and Filon and Harris's work. However, the formula does not satisfy the results obtained by Primak and Post, nor does it agree with data at longer wavelengths.

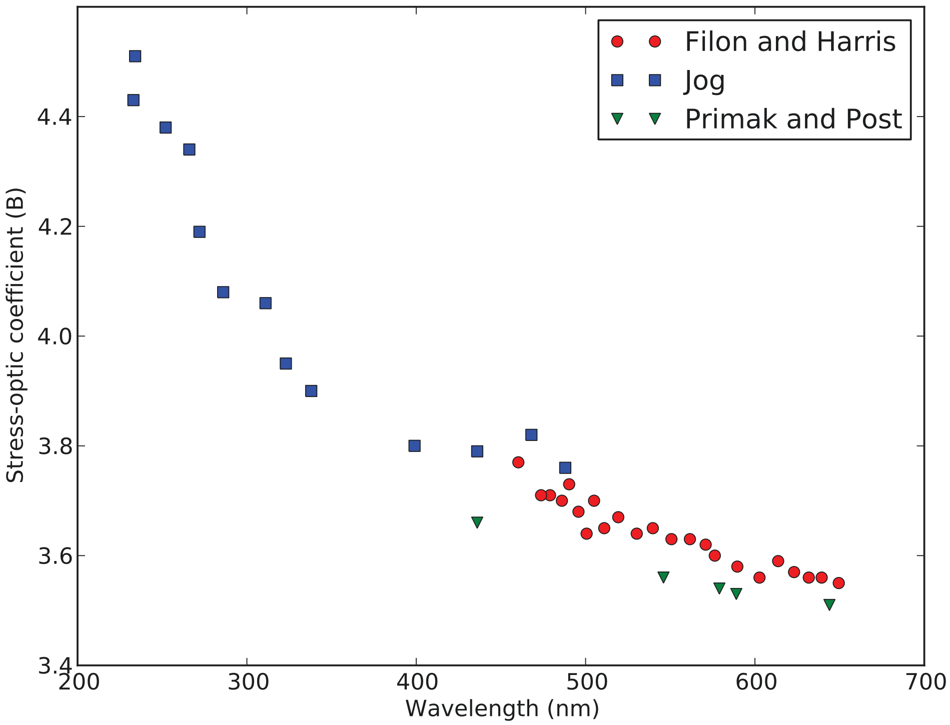

Figure 2.4: Dispersion of the stress-optic coefficient of fused silica. Values from [40] and [47].

The stress-optic coefficient of silicate glasses containing B_2O_3, Al_2O_3, K_2O, ZnO, Sb_2O_3, Na_2O, PbO, BaO, F and CaO has been reported by Vasudevan and Krishnan for the wavelength range $320 \leq \lambda \leq 575$nm [50]. Note here that the published values for the coefficient have the opposite sign as expected; this is due to an omitted negative sign in the calculation. For most glasses, the stress-optic coefficient decreased with decreasing wavelength; however, fused quartz saw an increase in C as λ decreased. The magnitude and dispersion of the birefringence were related to Mueller's lattice and atomic effects. Typically, the refractive index of a glass increases with shorter wavelengths. Since the lattice effect is related to n and the atomic effect is relatively constant, they argue that C should become more and more "positive" (negative with the appropriate sign) as λ decreases. This theory matches well with the reported values for the glasses excluding fused quartz. No attempt was made to explain this discrepancy.

Recent work has been done in our research group on the dispersive nature of the stress-optic response in oxide glasses [51]. In her Master's thesis, Thomas examined the broadband birefringence of tin phosphate, tin silicate, sodium phosphate and sodium silicate glasses in the visible spectrum. For all glasses, dispersive effects were seen near the band edge. The tin glasses showed only decreasing stress-optic coefficient with decreasing λ, while the sodium glasses had both increasing and decreasing C with wavelength. Thomas proposed that dispersive effects will be greater when the glass structure is composed primarily of bridging oxygens, i.e. ionic bonds, while the least amount of dispersion will occur when the glass structure is primarily composed of non-bridging oxygens, i.e. covalent bonds. However, this hypothesis does not consider whether the stress-optic coefficient will increase or decrease with wavelength.

Fukazawa et al. examined the photoelasticity of lead silicate glasses [52]. This work is particularly interesting as it is perhaps the only published example of stress-optic coefficients of glass determined using ellipsometry. They examined lead silicates containing 40-43 mol % PbO. For all glasses, stress-optic coefficient decreased with decreasing wavelength. Furthermore, two of the glasses showed zero stress-optic composition, which shifted to higher wavelength as lead content increased. They considered their results with respect to Mueller's lattice effect (proportional to $(n^2 - 1)^2/n^4$ according to Equation 2.23) and the atomic effect (proportional to $(n^2 - 1)(n^2 + 2)/n^4$ from Equation 2.23) and suggested that the negative values resulting from the lattice effect become dominant as refractive index (lead content) increases. However, this argument does not extend to glasses with positive stress optic-coefficients that increase with decreasing wavelength (and increasing index).

The motivation for this research was to measure the wavelength dependence of C for a variety of glass formers and modifiers, and to correlate glass composition with the dispersive properties of the stress-optic coefficient.

The glass formers considered in this study are SiO_2, B_2O_3, P_2O_5 and TeO_2. Glass modifiers include typically "positive" and "negative" additives according to the empirical model: alkali metal oxides Na_2O and Li_2O, alkaline earth oxides CaO and BaO, transition metal oxide ZnO, and metal oxides SnO, PbO and Bi_2O_3.

The stress-optic coefficients of many of these glass compositions have been measured at single wavelengths [1, 36–38, 42–44, 53–55]. However, there are currently no data or theories which predict when C will increase, decrease or remain constant with wavelength. As such, we have considered the effect of additive type and content on the dispersive nature of the stress-optic response with the goal of developing a predictive model.

2.5.2 Brillouin Measurements of p_{ijkl}

Brillouin spectroscopy is an inelastic light scattering technique that distinguishes the acoustic modes of a material. It is typically used to determine the elastic moduli of transparent materials and it is often used in conjunction with Raman or IR spectroscopy to determine the compositional evolution of structure and properties [56–63]. Brillouin scattering can also be used to determine a material's elasto-optic response [10, 13, 21, 64–67]. Although this technique is less commonly used in glasses, it yields all independent elements of the elasto-optic tensor, whereas other common techniques used to measure the photoelastic properties of a glass typically only measure the shear component, p_{44}.

There have been some investigations on the Brillouin scattering of glasses as a function of composition, as well as efforts to relate the measured p_{ij} to glass properties. Some experiments were concerned exclusively with commercially available glasses [21, 64, 65, 67], while others considered the effects of glass composition on p_{ij} in binary, ternary and doped systems [10, 13, 66]. The latter category is composed almost entirely of silicate-based glasses with typically positive stress-optic additives. These studies found that the magnitude of p_{44} varies more rapidly than that of p_{12} [64].

The ratio of the transverse and longitudinal velocities, v_T/v_L, tends toward a constant value for all glasses, regardless of composition; this result might suggest a relationship between shear and compressive restoring forces [65]. It was also suggested that both density and compositional fluctuations lead to Brillouin scattering in a material; the variations with composition were quantified by attenuation [10, 63, 68].

Values for the elasto-optic tensor elements for binary and ternary glass systems with known composition [10, 21, 65, 66] are reproduced here. Figure 2.5 shows the change in p_{12} with mol % additive, while Figure 2.6 shows the same dependence for p_{44}. Some compositional trends are apparent for these silicate-based glasses. p_{12} generally decreases with increasing additive, while p_{44} increases with additive. Also, the signs of the two tensor elements are opposite, with p_{12} showing positive, larger values. The glass systems studied with known compositions all have negative p_{44}, which translates to positive stress-optic response. And, in fact, most theories developed to

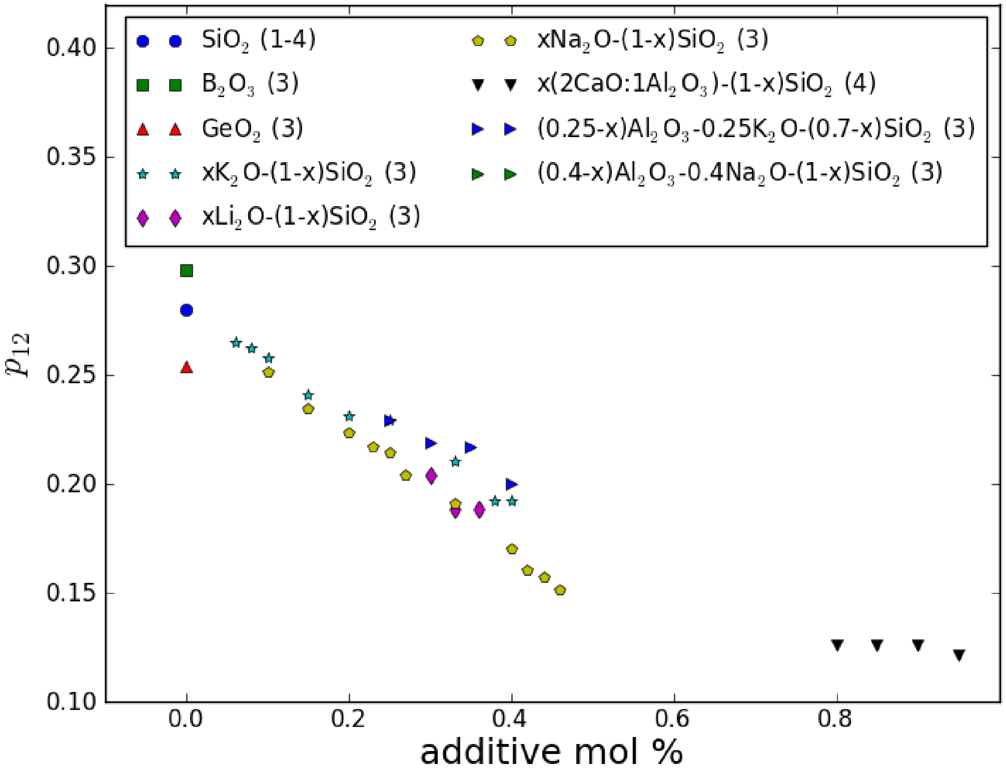

Figure 2.5: Some previously measured p_{12} values for binary and ternary glass systems. (1) from reference [21], (2) from [65], (3) from [10], (4) from [66].

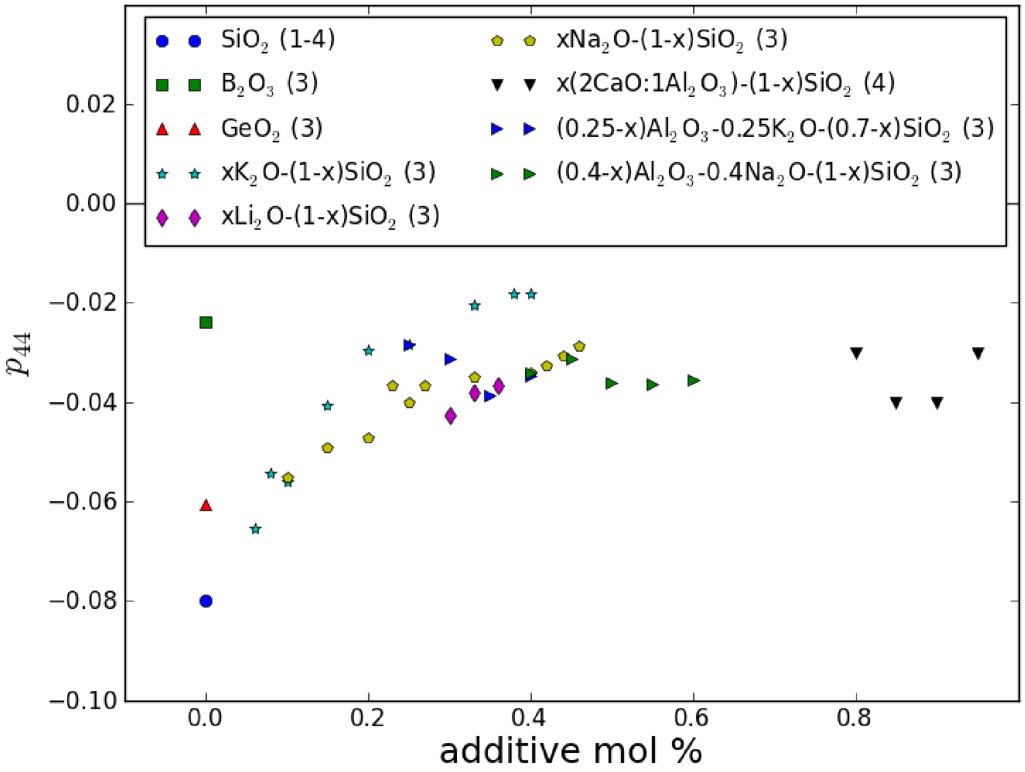

Figure 2.6: Some previously measured p_{44} values for binary and ternary glass systems. (1) from reference [21], (2) from [65], (3) from [10], (4) from [66].

describe the elasto-optic tensor elements of a glass diverge from experimental values as p_{44} goes to zero. Varying the glass former can also have a significant effect on elasto-optic tensor elements; for example, calcium alumino-silicates with less than 20 mol % SiO_2 have much lower p_{12} than silicate-rich glasses [66]. Furthermore, pure glass formers SiO_2, B_2O_3 and GeO_2 have significantly different values of p_{12} and p_{44}; however, information available on the relationship between glass former and p_{ij} is very limited.

The effect of glass composition on the elasto-optic tensor elements p_{ij} is not well understood, but is of interest industrially. In a review of the current and future directions of glass science in the US, researchers at Corning Incorporated stated that the Brillouin scattering spectra of glass is an area that merits further investigation [4]. It is important, then, to study the effect of glass formers and of additives with both positive and negative stress-optic response on the elasto-optic tensor of glasses.

To this effect, we have considered binary glass systems with positive, negative and zero stress-optic response. It is not well understood what effect negative stress-optic additives have on p_{12} for glasses with known composition. We have also examined the effect of glass former on the sign and magnitude of the elasto-optic tensor elements. The glass systems studied here are lead and barium borates, phosphates and silicates. Both barium oxide and lead oxide decrease the stress-optic coefficient in a glass, with the lead-based glasses transitioning to zero and negative stress-optic response at high additive content. The goal of this research was to determine the complete elasto-optic tensor for these glass systems, to determine what properties of a glass (n, G, d/N_c etc.) affect the sign and magnitude of p_{ij} and to develop a theoretical understanding of the empirical parameter d/N_c that has been so successful in predicting zero-stress optic compositions.

2.5.3 Photoelasticity in Chalcogenide Glasses

Compared to oxide glasses, relatively little work has been done on the stress-optic response of chalcogenide glasses. Chalcogenides are glasses that replace oxygen with another chalcogen - namely, sulfur, selenium or tellurium. The chalcogen is treated as the 'anion' of the system, even though bonding is covalent. The stress-optic coefficients of chalcogenides are typically much larger than those of oxide glasses, and the amount of chalcogen can be non-stoichiometric; in other words, it can be in excess or deficit. Bonding behaviour such as anion-anion or cation-cation bonding, while not present in oxide glass systems, is common in non-oxide glasses.

Most of the research on birefringence in chalcogenide glasses was done decades ago by Linke [69] and Anderson and Varshneya [70]. Linke measured the stress-optic coefficients for glasses in the systems Ge-Se, As-Se, Ge-As-Se, Ge-As-S, Ge-S-Se, As-S-Se,and As-Sb-S at a wavelength of 1500 nm, while Anderson and Varshneya focused on Ge-As-Se glasses measured at 1800 nm and attempted unsuccessfully to to correlate C to the average coordination number of the glass. These works are also inconclusive as to the effect of adding or removing the chalcogen from the glassy system.

The motivation of this research was to extend the empirical model of oxide glasses (Section 2.4) to include non-oxide glasses, to examine the effect of non-stoichiometric bonding on stress-optic response, and to compare the magnitudes of C for oxide and non-oxide glasses. The systems Ge-P-S and Ge-Sb-S were chosen for the in-depth analysis of the photoelastic response of non-oxide glasses as their structures have been studied extensively [71–73] and no data on the stress-optic coefficients have been published. The structural units and expected photoelastic response for these glass systems are discussed in detail in the included article manuscript in Chapter 4.

Chapter 3

Theory and Techniques

The properties of a glass important in describing its photoelastic response include the elastic moduli, density, stress-optic and elasto-optic coefficients, and refractive index. These properties and their measurement techniques will be described, followed by the derivation of the theories of reflection of polarized light (ellipsometry) and Brillouin scattering in glasses.

3.1 Optical, Elastic and Photoelastic Properties of Glass

3.1.1 The Elastic Tensor

When stress is applied to a material, the shape of the material is affected according to its elastic properties [74]. For stresses below the elastic limit, the material will revert to its original shape in the absence of stress. According to Hooke's law, for small applied stresses σ, the amount of strain s is proportional to the applied stress. The proportionality describes the elastic properties of the material. However, stress and strain are directional properties, and a tensor equation is necessary to describe their relationship:

$$\begin{aligned} \sigma_{ij} &= C_{ijkl} s_{kl}, \\ s_{ij} &= S_{ijkl} \sigma_{kl}. \end{aligned} \tag{3.1}$$

Here, C_{ijkl} are the elastic constants of the material, and $S_{ijkl} = C_{ijkl}^{-1}$ are the compliances. Simplifications due to the symmetry conditions of isotropic solids allow an abbreviated notation to be used for the subscripts:

$$11 \to 1,\ 22 \to 2,\ 33 \to 3,\ 23 \to 4,\ 13 \to 5,\ 12 \to 6.$$

For an isotropic material such as glass, there are three unique tensor elements, and only two are independent:

$$C_{44} = \frac{1}{2}(C_{11} - C_{12}). \tag{3.2}$$

The elastic properties of a material are most commonly described by Young's modulus E, the shear modulus G, and Poisson's ratio ν. In fact, all elastic components of an isotropic material can be determined from a knowledge of any two elastic moduli. The commonly presented moduli are related to the elastic tensor elements by

$$\begin{aligned} C_{11} &= \frac{E(1-\nu)}{(1+\nu)(1-2\nu)}, \\ C_{12} &= \frac{E\nu}{(1+\nu)(1-2\nu)}, \\ C_{44} &= G = \frac{E}{2(1+\nu)}, \end{aligned} \tag{3.3}$$

and to the compliance tensor elements by

$$\begin{aligned} S_{11} &= \frac{1}{E}, \\ S_{12} &= \frac{-\nu}{E}, \\ S_{44} &= \frac{1}{G} = \frac{2(1+\nu)}{E}. \end{aligned} \tag{3.4}$$

The shear and Young's modulus of a glass are on the order of GPa. The elastic limit of glass, on the other hand, is typically on the order of MPa. As such, stresses applied to the glasses in this study are kept in the MPa range. Typically, imperfections in the surfaces and parallelicity of a glass will cause a stressed glass to break well before it reaches the elastic limit.

3.1.2 The Ultrasonic Method for Determining Elastic Properties

The elastic properties of a glass can be determined from the velocity of sound traveling through the glass (pp. 162–168 of [3]). There are two types of sound waves which can propagate in a glass: longitudinal and transverse. The shear component of the elastic tensor, C_{44}, is determined from the transverse sound wave,

$$C_{44} = \rho v_T^2, \tag{3.5}$$

while deformations along the stress axis are determined from the longitudinal sound wave,

$$C_{11} = \rho v_L^2. \tag{3.6}$$

These tensor elements can be related to Young's modulus, the shear modulus and the Poisson ratio through Equation 3.3.

Ultrasonic wave techniques are often used to determine the elastic moduli of a glass; see pp. 162–168 of [3]. In this method, an ultrasonic pulse is sent through the glass by either a longitudinal or transverse wave transducer. The pulse reflects from the back face of the glass, and the total travel time of the wave t is measured by an oscilloscope. Then, for a material with known thickness d, the velocity is determined from the simple relationship $v_{L,T} = d/(2t)$.

3.1.3 Archimedes Method for Determining Density

Densities of glasses are commonly measured using Archimedes' principle. According to this method, the buoyancy of the sample suspended in a general fluid is equal to the weight of the displaced fluid. The buoyancy is defined as

$$F_B = W_a - W_f = \rho_f g V, \tag{3.7}$$

where W_a is the weight of the sample in air, g is the gravitational acceleration, and W_f, ρ_f and V are the the weight of the sample suspended in the fluid, the density of the fluid, and the volume of the displaced fluid respectively. The displaced volume V must also be equal to the volume of the sample, and so the density of the material can be determined from

$$\rho = \frac{m_{air}}{V} = m_{air}\frac{\rho_f g}{W_{air} - W_f} = \frac{m_{air}}{m_{air} - m_f}\rho_f, \tag{3.8}$$

where m denotes the mass of the sample in either air or fluid.

3.1.4 Analysis of Polarized Light Traveling Through Stressed Glass

An analysis of the propagation of polarized light through stressed glass is necessary in understanding and measuring birefringence. Consider light traveling along the z-axis and linearly polarized at 45° to the x- and y-axes:

$$\mathbf{E}(z,t) = \mathbf{E}_0 e^{i(kz-\omega t)}\Big(\hat{x} + \hat{y}\Big). \tag{3.9}$$

Here, $\mathbf{E}_0$ is the amplitude of the light wave, k is the wavenumber and ω is the angular frequency.

For a glass with stress applied along the y-axis (or extraordinary axis) as shown in Figure 2.1, the different indices of refraction along the $\hat{x}$ and $\hat{y}$ directions result in different wavenumbers for light polarized along those axes. Then as the polarized light described in Equation 3.9 travels through a stressed glass with thickness d along the z-axis, the light will undergo a change in its polarization state:

$$\begin{aligned}\mathbf{E}(z+d,t_1) &= \mathbf{E}_0 e^{i(kz-\omega t_1)}\left(e^{ik_o d}\hat{x} + e^{ik_e d}\hat{y}\right) \\ &= \mathbf{E}_0 e^{i(kz-\omega t_1)}\left(e^{i2\pi n_o d/\lambda}\hat{x} + e^{i2\pi n_e d/\lambda}\hat{y}\right) \qquad (3.10) \\ &= \mathbf{E}_0 e^{i(kz-\omega t_1)} e^{i2\pi n_o d/\lambda}\left(\hat{x} + e^{i2\pi(n_e-n_o)d/\lambda}\hat{y}\right).\end{aligned}$$

The induced phase shift Δ between the $\hat{x}$ and $\hat{y}$ components of light exiting the glass can then be related to the stress-optic coefficient through Equation 2.2:

$$\Delta = \frac{2\pi d}{\lambda}(n_e - n_o) = \frac{2\pi d}{\lambda}C\sigma. \qquad (3.11)$$

3.1.5 Sénarmont Compensator Method for Determining C

In order to determine the stress-optic coefficient of a glass, one needs to analyze the polarized light which has passed through the stressed glass. While there are many methods that can be employed to measure birefringence, our research group uses the Sénarmont compensator method. Here, light travels through a linear polarizer, the stressed glass, a quarter-wave plate and finally a second rotatable linear polarizer called the analyzer. The analyzer angle which minimizes the intensity of light can be used to determine the phase shift Δ induced in a stressed glass.

The initial polarizer is oriented to produce light according to Equation 3.9. Then as the linearly polarized light travels through the stressed glass, it picks up a phase shift between ordinary and extraordinary axes according to Equation 3.10. At this point, it is beneficial to use the Jones matrix method [75] to simplify the analysis. The relevant Jones matrices for the calculation are summarized in Table 3.1.

The light exiting the stressed glass can be rewritten as

$$\mathbf{E} = E_0 e^{i\Delta/2}\begin{bmatrix} e^{-i\Delta/2} \\ e^{i\Delta/2} \end{bmatrix}. \qquad (3.12)$$

Table 3.1: Jones matrices.

Optical element	Jones matrix
Quarter-wave plate with fast axis oriented along the x-axis "Q(x)"	$e^{i\pi/4}\begin{bmatrix} 1 & 0 \\ 0 & i \end{bmatrix}$
Linear polarizer oriented at ± 45° to the x-axis "L(45)"	$\frac{1}{2}\begin{bmatrix} 1 & \pm 1 \\ \pm 1 & 1 \end{bmatrix}$
Rotation matrix "R(θ)"	$\begin{bmatrix} \cos\theta & \sin\theta \\ -\sin\theta & \cos\theta \end{bmatrix}$

The quarter-wave plate is oriented such that its fast axis is parallel to $(\hat{x}+\hat{y})$. Then as the light passes through the quarter-wave plate, its polarization changes according to

$$\begin{aligned} \mathbf{E} &= R(-45°)Q(x)R(45°)E_0 e^{i\Delta/2}\begin{bmatrix} e^{-i\Delta/2} \\ e^{i\Delta/2} \end{bmatrix} \\ &= E_0 e^{i\pi/4} e^{i\Delta/2}\begin{bmatrix} \cos(\Delta/2)+\sin(\Delta/2) \\ \cos(\Delta/2)-\sin(\Delta/2) \end{bmatrix}. \end{aligned} \tag{3.13}$$

The analyzer is initially aligned perpendicularly to the incident light, along the $\pm(\hat{x}-\hat{y})$ direction. It is rotated to angle θ from this direction to find the minimum intensity of light. The light exiting the analyzer has electric field vector

$$\begin{aligned} \mathbf{E} &= E_0 e^{i\pi/4} e^{i\Delta/2} R(-\theta)L(-45°)R(\theta)\begin{bmatrix} \cos(\Delta/2)+\sin(\Delta/2) \\ \cos(\Delta/2)-\sin(\Delta/2) \end{bmatrix} \\ &= E_0 e^{i\pi/4} e^{i\Delta/2}\frac{1}{2}\begin{bmatrix} \cos\frac{\Delta}{2}+\sin\frac{\Delta}{2}+\sin\left(\frac{\Delta}{2}+2\theta\right)-\cos\left(\frac{\Delta}{2}+2\theta\right) \\ \cos\frac{\Delta}{2}-\sin\frac{\Delta}{2}-\sin\left(\frac{\Delta}{2}+2\theta\right)-\cos\left(\frac{\Delta}{2}+2\theta\right) \end{bmatrix}. \end{aligned} \tag{3.14}$$

The intensity of a general light wave, $\mathbf{A} = \begin{bmatrix} A_x \\ A_y \end{bmatrix}$, is $I = A_x^2 + A_y^2$. Thus, the intensity of light exiting the rotatable analyzer is

$$I = 4 + 2\sin\Delta - 2\cos(\Delta + 2\theta) \tag{3.15}$$

Since Δ is a constant value for a given applied stress, then the intensity is minimized when the analyzer is rotated to

$$2\theta = -\Delta \pm \frac{\pi}{2}. \tag{3.16}$$

With this relationship for the experimentally determined angle of extinction θ and Equation 3.11, the stress-optic coefficient C can be determined.

3.1.6 Dispersion of the Refractive Index

The stress-optic coefficient is dependent on the index of refraction, which itself is dependent on the wavelength of the incident light. Normal dispersion occurs when the refractive index increases with decreasing wavelength. Otherwise, the dispersion is anomalous; this occurs near or at the absorption bands of the glass [76]. This is seen in Figure 3.1.

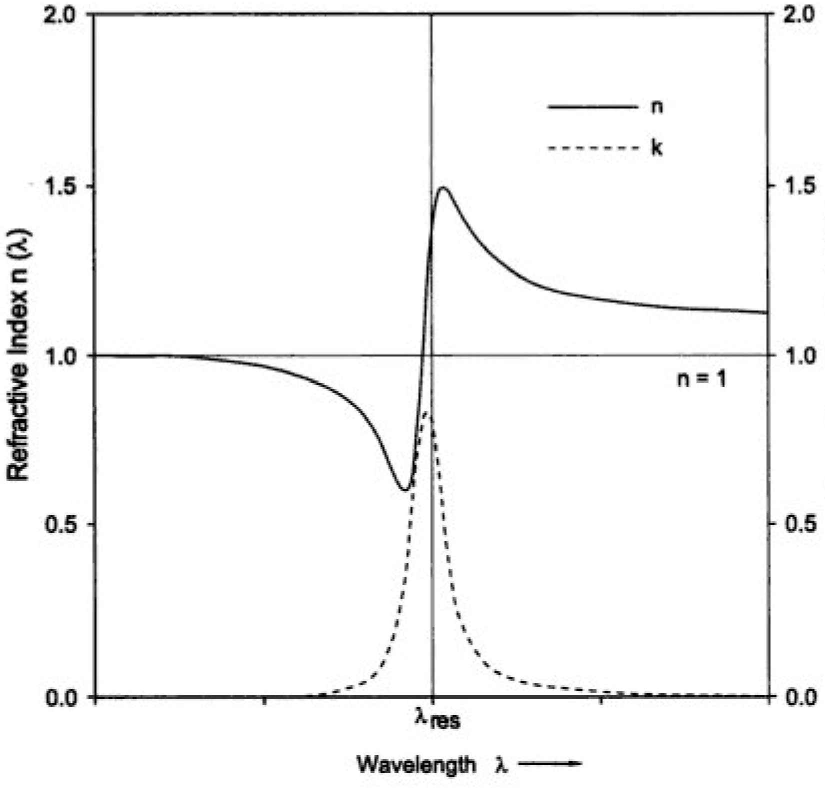

Figure 3.1: Absorption coefficient and refractive index of light in a dielectric medium. Here, n is the real part of the refractive index and k is the imaginary part. Materials absorb all incident light at the resonance wavelength λ_{res}. Image from reference [76].

In order to understand the dispersion of the refractive index, an electromagnetic approach is necessary [75–77]. A glass can be considered as a collection of many small, polarizible charges (electrons). Each electron oscillates about its equilibrium position with resonant frequency ω_0. When an electromagnetic wave such as light impinges on the glass, the electrons vibrate at the frequency of the incident wave. Each charge can be considered to be a forced oscillator driven by the electric field of the light wave. The equation of motion is

$$m\left(\ddot{\mathbf{x}} + \gamma\dot{\mathbf{x}} + \omega_0^2\mathbf{x}\right) = q\mathbf{E}(\mathbf{x}, t) = q\mathbf{E}_0\cos(\omega t), \tag{3.17}$$

where m is the mass of the electron, q is the charge of the electron, γ is the damping coefficient, and ω is the frequency of the incident wave. Assuming that the charge will oscillate at the same frequency as the electric field, the solution for $\mathbf{x}$ is guessed to be

$$\mathbf{x}(t) = \mathbf{x}_0 e^{-i\omega t} \tag{3.18}$$

and the equation of motion simplifies to

$$\mathbf{x}(t) = \frac{q}{m(\omega_0^2 - \omega^2 - i\omega\gamma)}\mathbf{E}(t). \tag{3.19}$$

The polarization, or density of dipole moments, can be related to the electric field as

$$\mathbf{P}(t) = (\epsilon - \epsilon_0)\mathbf{E}(t), \tag{3.20}$$

where ϵ is the dielectric constant of the material and ϵ_0 is the dielectric constant in vacuum. Furthermore, the dipole moment is equal to the charge times its displacement, so for N atoms,

$$\mathbf{P}(t) = qN\mathbf{x}(t) = \frac{q^2 N}{m(\omega_0^2 - \omega^2 - i\omega\gamma)}\mathbf{E}(t). \tag{3.21}$$

Combining these equations, we find that

$$\epsilon = \epsilon_0 + \frac{\mathbf{P}(t)}{\mathbf{E}(t)} = \epsilon_0 + \frac{q^2 N}{m(\omega_0^2 - \omega^2 - i\omega\gamma)}. \tag{3.22}$$

This can be simplified to the refractive index using the relation $n^2(\omega) = \epsilon/\epsilon_0$. Now supposing that there are N atoms per unit volume with Z electrons per atom, and that instead of one binding frequency ω_0 for all electrons, there are f_j electrons per atom with binding frequency ω_j and damping coefficient γ_j, the dispersive equation for the refractive index is

$$n^2(\omega) = 1 + \frac{q^2 N}{m\epsilon_0} \sum_j \frac{f_j}{(\omega_0^2 - \omega_j^2 - i\omega_j\gamma_j)} \tag{3.23}$$

where the oscillator strengths f_j satisfy the sum $\sum_j f_j = Z$.

Since the refractive index is wavelength dependent, some dispersion of the stress-optic coefficient is expected. However, C can either increase or decrease with decreasing wavelength. Since n only increases with decreasing λ, it is clear that the refractive index is not the only source of dispersion in the birefringence of a glass.

3.2 Ellipsometry

Spectroscopic ellipsometry is a technique that characterizes the optical properties of materials, typically thin films. Polarized light is reflected from a sample's surface, and the change in amplitude and phase of the light is measured. In this way, information such as the thickness of a thin film, the real and imaginary refractive indices, and the surface roughness of a sample can be determined. The follow sections describe the reflection and transmission of light at an interface, the optical components of an ellipsometer, and the determination of refractive index from the ellipsometric measurements.

3.2.1 Reflection of Light at an Interface

Typically, spectroscopic ellipsometry measures light that has been reflected from a material's surface. The following discussion of the reflection and transmission of light is based on reference [77].

When light is incident on a transparent material at some angle θ_I, part of the light is reflected and part is transmitted through the material; this is shown in Figure 3.2. The amounts of reflected and transmitted beams depend on the initial polarization of the incident light. In ellipsometry, it is typical to call light with electric field perpendicular to the plane of incidence "s-polarized", while light polarized within this plane is called "p-polarized". The magnetic fields are orthogonal to both the electric fields and the direction of propagation.

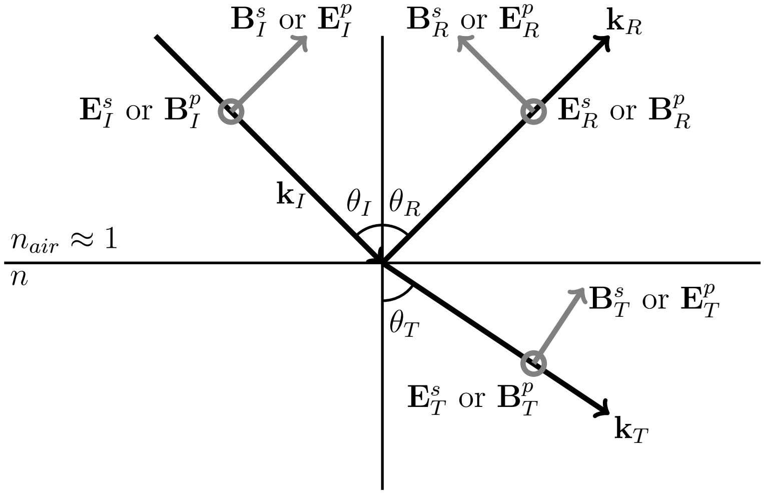

Figure 3.2: Light incident on the surface of a transparent material is partially reflected and partially transmitted. The initial polarization of the light (s or p, according to the conventions of ellipsometry) determines the reflection and transmission coefficients.

The electric and magnetic fields are

$$\begin{aligned} \mathbf{E}_m &= \mathbf{E}_{0m} e^{i\mathbf{k}_m \cdot \mathbf{r} - i\omega t}, \\ \mathbf{B}_m &= \frac{n}{c} \frac{\mathbf{k}_m \times \mathbf{E}_m}{k_m}, \end{aligned} \tag{3.24}$$

where the subscript $m = I, R, T$ denotes the incident, reflected or transmitted field. The boundary conditions of the system specify that at the point of incidence on the material, all variations of the fields must be equal. All phase factors are equal,

$$\mathbf{k}_I \cdot \mathbf{r} = \mathbf{k}_R \cdot \mathbf{r} = \mathbf{k}_T \cdot \mathbf{r}, \tag{3.25}$$

and the normal components of **B** and **D** are continuous, as are the tangential components of **E** and **H**. For s-polarized light, this yields

$$\begin{aligned} & E_{0I}^s + E_{0R}^s = E_{0T}^s, \\ & \frac{n_{air}}{c} \left(E_{0I}^s - E_{0R}^s\right) \cos\theta_I = \frac{n}{c} E_{0T}^s \cos\theta_T, \end{aligned} \tag{3.26}$$

which can be solved for the reflected and transmitted amplitudes:

$$\begin{aligned} R^s &= \frac{E_{0R}^s}{E_{0I}^s} = \frac{n_{air}\cos\theta_I - n\cos\theta_T}{n_{air}\cos\theta_I + n\cos\theta_T} = \frac{\cos\theta_I - \sqrt{n^2 - \sin^2\theta_I}}{\cos\theta_I + \sqrt{n^2 - \sin^2\theta_I}}, \\ T^s &= \frac{E_{0T}^s}{E_{0I}^s} = \frac{2n_{air}\cos\theta_I}{n_{air}\cos\theta_I + \frac{\mu_{air}}{\mu} n\cos\theta_T} = \frac{2\cos\theta_I}{\cos\theta_I + \sqrt{n^2 - \sin^2\theta_I}}, \end{aligned} \tag{3.27}$$

where $n_{air} \approx 1$, and Snell's law ($n_{air} \sin\theta_I = n \sin\theta_T$) has been applied to convert the angle of transmission θ_T to the incident angle. Likewise, for p-polarized light, the boundary conditions give

$$\begin{aligned} (E^p_{0I} - E^p_{0R}) \cos\theta_I &= E^p_{0T} \cos\theta_T, \\ \frac{n_{air}}{c} (E^p_{0I} + E^p_{0R}) &= \frac{n}{c} E^p_{0T}. \end{aligned} \tag{3.28}$$

The reflected and transmitted intensities are then

$$\begin{aligned} R^p &= \frac{E^p_{0R}}{E^p_{0I}} = \frac{n\cos\theta_I - n_{air}\cos\theta_T}{n\cos\theta_I + n_{air}\cos\theta_T} = \frac{n^2\cos\theta_I - \sqrt{n^2 - \sin^2\theta_I}}{n^2\cos\theta_I + \sqrt{n^2 - \sin^2\theta_I}}, \\ T^p &= \frac{E^p_{0T}}{E^p_{0I}} = \frac{1}{n}\frac{2n\cos\theta_I}{n\,n\cos\theta_I + n_{air}\cos\theta_T} = \frac{2n\cos\theta_I}{n^2\cos\theta_I + \sqrt{n^2 - \sin^2\theta_I}}. \end{aligned} \tag{3.29}$$

3.2.2 Fresnel Equations and the Brewster's Angle

For p-polarized light (*i.e.* light polarized in the plane of incidence), there is an angle for which no light is reflected; this angle is called the Brewster's angle. Since $R^p = 0$, Equation 3.29 becomes

$$n^2 \cos\theta_I = \sqrt{n^2 - \sin^2\theta_I}, \tag{3.30}$$

or

$$n^4 = \frac{n^2}{\cos^2\theta_I} - \frac{\sin^2\theta_I}{\cos^2\theta_I}. \tag{3.31}$$

Then, with the relationships $\tan\theta = \sin\theta/\cos\theta$ and $\sec^2\theta = 1 + \tan^2\theta$, the Brewster's angle can be written as

$$\theta_B = \tan^{-1}(n). \tag{3.32}$$

This angle can be used to determine the refractive index of the glass.

3.2.3 Spectroscopic Ellipsometry

The polarization state of light reflected from a material can be measured by spectroscopic ellipsometry. A schematic of this reflection process is seen in Figure 3.3. The reflected light often becomes elliptically polarized, which is expressed in polar coordinates as

$$\rho = \frac{E^p_R}{E^s_R} = \tan\Psi e^{i\Delta}, \tag{3.33}$$

where Δ is the phase shift induced between the s- and p-components of the beam, and $\tan\Psi = |E^p_R|/|E^s_R|$ is the ratio of amplitudes.

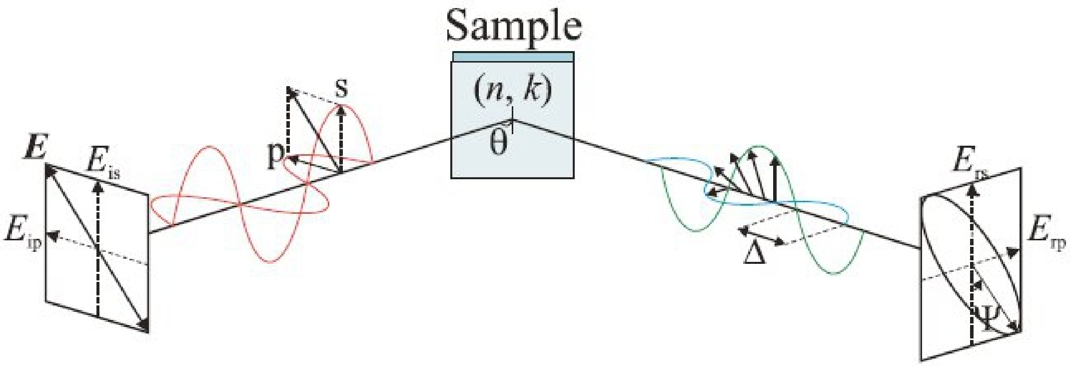

Figure 3.3: Ellipsometry can measure the phase shift Δ and relative intensity $\tan\Psi$ of *s*- and *p*-polarized light. Image from [78].

The Woollam M-2000 variable angle spectroscopic ellipsometer used for these measurements is a rotating-compensator ellipsometer (RCE). The ellipsometer, located in the Dahn lab at Dalhousie University, measures the intensity and phase of light with wavelengths between 210 and 1000 nm, and the angle of incidence of the beam can vary from 45° to 90° (transmission mode). A schematic of the optical elements of the M-2000 are shown in Figure 3.4.

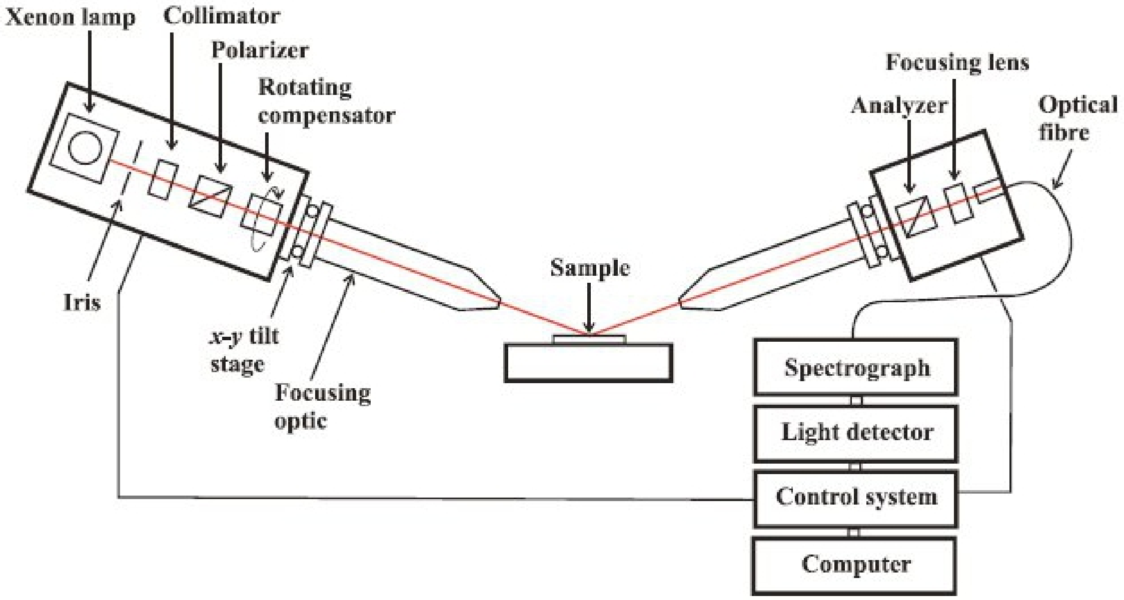

Figure 3.4: A schematic of optical components within the Woollam M-2000 ellipsometer, located in the Dahn lab at Dalhousie University. Image from [78].

The optical components of the ellipsometer are similar to those used in the Sénarmont compensator discussed in Section 3.1.5. Each element is briefly described below, based on the discussion in reference [78]. The light source is a Xe arc lamp, emitting light in the range 195-2000 nm. The lamp has sharp emission peaks between 800 and 1000 nm, which can result in artifacts in the collected intensity spectrum. The light is collimated and then passes through a Glan-Taylor linear polarizer oriented at 45° between the *s* and *p* axes. As such, the resulting beam has equal *s*- and *p*-polarization amplitudes. The light then passes through the rotating compensator, which induces a phase shift of $\pi/2$ and converts the beam to circular polarization. This allows measurement sensitivity near $\Delta = 0^\circ$ and $\delta = 180^\circ$, as well as the determination of the handedness of induced phase shifts [79]. The beam is then incident on the sample; for incident angles $\theta_I < 90^\circ$, the beam can be focused to smaller spot size using focusing probes. The reflected light, with amplitude and phase shifts as described in the previous section, passes through another Glan-Taylor linear polarizer, which acts as an analyzer. The resulting linearly polarized light is then filtered by a grating onto the detector, a silicon photodiode array, which measures the polarization state and intensity of the reflected beam at all wavelengths simultaneously. The phase shift Δ between *s* and *p* components of the light and the relative intensity $\tan\Psi$ are determined directly by the accompanying software CompleteEASE, which performs a Fourier analysis of the intensity. The stress-optic coefficient of light transmitted through or reflected from the back face of a glass can be determined from this experimentally measured Δ and Equation 3.11.

3.2.4 Refractive Index and the Cauchy Model

The refractive index of a material can be determined using ellipsometry from the wavelength-dependent measurement of Ψ as well as Equations 3.27 and 3.29. By solving $\tan\Psi = |R^p|/|R^s|$, the refractive index is found to be

$$n^2 = \frac{\sin^2\theta_I(1+\tan\Psi)^2 - 4\sin^4\theta_I\tan\Psi}{\cos^2\theta_I(1+\tan\Psi)^2}. \tag{3.34}$$

The CompleteEASE software fits the refractive index to Ψ using different models; in this case, a Cauchy model was used to determine n. For transparent materials, the

Cauchy model is

$$n(\lambda) = A + \frac{B}{\lambda^2} + \frac{C}{\lambda^4} + ... \tag{3.35}$$

Typically, orders above $(1/\lambda^4)$ are ignored since they do not contribute significantly to n. The parameters A, B and C are fitted by the software to minimize the difference between model and experimental Ψ, and the wavelength-dependent $n(\lambda)$ is determined.

3.3 Brillouin Scattering in Amorphous Materials

When electromagnetic waves propagate through transparent materials, a small fraction of the waves will interact with and scatter from sound waves moving in the material. This is known as Brillouin scattering. A typical Brillouin spectra (seen for glass in Figure 3.5) measures the scattered photon intensity as a function of the light's frequency shift relative to the incident wavelength. The frequency shifts of the scattered light from the central Rayleigh line give information about the sound velocities and elastic moduli of the glass, while the intensities of the shifted Brillouin peaks give information about the photoelastic properties of the glass. In the following sections, these relationships will be derived, and the Fabry-Perot interferometer used to collect Brillouin spectra will be discussed.

3.3.1 Frequency Shifts and the Elastic Moduli

Brillouin scattering can be described as the interaction between a light wave and a density wave in a material [7, 80–82]. The density wave originates from the thermal motion of atoms in the material (corresponding to acoustic phonons at the Brillouin zone center) and will scatter a fraction of the incident light. This type of scattering is inelastic and occurs with low frequencies. The photon can either lose energy and create a phonon (Stokes scattering) or gain energy by absorbing a phonon (Anti-Stokes scattering). The wave vectors $\mathbf{k}$ and frequencies $\boldsymbol{\omega}$ of the scattering process are

$$\begin{gathered} \mathbf{k}_S = \mathbf{k}_I \pm \mathbf{q}, \\ \boldsymbol{\omega}_S = \boldsymbol{\omega}_I \pm \boldsymbol{\omega}_q, \end{gathered} \tag{3.36}$$

where I indicates incident photons, S indicates scattered photons, q indicates the created or absorbed phonon and the $-$ $(+)$ indicates Stokes (Anti-Stokes) scattering.

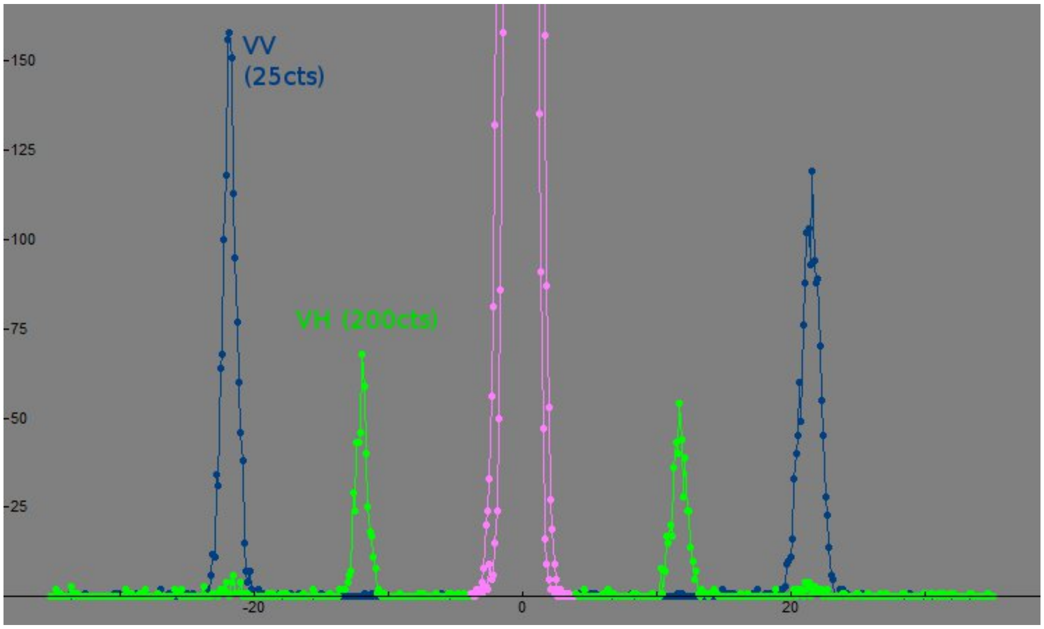

Figure 3.5: A typical Brillouin spectra showing scattered light's intensity as a function of frequency shift. Inelastic scattering from longitudinal waves are measured in VV configuration (blue), while transverse waves are measured in VH configuration (green). The unshifted, elastically scattered Rayleigh line is in pink.

The density fluctuations in the material lead to periodic fluctuations of the dielectric tensor (refractive index) which act like a diffraction grating. The light scattered at angle $\theta/2$ will interfere constructively according to Bragg's law:

$$\frac{\lambda}{n} = 2\Lambda \sin(\theta/2). \tag{3.37}$$

Here, n is the refractive index of the scattering material, λ is the wavelength of incident light, and Λ is the wavelength of the density fluctuations. This wavelength can be related to the wavevector of the phonons created or destroyed in the scattering process:

$$q = \frac{2\pi}{\Lambda} = \frac{4\pi n}{\lambda} \sin(\theta/2). \tag{3.38}$$

Since the light is scattered from a moving object (in this case, a density wave), its frequency will undergo a Doppler shift:

$$\Delta\omega_B = 2\pi\Delta f_B = qv_B, \tag{3.39}$$

where q is the wavevector of the incident phonons and v_B is the sound velocity of the scattering medium. Isotropic media have two sound velocities: longitudinal, v_L, and transverse, v_T. The two independent elastic moduli are then

$$C_B = \rho v_B^2 = \rho \left(\frac{\Delta\omega_B \lambda}{4\pi n \sin(\theta/2)} \right)^2 , \tag{3.40}$$

with C_{11} and C_{44} found from the longitudinal and transverse sound velocities, respectively.

3.3.2 Brillouin Intensity and the Elasto-Optic Constants

This derivation of the relationship between Brillouin scattering intensity and elasto-optic coefficients p_{ijkl} is based on the scattering theory found in references [82, 83]. In amorphous materials such as glass, the average dielectric constant is equal in all directions. However, sound waves of wave vector $\mathbf{q}$ and frequency ω_q traveling through the material will induce small fluctuations in the dielectric constant, $\delta\epsilon_{ik}$, which tend to be anisotropic.

When light is incident on such a material, its electric field $\mathbf{E}_I$ will induce polarization. The part of the polarization which is due to the dielectric fluctuations will emit a scattered electric field $\mathbf{E}_S$ at some point $\mathbf{R}_0$ away from the scattering event. The propagation of the scattered wave is described by the relationship between electric induction and field, the components of which are $D_{Si} = \epsilon_S E_{Si} + \delta\epsilon_{ij} E_{Ij}$. Here, ϵ_s represents the dielectric constant measured at the scattered frequency ω_s, and $\delta\epsilon_{ij}$ is the change in the tensor element of the dielectric permeability which describes the scattering properties of the material. Since the frequency shift between the incident and scattered light is small, we can approximate $\epsilon_s \approx \epsilon$. In vector form, the propagation is then described by

$$\mathbf{D}_S = \epsilon \mathbf{E}_S + (\delta\boldsymbol{\epsilon} \cdot \mathbf{E}_I), \tag{3.41}$$

where $(\delta\boldsymbol{\epsilon} \cdot \mathbf{E}_I)$ is shorthand for the vector with components $\delta\epsilon_{ij} E_{Ij}$.

We can apply Maxwell's equations to the electric induction and field to find that $\nabla \times \mathbf{E}_S = \frac{i\omega_S}{c}\mathbf{H}_S$ and $\nabla \times \mathbf{H}_S = \frac{-i\omega_S}{c}\mathbf{D}_S$, which combine to give the relationship

$$\nabla \times \nabla \times \mathbf{E}_S = \frac{\omega_S^2}{c^2}\mathbf{D}_S. \tag{3.42}$$

Substituting Equation 3.41 into Equation 3.42, and noting that:
i) $\nabla \times \nabla \times \mathbf{D}_S = \nabla(\nabla \cdot \mathbf{D}_S) - \nabla^2 \mathbf{D}_S$, ii) $\nabla \cdot \mathbf{D}_S = 0$, and iii) $k_s^2 = \omega_s^2/(\epsilon_s c^2)$, we

obtain the equation

$$\nabla^2 \mathbf{D}_S + k_S^2 \mathbf{D}_S = -\nabla \times \nabla \times (\delta\boldsymbol{\epsilon} \cdot \mathbf{E_I}). \tag{3.43}$$

To solve this equation, we must divide the material into small scattering regions (with dimensions still larger than the distance between structural units) and treat the scattering from one area as an individual event that is not affected by travel through the rest of the material. Thus, the scattered field at large distance from the scattering region (analogous to the large distance between material and detector) can be calculated.

At this point, we note that Equation 3.43 looks like a retarded potential of the form

$$\nabla^2 \phi + k^2 \phi = -4\pi\rho \tag{3.44}$$

with the solution

$$\phi = \int \rho \frac{e^{ikR}}{R} dV, \tag{3.45}$$

where ϕ and ρ depend on time through the factor $e^{-i\omega t}$ [84]. In this coordinate system, the origin (or scattering point) is located inside the scattering region. The radius vector from origin to the point P (where the field is calculated) is $\mathbf{R}_0$, with unit vector $\mathbf{n}$. The radius of the scattering region is $\mathbf{r}$, and $\mathbf{R} = \mathbf{R}_0 - \mathbf{r}$ is the distance from the scattering volume to the point P. At large distances from the scattering volume, $R_0 \gg r$ and

$$R = |\mathbf{R}_0 - \mathbf{r}| \approx R_0 - \mathbf{r} \cdot \mathbf{n}. \tag{3.46}$$

We can substitute this into Equation 3.45, noting that in the denominator $R \approx R_0$ and that the scattering wave vector $\mathbf{k}_s$ is in the direction of $\mathbf{R}_0$. Thus, the required solution for Equation 3.43 is

$$\mathbf{D}_S = \frac{e^{ik_s R_0}}{R_0} \int \left(\frac{1}{4\pi} \nabla \times \nabla \times (\delta\boldsymbol{\epsilon} \cdot \mathbf{E}_I) \right) e^{-i\mathbf{k}_s \cdot \mathbf{r}} dV. \tag{3.47}$$

Applying the curl to the exponential function in the integrand, Equation 3.47 simplifies to

$$\mathbf{D}_S = -\frac{e^{ik_s R_0}}{4\pi R_0} \mathbf{k}_s \times \mathbf{k}_s \times \int (\delta\boldsymbol{\epsilon} \cdot \mathbf{E}_I) e^{-i\mathbf{k}_s \cdot \mathbf{r}} dV. \tag{3.48}$$

Since we are assuming that the light does not interact with the material beyond the scattering incident, the relationship between $\mathbf{D}_S$ and $\mathbf{E}_S$ at the point being considered is simply $\mathbf{D}_S = \epsilon \mathbf{E}_S$. The electric field of incident light is periodic in its propagation, $\mathbf{E}_I = \mathbf{E}_0 e^{i\mathbf{k}\cdot\mathbf{r}}$. We introduce the simplifying notation for the scattering vector,

$$\mathbf{G} = \int (\delta\boldsymbol{\epsilon} \cdot \mathbf{E}_I) e^{-i\mathbf{k}_s\cdot\mathbf{r}} dV = \int (\delta\boldsymbol{\epsilon} \cdot \mathbf{E}_0) e^{i\mathbf{q}\cdot\mathbf{r}} dV, \tag{3.49}$$

where the phonon wave vector is defined in terms of the light's initial and scattered wave vectors as $\mathbf{q} = \mathbf{k}_s - \mathbf{k}_i$. Then Equation 3.48 becomes

$$\mathbf{E}_S = -\frac{e^{ik_s R_0}}{4\pi R_0 \epsilon} \mathbf{k}_s \times \mathbf{k}_s \times \mathbf{G}. \tag{3.50}$$

The change in dielectric tensor element can be related to the elasto-optic properties of the material through the relationship

$$\delta(\epsilon^{-1})_{ij} = p_{ijkl} u_{kl} \tag{3.51}$$

where p_{ijkl} are the elasto-optic tensor elements and u_{kl} are the strain tensor elements. Since the fluctuations in the dielectric are small, we note that $\delta(\epsilon^{-1})_{ij} = 1/\epsilon - 1/\epsilon_{ij} = (\epsilon_{ij} - \epsilon)/(\epsilon\epsilon_{ij}) \approx -(\delta\epsilon_{ij})/\epsilon^2$. For isotropic materials, which have only two independent elasto-optic tensor elements, the fluctuation in the dielectric tensor becomes

$$\delta\epsilon_{ij} = -\epsilon^2 \left[2p_{44} u_{ij} + p_{12} u_{ll} \delta_{ij}\right]. \tag{3.52}$$

(This simplification can be shown by expanding the sum in Equation 3.51 over kl and considering the cases where $i = j$ and $i \neq j$.) The displacement vector associated with the excitation of the wave vector $\mathbf{q}$ is

$$\mathbf{u} = \mathbf{u}_0 e^{i\mathbf{q}\cdot\mathbf{r}}, \tag{3.53}$$

and individual tensor elements are found by the symmetric combination of the displacement gradients:

$$u_{ij} = \frac{1}{2}\left(\frac{\partial u_i}{\partial x_j} + \frac{\partial u_j}{\partial x_i}\right) = \frac{1}{2} i \left(u_{0i} q_j + u_{0j} q_i\right) e^{i\mathbf{q}\cdot\mathbf{r}}. \tag{3.54}$$

With this, we can find the components of the scattering vector $\mathbf{G}$:

$$G_i = \int \delta\epsilon_{ij} E_{0j} e^{-i\mathbf{q}\cdot\mathbf{r}} dV = -\epsilon^2 \int \left[2p_{44} u_{ij} + p_{12} u_{ll} \delta_{ij}\right] E_{0j} e^{-i\mathbf{q}\cdot\mathbf{r}} dV. \tag{3.55}$$

Noting that the volume integral for a general strain tensor elements is

$$\int u_{ij} e^{-i\mathbf{q}\cdot\mathbf{r}} dV = \int (1/2) i \left(u_{0i} q_j + u_{0j} q_i\right) e^{i\mathbf{q}\cdot\mathbf{r}} dV = (1/2) i V (u_{0i} q_j + u_{0j} q_i), \tag{3.56}$$

Equation 3.55 becomes

$$G_i = -\epsilon^2 iV \left(p_{44}(u_{0i}q_j + u_{0j}q_i) + p_{12}u_{0l}q_l\delta_{ij}\right) E_{0j}, \tag{3.57}$$

which, in vector form, is

$$\mathbf{G} = -\epsilon^2 iV \left[p_{44}(\mathbf{u}_0(\mathbf{q} \cdot \mathbf{E}_0) + \mathbf{q}(\mathbf{u}_0 \cdot \mathbf{E}_0)) + p_{12}\mathbf{E}_0(\mathbf{u}_0 \cdot \mathbf{q})\right]. \tag{3.58}$$

The power dP scattered into the solid angle $d\Omega$ is

$$\frac{1}{LP_0}\left(\frac{dP}{d\Omega}\right) = \frac{R_0^2}{V|E_I|^2}|E_S|^2, \tag{3.59}$$

where L is the length of the interaction volume V, and P_0 is the incident power. This is equivalent to the power I_{ab} of light scattered per unit solid angle in an amorphous material normalized by initial light power I_0 and scattering volume V where, a and b represent the polarizations of incident and scattered light, respectively. Since light is scattered from fluctuations due to sound waves propagating in the material, we need to consider the scattering by both longitudinal and transverse phonons.

First, we will consider the power scattered by transverse sound waves. In this case, the displacement vector $\mathbf{u}$ is perpendicular to the phonon wave vector $\mathbf{q}$. Thus, $\mathbf{u}_0 \cdot \mathbf{q} = 0$ and Equation 3.58 becomes

$$\mathbf{G} = -\epsilon^2 iVp_{44} \left[\mathbf{u}_0(\mathbf{q} \cdot \mathbf{E}_0) + \mathbf{q}(\mathbf{u}_0 \cdot \mathbf{E}_0)\right]. \tag{3.60}$$

There are two independent directions of polarization possible with a transverse sound wave: $\mathbf{u}$ can be parallel to the plane containing $\mathbf{k}_S$ and $\mathbf{k}_I$ (often called the horizontal plane), or it can be perpendicular to this plane (called the vertical axis, with direction $\mathbf{k}_S \times \mathbf{k}_I$). This is depicted in Figure 3.6, where θ is the angle between incident and scattered wave vectors, and the incident electric field vector is polarized in the plane perpendicular to $\mathbf{k}_I$. The angle between the vertical $\mathbf{k}_S \times \mathbf{k}_I$ axis and the vector $\mathbf{E_0}$ is denoted by ψ. It is measured CW from the vertical axis.

For the case where $\mathbf{u}$ is in the plane of $\mathbf{k}_S$ and $\mathbf{k}_I$, we note that

$$\begin{aligned} \mathbf{q} \cdot \mathbf{E}_0 &= qE_0 \cos(\theta/2) \sin\psi, \\ \mathbf{u}_0 \cdot \mathbf{E}_0 &= u_0 E_0 \sin(\theta/2) \sin\psi, \end{aligned} \tag{3.61}$$

so that Equation 3.60 simplifies to

$$\mathbf{G} = -\epsilon^2 iVp_{44} \left[qE_0 \cos(\theta/2) \sin\psi \mathbf{u}_0 + u_0 E_0 \sin(\theta/2) \sin\psi \mathbf{q}\right]. \tag{3.62}$$

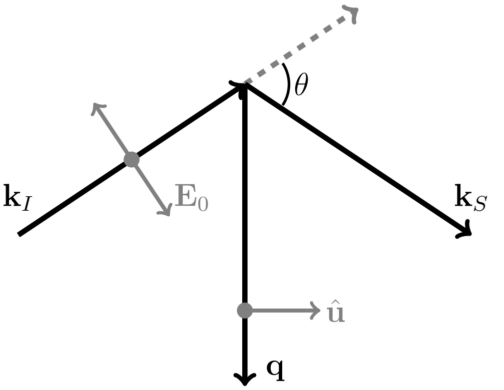

Figure 3.6: A schematic example of the scattering process of light from a fluctuating dielectric constant. The plane of $\mathbf{k}_S \times \mathbf{k}_I$ is in the page, while vectors perpendicular to this (i.e. coming out of the page) are represented by filled filled circles.

We can find the magnitude and direction of the scattered electric field using Equation 3.50, and noting that

$$\begin{aligned} \mathbf{k}_S \times \mathbf{k}_S \times \mathbf{u}_0 &= \mathbf{k}_S(\mathbf{k}_S \cdot \mathbf{u}_0) - k_S^2\mathbf{u}_0 = k_S u_0 \cos(\theta/2)\mathbf{k}_S - k_S^2\mathbf{u}_0, \\ \mathbf{k}_S \times \mathbf{k}_S \times \mathbf{q} &= \mathbf{k}_S(\mathbf{k}_S \cdot \mathbf{q}) - k_S^2\mathbf{q} = k_S q \sin(\theta/2)\mathbf{k}_S - k_S^2\mathbf{q}, \end{aligned} \tag{3.63}$$

the scattered electric field is

$$\begin{aligned} \mathbf{E}_S = \frac{e^{ik_S R_0}}{4\pi R_0 \epsilon}\epsilon^2 i V p_{44} E_0 \Big[& q\cos\frac{\theta}{2}\sin\psi\left(k_S u_0\cos\frac{\theta}{2}\mathbf{k}_S - k_S^2\mathbf{u}_0\right) \\ & + u_0 \sin\frac{\theta}{2}\sin\psi\left(k_S q\sin\frac{\theta}{2}\mathbf{k}_S - k_S^2\mathbf{q}\right)\Big] \\ = \frac{e^{ik_S R_0}}{4\pi R_0}\epsilon i V p_{44} E_0 q k_S^2 u_0 & \left[\sin\psi\hat{\mathbf{k}}_S - \sin\psi\left(\cos\frac{\theta}{2}\hat{\mathbf{u}}_0 + \sin\frac{\theta}{2}\hat{\mathbf{q}}\right)\right]. \end{aligned} \tag{3.64}$$

For the scattering orientation, $\cos\frac{\theta}{2}\hat{\mathbf{u}}_0 + \sin\frac{\theta}{2}\hat{\mathbf{q}} = \hat{\mathbf{k}}_S$, and thus we conclude that transverse waves propagating in the horizontal plane do not contribute to the Brillouin intensity.

Next, we consider displacement waves $\mathbf{u}$ parallel to $\mathbf{k}_S \times \mathbf{k}_I$. We have the relationships

$$\begin{aligned} \mathbf{q} \cdot \mathbf{E}_0 &= qE_0\cos(\theta/2)\sin\psi, \\ \mathbf{u}_0 \cdot \mathbf{E} &= u_0 E_0 \cos\psi, \end{aligned} \tag{3.65}$$

which lead to the scattering term

$$\mathbf{G} = -\epsilon^2 i V p_{44}\left[qE_0\cos(\theta/2)\sin\psi\mathbf{u}_0 + u_0E_0\cos\psi\mathbf{q}\right]. \tag{3.66}$$

Again, the magnitude and direction of the scattered electric field are found using Equation 3.50, with the cross products

$$\begin{aligned} \mathbf{k}_S \times \mathbf{k}_S \times \mathbf{u}_0 &= \mathbf{k}_S(\mathbf{k}_S \cdot \mathbf{u}_0) - k_S^2\mathbf{u}_0 = -k_S^2\mathbf{u}_0, \\ \mathbf{k}_S \times \mathbf{k}_S \times \mathbf{q} &= \mathbf{k}_S(\mathbf{k}_S \cdot \mathbf{q}) - k_S^2\mathbf{q} = k_S q \sin(\theta/2)\mathbf{k}_S - k_S^2\mathbf{q}. \end{aligned} \tag{3.67}$$

The electric field of the scattered light is

$$\begin{aligned} \mathbf{E}_S &= \frac{e^{ik_S R_0}}{4\pi R_0 \epsilon}\epsilon^2 iVp_{44}E_0\left[-qk_S^2\cos\frac{\theta}{2}\sin\psi\mathbf{u}_0 + u_0\cos\psi\left(k_S q\sin\frac{\theta}{2}\mathbf{k}_S - k_S^2\mathbf{q}\right)\right] \\ &= \frac{e^{ik_S R_0}}{4\pi R_0}\epsilon iVp_{44}E_0 q u_0 k_S^2\left[-\sin\psi\cos\frac{\theta}{2}\hat{\mathbf{u}}_0 + \cos\psi\left(\sin\frac{\theta}{2}\hat{\mathbf{k}}_S - \hat{\mathbf{q}}\right)\right] \\ &= -\frac{e^{ik_S R_0}}{4\pi R_0}\epsilon iVp_{44}E_0 q u_0 k_S^2\left[\sin\psi\cos\frac{\theta}{2}\hat{\mathbf{u}}_0 + \cos\psi\cos\frac{\theta}{2}(\hat{\mathbf{k}}_S \times \hat{\mathbf{u}}_0)\right]. \end{aligned} \tag{3.68}$$

The scattered light is polarized in the plane perpendicular to the wave vector $\mathbf{k}_S$ as expected.

At this point, we can compare the polarization of the scattered electric field to that of the incident light. The incident light is polarized in the plane perpendicular to $\mathbf{k}_I$, such that

$$\mathbf{E}_0 = E_0\left(\sin\psi(\hat{\mathbf{k}}_I \times \hat{\mathbf{u}}_0) + \cos\psi\hat{\mathbf{u}}_0\right). \tag{3.69}$$

The polarization of the scattered light, as seen in Equation 3.68, is simplified to

$$\mathbf{E}_S = E_S'\sin\frac{\theta}{2}\left(\cos\psi(\hat{\mathbf{k}}_S \times \hat{\mathbf{u}}_0) + \sin\psi\hat{\mathbf{u}}_0\right), \tag{3.70}$$

and we can see that the two electric fields are perpendicularly polarized for transverse sound waves.

We can relate the intensity of the scattered light to the elasto-optic coefficient p_{44} through Equation 3.59. Taking the dot product of $\mathbf{E}_s$ from Equation 3.68, we get

$$|E_S|^2 = \frac{\epsilon^2 V^2 p_{44}^2 |E_0|^2 q^2 \overline{|u_0|}^2 k_S^4}{(4\pi R_0)^2}\cos^2\frac{\theta}{2}\left[\sin^2\psi + \cos^2\psi\right]. \tag{3.71}$$

Since the sound wave is a thermodynamic fluctuation, it can be considered to be a combination of two oscillators with total mean kinetic energy $k_B T$. The sound wave has frequency $\omega_q = qv_T$, where v_T is the transverse sound velocity, so the mean kinetic energy is

$$\frac{1}{2}V\rho\overline{\dot{\mathbf{u}}^2} = \frac{1}{4}V\rho(v_T q)^2\overline{|u_0|^2} = k_B T. \tag{3.72}$$

The scattered wave vector in the material can be written as $k_S^2 = \epsilon(\omega_S/c)^2 = \epsilon(2\pi/\lambda)^2$; then the scattered power is

$$\frac{1}{LP_0}\left(\frac{dP}{d\Omega}\right) = \frac{4\pi^2 k_B T \epsilon^4}{\lambda^4 \rho v_T^2} p_{44}^2 \cos^2\frac{\theta}{2}. \tag{3.73}$$

It is of interest to note that the angle of polarization of the incident light does not affect the scattering intensity; however, light scattered from these transverse waves will be polarized perpendicularly to the incident light. The power of light scattered for transverse-acoustic phonons is usually measured experimentally as

$$I_{VH} = I_{HV} = I_0 V \frac{4\pi^2 k_B T}{\lambda^4}\frac{\epsilon^4 p_{44}^2}{\rho v_T^2}\cos^2\frac{\theta}{2}, \tag{3.74}$$

where V and H denote incident and scattered polarizations vertical or horizontal to the scattering plane containing $\mathbf{k}_I$ and $\mathbf{k}_S$.

Longitudinal sound waves have a displacement vector $\mathbf{u}$ parallel to the phonon wave vector $\mathbf{q}$. Writing

$$\begin{aligned}
\mathbf{q}\cdot\mathbf{E}_0 &= qE_0\cos\frac{\theta}{2}\sin\psi,\\
\mathbf{u}_0\cdot\mathbf{E}_0 &= u_0E_0\cos\frac{\theta}{2}\sin\psi,\\
\mathbf{u}_0\cdot\mathbf{q} &= u_0 q,
\end{aligned} \tag{3.75}$$

equation 3.58 becomes

$$\begin{aligned}
\mathbf{G} &= -\epsilon^2 iV\left[p_{44}\left(qE_0\cos\frac{\theta}{2}\sin\psi\mathbf{u}_0 + u_0E_0\cos\frac{\theta}{2}\sin\psi\mathbf{q}\right) + p_{12}u_0q\mathbf{E}_0\right]\\
&= -\epsilon^2 iVqu_0E_0\left[2p_{44}\cos\frac{\theta}{2}\sin\psi\hat{\mathbf{q}} + p_{12}\hat{\mathbf{E}}_0\right].
\end{aligned} \tag{3.76}$$

With this, and the relationships

$$\begin{aligned}
\mathbf{k}_S\times\mathbf{k}_S\times\hat{\mathbf{q}} &= \mathbf{k}_S(\mathbf{k}_S\cdot\hat{\mathbf{q}}) - k_S^2\hat{\mathbf{q}} = k_S^2\sin\frac{\theta}{2}\hat{\mathbf{k}}_S - k_S^2\hat{\mathbf{q}},\\
\mathbf{k}_S\times\mathbf{k}_S\times\hat{\mathbf{E}}_0 &= \mathbf{k}_S(\mathbf{k}_S\cdot\hat{\mathbf{E}}_0) - k_S^2\hat{\mathbf{E}}_0 = k_S^2\sin\theta\sin\psi\hat{\mathbf{k}}_S - k_S^2\hat{\mathbf{E}}_0,
\end{aligned} \tag{3.77}$$

we can determine (using Equation 3.50) the field scattered from longitudinal sound waves:

$$\begin{aligned}
\mathbf{E}_s &= \frac{e^{ik_sR_0}}{4\pi R_0\epsilon}\epsilon^2 iVqu_0E_0\left[2p_{44}\cos\frac{\theta}{2}\sin\psi\left(k_S^2\sin\frac{\theta}{2}\hat{\mathbf{k}}_S - k_S^2\hat{\mathbf{q}}\right) + p_{12}\left(k_S^2\sin\theta\sin\psi\hat{\mathbf{k}}_S - k_S^2\hat{\mathbf{E}}_0\right)\right] \\
&= \frac{e^{ik_sR_0}}{4\pi R_0}\epsilon iVqu_0E_0k_S^2\left[2p_{44}\cos\frac{\theta}{2}\sin\psi\left(\sin\frac{\theta}{2}\hat{\mathbf{k}}_S - \hat{\mathbf{q}}\right) + p_{12}\left(\sin\theta\sin\psi\hat{\mathbf{k}}_s\right.\right. \\
&\qquad\qquad \left.\left. - \left(\sin\psi\hat{\mathbf{E}}_{0H} + \cos\psi\hat{\mathbf{E}}_{0V}\right)\right)\right] \\
&= \frac{e^{ik_sR_0}}{4\pi R_0}\epsilon iVqu_0E_0k_S^2\left[-2p_{44}\cos^2\frac{\theta}{2}\sin\psi\left(\hat{\mathbf{k}}_S\times\hat{\mathbf{E}}_{0V}\right) - p_{12}\cos\theta\sin\psi\left(\hat{\mathbf{k}}_S\times\hat{\mathbf{E}}_{0V}\right)\right. \\
&\qquad\qquad \left. - p_{12}\cos\psi\hat{\mathbf{E}}_{0V}\right] \\
&= -\frac{e^{ik_sR_0}}{4\pi R_0}\epsilon iVqu_0E_0k_S^2\left[\sin\psi\left(2p_{44}\cos^2\frac{\theta}{2} + p_{12}\cos\theta\right)\left(\hat{\mathbf{k}}_s\times\hat{\mathbf{E}}_{0V}\right) + p_{12}\cos\psi\hat{\mathbf{E}}_{0V}\right].
\end{aligned} \tag{3.78}$$

We can see that the scattered light is polarized in the plane perpendicular to the wave vector $\mathbf{k}_S$. If incident light is polarized vertically ($\psi = 0°$), then the light scattered will also be polarized in the vertical direction. Likewise, if light is initially polarized in the scattering plane ($\psi = 90°$), then scattered light will also be polarized in this plane. The scattered power, from Equation 3.59, is

$$\frac{1}{LP_0}\left(\frac{dP}{d\Omega}\right) = \frac{4\pi^2k_BT}{\lambda^4}\frac{\epsilon^4}{\rho v_L^2}\left[\sin^2\psi\left(2p_{44}\cos^2\frac{\theta}{2} + p_{12}\cos\theta\right)^2 + p_{12}^2\cos^2\psi\right]; \tag{3.79}$$

for vertical and horizontal incident polarized light, this simplifies to

$$\begin{aligned}
I_{VV} &= I_0V\frac{4\pi^2k_BT}{\lambda^4}\frac{\epsilon^4}{\rho v_L^2}p_{12}^2, \\
I_{HH} &= I_0V\frac{4\pi^2k_BT}{\lambda^4}\frac{\epsilon^4}{\rho v_L^2}\left(2p_{44}\cos^2\frac{\theta}{2} + p_{12}\cos\theta\right)^2.
\end{aligned} \tag{3.80}$$

3.3.3 Principles of Multiple Beam Interference

In order to experimentally measure these scattering intensities at low frequency shifts, we turn to the method of Fabry-Perot interferometry and multiple beam interference [7, 75]. Fabry-Perot interferometers are used to analyze the detailed structure of spectral lines by measuring the interference patterns from light near to normally incident on plane parallel plates. Typically, these plates will be coated on one side with a metallic film in order to increase their reflectivity.

When light is incident on a transparent, plane parallel glass plate, a large number of reflections will occur at the plate surfaces. This results in a series of beams with decreasing amplitudes on either side of the plate. Consider such a glass plate with thickness d and refractive index n', surrounded by a material with index n. If a monochromatic light wave $\mathbf{E}$ with amplitude E_0 is incident on the plate with angle θ, then the wave will be reflected and transmitted at both parallel surfaces. Here, for waves entering the glass plate, r and t are the reflection and transmission coefficients, or the ratio of reflected or transmitted and incident amplitudes. Similarly, r' and t' are the reflection and transmission coefficients for light exiting the plate; these are defined by Equation 3.27 or 3.29 for incident light that is s- or p-polarized. A schematic of the multiple beam reflection is seen in Figure 3.7.

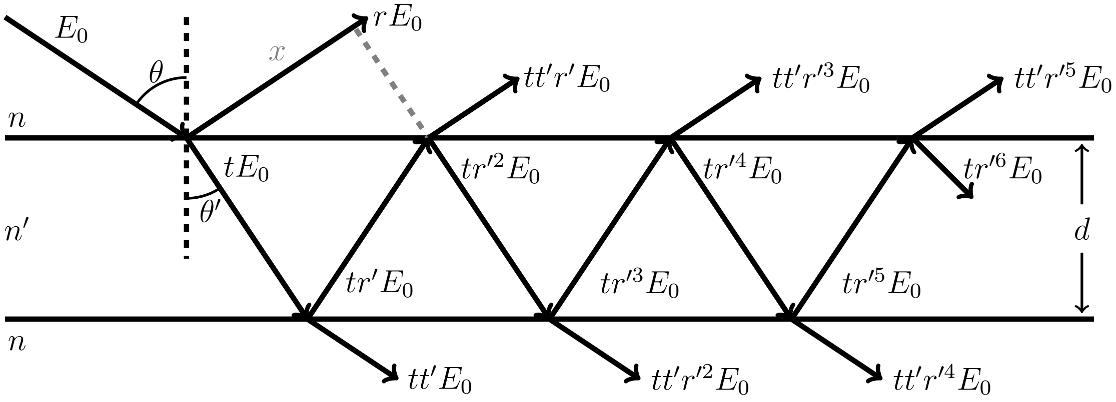

Figure 3.7: Multiple internally reflecting beams in a transparent parallel plane glass plate. A series of waves with decreasing amplitudes exit on either side of the plate.

The complex amplitudes of the reflected waves are

$$rE_0, \qquad tt'r'E_0e^{i\delta}, \qquad tt'r'^3E_0e^{2i\delta}, \qquad ..., \tag{3.81}$$

and the complex amplitudes of waves transmitted through the plate (ignoring the unimportant phase factor between reflected and transmitted waves) are

$$tt'E_0, \qquad tt'r'^2E_0e^{i\delta}, \qquad tt'r'^4E_0e^{2i\delta}, \qquad ... \tag{3.82}$$

From the principle of reversibility, we come to the conclusion that $r' = -r$ and $tt' + r^2 = 1$ so long as none of the energy is absorbed. The phase difference between subsequent transmitted or reflected waves is δ, which corresponds to double traversal of the glass plate. To find this phase difference in terms of the properties of the glass plate and light source, we consider the optical path length difference Λ between reflected light beams with amplitudes rE_0 and $tt'r'E_0$:

$$\Lambda = n'(\frac{2d}{\cos\theta'}) - nx. \tag{3.83}$$

Here, x is the distance that the reflected light with amplitude rE_0 has traveled before the second reflected light ray reaches the top surface of the plate; see Figure 3.7. Then, with the relationships $x = 2d\tan\theta'\sin\theta$, and $n'\sin\theta' = n\sin\theta$, the optical path length difference becomes

$$\Lambda = 2n'd\cos\theta' \tag{3.84}$$

and the phase difference between subsequent reflected or transmitted waves is given by

$$\delta = \frac{2\pi\Lambda}{\lambda_0} = \frac{4\pi n'd}{\lambda_0}\cos\theta', \tag{3.85}$$

where λ_0 is the wavelength of light outside of the glass plate.

Since the waves are mutually coherent, if they are focused by a lens at a specific point (P for reflecting waves and P' for transmitted waves), they will interfere, giving summed amplitudes E_{0R} for reflection from the first surface and E_{0T} for transmission from the second surface. For the most general case with unknown phase shift δ, the amplitude of the reflected waves interfering at point P is

$$\begin{aligned} E_{0R} &= rE_0 - tt'rE_0\left(e^{i\delta} + r^2e^{2i\delta} + r^4e^{3i\delta} + r^6e^{4i\delta} + ...\right) \\ &= rE_0 - tt'rE_0e^{i\delta}\left(1 + (r^2e^{i\delta}) + (r^2e^{i\delta})^2 + (r^2e^{i\delta})^3 + ...\right) \\ &= rE_0 - \frac{tt'rE_0e^{i\delta}}{1-r^2e^{i\delta}} = rE_0\left(\frac{1-e^{i\delta}}{1-r^2e^{i\delta}}\right). \end{aligned} \tag{3.86}$$

Here, we note that for the special case where $\delta = 2\pi m$ and m is an integer value, the interference of the reflected waves at point P is entirely destructive. For a non-absorbing material, since there are no reflections from the first surface, all light must be transmitted. On the other hand, if $\delta = (2m+1)\pi$, then the amplitude of the reflected light's electric field is at its maximum. The intensity of the reflected light is simply

$$I_R = E_{0R}E_{0R}^* = r^2E_0^2\left(\frac{1-e^{i\delta}}{1-r^2e^{i\delta}}\right)\left(\frac{1-e^{-i\delta}}{1-r^2e^{-i\delta}}\right) = 2r^2e_0^2\frac{1-\cos\delta}{(1+r^4)-2r^2\cos\delta}. \tag{3.87}$$

We can perform a similar analysis of the transmitted waves. The amplitude of the waves interfering at point P' is

$$E_{0T} = tt'E_0\left(1 + r'^2e^{i\delta} + r'^4e^{2i\delta} + r'^6e^{3i\delta} + r'^8e^{4i\delta} + ...\right) = \frac{(1-r^2)E_0}{1-r^2e^{i\delta}} \tag{3.88}$$

and the intensity of the transmitted light is

$$I_T = E_{0T}E^*_{0T} = (1-r^2)^2E_0^2\left(\frac{1}{1-r^2e^{i\delta}}\right)\left(\frac{1}{1-r^2e^{-i\delta}}\right) = \frac{(1-r^2)^2e_0^2}{(1+r^4)-2r^2\cos\delta}. \tag{3.89}$$

For the case when $\delta = 2\pi m$ and no light is reflected, the transmitted amplitude is $E_{0T} = E_0$ which corresponds to all light being transmitted. Equations 3.87 and 3.89 can be simplified by substituting $\cos\delta = 1 - 2\sin^2(\delta/2)$:

$$\begin{aligned} I_R/I_0 &= \frac{(2r^2/(1-r^2))^2\sin^2\frac{\delta}{2}}{1+(2r^2/(1-r^2))^2\sin^2\frac{\delta}{2}} = \frac{F\sin^2\frac{\delta}{2}}{1+F\sin^2\frac{\delta}{2}} \\ I_T/I_0 &= \frac{1}{1+(2r^2/(1-r^2))^2\sin^2\frac{\delta}{2}} = \frac{1}{1+F\sin^2\frac{\delta}{2}}, \end{aligned} \tag{3.90}$$

where $I_0 = E_0^2$ and $F = (2r^2/(1-r^2))^2$ is called the coefficient of finesse, or finesse factor. This value will depend on the mirror reflectivity and flatness.

To this point, we have considered glass plates with no metallic coating. However, the partially transparent metallic films on the mirrors within an FP interferometer will absorb a fraction of the light intensity. The expression for transmittance and reflectivity must be rewritten to include the absorbtance term A:

$$tt' + r^2 + A = 1. \tag{3.91}$$

With this, the normalized transmitted intensity becomes

$$I_T/I_0 = \left(1 - \frac{A}{1-r^2}\right)^2\frac{1}{1+F\sin^2\frac{\delta}{2}}. \tag{3.92}$$

The light wave will also undergo an additional shift ϕ upon reflection from the metallic surface. Then the phase shift δ becomes

$$\delta = \frac{2\pi n'd}{\lambda_0}\cos\theta' + 2\phi. \tag{3.93}$$

Generally speaking, d is large enough and λ_0 small enough that the effects due to ϕ can be neglected.

3.3.4 Fabry-Perot Interferometry

This discussion of Fabry-Perot interferometry is based on references [7, 75, 82, 85, 86].

The multiple beam interference patterns from plane parallel plates are used in Fabry-Perot (FP) interferometers, allowing measurement of the Brillouin spectra to a resolution of GHz or MHz frequencies. Within the FP are two very flat, highly reflecting semi-transparent surfaces. These are typically glass plates mounted exactly parallel to each other and with adjustable spacing d between them; the gap is usually filled with air such that $n' = 1$. The inner surfaces of the plates are coated with semi-transparent metallic films with high reflectivity, and the outer surfaces are slightly prismatic to avoid unwanted glass-air reflections. Light is typically incident normal to the mirrors within the interferometer, such that $\cos\theta' = 1$. The air gap d is on the order of millimeters to centimeters for interferometers; if the spacing is much larger, the mirror apparatus can be used as a resonant laser cavity.

For a set mirror spacing d, the FP will only measure maximum transmission for specific wavelengths, determined by Equations 3.85 and 3.92. For maximum transmission, it is necessary that $\delta = 2\pi m$. Thus the relationship

$$m\lambda_0 = 2n'd\cos\theta' = 2d \tag{3.94}$$

determines maximum transmission of light with wavelength λ_0. The FP acts like tunable filter, where transmission will be close to maximum over a very narrow wavelength range, and will drop to near zero outside of this range.

Since δ is a function of λ_0, if the light source contains multiple wavelengths then the interference pattern will be the sum of intensity distributions from each individual monochromatic wavelength component. If the wavelengths cover a range $\Delta\lambda_0$ (often called the free spectral range, FSR), then the fringe maximum coefficient m will also be spread over a distance Δm. Differentiating Equation 3.94, we find that

$$m\Delta\lambda_0 = -\lambda_0\Delta m. \tag{3.95}$$

From this (ignoring the negative, which simply indicates that order decreases as wavelength increases), it follows that the FSR depends inversely on mirror spacing:

$$\Delta\lambda_0 = \frac{\lambda_0^2\Delta m}{2d}. \tag{3.96}$$

Furthermore, the finesse is related to the FSR and the width of a transmission peak from one wavelength component, $\delta\lambda_0$, as

$$F = \frac{\Delta\lambda_0}{\delta\lambda_0}. \tag{3.97}$$

In practice, the spacing d is varied to scan the intensity of light at different wavelengths. However, all wavelengths that satisfy Equation 3.94 will contribute to the measured Brillouin intensity. As the difference between wavelengths becomes larger, overlapping peaks will separate. For example, the m-th order fringe for λ_0 approaches the $(m+1)$-th order fringe for $(\lambda_0 - \Delta\lambda_0)$. In order to accurately interpret the Brillouin spectra, it would be beneficial to increase the range $\Delta\lambda_0$. Then the range of incident light will be contained within the FSR and overlapping will be minimized. This can be achieved by decreasing the mirror spacing; however, since the finesse is fixed, this would also broaden the width of transmission peaks and decrease resolution. Experimentally, the finesse F is limited to values of about 100 due to the quality of reflective coatings.

It is possible to increase the free spectral range at fixed resolution by placing multiple FPs (typically 2) with similar spacings in series (tandem). Light will pass through each FP many times (multi-pass), and both must transmit the same wavelength simultaneously. Thus the spacings for each interferometer must satisfy $\lambda_0 = 2m_1d_1$, $\lambda_0 = 2m_2d_2$ and so on, where m_i are integers. Since both FPs have slightly different FSRs, one FP will block the neighbouring overlapping interferences. That is to say, higher orders of light transmitted through the first FP (say $\Delta m_1 = 1$) will not be transmitted through the second interferometer. So if the mirror spacings are set to transmit a specific wavelength λ_0, then the transmission spectra will resolve both peaks; see Figure 3.8(c). The intensity of light transmitted through the two FPs is

$$I_T/I_0 = \left(1 - \frac{A_2}{1-r_2^2}\right)^2 \frac{1}{1+F_2\sin^2\frac{\delta_2}{2}} \left(1 - \frac{A_1}{1-r_1^2}\right)^2 \frac{1}{1+F_1\sin^2\frac{\delta_1}{2}} \tag{3.98}$$

Experimentally, the multiple interferometers will be scanned by simultaneously changing the mirror spacings (typically by 1-2μm) such that, for two FPs, $\frac{\delta L_1}{\delta L_2} = \frac{L_1}{L_2}$. This synchronization condition can be satisfied by having the scanning mirrors of two interferometers mounted on the same translation stage, with angular offset; this is seen in Figure 3.9. Typically, light will pass multiple times through each interferometer.

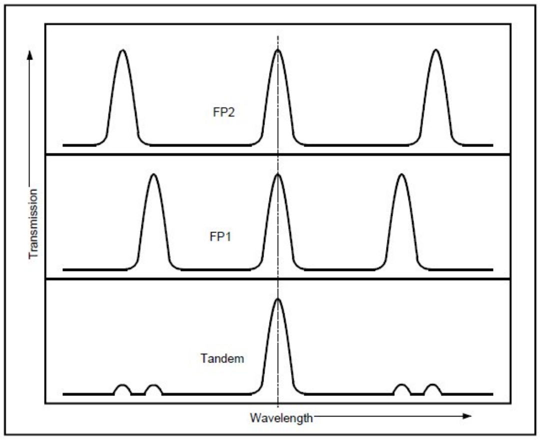

Figure 3.8: Using more than one FP mirror set allows the resolution of Brillouin peaks. Image from [86].

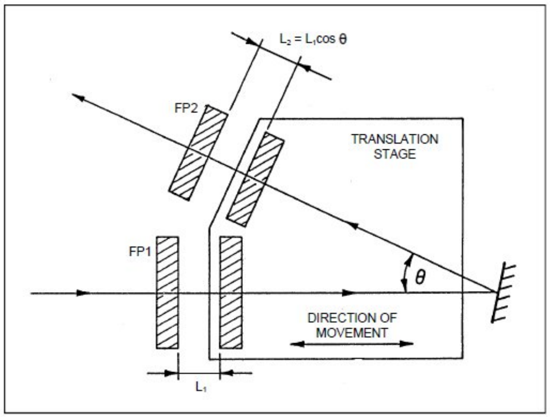

Figure 3.9: Schematic of a tandem Fabry-Perot interferometer. Both scanning mirrors move to satisfy the condition $\frac{\delta L_1}{\delta L_2} = \frac{L_1}{L_2}$. Image from [86].

3.3.5 Determining p_{ij} from Brillouin Spectra

In order to determine the elasto-optic coefficients from the FP-collected Brillouin spectra, a few special considerations are necessary. These include comparing sample intensities to reference intensities, accounting for the reflection of light at interfaces, and determining the relative signs of p_{12} and p_{44}.

For right-angle scattering geometry ($\theta = 90°$) with incident and scattered light vertically or horizontally polarized, the scattered light intensities from Equations 3.74

and 3.80 become

$$\begin{aligned}
I_{VV} &= \left(I_0 V \frac{4\pi^2 k_B T}{\lambda^4}\right) \frac{\epsilon^4}{\rho v_L^2} p_{12}^2 = A \frac{\epsilon^4}{\rho v_L^2} p_{12}^2, \\
I_{HH} &= \left(I_0 V \frac{4\pi^2 k_B T}{\lambda^4}\right) \frac{\epsilon^4}{\rho v_L^2} p_{44}^2 = A \frac{\epsilon^4}{\rho v_L^2} p_{44}^2, \\
I_{VH} &= \left(I_0 V \frac{4\pi^2 k_B T}{\lambda^4}\right) \frac{\epsilon^4}{2\rho v_L^2} p_{44}^2 = A \frac{\epsilon^4}{2\rho v_L^2} p_{44}^2.
\end{aligned} \tag{3.99}$$

Note that these intensities can be separated into the sample independent factor $A = I_0 V(4\pi^2 k_B T/\lambda^4)$, and sample dependent factors of dielectric constant (or refractive index), density, sound velocity and elasto-optic coefficient. This does assume that the scattering volume V is equal for all samples.

The factor A can be difficult to measure experimentally. Absolute values of p_{ij} are found by comparing the measured intensities of the samples to those for reference materials with known density, refractive index and elastic and elasto-optic properties [13, 21, 64, 65, 67]. In this way, the sample independent factor is removed from the intensity ratios. Typically, toluene or fused quartz are used as reference materials.

The transmission of light through the air-sample interfaces must also be accounted for. At normal incidence, the transmissivity is

$$T = \left(\frac{2}{n+1}\right)^2 \left(\frac{2n}{1+n}\right)^2, \tag{3.100}$$

where n is the refractive index of the sample ($\epsilon = n^2$) [7, 21, 64]. The experimentally measured intensities are thus

$$I_{\alpha\beta}^{ex} = T I_{\alpha\beta} \tag{3.101}$$

and the elasto-optic coefficient is measured from

$$\begin{aligned}
(p_{12})_g &= \left(\frac{\rho_g (I_{VV}^{ex})_g}{\rho_r (I_{VV}^{ex})_r} \frac{T_r}{T_g}\right)^{1/2} \left(\frac{n_r}{n_g}\right)^4 \frac{(v_L)_g}{(v_L)_r} (p_{12})_r \\
&= \left(\frac{\rho_g (I_{VV}^{ex})_g}{\rho_r (I_{VV}^{ex})_r}\right)^{1/2} \left(\frac{n_r}{n_g}\right)^5 \left(\frac{n_g+1}{n_r+1}\right)^2 \frac{(v_L)_g}{(v_L)_r} (p_{12})_r,
\end{aligned} \tag{3.102}$$

where the notations g and r represent properties for the glass and reference samples, respectively. The shear elasto-optic coefficient was found by comparing the sample's longitudinal and transverse peak intensities:

$$p_{44} = \frac{v_T}{v_L} \left(\frac{I_{VH}^{ex}}{I_{VV}^{ex}}\right)^{1/2} p_{12}. \tag{3.103}$$

The relative signs of p_{44} and p_{12} are determined from the HH and VH spectra. For scattering angle θ, the ratio of HH and VH intensities (which both depend on θ) is

$$J(\theta) = \frac{I_{HH}}{I_{VH}} = \frac{v_L}{v_T}\left(\frac{2p_{44}\cos^2\frac{\theta}{2} + p_{12}\cos\theta}{p_{44}\cos\frac{\theta}{2}}\right)^2. \tag{3.104}$$

By measuring how the ratio $J(\theta)$ behaves with small variations of θ around 90°, the sign of p_{12}/p_{44} can be measured:

$$\left.\frac{dJ(\theta)}{d\theta}\right|_{\theta=90^\circ} = \frac{2v_L}{v_T}\left(\frac{1}{2^{1/2}} + \frac{1}{2^{3/2}}\right)\left(-1 - \frac{p_{12}}{p_{44}}\right) \propto -\frac{p_{12}}{p_{44}} \tag{3.105}$$

Thus $J(\theta)$ is an increasing (decreasing) function of θ depending on whether the signs of p_{12} and p_{44} are different (the same).

Chapter 4

Photoelasticity of Non-Oxide Glasses

The photoelastic response of stoichiometric $(GeS_2)_{1-x}(P_2S_5)_x$ and $(GeS_2)_{1-x}(Sb_2S_3)_x$ and non-stoichiometric $Ge_2.5PS_x$ glasses has been investigated. The purpose of this research is to extend the parameters of the empirical model of photoelasticity to include non-oxide glass compounds. These systems provide a good starting point as their compositionally-dependent structures and bonding environments are well understood. The effect of excess and deficit sulfur on the stress-optic coefficient is considered with respect to the structure of the non-stoichiometric glasses, and the magnitude of the stress-optic response in sulfides is compared to that of oxide glasses.

The results and discussion of the stress-optic response in non-oxide glasses have been published in the Journal of Non-Crystalline Solids [87]. The manuscript of this article is included in this chapter. Bruce Aitken's contributions to the research included the synthesis of the sulfide glasses and review of the manuscript. Josef Zwanziger collaborated on the discussion and analysis of results.

4.1 Experimental Procedure

4.1.1 Glass Synthesis

Glasses were synthesized by Bruce Aitken and Steve Currie at Corning Incorporated. The glass-making procedure is described in references [71, 72] and summarized in Section 2.1 of the included manuscript. Glasses were cut, polished and measured at Dalhousie University.

4.1.2 Density, Elastic Moduli and Refractive Index Measurements

The procedures for obtaining the densities, shear moduli and refractive indices of the chalcogenide glasses are described in Section 2.3 of the included manuscript.

4.1.3 Initial Calibration of Sénarmont Optics

The near-IR stress-optic coefficients of sulfide glasses are measured using the Sénarmont compensator method. The optical components of the experiment are described in Section 2.2 of the included manuscript. Before measurements could be taken, the polarizer, analyzer and LCVR needed to be calibrated for 1550 nm light.

First, the angle of extinction of the analyzer was verified. The polarizer was placed after the laser with its axis at 45° to the horizontal, i.e. aligned with the x-axis of the system. The analyzer, mounted in an electronic rotation stage, was placed between the polarizer and the power sensor. At its initial angle, $\theta = 0$, the analyzer is approximately perpendicular to the polarizer but due to its placement in the rotation stage, an offset is expected. To determine this offset, θ was varied from -95° to 95° in 5° increments. The intensity of light was recorded at each step, resulting in a roughly sinusoidal curve; see Figure 4.1. The curve was fitted and the minimum intensity, i.e. the angle at which the polarizer and analyzer are crossed, was found to be -2.3°.

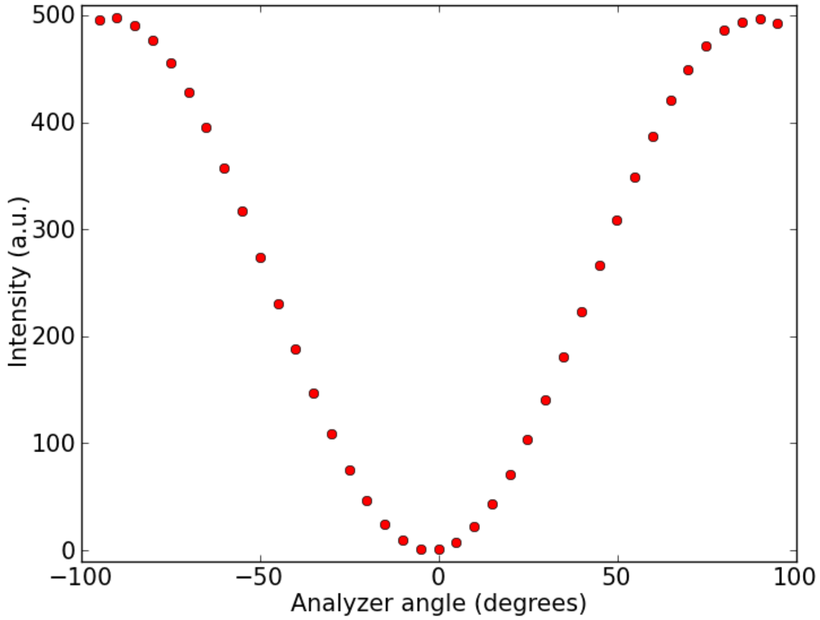

Figure 4.1: Intensity of linearly polarized 1550 nm light passing through a rotatable analyzer as a function of analyzer angle θ. The minimum intensity occurs when the analyzer axis is perpendicular to the initial polarization axis of the light ($\theta = -2.3°$).

Next, the LCVR must be set to act as a quarter-wave plate in the system. It is necessary to determine the fast axis angle of the LCVR, as well as the voltage at which the LCVR acts as a quarter-wave plate for 1550 nm. The fast axis was determined by setting the LCVR between the crossed polarizer and analyzer and rotating the LCVR until intensity was a minimized. At this angle, the fast axis is aligned with the axis of the first polarizer. To determine the retardance, the LCVR was rotated by 45° so that its fast axis is along the vertical direction. If the LCVR is acting as a quarter-wave plate, the incident linearly polarized light will become circularly polarized and the intensity of the resulting light should be the same for all θ. The voltage applied to the LCVR was incrementally increased until the intensity measured for $\theta = 0°$ equalled the intensity at $\theta = \pm 90°$. To verify that the light is circularly polarized at this voltage, intensity measurements were recorded for $-95° \leq \theta \leq 95°$ in 5° steps. The intensity of light does not vary significantly with analyzer angle; see Figure 4.2. Thus the light is circularly polarized, and the LCVR acts as a quarter-wave plate at this voltage (V = 2.750 V for 1550 nm). The calibrated optics can now be used to determine the phase shift of light travelling through stressed glass.

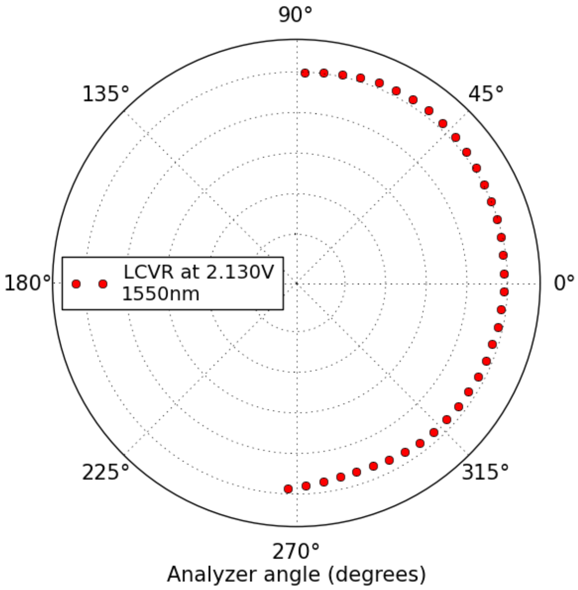

Figure 4.2: Intensity (a.u.) of linearly polarized 1550 nm passing through i) an LCVR (V = 2.13 V) with fast axis at 45° to the polarization axis and ii) a rotatable analyzer as a function of analyzer angle θ. The intensity does not vary significantly with θ, which shows that the light is circularly polarized.

4.1.4 Applying Stress to Glass Samples

In order to accurately and precisely measure the stress-optic coefficient of a glass, homogeneous stress is necessary. Our group uses a custom-built strain gage, pictured in Figure 4.3. The gage consists of a cage system with two solid aluminum plates, a motorized screw, and a load cell. The glass sample sits between the two parallel plates, and the screw descends onto the top plate to stress the glass. Often, a compliant plastic layer is placed between the glass and the aluminum to ensure the stress is as uniform as possible. A load cell, located below the bottom plate, measures the force F acting on the glass sample. The stress σ can then be determined from

$$\sigma = \frac{F}{A}, \tag{4.1}$$

where A is the area of the face of the glass sample to which force is applied.

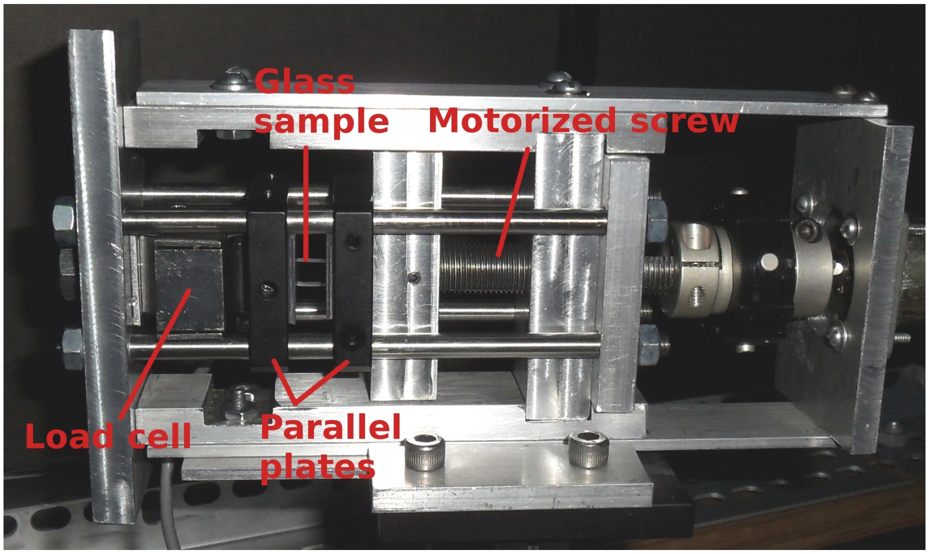

Figure 4.3: Glasses are stressed using a custom-built strain gage.

The uniformity of the applied stressed is visually inspected using a polariscope (Strainoptics PS-100). The polariscope, or light table, is a Sénarmont compensator with a fluorescent bulb providing white light. The strain gage is placed between the table's two crossed polarizers, and the analyzer is rotated to determine the minimum intensity of light. If the stress is applied homogeneously, then phase shift of polarized light traveling through the glass will be equal at all spots and the intensity of light will be minimized uniformly across the sample. An evenly stressed glass is pictured in Figure 4.4.

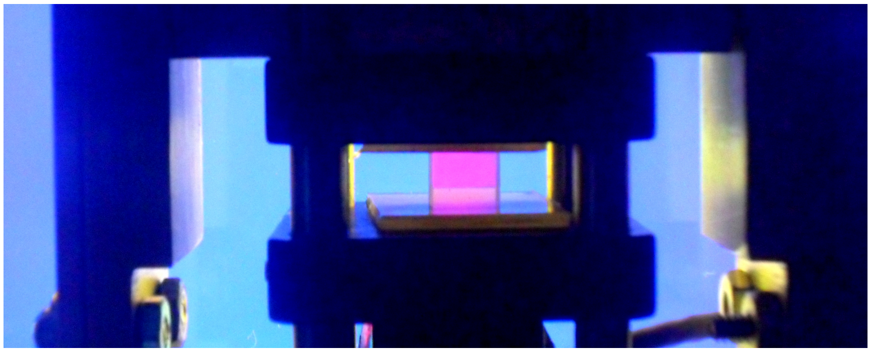

Figure 4.4: A uniformly stressed glass sample exhibiting birefringence. As the linearly polarized light travels through the glass, its polarization changes. The analyzer angle that gives the minimum intensity of light in the glass (shown in pink) is offset from $\theta = 0$. The colour of the intensity of light comes from a tint plate between the sample and the analyzer.

4.1.5 Determining the Stress-Optic Coefficient

Once the optics have been calibrated and the glass uniformly stressed, the strain gage is placed on a goniometer and the glass sample is aligned with the light beam. A red alignment laser (650 nm) in conjunction with near-IR fluorescing pinholes are used to ensure linear back-reflectance of the 1550 nm laser from all optical components. Individual stress-optic trials are taken by decreasing the pressure from a maximum value to a minimum; approximately 10 pressures are applied per trial. For each pressure, the force applied to the glass is recorded from the strain gage. The analyzer is rotated by 16° on either size of the angle of minimum intensity in 2° steps. At each angular step, the intensity is recorded by the PM-100 sensor software for one second with a rate of 100 counts per second. The intensities are averaged and parabolically fit to determine the minimum transmission angle, θ, for the applied pressure. Multiple decreasing pressure trials are performed for light incident on one spot on the face of the glass, and at least three unique spot locations are measured.

The relationship between angle of minimum intensity θ, phase shift Δ, applied force F and applied stress σ is determined by combining Equations 3.11. 3.16, and 4.1. By convention, compressive forces and stresses are negative. Figure 4.5 shows phase shifts vs applied stress from all trials for one glass sample. The stress-optic coefficient is determined from the slope of Δ vs σ and the known properties λ, d and A. The uncertainty in C is determined from the deviation of the slope.

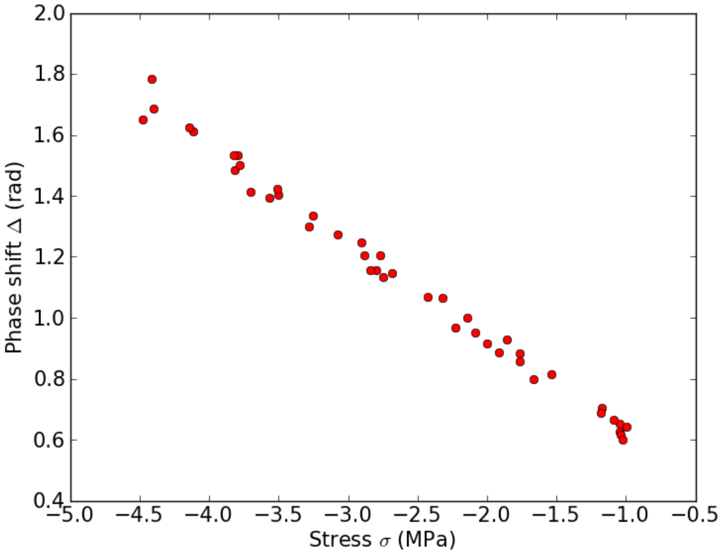

Figure 4.5: Phase shift Δ of 1550 nm light as a function of stress σ applied to the chalcogenide glass with composition $0.33GeS_2$-$0.67Sb_2S_3$. The stress-optic coefficient is determined from the slope of Δ vs σ and Equation 3.11.

4.2 Manuscript: "Correlating Structure with Stress-Optic Response in Non-Oxide Glasses"

The results of the photoelastic response of sulfide glasses and a discussion of the suitability of the empirical model for non-oxide glasses have been published in the Journal of Non-Crystalline Solids (doi:10.1016/j.jnoncrysol.2014.07.023) [87]. The pre-print article is included here. Further discussion of the photoelastic trends follows in Section 4.3.

Correlating structure with stress-optic response in non-oxide glasses

J. Galbraith[a,b], J. W. Zwanziger[a,b,c,*], B. G. Aitken[d]

[a] *Department of Physics and Atmospheric Sciences, Dalhousie University, Halifax, NS B3H 4R2 Canada*
[b] *Institute for Research in Materials, Dalhousie University, Halifax, NS B3H 4R2 Canada*
[c] *Department of Chemistry, Dalhousie University, Halifax, NS B3H 4R2 Canada*
[d] *Corning Incorporated, Corning, NY 14831, USA*

Abstract

The stress-induced birefringence, known as the stress-optic response, of glasses in the Ge-P-S and Ge-Sb-S families were measured and correlated with structure. Birefringence of the samples was measured as a function of stress load, using the Sénarmont method. In addition, density, index of refraction, and shear moduli were determined. It was found that the glass structure correlated well with the stress-optic response, through a combination of the bond lengths and coordination numbers, as found previously for oxides. However, the zero stress-optic threshold behavior and magnitude of the effect differ from oxides, and these features are explained based on bonding differences and the smaller shear moduli in sulfides.

Keywords:
Stress-optic response, Non-oxide glass, Photoelastic response

---

[*] Corresponding author. Tel: +1-902-494-1960; Fax: +1-902-494-1310
Email address: `jzwanzig@dal.ca` (J. W. Zwanziger)

Preprint submitted to Journal of Non-Crystalline Solids *June 3, 2014*

1. Introduction

Glass is optically isotropic, but when a uniaxial stress is applied, usually becomes birefringent. This effect is known as photoelasticity and has been extensively studied in oxides [1–13]. Early theories of photoelasticity relate birefringence to atomic structure and polarizability of ions [2], while a recent empirical model of photoelasticity uses bond length and cation coordination to predict new zero-stress optic oxide glasses [9]. These non-birefringent glasses are key components in many products, including fiber optics, optical research instruments, and projection optics.

Information on the photoelastic response of non-oxide glasses is rather more limited [14–18]. Chalcogenide glasses have attracted attention due to their high refractive indices, low phonon energies and superior infrared transmission relative to oxides. They can potentially be used in fiber optics and telecommunications, photonic devices, and non-linear optics. Understanding how non-oxide glasses react to external stress would be beneficial to the design of zero-stress optic chalcogenide glasses for birefringent-sensitive applications.

In this report, we examine the photoelastic response in several sulfide glass families, including the stoichiometric systems $(\mathrm{GeS_2})_{1-x}(\mathrm{P_2S_5})_x$ and $(\mathrm{GeS_2})_{1-x}(\mathrm{Sb_2S_3})_x$, and the non-stoichiometric system $\mathrm{Ge_{2.5}PS}_x$. The structure of these Ge-P-S glasses has been studied extensively [19, 20] and a considerable amount is known about the bonding and atomic coordination. Furthermore, from previous studies on photoelasticity, $\mathrm{GeS_2}$ is expected to have positive contribution to the stress-optic coefficient, and $\mathrm{Sb_2S_3}$ negative contribution [17]. We thus expect at least one series to contain zero and negative stress-optic glasses. With this structural data and photoelastic data, we will investigate the empirical relationship between bond length (metallicity), coordination and stress-optic coefficient and determine whether the model that has been successful in oxide glasses [9] can be extended to include non-oxide glass systems.

2. Experimental Methods

2.1. Glass preparation

Glasses were synthesized at Corning Incorporated; their preparation has been described in detail previously [19, 20]. Samples were prepared by melting mixtures of high purity elements sealed in evacuated (10^{-5} Torr) silica ampules. They were heated to 925 °C in a rocking furnace for 48 hrs, then at to 850 °C for 10 min. Cylindrical glass rods were formed by quenching the hot ampules in water. Samples were annealed just below T_g, and the rods were cut to obtain rectangular samples with parallel sides to within 0.03 mm. Two opposite sides were polished with diamond paste to between 1–15 μm.

2.2. Measurement of the stress-optic coefficient

Under uniaxial stress, glass typically exhibits an index of refraction n_e in the stress direction (the extraordinary direction) that differs from the index of refraction in the perpendicular direction (n_o, the ordinary direction). The difference results in birefringence in the glass, $b = \Delta/l = n_e - n_o$, where Δ is the phase difference between ordinary and extraordinary rays and l is the thickness of the glass. For stress loads within the elastic region, the birefringence of a glass is proportional to the applied stress σ:

$$\Delta = Cl\sigma. \tag{1}$$

The constant of proportionality, called the stress-optic coefficient C, is used to characterize the glass. Its unit is Brewsters, where 1 B equals 10^{-12} Pa^{-1}.

The stress-optic coefficient was measured at 1550 nm using the Sénarmont compensator method. The optical components consisted of a collimated laser diode module (Thorlabs LDM1550), a fixed Glan-Taylor linear polarizer, the stressed glass sample, a liquid-crystal variable retarder (LCVR) tuned to act as a quarter-wave plate at 1550 nm (Thorlabs LCR-1-IR1), a rotatable analyzer identical to the initial polarizer, and a Ge Photodiode power sensor (Thorlabs S122C).

Fluorescing disks were used to align the laser beam and optical components. Stress was applied to the glass samples using a custom load stage. Glass samples were placed between parallel cage-mounted plates, with a compliant plastic or hard cotton layer placed on either side to promote even stress and prevent cracking. A motorized screw applied load to the plates, which was measured using a load cell and meter (Omegadyne).

The glass sample was oriented such that its stress axis was at 45° to the initial polarizer axis. The LCVR fast axis was aligned with the polarizer axis, and the rotatable polarizer was initially set to 90°. The polarizer was rotated by an angle of $\Delta/2$ to obtain extinction of the light. The birefringence is $b = \Delta\lambda/l$, where λ is the wavelength of incident light and l is the path length of the glass. Plotting Δ as a function of σ then allows the stress optic coefficient C to be determined from Eq. 1.

2.3. Density, shear modulus and refractive index

Densities of the glasses were measured by Archimedes method with a Mettler Toledo density determination kit. Due to the hygroscopic nature of some of the P-containing glasses, 99+% ethanol was used as the immersion fluid.

Elastic properties were determined with a Panametrics-NDT 25DL ultrasonic thickness gauge. This device uses sound pulses and their echoes for samples with known thicknesses to measure longitudinal and shear sound velocities. The shear modulus G is then derived from $G = \rho v_t^2$, where ρ is the density and v_t the transverse sound velocity.

Refractive indices were measured at 1550 nm using a collimated laser diode module (Thorlabs LDM1550), a Glan-Taylor linear polarizer, a manual rotation mount oriented horizontally and a Ge photodiode power sensor (Thorlabs S122C). The Brewster's angles, θ_B, were determined by reflecting horizontally-polarized light from the glass and rotating to angles of minimum reflectance. Intensities around this minimum were collected in 1° intervals and fit to find θ_B. The uncertainty in this value is estimated to be 1°. The refractive index was then determined from the relationship $\theta_B = \arctan(n_{glass}/n_{air})$.

3. Results

Results for density, transverse sound velocity, and index of refraction are compiled in Table 1.

In order to check the accuracy and precision of the optical apparatus, the stress-optic coefficient of a fused silica sample was measured and found to be 3.3±0.1 B at 1550 nm. This value agrees with reported literature values, either directly or when extrapolated [3, 5, 18, 21–23].

The measured stress-optic coefficients C of three glass families, namely

Table 1: Density ρ in g cm^{-3}, transverse sound velocity v_t in mm μsec^{-1}, and index of refraction n for sulfide glasses studied here.

Family	x	ρ	v_t	n
$(GeS_2)_{1-x}(P_2S_5)_x$	0.10	2.619(5)	1.559(8)	1.92(11)
	0.17	2.548(5)	1.514(1)	2.05(13)
	0.30	2.377(5)	1.396(3)	2.03(12)
	0.40	2.283(5)	1.325(1)	1.96(12)
$Ge_{2.5}PS_x$	5.0	2.702(5)	1.549(9)	2.02(13)
	5.5	2.593(5)	1.48(1)	1.99(12)
	5.8	2.601(5)	1.442(3)	1.96(12)
	6.0	2.595(5)	1.477(1)	1.99(13)
	6.5	2.591(5)	1.530(4)	1.96(12)
	7.0	2.536(5)	1.499(2)	2.02(12)
	7.5	2.548(5)	1.514(1)	2.05(13)
	8.0	2.486(5)	1.467(5)	1.90(11)
	10.5	2.413(5)	1.389(3)	1.91(11)
	14	2.331(5)	1.337(3)	1.94(12)
$(GeS_2)_{1-x}(Sb_2S_3)_x$	0.17	3.099(5)	1.506(1)	2.06(9)
	0.33	3.385(5)	1.477(3)	2.2(1)
	0.50	3.633(5)	1.481(1)	2.4(1)
	0.67	3.855(5)	1.488(4)	2.6(1)

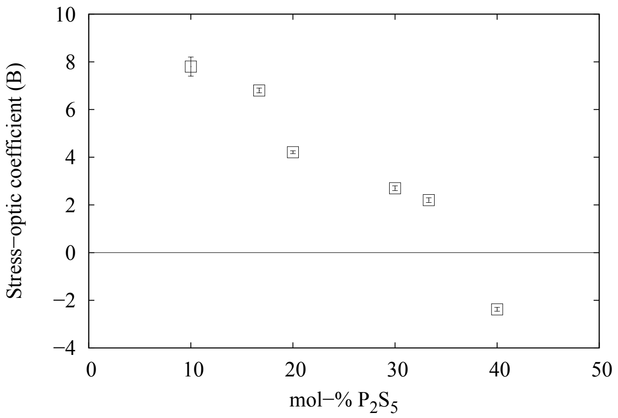

Figure 1: Stress optic coefficient C in Brewsters as a function of P_2S_5 content for stoichiometric $(GeS_2)_{1-x}(P_2S_5)_x$ glasses. Uncertainties are determined from repeated measurements.

$(GeS_2)_{1-x}(P_2S_5)_x$, $Ge_{2.5}PS_x$, and $(GeS_2)_{1-x}(Sb_2S_3)_x$, are reported in Figs. 1–3 respectively. Both stoichiometric families show roughly linear dependence of C on composition (P_2S_5 or Sb_2S_3 content), but with larger variation in the magnitude of C than is typically observed in oxides. The nonstoichiometric family shows a strongly nonlinear variation of C with composition.

4. Discussion

All the data sets shown indicate that, as expected, the stress-optic coefficient is strongly dependent upon composition, and also that the magnitude of the effect exceeds that observed in oxide glasses. We now outline an explanation for these observations based on the structural model previously developed for oxide glasses.

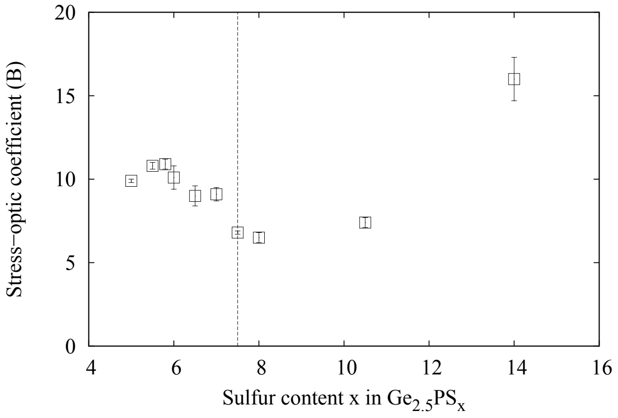

Figure 2: Stress optic coefficient as a function of sulfur content for non-stoichiometric $Ge_{2.5}PS_x$ glasses. Uncertainties are determined from repeated measurements. Vertical dashed line demarcates sulfur-deficient compositions, to the left, and sulfur-excess compositions, to the right.

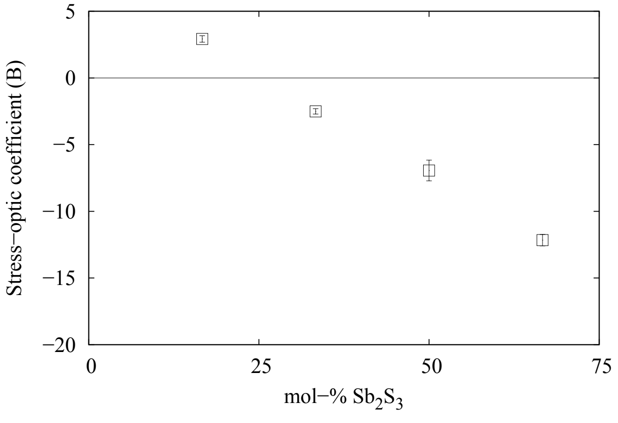

Figure 3: Stress optic coefficient as a function of Sb_2S_3 content for stoichiometric $(GeS_2)_{1-x}(Sb_2S_3)_x$ glasses. Uncertainties are determined from repeated measurements.

4.1. Empirical model of photoelasticity

The empirical model of photoelasticity for oxide glasses predicts the sign of the stress-optic response based on glass composition and crystalline bonding information [9]. The model conjectures that bond metallicity (correlated with anion-cation bond length d) and metal-oxygen coordination number N_c are important in describing the photoelastic response. For zero and negative stress-optic glasses, high metallicity and low coordination numbers allow bonds to be distorted orthogonal to the stress direction. Lower metallicity and higher coordination are needed for a positive response. In the linear optical regime, with wavelengths of 400–700 nm, the response is the average of these two kinds of contributions. Empirically, zero-stress optic glasses, where the two effects just balance each other, can be found using the rule

$$\langle d/N_c \rangle = \sum_i x_i \left(\frac{d}{N_c} \right)_i \approx 0.5 \text{ Å}, \tag{2}$$

where the sum is over all compounds in the glass, and x_i is the mole fraction of the ith compound. For sums less than 0.5 Å, glasses are found empirically to have positive stress-optic coefficients, and are found to have negative coefficients for sums greater than 0.5 Å.

We can begin to apply the empirical model to chalcogenide glasses by considering the stress-optic coefficients of some stoichiometric compositions as measured by Linke and co-workers [17]. Structural data for the components making up these systems (as well as the thiophosphates studied here) are summarized in Table 2. The correlation of the measured stress-optic coefficients [17] with the molar averaged d/N_c for stoichiometric families is presented in Fig. 4. In all cases, the stress-optic coefficient increases as the

Table 2: Bond length d, metal-chalcogen coordination number N_c, and ratio d/N_c for components of glasses examined in the present work.

Compound	d (Å)	N_c	d/N_c (Å)
Sb_2S_3	2.54	3	0.85
As_2Se_3	2.43	3	0.81
As_2S_3	2.25	3	0.75
GeS_2	2.2	4	0.55
P_2S_5	2.1	4 (3)	0.53 (0.70)
S_8	1.71	2	0.86

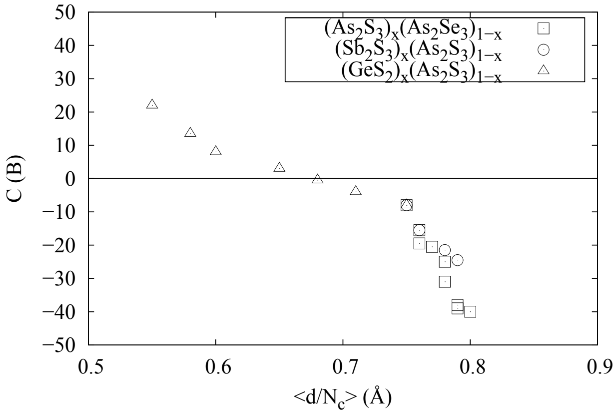

Figure 4: Correlation of stress-optic coefficient C, in Brewsters, with molar averaged d/N_c, in Ångstroms, for stoichiometric non-oxide glasses. Data for C and compositions from ref. [17], Table 1, and values for d/N_c for the components from our Table 2.

d/N_c ratio decreases, matching the trend for oxide glasses. This finding suggests that the empirical model developed for oxides may be extensible to the non-oxide case. In addition, the $(\mathrm{GeS_2})_x(\mathrm{As_2S_3})_{1-x}$ glass series contains glasses with both positive and negative stress-optic coefficients. The zero-stress optic composition is thus estimated to occur when when $\langle d/N_c\rangle$ is between 0.65 and 0.68 Å, somewhat larger than the empirically determined 0.50 Å found for oxide glasses. This increase will be discussed more in the following section.

4.2. Stoichiometric $(GeS_2)_{1-x}(P_2S_5)_x$ and $(GeS_2)_{1-x}(Sb_2S_3)_x$ glasses

The structure of thiogermanophosphate glasses has been investigated by Cherry *et al.* [19]. The $(\mathrm{GeS_2})_{1-x}(\mathrm{P_2S_5})_x$ series contains two types of phosphorus structures: 3-coordinated $\mathrm{PS_{3/2}}$, and 4-coordinated $\mathrm{S{=}PS_{3/2}}$. The germanium atoms are found exclusively in 4-coordinated $\mathrm{GeS_{4/2}}$ polyhedra. There is no P-P or Ge-Ge bonding, but some excess sulfur (from the formation of $\mathrm{PS_{3/2}}$) is found in -S-S- chains. The relative quantities of these components are re-plotted in Figure 5 for convenience. Broadly, as $\mathrm{P_2S_5}$ content increases, $\mathrm{PS_{3/2}}$ and $\mathrm{S{=}PS_{3/2}}$ units increase, with a ratio of about 1:3, while the $\mathrm{GeS_{4/2}}$ content decreases.

The stress-optic coefficient decreases monotonically as the $\mathrm{P_2S_5}$ content increases. From the data in Table 2 and the structural data in Fig. 5 and ref. [19], we can estimate $\langle d/N_c\rangle$ in these glasses and correlate it to the stress-optic coefficient. The results are plotted in Fig. 6. The correlation is strong and negative, similar to the results in Fig. 4. We note that the zero stress-optic composition occurs at $\langle d/N_c\rangle \approx 0.557$ Å, larger than observed in oxides. Also, we found that if the detailed structural components of Fig. 5 are not

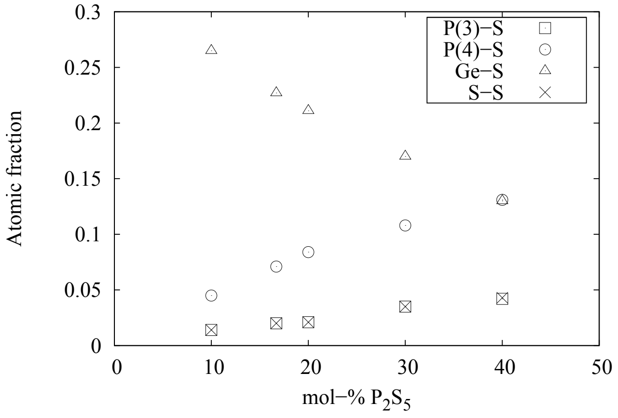

Figure 5: Estimated atomic fraction of Ge, P and S participating in various possible bonds in $(GeS_2)_{1-x}(P_2S_5)_x$ glasses as a function of P_2S_5 content, after ref. [19].

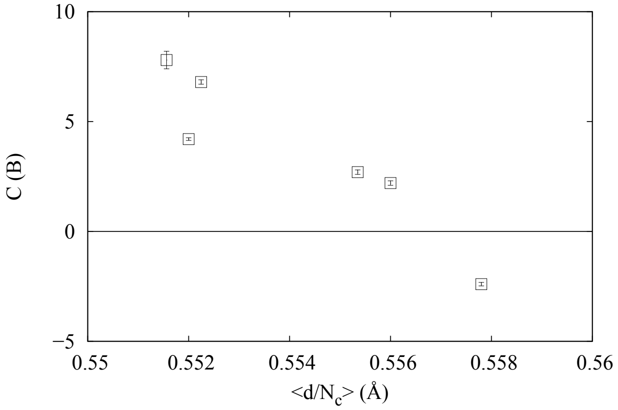

Figure 6: Correlation of stress-optic coefficient C in Brewsters with molar averaged d/N_c for $(GeS_2)_{1-x}(P_2S_5)_x$ glasses, using structural data from ref. [19].

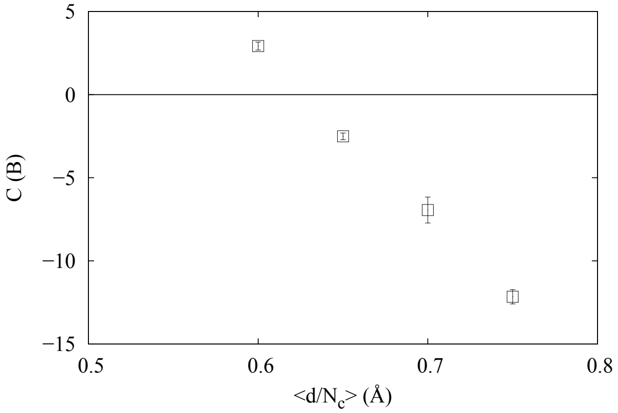

Figure 7: Correlation of stress-optic coefficient C in Brewsters with molar averaged d/N_c for $(GeS_2)_{1-x}(Sb_2S_3)_x$ glasses, using crystalline data from Table 2.

used, but only the crystalline data from Table 2 to estimate $\langle d/N_c \rangle$, then the correlation with C is poor and has the wrong sign. In oxides the d/N_c model also requires detailed structural input (beyond just the crystalline component data) in cases where the glass former undergoes significant changes in coordination, as in borates [10].

The structures of stoichiometric $(GeS_2)_{1-x}(Sb_2S_3)_x$ glasses have been studied by IR and Raman spectroscopies, and are described in terms primarily of $GeS_{4/2}$ and $SbS_{3/2}$ units. The Ge-Sb-S glass family may also contain small amounts of Ge-Ge or Sb-Sb bonds in the Ge-rich or Sb-rich compositions respectively; no evidence for -S-S- groups is seen in the stoichiometric compositions [24]. We observe that the stress-optic coefficient in these glasses decreases with Sb_2S_3 content; using a simple structural model based only on $GeS_{4/2}$ and $SbS_{3/2}$, and the data in Table 2, we can correlate $\langle d/N_c \rangle$ with C. The results are plotted in Fig. 7. The correlation is again excellent, with the zero stress-optic composition occurring at $\langle d/N_c \rangle \approx 0.625$ Å.

While the quantity d/N_c correlates with the stress-optic coefficient in the stoichiometric glasses studied above, we note in every case that zero stress-optic response is obtained for d/N_c significantly greater than the value of 0.5 Å seen in oxides. An explanation can be proposed based a reconsideration of the assumptions made in the original d/N_c model. In particular, the bond metallicity was considered to be an important factor in determining the stress-optic response [9], and metallicity was represented through its correlation with bond length d [25]. In order to compare different families, though, Wemple [25] showed that metallicity correlates with dZ_a, where Z_a is the anion valence. In oxides, where the electronegativity difference between the anion (oxide) and cation is inevitably great, Z_a could be taken as -2 in nearly all cases. In sulfides, on the other hand, with smaller electronegativity differences, Z_a is again nominally -2 but would reasonably expected to be effectively reduced. For example, in the presence of -S-S- bonding as observed in the $(\mathrm{GeS}_2)_{1-x}(\mathrm{P}_2\mathrm{S}_5)_x$ samples (Fig. 5), one could obtain a Z_a as small as 0. Generally we would expect a weighted average reduced from -2.

If the empirical model is extended to include a factor Z_a, we would predict that in oxides, zero stress-optic response is obtained at

$$\frac{dZ_O}{N_c} \approx 0.5 Z_O \text{ Å}, \tag{3}$$

while in sulfides, using an average of our above results,

$$\frac{dZ_S}{N_c} \approx 0.6 Z_S \text{ Å}. \tag{4}$$

If the general correlation with dZ_a/N_c is correct, the left-hand sides of these two relation should be equal and thus we obtain

$$\frac{Z_O}{Z_S} \approx \frac{0.6}{0.5} = 1.2. \tag{5}$$

We thus get the reasonable result that the oxide valency is larger than the (effective) sulfide valency. One could also expect the effective selenide valency to be lower than that of both the oxides and the sulfides, due to further decrease in the electronegativity difference between anion and cation. Based on the arguments above, this would lead an even larger $\langle d/N_c \rangle$ threshold for zero-stress optic selenide glass. Indeed, we see that for Se-based glass families (Fig. 4), the zero-stress optic ratio occurs when $\langle d/N_c \rangle$ is between 0.65 and 0.68 Å.

While not a proof of correctness of course, this argument does suggest a reason why zero stress-optic response in sulfides occurs at higher d/N_c, in a way consistent with other chemical principles.

4.3. Non-stoichiometric $Ge_{2.5}PS_x$ glasses

The $Ge_{2.5}PS_x$ glass with $x = 7.5$ is also part of the $(GeS_2)_{1-x}(P_2S_5)_x$ series (with $x = 0.167$); from this composition, the amount of sulfur is varied to be either in excess or in deficit of the stoichiometric level. The structures of these non-stoichiometric glasses, discussed in detail by Cherry *et al.*, are more complex than those of the stoichiometric Ge-P-S series, due to these sulfur excesses and deficiencies [20]. Again for convenience the atomic fractions of the various species determined in the previous study are reproduced here, in Figure 8. For the case of excess sulfur, the amount of phosphorus in molecular rings and cages decreases, and the number of 4-coordinated $S{=}PS_{3/2}$ sites increases. The amount of -S-S- bonding increases also. In the extreme excess case with $x = 14$, the formation of S_8 rings was detected. As the amount of sulfur is decreased below the stoichiometric composition, there is a large increase in the amount of 3-coordinated $PS_{3/2}$ as the non-bridging $S{=}PS_{3/2}$

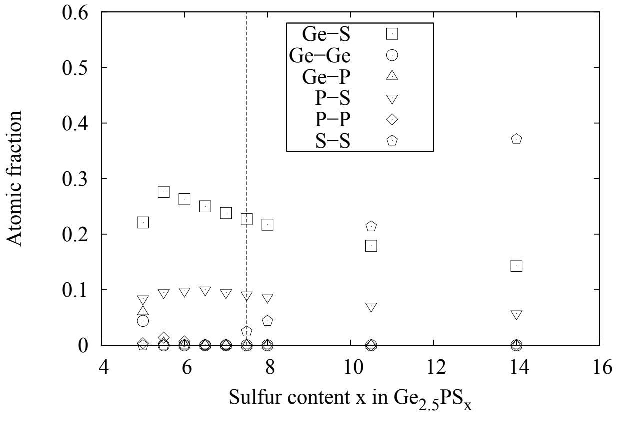

Figure 8: Estimated atomic fraction of Ge, P and S participating in various possible bonds in $Ge_{2.5}PS_x$ glasses as a function of sulfur content, after ref. [20]. Vertical dashed line demarcates sulfur-deficient compositions, to the left, and sulfur-excess compositions, to the right.

is lost. Below $x = 6$, a new phosphorus cluster (P_4S_3) is introduced, and Ge-Ge, Ge-P and P-P bonding begins to occur. In these sulfur deficient samples, even though the total coordination number of Ge remains 4, the coordination of Ge by S is less than 4 due to the progressive formation of Ge-P and Ge-Ge bonds.

The value of the stress-optic coefficient at 1550 nm varies significantly with excess and deficit sulfur. Below the stoichiometric level, C increases with decreasing S content until $x = 5.5$. The relative amount of $GeS_{4/2}$ also increases in this range (represented in the model by a decreasing d/N_c ratio), while phosphorus units transition from mostly 4-coordinated to mostly 3-coordinated (represented in the model by an increasing d/N_c ratio). These structural changes in the glass system could account for the drop in the rate of increase of C in this range. Below $x = 5.5$, the coefficient begins to decrease. This decrease is mirrored in the structural data by a decrease in $GeS_{4/2}$ units and an increase in metallic Ge-Ge and Ge-P bonding, with P-S units predominantly 3-coordinated. The lower value of C is consistent with the predictions of the empirical model, as a decrease in higher coordinated $GeS_{4/2}$ and an increase in lower coordinated $PS_{3/2}$ would result in larger d/N_c value. Also, the Ge-Ge and Ge-P bonds are more metallic than Ge-S and P-S bonds, corresponding in the model to a larger d/N_c ratio. Their introduction into the glassy network could lead to a decrease in the stress-optic coefficient.

In excess of the stoichiometric level, C increases dramatically with increasing S content. Based on the empirical model, the conversion of 3-coordinated $PS_{3/2}$ to 4-coordinated $S{=}PS_{3/2}$ would increase the stress-optic coefficient. From the structural information, we also see that the amount of -S-S- bonds increase as S increases above the stoichiometric composition, and in particular at the highest sulfur excess, S_8 rings form. It may be that the increase in C is driven by the increase in -S-S- bonding in two ways. First, as argued above, the quantity dZ_S, which reflects bond metallicity, would be expected to decrease as more homopolar -S-S- bonds form, because of the decrease in effective anion valence Z_S. Smaller metallicity favors positive stress-optic response, so the effect would be to increase C. Secondly, in the extreme case of S_8 ring formation, a large increase in C may occur because these units would essentially decouple from the rest of the network, and the effect of other bonds such as Ge-S, which are positive stress-optic contributors, would be appear to be greatly enhanced, although their total content has not changed much.

Due to the complexity of structures in non-stoichiometric glasses, it is unlikely that the empirical model of photoelasticity can be applied in this case to predict zero stress-optic compositions. However, it can be used in conjunction with the structural information to describe the photoelastic response in chalcogenide glasses.

4.4. Magnitude of Stress Optic Response

In addition to the variation in d/N_c for zero stress optic sulfide glass as compared to oxides, it is also notable that the general magnitude of the stress-optic response is much larger. In oxides, C is typically in the range from -4 to +8 B, while in chalcogenides (Fig. 4), C ranges from -40 to 20 B. To study this difference we used the experimental data in Table 1 to determine the shear modulus G and shear photoelastic tensor element p_{44}. The shear modulus G was determined through

$$G = \rho v_t^2, \tag{6}$$

and the photoelastic tensor element through

$$p_{44} = -\frac{2GC}{n^3}. \tag{7}$$

These derived quantities are presented in Table 3.

Matusita and co-workers have compiled similar data on G and p_{44} for borate, phosphate and silicate glasses [4–6]. In our data we find that p_{44} spans a range from -0.016 to +0.013, while in lead borates, p_{44} ranges from -0.0230 to +0.00965, thus about the same magnitudes for positive and negative values. The index of refraction of lead oxide glasses are similar to those observed here in sulfides. On the other hand, the typical shear moduli of the sulfide

Table 3: Shear modulus in GPa and shear photoelastic tensor element p_{44} for the sulfide glasses studied here. Quantities are derived from Eqs. 6 and 7 using Table 1 data, and errors derived by propagation.

Family	x	G	p_{44}
$(GeS_2)_{1-x}(P_2S_5)_x$	0.10	6.37(6)	-0.014(3)
	0.17	5.84(1)	-0.0093(17)
	0.30	4.63(2)	-0.0030(5)
	0.40	4.01(1)	0.0026(5)
$Ge_{2.5}PS_x$	5.0	6.48(8)	-0.016(3)
	5.5	5.68(7)	-0.016(3)
	5.8	5.41(2)	-0.016(3)
	6.0	5.66(1)	-0.015(3)
	6.5	6.06(4)	-0.015(3)
	7.0	5.70(2)	-0.0127(23)
	7.5	5.84(1)	-0.0093(17)
	8.0	5.35(3)	-0.0102(18)
	10.0	4.65(2)	-0.0100(18)
	14.0	4.16(2)	-0.018(4)
$(GeS_2)_{1-x}(Sb_2S_3)_x$	0.17	7.03(2)	-0.0043(3)
	0.33	7.38(3)	0.0030(3)
	0.50	7.96(3)	0.0076(9)
	0.67	8.53(5)	0.0130(10)

glasses are much smaller than those in lead borates, by a factor of 3–5. As the stress-optic coefficient C is related to all these quantities through

$$C = -\frac{n^3}{2G} p_{44}, \tag{8}$$

we can conclude that the large variation in C relative to oxides is due to the relatively small shear moduli, not p_{44}. In other words, the difference in stress-optic response is primarily mechanical, not photoelastic.

5. Conclusion

The photoelastic trends for stoichiometric sulfide glasses correlate well with predictions based on anion-cation bond information, or d/N_c ratio. An empirical model for sulfide glasses, similar to that for oxide glasses, is suggested that can be used to predict new zero-stress optic chalcogenide glasses. However, while in oxides zero stress-optic behavior has been shown to occur at the threshold $\langle d/N_c \rangle \approx 0.5$ Å, the data shown here indicate that in sulfides the threshold is higher, about 0.6–0.65 Å. We explain this difference by expanding the treatment of metallicity in the empirical model through the replacement $d \to dZ_a$ [25], and noting that in sulfide glasses, the magnitude of Z_a is expected to be somewhat reduced as compared to oxides, due to reduced electronegativity differences. Furthermore, we show that the much expanded range of stress-optic coefficients observed in sulfide glasses compared to oxides, is a result of their decreased shear moduli and not the photoelastic response.

Acknowledgments

We thank S. C. Currie of Corning Incorporated for assistance in preparation of the glass samples.

References

[1] F. Pockels, Über die änderung des optischen Verhaltens verschiedner Gläser durch elastische Deformation, Ann. d. Phys. 7 (1902) 745–769.

[2] H. Mueller, The theory of photoelasticity, J. Am. Ceram. Soc. 21 (1938) 27–33.

[3] E. S. Jog, R. S. Krishnan, Dispersion of the photoelastic constants of fused silica, Nature 179 (1957) 540–541.

[4] K. Matusita, R. Yokota, T. Kimijima, T. Komatsu, C. Ihara, Compositional trends in photoelastic constants of borate glasses, J. Am. Ceram. Soc. 67 (4) (1984) 261–265.

[5] K. Matusita, C. Ihara, T. Komatsu, R. Yokota, Photoelastic effects in silicate glasses, J. Am. Ceram. Soc. 67 (10) (1984) 700–704.

[6] K. Matusita, C. Ihara, T. Komatsu, R. Yokota, Photoelastic effects in phosphate glasses, J. Am. Ceram. Soc. 68 (7) (1985) 389–391.

[7] D. Donadio, M. Bernasconi, F. Tassone, Photoelastcity of crystalline and amorphous silica from first principles, Phys. Rev. B 68 (2003) 134202.

[8] D. Donadio, M. Bernasconi, F. Tassone, Photoelasticity of sodium glass from first principles, Phys. Rev. B 70 (2004) 214205.

[9] M. Guignard, L. Albrecht, J. W. Zwanziger, Zero-stress optic glass without lead, Chem. Mater. 19 (2007) 286–290.

[10] V. Martin, B. Wood, U. Werner-Zwanziger, J. Zwanziger, Structural aspects of the photoelastic response in lead borate glasses, J. Non-Cryst. Solids 357 (2011) 2120–2125.

[11] M. Smedskjaer, S. Saxton, A. Ellison, J. Mauro, Photoelastic response of alkaline earth aluminosilicate glasses, Opt. Lett. 37 (3) (2012) 293–295.

[12] V. Martin, U. Werner-Zwanziger, J. Zwanziger, R. Dunlap, Correlation of structure and photoelastic response in tin phosphate glass, Int. J. Appl. Glass Sci. 2 (2011) 282–289.

[13] M. M. Smedskjaer, M. Potuzak, X. Guo, J. C. Mauro, Compositional control of the photoelastic response of silicate glasses, Opt. Mater. 35 (2013) 2435–2439.

[14] R. Galkiewicz, J. Tauc, Photoelastic properties of amorphous As_2S_3, Solid State Commun. 10 (12) (1972) 1261–1264.

[15] B. A. Weinstein, R. Zallen, M. L. Slade, A. deLozanne, Photoelastic trends for amorphous and crystalline solids of differing network dimensionality, Phys. Rev. B 24 (1981) 4652–4665.

[16] B. Weinstein, R. Zallen, M. Slade, J. M. Jr., Pressure-Optical Studies of GeS_2 Glasses and Crystals: Implications for Network Topology, Phys. Rev. B 25 (1982) 781–792.

[17] D. Linke, Correlations between properties of chalcogenide glasses .10. photoelastic trends for infrared-transmitting chalcogenide glasses of differing network dimensionality, Z. Anorg. Allg. Chem. 541 (1986) 142–162.

[18] P. C. Anderson, A. K. Varshneya, Stress-optic coefficient of Ge-As-Se chalcogenide glasses, J. Non-Cryst. Solids 168 (1994) 125–131.

[19] B. Cherry, J. W. Zwanziger, B. G. Aitken, The structure of GeS_2-P_2S_5 glasses, J. Phys. Chem. B 106 (2002) 11093–11101.

[20] B. Cherry, J. W. Zwanziger, B. G. Aitken, Structure and properties of $Ge_{2.5}PS_x$ glasses, J. Non-Cryst. Solids 333 (2004) 28–36.

[21] N. K. Sinha, Normalised dispersion of birefringence of quartz and stress optical coefficient of fused silica and plate glass, Phys. Chem. Glasses 19 (4) (1978) 69–77.

[22] L. Filon, F. Harris, The photo-elastic dispersion of vitreous silica, Proc. R. Soc. London, Ser. A 130 (813) (1931) 410–431.

[23] W. Primak, D. Post, Photoelastic constants of vitreous silica and its elastic coefficient of refractive index, J. Appl. Phys. 30 (5) (1959) 779–788.

[24] L. Petit, N. Carlie, F. Adamietz, M. Couzi, V. Rodriguez, K. Richardson, Correlation between physical, optical and structural properties of sulfide glasses in the system Ge–Sb–S, Mater. Chem. Phys. 97 (1) (2006) 64–70.

[25] S. H. Wemple, Optical oscillator strengths and excitation energies in solids, liquids, and molecules, J. Chem. Phys. 67 (1977) 2151–2168.

4.3 Discussion

4.3.1 Improving the Empirical Model with Glass Structure

According to the empirical model of photoelasticity, compounds with larger d/N_c values will have negative contribution to the stress-optic coefficient, while materials with small d/N_c will contribute positively to C. Table 4.1 shows individual d/N_c values for various crystalline sulfur, selenium and tellurium compounds. It has been shown for oxide glasses that the predictions based on $\langle d/N_c \rangle$ can be improved by considering the glassy structure of compounds. For example, in crystalline B_2O_3, boron is bonded to 3 oxygen, but in a glass it can be found in 3- or 4-coordinated units. Incorporating both coordinations into the empirical model closes the gap between predictive and experimental zero-stress optic compositions in lead borates [42]. The empirical model is also improved in non-oxides by using the glass structure rather than crystalline information. Consider the stoichiometric sulfide series $(GeS_2)_{1-x}(P_2S_5)_x$. From their crystalline structural units, P_2S_5 has bond length $d = 2.1$ Å and coordination $N_c = 4$ (or $d/N_c = 0.53$ Å) and GeS_2 has bond length $d = 2.2$ Å and coordination $N_c = 4$ (or $d/N_c = 0.55$ Å). According to the empirical model, increasing P_2S_5 (decreasing $\langle d/N_c \rangle$ of the glass) should increase the stress-optic coefficient; experimentally, however, increasing P_2S_5 decreases C. This can be explained from the structural information of the $(GeS_2)_{1-x}(P_2S_5)_x$ glasses. In these glass, many of the phosphorus units are surrounded by 4 sulfur atoms, but a significant amount (20 to 25 %) are 3-coordinated by S [71]. When these different bonding environments are taken into account, the effective empirical parameter is $d/N_c \approx 0.57$ Å for P_2S_5. Now, using this improved ratio, the model predicts that increasing P_2S_5 will decrease C, which is consistent with the experimental results.

4.3.2 Metallicity, Bond Length and Anion Valence

Glasses with zero-stress optic coefficients are found when $\langle d/N_c \rangle \approx 0.5$ Å for oxides, and when $\langle d/N_c \rangle \approx 0.6$ Å for sulfides. The discrepancy in these predictive parameters can be explained by the correlation of metallicity with bond length, as discussed in Section 4.2 of the included manuscript on Ge-P-S and Ge-Sb-S glasses (Chapter 4). According to Wemple [17], metallicity is correlated not just with bond length d but

Table 4.1: Anion-cation bond length d (Å), cation coordination number N_c and empirical parameter d/N_c (Å) for crystalline non-oxide compounds

S	d	N_c	d/N_c	Se	d	N_c	d/N_c	Te	d	N_c	d/N_c
Tl_2S	2.68	3	0.89	K_2Se	3.33	4	0.83	Cs_2Te	3.705	4	0.93
Sb_2S_3	2.54	3	0.85	As_2Se_3	2.43	3	0.81	K_2Te	3.537	4	0.88
K_2S	3.176	4	0.79	P_2Se_5	2.25	3	0.75	Na_2Te	3.174	4	0.79
As_2S_3	2.25	3	0.75	Na_2Se	2.943	4	0.74	Li_2Te	2.822	4	0.71
Cs_2S	3.712	5	0.74	Li_2Se	2.605	4	0.65	CdTe	2.805	4	0.70
SnS	2.91	4	0.73	ZnSe	2.471	4	0.62	ZnTe	2.632	4	0.66
Na_2S	2.831	4	0.71	SnSe	3.049	5	0.61	Ga_2Te_3	2.553	4	0.64
Ag_2S	2.699	4	0.67	Sb_2Se_3	2.984	5	0.60	BaTe	3.42	6	0.57
CdS	2.516	4	0.63	Ga_2Se_3	2.367	4	0.59	PbTe	3.231	6	0.54
Li_2S	2.476	4	0.62	$GeSe_2$	2.359	4	0.59	Sb_2Te_3	3.168	6	0.53
B_2S_3	1.82	3	0.61	$SiSe_2$	2.225	4	0.56	SnTe	3.159	6	0.53
ZnS	2.342	4	0.59	BaSe	3.3	6	0.55	Bi_2Te_3	3.066	6	0.51
Ga_2S_3	2.272	4	0.57	PbSe	3.061	6	0.51	$SiTe_2$	3.044	6	0.51
GeS_2	2.2	4	0.55	Bi_2Se_3	2.862	6	0.48	As_2Te_3	2.927	6	0.49
SiS_2	2.131	4	0.53	CdSe	2.77	6	0.46				
BaS	3.187	6	0.53								
Bi_2S_3	3.05	6	0.51								
P_2S_5	2.1	4	0.53								
PbS	2.967	6	0.49								

with dZ_a, where Z_a is the anion valence. Oxides will have oxygen valence of -2 for all compounds due to the large electronegativity differences between O and the cation. In sulfides, however, Z_a is expected to be reduced from -2. This is because the electronegativity differences between anion and cation are smaller for sulfur than for oxygen. These reduced electronegativity differences can lead to anion-anion bonding in the glass network; for sulfur chains, Z_a could be as small as 0. Thus, if dZ_a/N_c is in fact the predictive parameter for zero-stress optic coefficients and is equal for all glass systems, one would expect $\langle d/N_c \rangle_O < \langle d/N_c \rangle_S$ (since $Z_O > Z_S$).

This argument can be extended to include selenium- and tellurium-based glasses. The electronegativity differences between anion and cation for the different chalcogens increase with atomic number (O > S > Se > Te). Then for glasses with zero-stress optic coefficient, we would expect the empirical parameter $\langle d/N_c \rangle$ to increase in a similar manner. Depending on the amount of non-stoichiometric anion-anion bonding in a glass, we might expect for the non-oxides that 0.55 Å $\leq \langle d/N_c \rangle \leq 0.65$ Å. The exact value will vary based on the structural similarities between the crystalline and glassy compounds, as well as the amount of anion-anion bonding in the network. Still, this range of $\langle d/N_c \rangle$ can be used as a starting point for predicting new non-oxide glasses with near-zero stress-optic coefficients.

It could also be possible to use the value of $\langle d/N_c \rangle$ for zero-stress optic non-oxide glasses to estimate the anion valence and thus the amount of anion-anion bonding in a glass series. For oxide glasses, the empirical parameter predicting zero-stress optic compositions is

$$\left(\frac{dZ_a}{N_c} \right)_O \approx -1.0 \text{ Å} \tag{4.2}$$

with some experimental variations expected due to the approximate nature of $\langle d/N_c \rangle \approx 0.5$ Å for oxide glasses. Since the value dZ_a/N_c should be equal for all anion types, a non-oxide glass series with zero-stress optic composition at $\langle d/N_c \rangle_{NO}$ will have an estimated anion valence of

$$(Z_a)_{NO} \approx \frac{-1 \text{ Å}}{\langle d/N_c \rangle_{NO}}. \tag{4.3}$$

Consider the glass series $(\mathrm{GeS_2})_{1-x}(\mathrm{P_2S_5})_x$. The glass composition with $C \approx 0$ B has the empirical value $\langle d/N_c \rangle_S \approx 0.557$ Å. The anion valence is then $Z_S \approx -1.8$, which corresponds to about 10 % of the sulfur participating in S-S bonds. This estimation is only slightly larger than the experimentally determined 5 % of sulfur participating in S-S bonding in the glass network [71]. On the other hand, IR and Raman structural studies of $(\mathrm{GeS_2})_{1-x}(\mathrm{Sb_2S_3})_x$ showed no evidence of S-S bonding [73], but the anion valence is $Z_a \approx -1.6$ as determined from the value $\langle d/N_c \rangle_S = 0.625$ Å for the zero-stress optic composition. This would, in contrast, suggest that up to 20 % of the sulfur is participating in S-S bonding.

4.3.3 Non-Stoichiometric Glass Compositions

Predicting the stress-optic response of glasses with excess or deficit chalcogen is more challenging than for glasses with stoichiometric amounts of chalcogen. For stoichiometric glasses, the sign of the stress-optic coefficient can be predicted using the empirical model and Table 4.1. If $\langle d/N_c \rangle_{NO} > 0.65$ Å, C is expected to be negative, while if $\langle d/N_c \rangle_{NO} < 0.55$ Å is expected to have positive coefficient. As discussed in the manuscript, increasing the amount of chalcogen in a glass sample to excess amounts could i) increase the coordination of cation units, which would increase C according to the empirical model, ii) increase the amount of anion-anion bonding in the system, which would decrease the valence and thus the metallicity, leading to an increase in C, or, if the amount of excess chalcogen is large enough such that chains or rings decouple from the network, iii) enhance the effect of other cation units in the network. This last effect is likely to increase C if the stoichiometric value is positive. On the other hand, if C is initially negative and the coordination of structural units within the network does not change, then the decoupling of chalcogen chains or rings is more likely to decrease the coefficient.

As the amount of chalcogen is reduced from a stoichiometric composition, the structure and photoelastic behaviour of the glass becomes complex. Deficit amounts of chalcogen could i) decrease the coordination of cation units, which would decrease C according to the empirical model, ii) increase the amount of metallic cation-cation bonding, which would increase the metallicity of the glass and lead to a decrease in C, or, iii) enhance the effect of cation units in the network as their relative amount in the glass increases with small chalcogen deficits. This last effect is likely to increase the magnitude of the stress-optic coefficient for both positively and negatively birefringent glasses.

From the discussion above, two general trends are expected:

1. If the stoichiometric C is initially positive, then increasing the chalcogen content will increase the stress-optic coefficient.
2. If the stoichiometric C is initially negative, then decreasing the chalcogen content will decrease the stress-optic coefficient.

For stoichiometric glasses with positive C, decreasing the amount of chalcogen could either increase or decrease the stress-optic coefficient, depending on the relative contributions of decreased coordination, increased metallicity, and enhanced effect of positive units in the glass. Likewise, increasing the amount of chalcogen in a stoichiometric glass with negative C could increase or decrease the coefficient depending on the increased coordination, decreased valency, and decoupling of chalcogen chains or rings from the network. A prior knowledge of the structure of these non-stoichiometric glass series could help in predicting these types of photoelastic behaviour. Or alternatively, the photoelastic trends of a non-stoichiometric series could yield insight to the structure of the glasses.

4.4 Summary

The stress-optic response of GeS_2-P_2S_5, $Ge_{2.5}PS_x$ and GeS_2-Sb_2S_3 glasses was measured at 1550 nm. In both stoichiometric glass families, the stress-optic coefficient decreased from positive values to negative values as the GeS_2 content decreased. These trends in the compositional dependence of the stress-optic coefficients are consistent with predictions based on the empirical model. As the empirical value $\langle d/N_c \rangle$ increases, C decreases. The predictions of the model are improved by incorporating the structure of the glass into the model. The discrepancy between values of $\langle d/N_c \rangle$ for zero-stress optic oxide and sulfide glasses can be explained by including the anion valence Z_a into the discussion of bond metallicity.

The stress-optic response of non-stoichiometric sulfide glasses is more complex. As the amount of sulfur is varied from excess to deficit, a variety of new bonding environments are introduced. The coordination of cations can be increased or decreased, and new S-S or metallic cation-cation bonds can be formed. A comprehensive structure knowledge of the glass system along with the principles of empirical model is successful in explaining the photoelastic behaviour.

The magnitudes of the stress-optic coefficients of the sulfide glasses are much larger than those for oxide systems which also contain zero-stress optic compositions. However, the elasto-optic coefficients p_{44} of both glass types are similar in size. Values of n also overlap, but the shear moduli G are much smaller in the sulfide glasses. Thus we conclude that the mechanical rather than optical properties cause this difference in C.

The stress-optic response of stoichiometric sulfide glasses will be further discussed in Chapter 7 with respect to other models of photoelasticity.

Chapter 5

Wavelength Dependence of the Stress-Optic Response in Oxide Glasses

The wavelength-dependence of the stress-optic coefficient for binary and ternary borates, phosphates, silicates, and tellurites has been measured. The motivation for this research is to determine the effect of various "positive" and "negative" glass formers and modifiers on the dispersive properties of C, and to examine whether the empirical model can describe the change in stress-optic coefficient with incident wavelength of light. Although no glasses with broadband zero-stress optic compositions were measured, glass families with non-dispersive stress-optic response have been identified.

5.1 Experimental Procedure

5.1.1 Glass Preparation

Glasses were prepared using conventional melt-quenching techniques. For this method, stoichiometric amounts of commercial-grade reagents were weighed, mixed, added to a crucible, and melted in a box furnace. For many glass compositions, the mixture was initially calcined at between 300-900°C below the melting temperature for many hours to remove water, ammonia, carbon dioxide and other unwanted compounds from the reagents. The temperature of the furnace was increased to the melting temperature of the glass, and the melt was held at this temperature for the length of time determined to ensure thorough mixing. The crucible was removed from the furnace and the melt was quickly poured into a metal mold to quench the glass. The mold was often placed on a hot plate and heated above room temperature to prevent the quenched glass from shattering. Bubble- and striation-free glasses were then annealed for 12-24 hr at T below the glass transition temperature to remove residual stresses.

The important details of the glass-making procedure for glasses investigated by ellipsometry are summarized in Table 5.1. Some of the glasses measured in this study were synthesized by other students and postdoctoral researchers in our lab group. Leanne Chapman prepared the lead phosphate, bismuth phosphate and lithium borate glasses. Lisa Zhang prepared the tin phosphate and sodium borate glasses. Marie Guignard prepared the tin silicate glasses. These glass samples were not quenched but cooled very slowly from liquid to room temperature; no annealing was required. Their single-wavelength stress-optic coefficients have been previously reported [1]. Jeremy Thorbahn prepared the zinc tellurite glasses; their single-wavelength stress-optic coefficients have been correlated with local structure [55]. The starting reagents, from Sigma Aldrich unless other wise noted, were ammonium phosphate monobasic ($NH_4H_2PO_4$, ACS reagent, $\geq$ 98 %), boron oxide (B_2O_3, 99 % after heating), silicon dioxide (SiO_2, purum p.a., powder), tellurium dioxide (TeO_2, $\geq$ 99 %), barium carbonate ($BaCO_3$, ACS reagent, $\geq$ 99 % or Alfa Aesar ACS 99-101 % powder), lead(II) oxide (PbO, powder, <10 μm, $\geq$ 99.9 %), zinc oxide (ZnO, puriss p.a., ACS reagent, $\geq$ 99 %), lithium carbonate (Li_2CO_3, puriss p.a., ACS reagent, $\geq$ 99 %), sodium carbonate (Na_2CO_3, ACS reagent, anhydrous, $\geq$ 99.5 %, granular), calcium oxide (CaO, 99.9 %), tin(II) oxide (SnO, Strem Chemicals 98 %) bismuth(III) oxide (Bi_2O_3, powder, 10 μm, 99.9 %).

Once annealed, the glasses were cut and polished for optical measurements. The specific requirements for the glass samples also measured by Brillouin spectroscopy (binary barium and lead borates, phosphates and silicates) will be discussed later in Section 6.1.1. For all other samples, the glasses were cut into rectangular cuboids of varying dimensions using a low-speed saw (Buehler IsoMet, with a Lapcraft diamond saw blade). Two sets of parallel faces were ground with 1200 grit silicon carbide to remove any imperfections that would affect the homogeneity of stress. The glasses were often affixed to a polishing screw so that the sides remained perfectly parallel when ground. One set of parallel sides was then polished to between 1 μm and 30 μm optical transparency using cotton polishing pads soaked with diamond paste of decreasing particle size (MetaDi polishing compounds, Buehler).

Table 5.1: Glass melting details for oxide glass families. The tin phosphates (†) were prepared in a glovebox. Glass families with (a) were prepared by Leanne Chapman, (b) by Lisa Zhang, (c) by Marie Guignard [1] and (d) by Jeremy Thorbahn [55].

Glass family	Melting temperature	Melting time	Temperature of metal mold	Annealing temperature
Barium borates	1500°C	1-2 hr	RT-200°C	650°C
Lead borates	1000-1100°C	8-12 hr	400-500°C	350-500°C
Lead barium borates	1100-1200°C	1 hr	RT-500°C	400-500°C
Lithium borates$^{(a)}$	1150°C	2 hr	200-350°C	450-500°C
Sodium borates$^{(b)}$	1000-1200°C	1 hr	100-200°C	400-500°C
Barium phosphates	1100-1300°C	12-36 hr	RT	450-550°C
Lead phosphates$^{(a)}$	1000°C	1-2 hr	300°C	150-350°C
Zinc phosphates	1150°C	1-2 hr	RT	450-650°C
Lead barium phosphates	1050-1200°C	2 hr	400°C	400°C
Lead zinc phosphates	1200°C	1 hr	RT	450°C
Barium zinc phosphates	1200°C	1-2 hr	RT-500°C	600°C
Calcium phosphates	1100-1400°C	2 hr	300°C	500°C
Tin phosphates$^{\dagger(b)}$	1050°C	0.5-1 hr	RT	
Bismuth phosphates$^{(a)}$	1050 °C			
Lead silicates	1000-1100°C	8-12 hr	RT	450°C
Lead barium silicates	1200-1400°C	2-4 hr	RT	450-550°C
Tin silicates$^{(c)}$	1500	0.5 hr	n/a	n/a
Zinc tellurites$^{(d)}$	800	15-20 min	420	325

5.1.2 Density, Elastic Moduli and Refractive Index Measurements

Densities, ρ, were measured by the Archimedes method (Section 3.1.3) using a Mettler Toledo density determination kit with > 99 % ethanol as the immersion fluid.

Transverse and longitudinal velocities v_T and v_L were measured by the ultrasonic method (Section 3.1.2) using a Panametric ultrasonic thickness gage. The velocities are related to the elastic moduli C_{11} and $C_{44} = G$ by Equation 3.40.

Refractive indices were determined by collecting the wavelength-dependent Ψ and Δ using a Woollam M-2000 ellipsometry and applying a Cauchy fit (Section 3.2.4). Reflection spectra were measured at 3-10 spots on the unstressed glass surface for incident angle $\theta_I = 50°$, well above the Brewster's angle for all glass samples. Data collection times were 20-30 seconds. Each set of Ψ data were fit using a Cauchy model and the resulting refractive indices were averaged over all collection locations to determine $n(\lambda)$; the uncertainty in refractive index was found from the deviation of n at different reflection locations.

5.1.3 Measurement of Stress-Optic Coefficients

The stress-optic measurements were taken with the ellipsometer in transmission mode, with $\theta_I = 0°$. For this orientation, the reflection coefficients (Equation 3.29) are

$$|R^s| = |R^p| = \frac{n-1}{n+1} \tag{5.1}$$

giving an amplitude ratio of

$$\Psi = \tan^{-1}\left(\frac{|R^p|}{|R^s|}\right) = \tan^{-1}(1) = \frac{\pi}{4}. \tag{5.2}$$

For all samples, regardless of applied stress load and wavelength, Ψ is experimentally measured to be 45°.

The wavelength-dependent parameter Δ is used to determine the stress-optic coefficient for glasses with known thickness d and stress according to Equation 3.11. Stress was applied to the glasses as described in Section 4.1.4. For a glass sample, the phase shifts Δ were measured as a function of decreasing stress σ, as shown in Figure 5.1. At least five stresses were applied between maximum and minimum σ, and data collection times were 1-2 seconds for each applied stress. This process was repeated multiple times, and the location of the incident light on glass face was varied.

The stress-optic coefficient was determined at each wavelength from the slope of Δ vs σ for all measurements at all locations on the glass surface; the variation of the slope gives uncertainty in C.

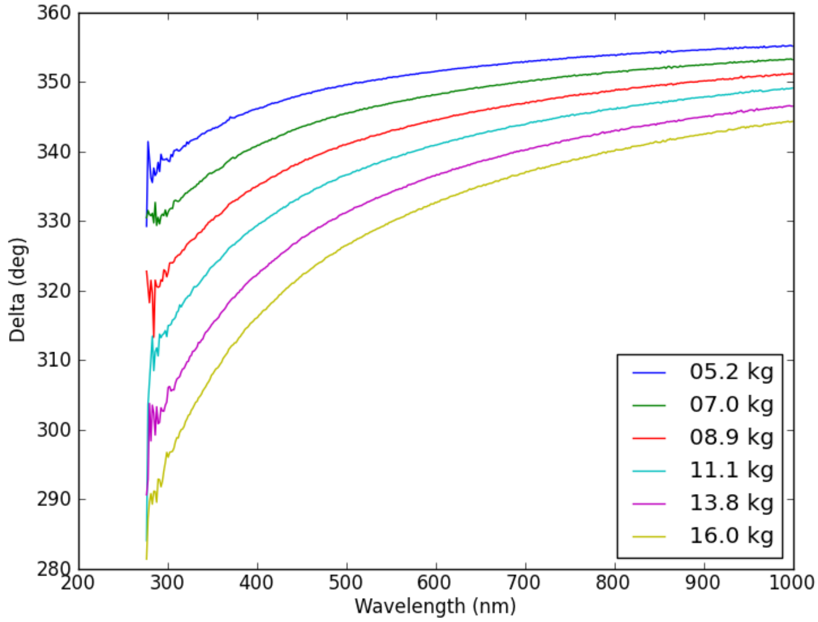

Figure 5.1: Measured Ψ and Δ for the glass sample 20BaO-80B_2O_3 with 16kg stress applied. The slope of Δ vs σ at each wavelength gives the stress-optic coefficient C.

5.2 Results

The stress-optic coefficient was measured as a function of wavelength for 21 glass families. Some glasses show an increase in C with decreasing wavelength; we will call this "positive dispersion". Likewise, "negative dispersion" will be used to describe decreasing C with decreasing wavelength. Since $C = -n^3 p_{44}/(2G)$, the dispersion of p_{44} typically shows the opposite trend as that of C. The change in C with λ often becomes more dramatic as the wavelength approaches the absorption edge; in the near-IR range, C typically plateaus, becoming fairly constant as λ increases.

The results will be presented in three categories: binary glasses showing positive dispersion in C, binary glasses with negative dispersion in C, and ternary glass systems which show both positive and negative dispersion.

Some measured glasses show sharp peaks between 800 and 1000 nm; these peaks are artifacts of the strong emission lines of the Xe arc lamp light source. Also, for most glasses measured, the uncertainty in C is less than 0.1 B. For glass systems with larger than average C, such as those rich in ZnO, the uncertainty in C can be as large as 0.5 B. Larger uncertainties and fluctuating values of C with λ typically correspond to glasses which are not completely annealed or unevenly stressed.

5.2.1 Binary Glass Systems with Positive Dispersion of C

The wavelength dependent stress-optic coefficients for barium phosphates and barium borates are shown in the left sides of Figures 5.2 and 5.3 respectively. Individual glass samples show C increasing by 0.4-0.9 B over the measured wavelength range. For both borates and phosphates, the dispersion becomes stronger as the amount of additive in the glass is decreased. The absorption edges for these barium containing glasses are fairly constant with composition, occurring between 250-300 nm. There is slightly less compositional variation in the dispersion of the elasto-optic coefficients p_{44}, shown in the right sides of Figures 5.2 and 5.3. Over the measured wavelength range, each p_{44} decreases by 0.003-0.005. Again, as the amount of additive is increased, glass samples show stronger dispersive effects in p_{44}.

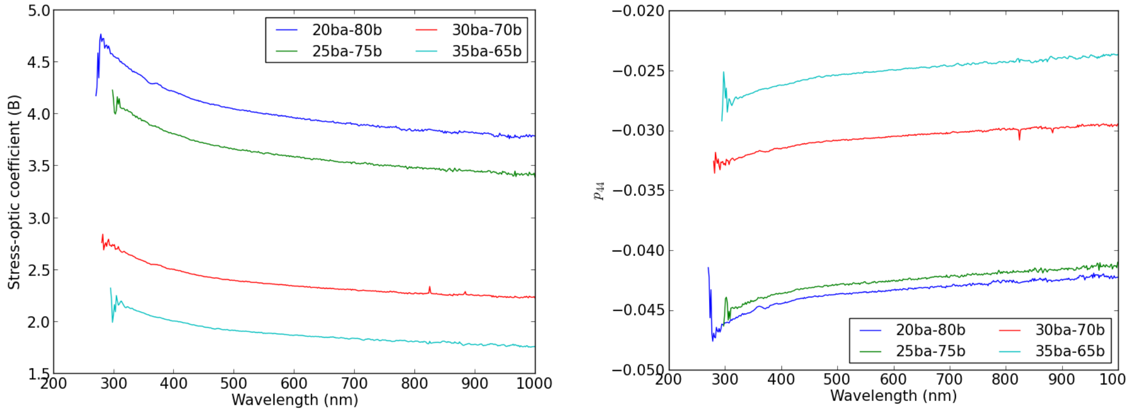

Figure 5.2: Stress-optic coefficient C (left) and elasto-optic tensor element p_{44} (right) as a function of wavelength for glasses with composition xBaO-(1-x)B_2O_3

The magnitude of the stress-optic and elasto-optic response for zinc phosphate glasses, shown as a function of wavelength in Figure 5.4, is much larger than that seen in barium phosphates. This is consistent with previous results [38]. The positive

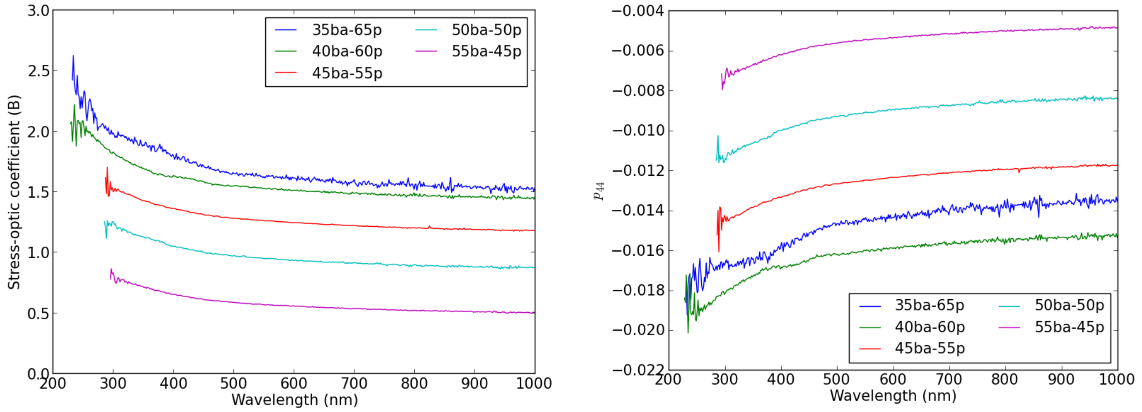

Figure 5.3: Stress-optic coefficient C (left) and elasto-optic tensor element p_{44} (right) as a function of wavelength for glasses with composition xBaO-(1-x)P_2O_5

dispersion in C is also stronger for these glasses, with the coefficient increasing by as much as 4 B over the wavelength range. The elasto-optic coefficients p_{44} show strong negative dispersion. For both coefficients, the amount of dispersion does not seem to be affected significantly by zinc content. The absorption edge, found at approximately 230 nm, is also fairly independent of composition.

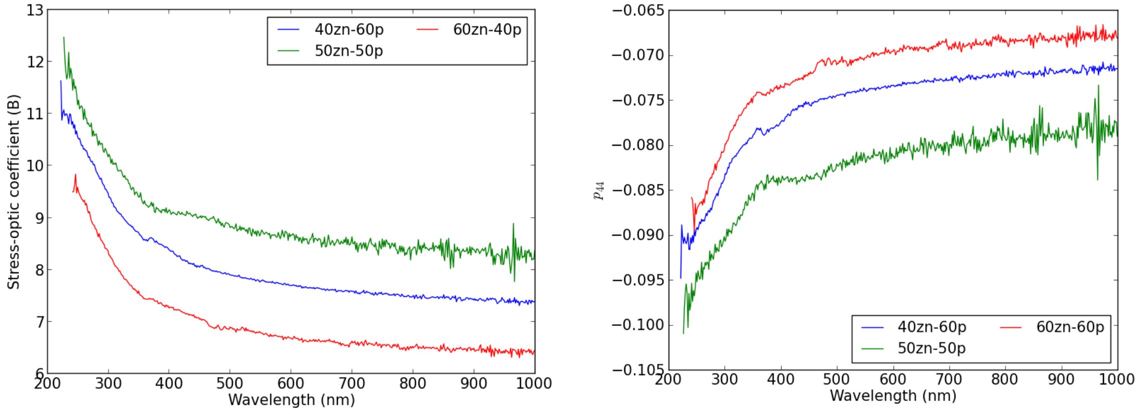

Figure 5.4: Stress-optic coefficient C (left) and elasto-optic tensor element p_{44} (right) as a function of wavelength for glasses with composition xZnO-(1-x)P_2O_5

The stress-optic and shear elasto-optic coefficients for calcium phosphate glasses are shown in Figure 5.5 as a function of incident wavelength. The magnitudes of C and p_{44} are smaller than zinc phosphates and larger than barium phosphates, but they vary less with composition. The glasses begin absorbing light at $\lambda_0 \approx 300$ nm, independent of calcium content, and the amount of dispersion in both C and p_{44} is equal to that of the barium phosphate (and borate) glasses.

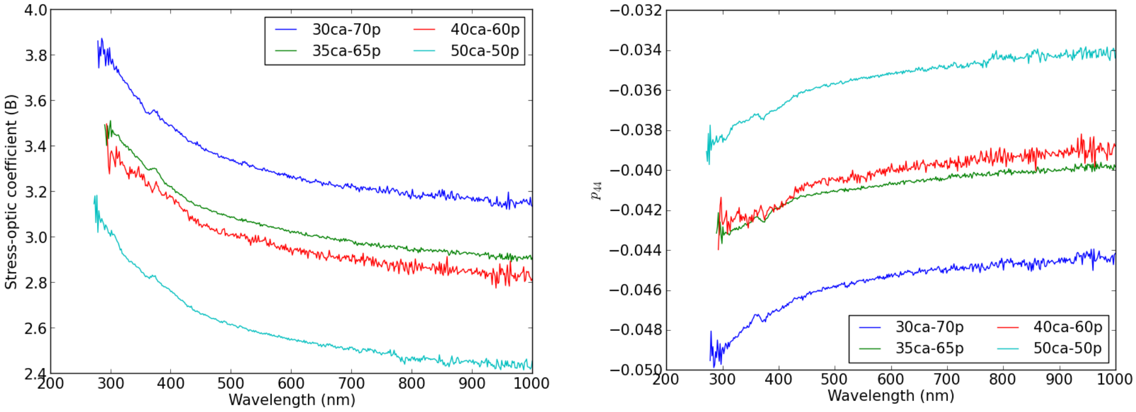

Figure 5.5: Stress-optic coefficient C (left) and elasto-optic tensor element p_{44} (right) as a function of wavelength for glasses with composition xCaO-(1-x)P_2O_5

Bismuth phosphates have stress-optic coefficients with similar magnitudes and amounts of dispersion as calcium phosphates; this is seen in the left side of Figure 5.6. The absorption edge for all measured glasses is just above 300 nm. The elasto-optic coefficient p_{44} (right side of Figure 5.6), however, shows atypical dispersive trends. The coefficient decreases with wavelength to about 400 nm, and then begins to increase with decreasing λ. While the uncertainty in p_{44} could account for this dip, it is unlikely due to its presence in all three glass samples. Below 400 nm, the refractive index of the bismuth phosphates begins to rapidly increase with decreasing wavelength, while C continues to increase at approximately the same rate. This is further enhanced by the large magnitudes of the refractive index. This is the only binary glass family measured where the dispersion in n surpasses that in C, resulting in positive dispersion in the spectra of both C and p_{44}.

The stress-optic and elasto-optic coefficients of sodium and lithium borates are shown in Figures 5.7 and 5.8. Both glass series show similar dispersive trends, with C increasing by 1-2 B over the measured wavelength range. The refractive indices for lithium borate samples with additive content $x = 0.15$ and $x = 0.25$ could not be measured, and as such their elasto-optic coefficients could not be determined. The glass samples $0.35Na_2O$-$0.65B_2O_3$ and $0.20Li_2O$-$0.80B_2O_3$ show anomalous behaviour in p_{44}. While the elasto-optic coefficient does generally decrease with decreasing

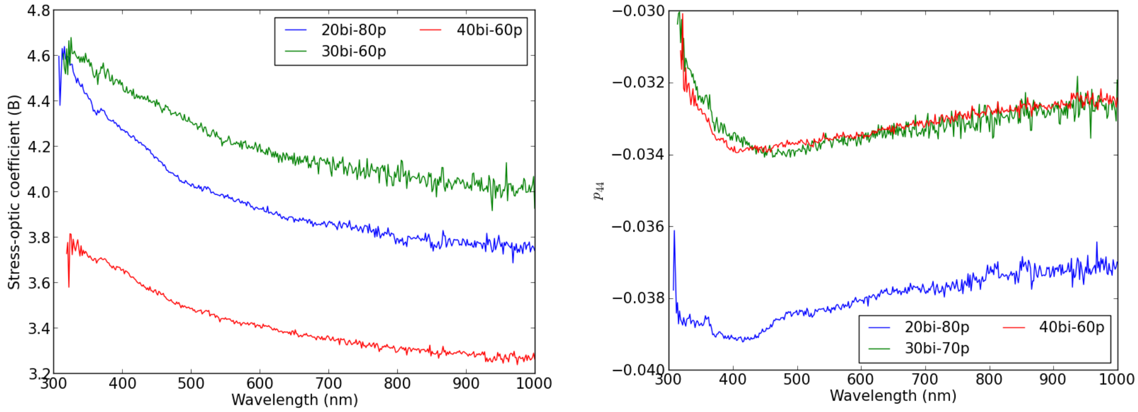

Figure 5.6: Stress-optic coefficient C (left) and elasto-optic tensor element p_{44} (right) as a function of wavelength for glasses with composition $x\mathrm{Bi_2O_3}$-(1-x)$\mathrm{P_2O_5}$

wavelength, there is some fluctuation of this value near 400 nm. However, the magnitude of these fluctuations is small compared to the experimental uncertainty. The variations likely result from the quality of the Cauchy fit for the refractive indices, and lead to a total amount of dispersion less than that of the other glasses. The absorption edges for all samples measured are in the uv-range and do not vary significantly with composition.

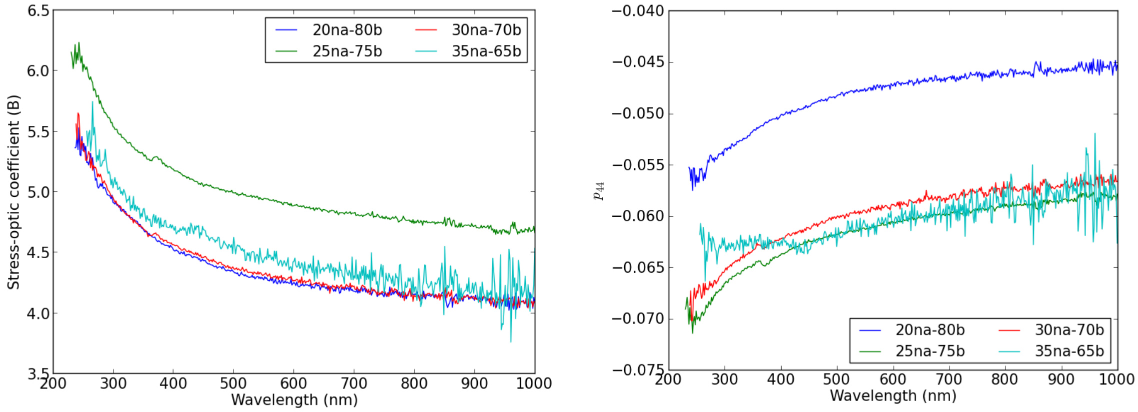

Figure 5.7: Stress-optic coefficient C (left) and elasto-optic tensor element p_{44} (right) as a function of wavelength for glasses with composition $x\mathrm{Na_2O}$-(1-x)$\mathrm{B_2O_3}$

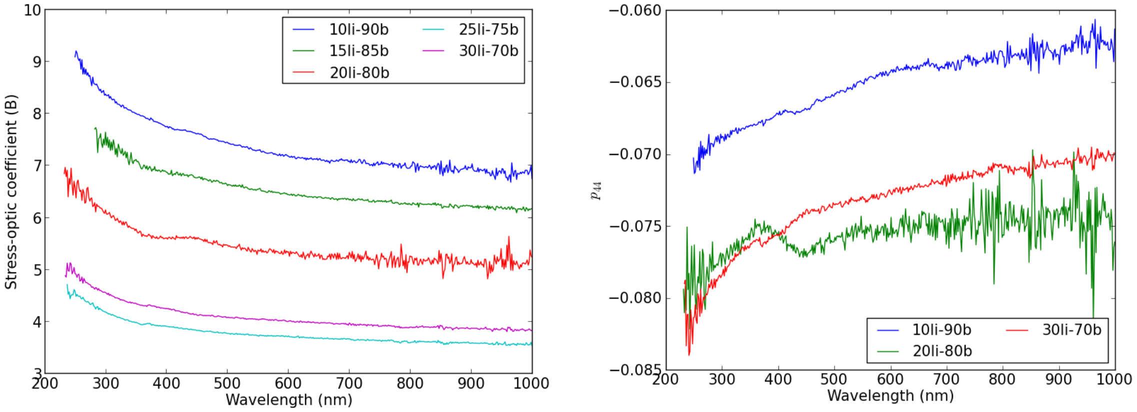

Figure 5.8: Stress-optic coefficient C (left) and elasto-optic tensor element p_{44} (right) as a function of wavelength for glasses with composition $x\mathrm{Li_2O}$-(1-x)$\mathrm{B_2O_3}$

5.2.2 Negative Dispersion in Binary Glasses

The wavelength dependence of the stress-optic and elasto-optic coefficients for lead borates, phosphates and silicates is shown in Figures 5.9, 5.10 and 5.11, respectively. The stress-optic coefficients for all lead-containing glasses show negative dispersion, with the amount of dispersion increasing with increasing additive content. This is most dramatic in the borate glasses. Here, for lead content $x = 0.35$, the dispersion in C is minimal, decreasing by about 0.3 B over the wavelength range, whereas for $x = 0.60$, the decrease grows dramatically to about 2 B. Lead phosphates and silicates show decreases in C of between 1 and 2.5 B for all glasses considered. The amount of dispersion in the elasto-optic coefficient p_{44} does not seem to depend on composition for the lead borates. This is due to increasing amounts of dispersion in the refractive indices of the glasses as lead content increases. In contrast, the p_{44} of the phosphate and silicate glasses become slightly more dispersive with increasing lead content. The absorption edge for lead borates is between 300 and 400 nm, shifting to the visible wavelength range with increasing lead content. For lead phosphates, the edge is further in the uv range, between 200 and 300 nm; lead silicates absorb at the low end of the visible range, between 400 and 500 nm.

The stress-optic coefficients of tin phosphates and silicates, seen in the left side of Figures 5.12 and 5.13, show increasing amounts of negative dispersion as the tin content increases. The highest change in coefficient occurs for the glass sample

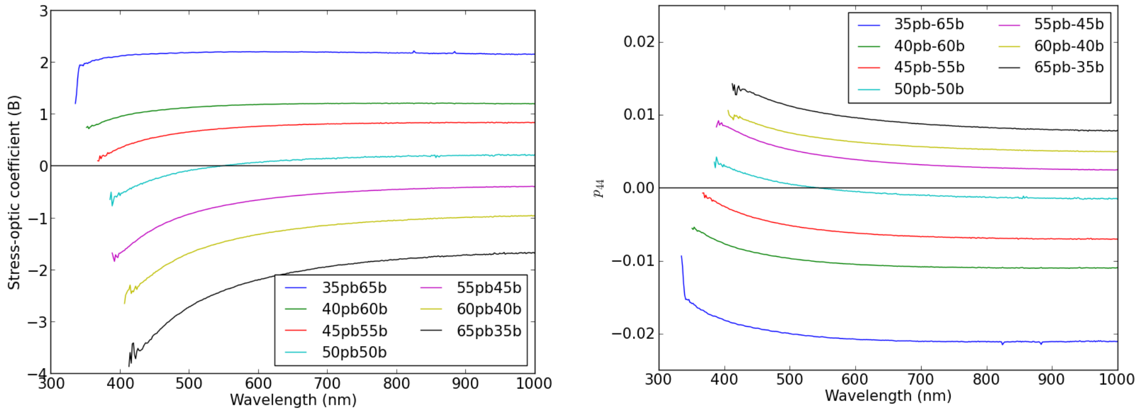

Figure 5.9: Stress-optic coefficient C (left) and elasto-optic tensor element p_{44} (right) as a function of wavelength for glasses with composition xPbO-(1-x)B_2O_3

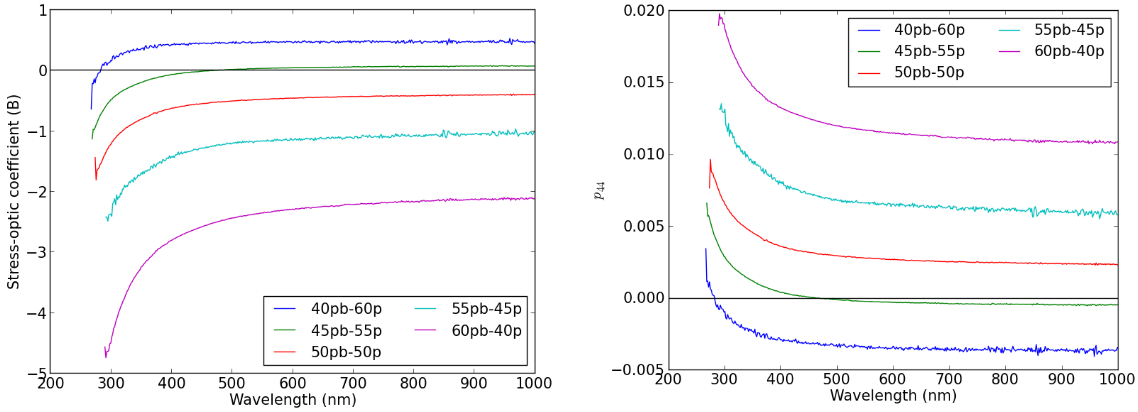

Figure 5.10: Stress-optic coefficient C (left) and elasto-optic tensor element p_{44} (right) as a function of wavelength for glasses with composition xPbO-(1-x)P_2O_5

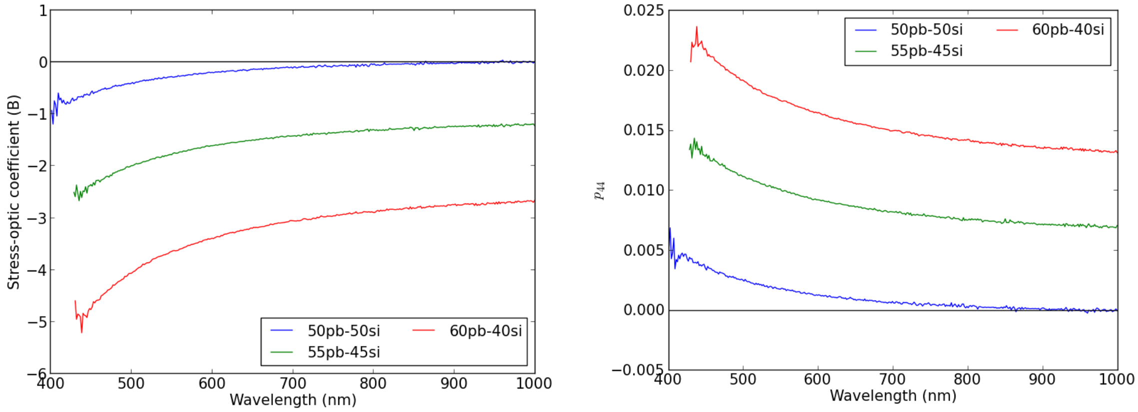

Figure 5.11: Stress-optic coefficient C (left) and elasto-optic tensor element p_{44} (right) as a function of wavelength for glasses with composition xPbO-(1-x)SiO_2

with composition 0.68SnO-0.32P_2O_5, where C decreases by 4.5 B. The amount of dispersion in p_{44} for the phosphates (right side of Figures 5.12) increases with increasing tin, while the dispersion in p_{44} for the silicates (right side of Figure 5.13) does not seem to depend on composition. The absorption edge for the tin phosphate glasses is in the uv range, around 350 nm. The tin silicate have absorption edge in the visible range, between 400 and 500 nm, and increasing with increasing tin content.

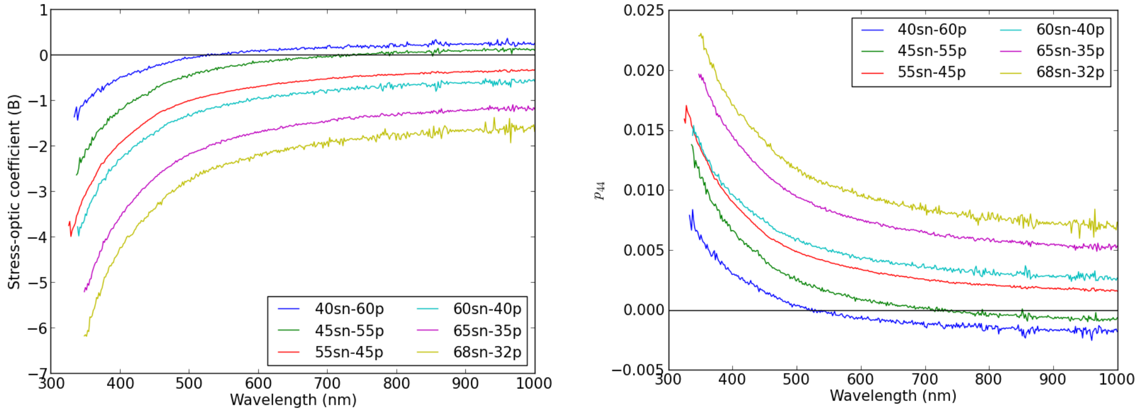

Figure 5.12: Stress-optic coefficient C (left) and elasto-optic tensor element p_{44} (right) as a function of wavelength for glasses with composition xSnO-(1-x)P_2O_5

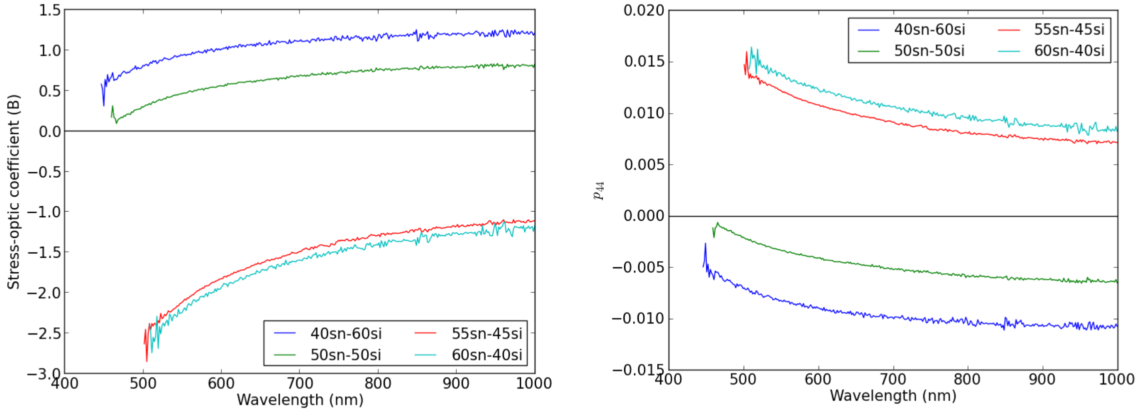

Figure 5.13: Stress-optic coefficient C (left) and elasto-optic tensor element p_{44} (right) as a function of wavelength for glasses with composition xSnO-(1-x)SiO_2

The stress-optic and elasto-optic coefficients for zinc tellurite glasses are seen in Figure 5.14. The amount of dispersion in C increases with increasing zinc content. This is a contrast to the behaviour of zinc in zinc phosphate glasses (Figure 5.4), where varying the amount of zinc in the glass did not affect the amount of dispersion. The elasto-optic coefficients p_{44} also show increasing amounts of dispersion with zinc content.

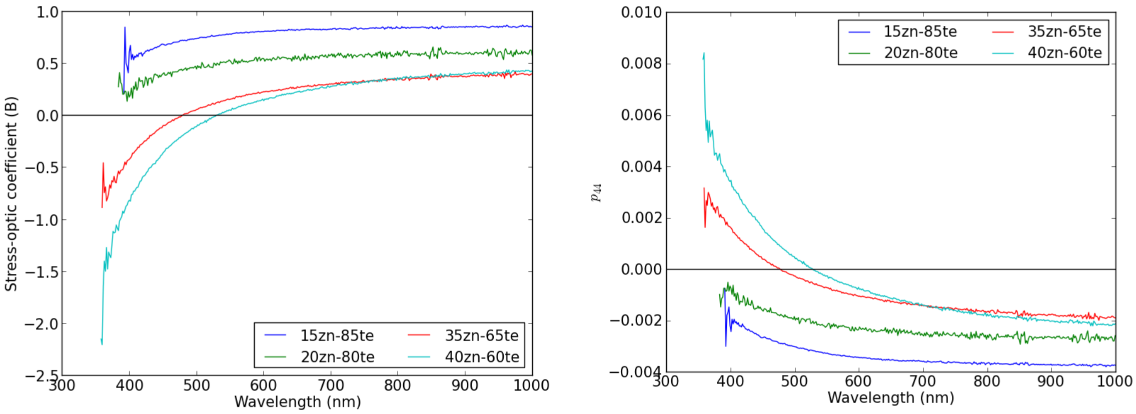

Figure 5.14: Stress-optic coefficient C (left) and elasto-optic tensor element p_{44} (right) as a function of wavelength for glasses with composition xZnO-(1-x)TeO$_2$

5.2.3 Ternary Glass Systems

For binary systems, different additives can cause either positive or negative dispersion in the stress-optic response of a glass. It is of interest, then, to investigate ternary systems with constant glass former and two glass modifiers which have opposite dispersive properties.

We first consider the substitution of lead oxide for barium oxide in borates, phosphates and silicates and its effect on the dispersion of the stress-optic response in these glasses. Figure 5.15 shows the stress-optic and elasto-optic coefficients for lead barium borates with 40 mol % B$_2$O$_3$. All glasses show negative dispersion in C; the amount of dispersion does not vary significantly with increasing lead content. The amount of dispersion in p_{44} decreases with increasing lead content.

The stress-optic coefficients and elasto-optic tensor elements for lead barium borates with 50 mol % B$_2$O$_3$ are shown in Figure 5.16. The stress-optic coefficient of 0.2PbO-0.3BaO-0.5B$_2$O$_3$ increases slightly with decreasing wavelength before beginning to decrease as the absorption edge is approached. However, this variation is small; C changes by only as much as 0.1 B over the measured wavelength range, which is equal to the experimental uncertainty. As the amount of lead oxide in

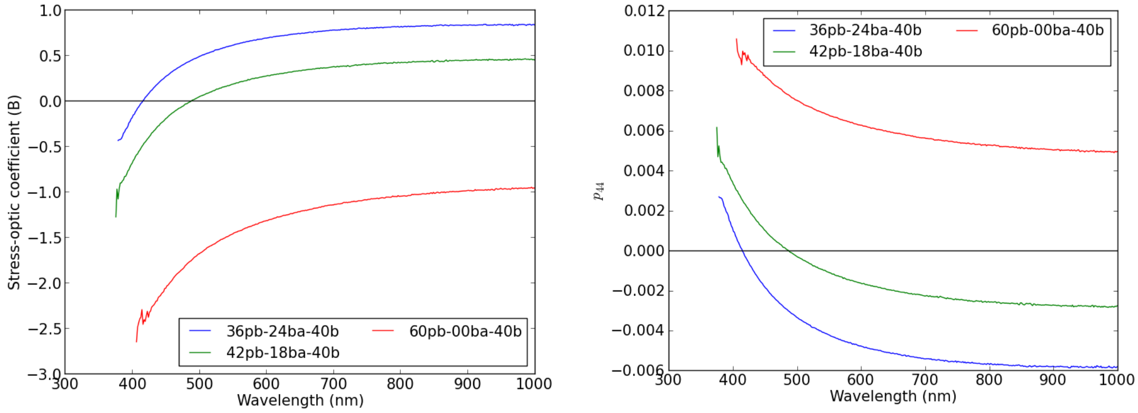

Figure 5.15: Stress-optic coefficient C (left) and elasto-optic tensor element p_{44} (right) as a function of wavelength for glasses with composition xPbO-(0.6-x)BaO-0.4B_2O_3

the glass is increased, C shows increasing amounts of negative dispersion over the measured wavelength range. The elasto-optic coefficients show positive dispersion for all samples; again, the amount of dispersion increases as barium is substituted for lead.

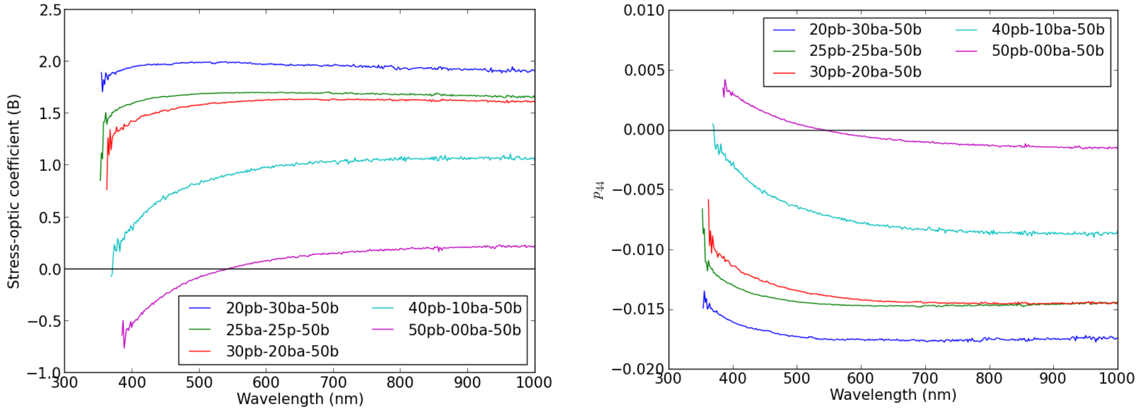

Figure 5.16: Stress-optic coefficient C (left) and elasto-optic tensor element p_{44} (right) as a function of wavelength for glasses with composition xPbO-(0.5-x)BaO-0.5B_2O_3

Figure 5.17 shows C and p_{44} for lead barium borates with 60 mol % B_2O_3. The barium-rich sample 0.16PbO-0.24BaO-0.60B_2O_3 shows positive dispersion in C; this increase is almost linear over the measured wavelength range. The lead-rich sample 0.24PbO-0.16BaO-0.60B_2O_3 shows slightly positive dispersion, but C begins to decrease as the wavelength approaches the absorption edge. Again, this variation in C is smaller than its experimental uncertainty. From this point, as lead content is increased, negative dispersion is measured for the stress-optic coefficient. The lead-rich samples all show positive dispersion of the elasto-optic coefficient; the barium-rich 0.16PbO-0.24BaO-0.60B$_2$O$_3$ shows a small decrease in p_{44} until about 500 nm, and an increase as the absorption edge is approached.

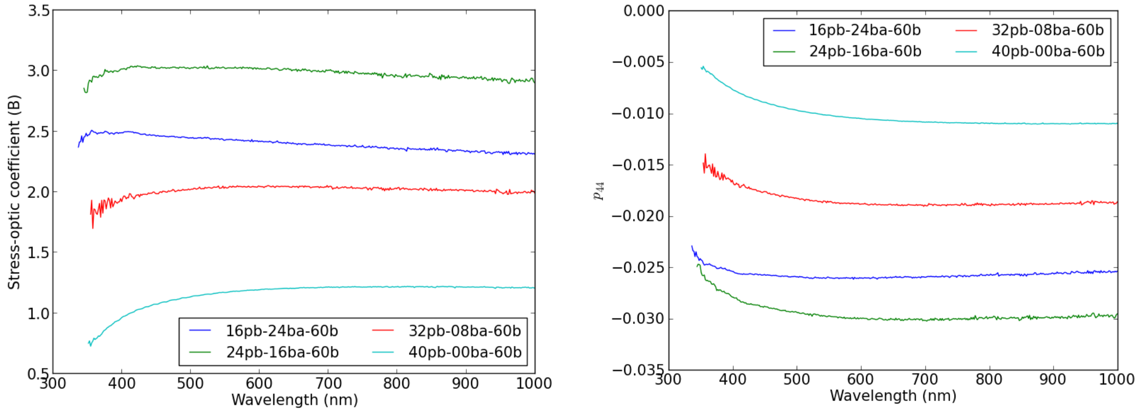

Figure 5.17: Stress-optic coefficient C (left) and elasto-optic tensor element p_{44} (right) as a function of wavelength for glasses with composition xPbO-(0.4-x)BaO-0.6B$_2$O$_3$

Ternary lead barium phosphates and silicates with constant 50 mol % glass former have also been measured. Figure 5.18 shows the stress-optic and elasto-optic coefficients for lead barium phosphate glasses. The barium-rich glass samples (PbO $<$ 30 mol %) show positive dispersion in C, while the lead-rich samples (PbO $\geq$ 30 mol %) have negative dispersion. The elasto-optic coefficients show similar behaviour as the additive content is varied. As the lead content of the glass is increased, the negative dispersion of p_{44} transitions to positive dispersion; however, this occurs near the absorption edge ($\lambda < 400$ nm) more quickly than for visible and near-IR wavelengths. For example, the glass with 10 mol % PbO has p_{44} that decreases until just below 400 nm, at which point the coefficient is wavelength independent. The glass with 20 mol % PbO is non-dispersive within its uncertainty.

The stress-optic and elasto-optic coefficients of lead barium silicates are shown in Figure 5.19. All glass samples have C with negative dispersion, and the amount of dispersion increases with increasing lead content. The elasto-optic tensor elements p_{44} are positively dispersive for all glasses measured in this system, and the amount of dispersion again increases as lead is substituted for barium in the composition.

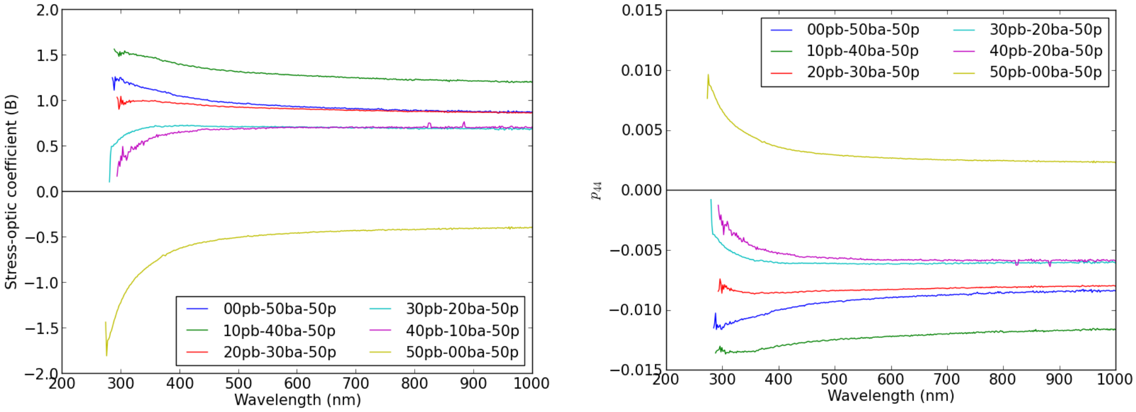

Figure 5.18: Stress-optic coefficient C (left) and elasto-optic tensor element p_{44} (right) as a function of wavelength for glasses with composition xPbO-(0.5-x)BaO-0.5P_2O_5

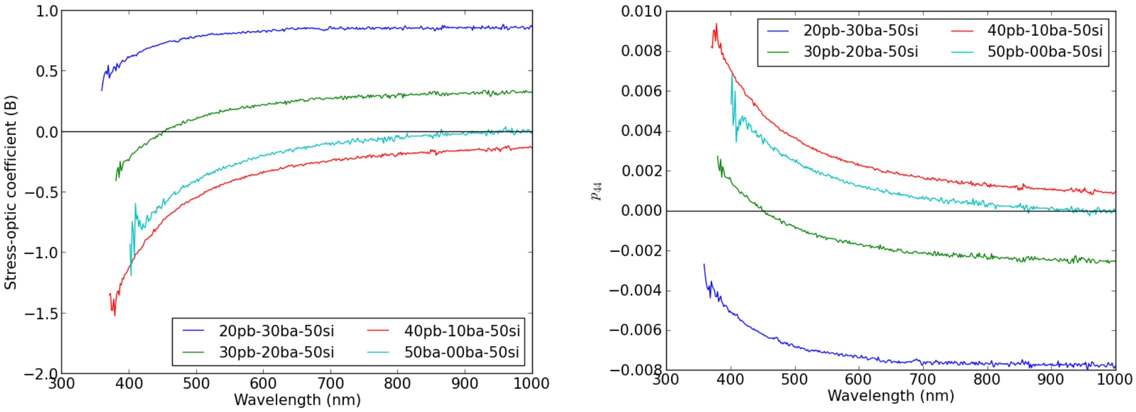

Figure 5.19: Stress-optic coefficient C (left) and elasto-optic tensor element p_{44} (right) as a function of wavelength for glasses with composition xPbO-(0.5-x)BaO-0.5SiO_2

The wavelength dependence of the stress-optic response of barium zinc phosphates and lead zinc phosphates with constant 50 mol % P_2O_5 were also measured. The binary barium phosphates and zinc phosphates both showed positive dispersion in C, with zinc phosphates having coefficients with much larger magnitudes and amounts of dispersion. Figure 5.20 shows the stress-optic and elasto-optic coefficients for the ternary barium zinc phosphates. As barium is substituted for zinc in the system, the stress-optic coefficient and the amount of positive dispersion both decrease. A similar trend is seen for p_{44}.

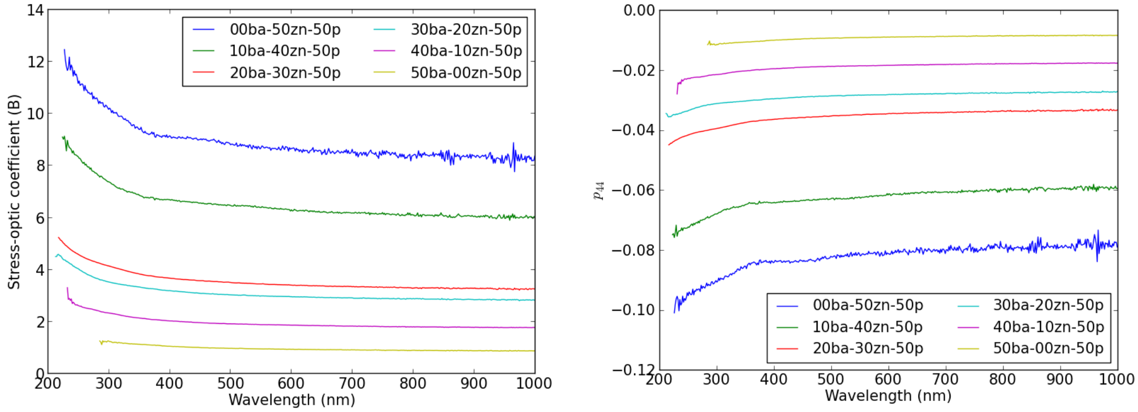

Figure 5.20: Stress-optic coefficient C (left) and elasto-optic tensor element p_{44} (right) as a function of wavelength for glasses with composition xBaO-(0.5-x)ZnO-0.5P_2O_5

Figure 5.21 shows the wavelength dependence of C and p_{44} for the ternary lead zinc phosphate glasses. The stress-optic coefficient transitions from having positive dispersion for the zinc-rich samples to negative dispersion for the lead-rich samples; the opposite trend is seen in the elasto-optic coefficient, as expected. The glass sample with 20 mol % PbO shows no dispersion in p_{44} within its experimental uncertainty.

5.3 Discussion

5.3.1 Zero-Stress Optic Compositions

Many of the glass families exhibiting negative dispersion contain glass compositions with zero-stress optic coefficient: lead borates, lead barium borates with 40 mol % B_2O_3, lead phosphates, lead silicates, lead barium silicates with 50 mol % SiO_2, tin phosphates, tin silicates, and zinc tellurites. Zero-stress optic compositions are also

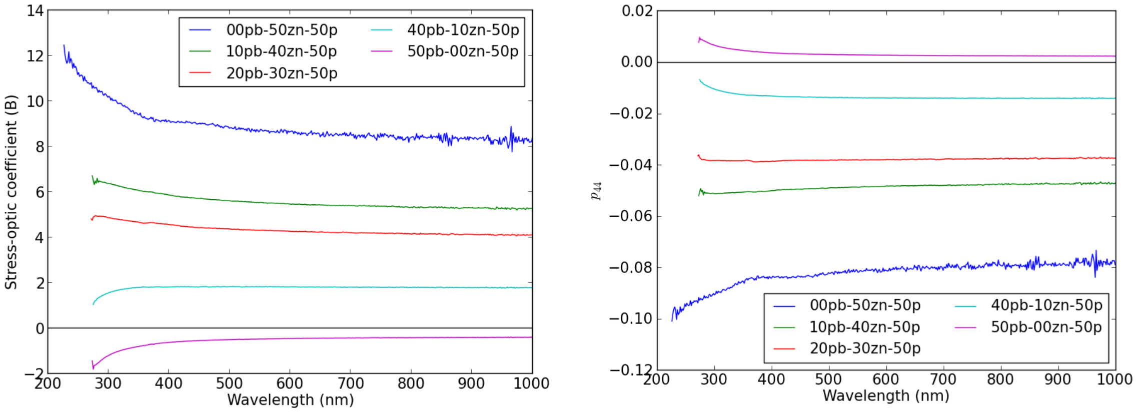

Figure 5.21: Stress-optic coefficient C (left) and elasto-optic tensor element p_{44} (right) as a function of wavelength for glasses with composition xPbO-(0.5-x)ZnO-0.5P_2O_5

expected for tin silicates, lead barium borates with 50 and 60 mol % B_2O_3, lead barium phosphates and lead zinc phosphates with 50 mol % P_2O_5. These glass families show C which transitions from positive to negative values. Some of the glass systems have multiple zero-stress optic compositions depending on the wavelength of incident light. For example, in Figure 5.10, 0.40PbO-0.60P_2O_5 has $C = 0$ B at about 280 nm, and 0.45PbO-0.55P_2O_5 has $C = 0$ B between 450 and 550 nm.

It can be interpolated that these negatively dispersive glass families have a narrow composition range for which $C = 0$ B across the probed wavelength range. The composition is bounded at the lower end by the smallest additive content necessary to induce $C = 0$ B at the absorption edge. At the upper end, the composition range is bounded by the largest additive content necessary to induce $C = 0$ B at 1000 nm. Since C typically plateaus as wavelength increases, the upper bound of the composition range is expected to have broadband near-IR and IR zero-stress optic coefficient.

For the glass families measured in this study, the lower and upper composition bounds for $C = 0$ B in this wavelength range are different by about 10 to 20 mol % of additive. This is within the experimental accuracy of the empirical model in predicting new zero-stress optic compositions, corresponding to a change in $\langle d/N_c \rangle$ of up to 0.03 Å depending on the additive and glass former types. It is of no immediate benefit, then, to incorporate the wavelength of incident light into the empirical model of photoelasticity. The value $\langle d/N_c \rangle$ remains an adequate initial predictor of near-zero stress optic compositions across the visible and near-IR wavelength range.

There are no experimentally measured glass compositions with broadband zero-stress optic coefficient. The transition between positive and negative dispersion occurs when $C > 0$ B at near-IR wavelengths; all glass samples with $C = 0$ B at any wavelength exhibit negative dispersion.

5.3.2 Effect of Glass Modifier on Dispersion

The binary glasses measured are composed of the glass formers SiO_2, B_2O_3, P_2O_5 and TeO_2 as well as the glass modifiers BaO, CaO, ZnO, PbO, SnO, Na_2O, Li_2O and Bi_2O_3. According to the empirical model of photoelasticity, BaO, CaO, Na_2O and Li_2O all contribute positively to the stress-optic coefficient, while PbO, SnO, and Bi_2O_3 are negatively contributing modifiers. Zinc oxide, with $d/N_c = 0.5$ Å, could have slightly positive or negative effect on C according to the model.

It is interesting to note that glasses compositions with positive additives have positive dispersion, while negative additives induce negative dispersion. One might expect bismuth-containing glasses to show negative dispersion; however, the empirical model predicts positive stress-optic coefficients for these glasses (they have $\langle d/N_c \rangle < 0.45$ Å) which could be an influencing factor in the type of dispersion. The zinc phosphate glasses, all with $\langle d/N_c \rangle < 0.45$ Å, have positive dispersion in C, while zinc tellurites, with $\langle d/N_c \rangle = 0.5$ Å, show negative dispersion.

In the ternary glass systems, as a positive glass additive is exchanged for a negative modifier (*i.e.* as $\langle d/N_c \rangle$ decreases), the dispersion in C can transition from positive to negative. This transition is seen in lead barium borates with 50 and 60 mol % B_2O_3, lead barium phosphates, and lead zinc phosphates.

5.3.3 Applicability of the Empirical Model

The empirical parameter $\langle d/N_c \rangle$ is important in describing the amount and type of dispersion seen in a glass sample. Figure 5.22 shows the amount of dispersion of a glass sample plotted as a function of $\langle d/N_c \rangle$. The amount of dispersion is quantified by the difference in stress-optic coefficient measured at the absorption edge ($C(\lambda_0)$) and away from the absorption edge ($C(\lambda_0 + 250\text{ nm})$). For borate glasses, the cation coordination number is estimated as $N_c = 3.5$ to more accurately reflect the glass network structure [42]. As $\langle d/N_c \rangle$ decreases, the amount of dispersion also decreases, transitioning from positive dispersion to negative dispersion at $\langle d/N_c \rangle \approx 0.45$ Å.

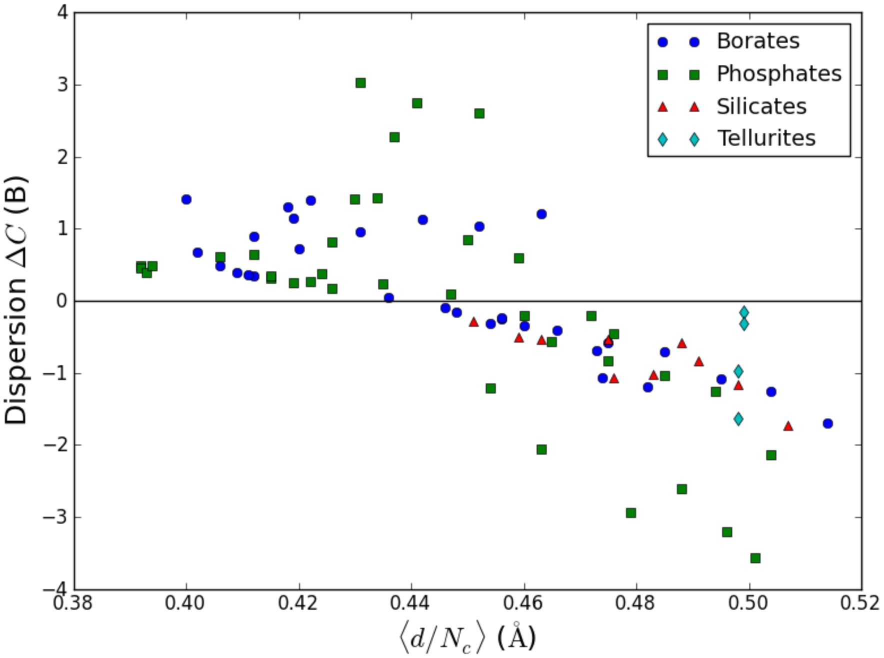

Figure 5.22: Amount of dispersion ΔC in a glass as a function of the $\langle d/N_c \rangle$ value. The amount of dispersion is defined in this report as $\Delta C = C(\lambda_0) - C(\lambda_1)$, where λ_0 is the absorption edge wavelength, and $\lambda_1 = \lambda_0 + 250$ nm.

From these results, it seems to be possible to predict the type of dispersion in a glass, as well as non-dispersive glass compositions. However, these results would also suggest that non-dispersive glasses will always have positive stress-optic coefficient since zero-stress optic coefficients are predicted when $\langle d/N_c \rangle \approx 0.5$ Å.

5.3.4 Relationship Between Wavelength and Stress-Optic Coefficient

The stress-optic and elasto-optic coefficients of many various glass systems have been measured as a function of incident wavelength; these coefficients are shown in Figures 5.3 to 5.21. The refractive index is another optical property which is wavelength dependent. Typically, the refractive index is fitted as a function of wavelength by the empirical Cauchy model:

$$n(\lambda) = A + \frac{B}{\lambda^2} + \frac{C}{\lambda^4}. \tag{5.3}$$

This model was introduced in Section 3.2.4. The coefficients A, B and C are experimentally determined for different glass compositions. Since the stress-optic coefficient is the constant of proportionality between induced birefringence $b = n_e - n_o$ and applied stress σ, it is reasonable that the wavelength dependence of C can be fitted using a model similar to the Cauchy model. Also, following the theories concerning the dispersion of p_{ijkl} in crystalline materials discussed in Section 2.3, it is prudent to normalize the incident wavelength of light by the absorption edge wavelength of the glass. Then the wavelength-dependent stress-optic coefficients of glass samples can be modelled using the pseudo-Cauchy model

$$C(\lambda) = a + b\left(\frac{\lambda_0}{\lambda}\right) + c\left(\frac{\lambda_0}{\lambda}\right)^2 . \tag{5.4}$$

A full Cauchy relationship, where C is dependent on $(\lambda_0/\lambda)^2$ and $(\lambda_0/\lambda)^4$, overestimates the wavelength dependence of C in glass series with positive additives.

Equation 5.4 does a good job at modelling the relationship between C and λ_0/λ for all glass compositions considered in this research. For example, the experimentally measured and Cauchy-fit stress-optic coefficients of lead borates are plotted in Figure 5.23 as a function of normalized incident wavelength (λ_0/λ).

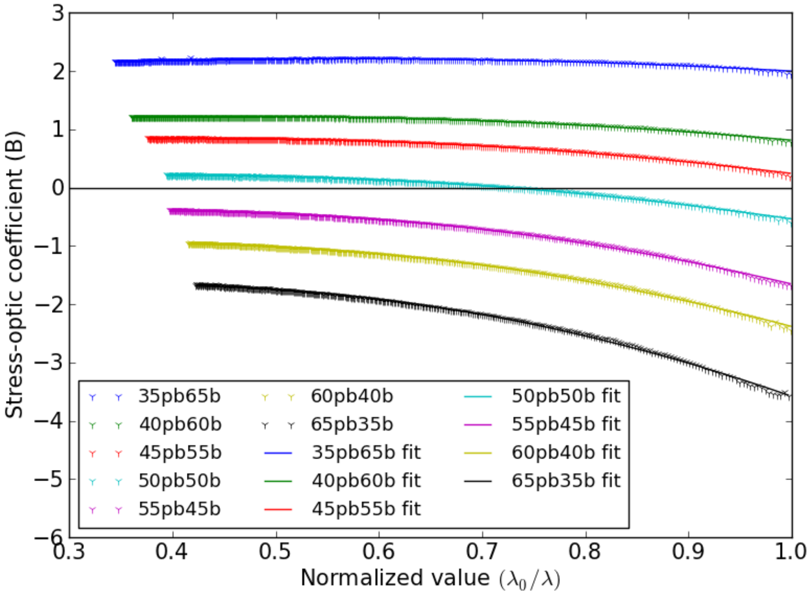

Figure 5.23: Experimentally measured and pseudo-Cauchy fitted stress-optic coefficients of lead borates as a function of (λ_0/λ).

The parameters a, b, and c as well as the sum of the residuals are given in Table B.1 of Appendix B for all glasses considered in this research. The quality of the fit can be determined numerically from the residual of the least-squares fit, which is defined as the square of the difference between the experimental measurement C_λ and the fitted value $C(\lambda)$ at each (λ_0/λ). Figure 5.24 shows the residual as a function of (λ_0/λ) for the lead phosphate glass series. There is little discrepancy between measured and fit stress-optic coefficients for most glasses. For all glass samples and at all wavelengths, the residual is close in value to the experiment uncertainty of the stress-optic coefficient. Most variations occur for glasses containing typically negative modifiers as the wavelength of light approaches the absorption edge, *i.e.* as $(\lambda_0/\lambda) \to 1$.

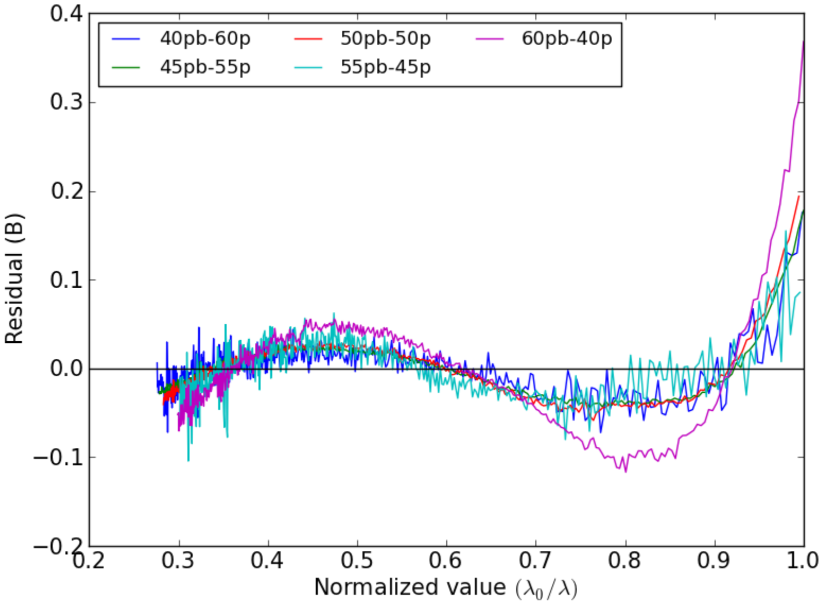

Figure 5.24: The residual, defined as the difference between the experimental stress-optic coefficient C_λ and the fitted value $C(\lambda)$ as a function of normalized wavelength λ_0/λ for lead phosphate glasses. Residuals near zero are representative of well-fit data.

The approximately sinusoidal relationship between residual and λ_0/λ is present to varying degrees in all glass families. The lack of randomness in the residual would seem to suggest that the simple pseudo-Cauchy fit does not entirely describe the wavelength dependence of C. A model including an exponential relationship between

C_λ and λ_0/λ might do better at describing the apparent long-wavelength 'plateau' of the stress-optic coefficient and the rapid increase of C near the absorption edge of the glass. Still, this model provides a fairly good and simple estimate of the dispersion of the stress-optic coefficient which could lead to new insights into the fundamental photoelastic mechanisms of different glass systems.

The fitted parameter a defines the long-wavelength stress-optic coefficient, while the parameters b and c give information on the type and amount of dispersion present. Based on the empirical model of photoelasticity, a relationship is expected between the long-wavelength stress-optic coefficient and the chemical bonding environment of the glass. Figure 5.25 shows the coefficient a of the pseudo-Cauchy fit stress-optic coefficient as a function of empirical value $\langle d/N_c \rangle$. These results are consistent with the empirical model: a (and C) decreases as $\langle d/N_c \rangle$ increases.

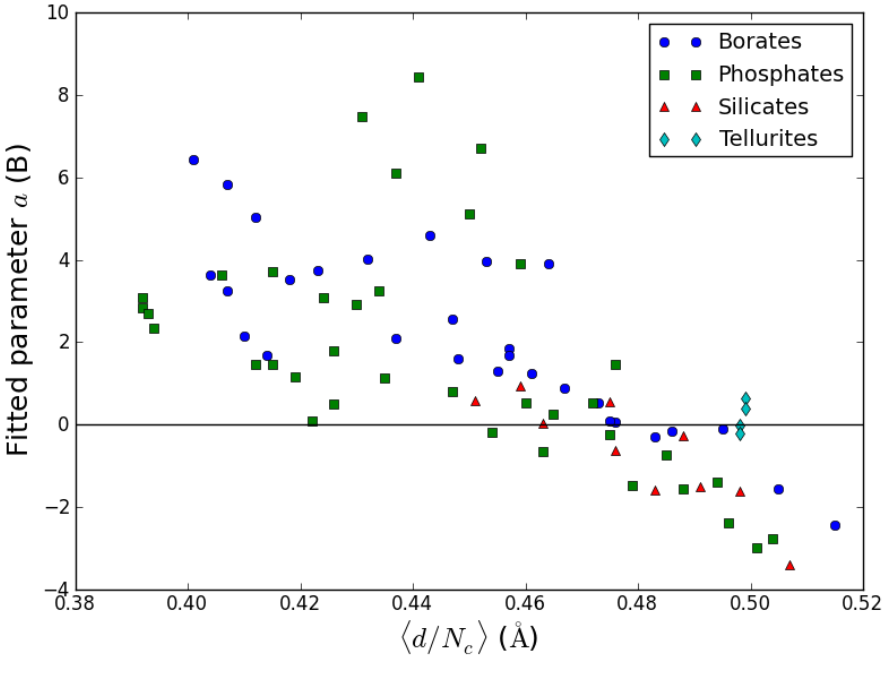

Figure 5.25: Fitted parameter a as a function of empirical parameter $\langle d/N_c \rangle$. The wavelength dependence of the stress-optic coefficient is fitted using a pseudo-Cauchy model, where $C(\lambda) = a + b(\lambda_0/\lambda) + c(\lambda_0/\lambda)^2$.

Positive and negative values of the parameter c indicate positive and negative dispersion of the stress-optic coefficient with wavelength, respectively. The size of this parameter reflects the amount of dispersion present in a glass sample. Larger magnitudes of c indicate that the stress-optic coefficient increases or decreases more dramatically with wavelength near the absorption edge. As the composition of a glass series evolves and the amount of glass additive (either positive or negative) increases, the magnitude of c decreases. In ternary glass systems with constant glass former content, exchanging a positive additive with a negative additive also decreases the parameter c. From the discussion of Section 5.3.3, a relationship is expected between the amount of dispersion and $\langle d/N_c \rangle$. Figure 5.26 shows the parameter c of the pseudo-Cauchy fit stress-optic coefficient as a function of empirical value $\langle d/N_c \rangle$. The decreasing relationship between c and $\langle d/N_c \rangle$ support the claim that the empirical model can be used to predict the type of dispersion in a glass. Based on these results, non-dispersive glass compositions are predicted by the empirical model when 0.44 Å $\leq \langle d/N_c \rangle \leq$ 0.46 Å.

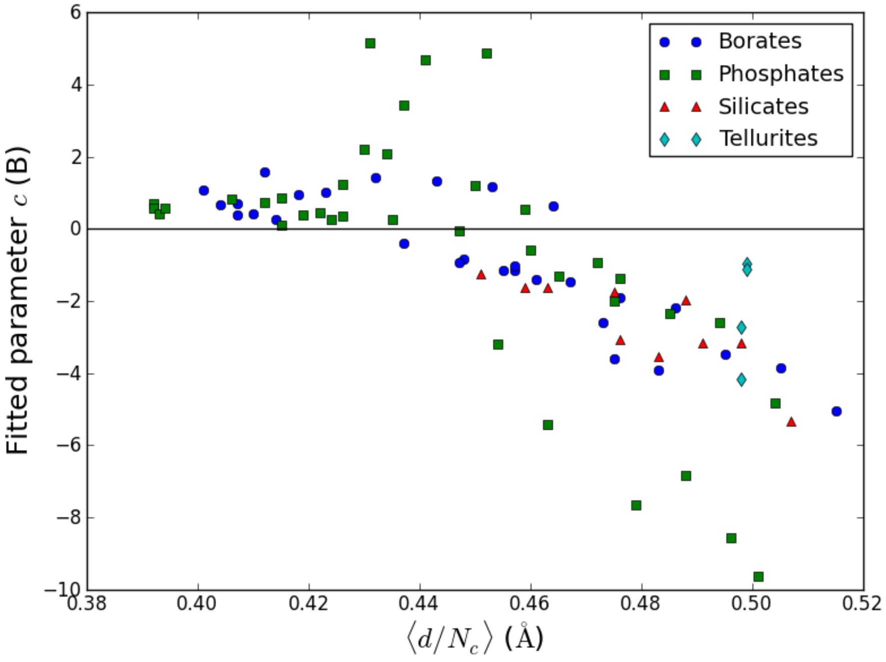

Figure 5.26: Fitted parameter c as a function of empirical parameter $\langle d/N_c \rangle$. The wavelength dependence of the stress-optic coefficient is fitted using a pseudo-Cauchy model, where $C(\lambda) = a + b(\lambda_0/\lambda) + c(\lambda_0/\lambda)^2$.

The minimum value of the fit $\lambda_0/\lambda = -b/2c$ gives an estimate of the wavelength at which the stress-optic coefficient plateaus. For this value to be physically reasonable, *i.e.* for all positive wavelengths λ, the signs of b and c must be opposite. Some glasses, typically those with positive additives, have minimums located at (unphysical) negative wavelengths. This simply indicates that the stress-optic coefficient will continue to slowly change as wavelength increases, never fully reaching a plateau. The model $C(\lambda) = a + b(\lambda_0/\lambda) + c(\lambda_0/\lambda)^2$ could be constrained to force the parameters b and c to have opposite sign. However, this constraint does not significantly affect the quality of the fit, or the sign or magnitudes of c or a, but simply results in $b \approx 0$ for the affected glasses.

Interestingly, the three fitted coefficients seem to be interrelated. Figure 5.27 shows a linear relationship between c and b. Likewise, Figure 5.28 shows a correlation between c and a which varies only slightly from linearity. This would suggest that the stress-optic coefficient could be empirically estimated as a function of normalized incident wavelength and only one of the pseudo-Cauchy parameters:

$$C(\lambda) = f_b(\lambda_0/\lambda, b) = f_b(\lambda_0/\lambda, b) = f_c(\lambda_0/\lambda, c). \tag{5.5}$$

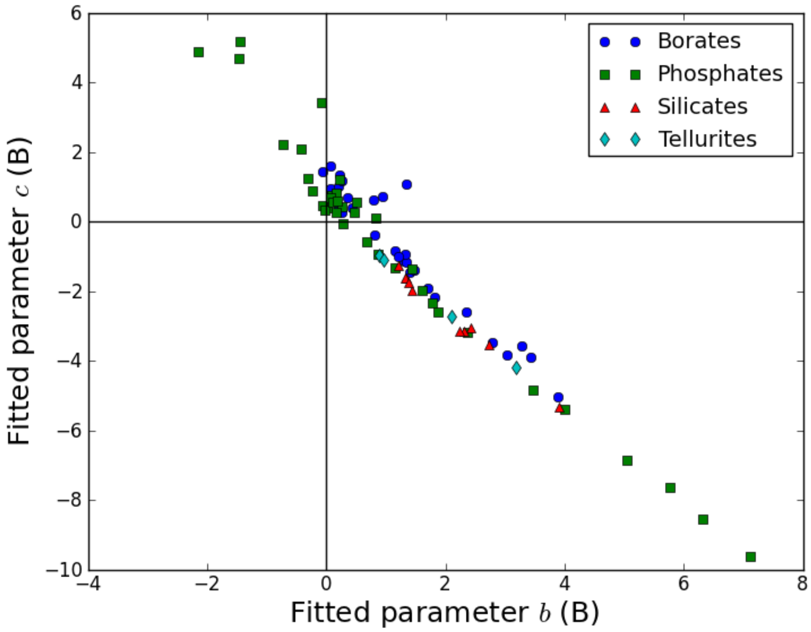

Figure 5.27: Fitted parameter c as a function of b. The parameters are determined from the pseudo-Cauchy model for the stress-optic coefficient, $C(\lambda) = a + b(\lambda_0/\lambda) + c(\lambda_0/\lambda)^2$.

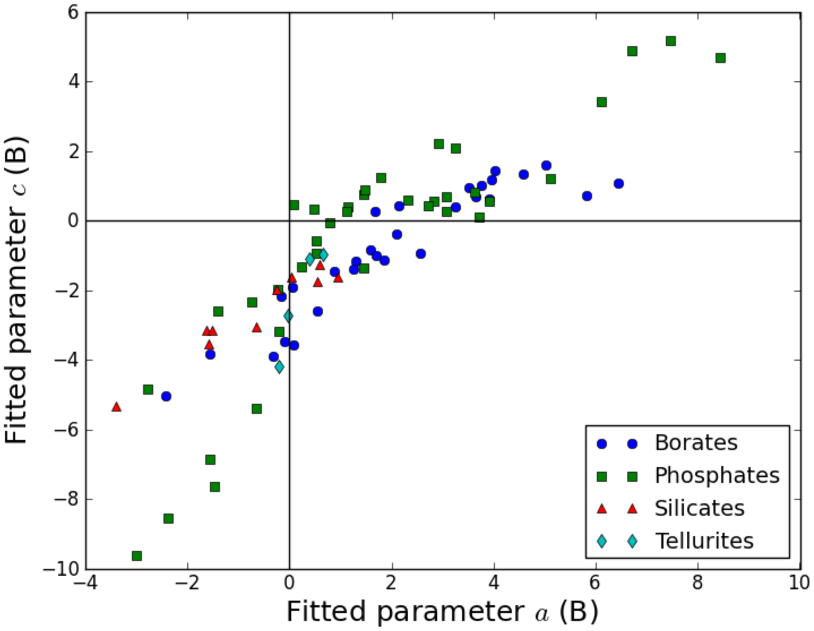

Figure 5.28: Fitted parameter c as a function of a. The parameters are determined from the pseudo-Cauchy model for the stress-optic coefficient, $C(\lambda) = a + b(\lambda_0/\lambda) + c(\lambda_0/\lambda)^2$.

5.4 Summary

The wavelength dependence of the stress-optic coefficient has been measured for binary and ternary borate, phosphate, silicate and tellurite systems. Glasses with typically positive modifiers show positive dispersion in C, while those with negative modifiers have coefficients which show negative wavelength dependence. Ternary systems have been synthesized with glass compositions exhibiting a transition from positive to negative dispersion in C as the positive modifier is gradually replaced by negative modifier. Interestingly, all glass samples with non-dispersion stress-optic coefficient have positive values of C.

The dispersion type was related to the empirical model of photoelasticity. A transition from positive to negative dispersion was observed when $\langle d/N_c \rangle \approx 0.45$ Å. This observation allows the prediction of new non-dispersive glass compositions. However, since $\langle d/N_c \rangle \approx 0.50$ Å, these glasses will always have positive stress-optic coefficients according to the empirical model.

A pseudo-Cauchy model,

$$C = a + b\left(\frac{\lambda_0}{\lambda}\right) + c\left(\frac{\lambda_0}{\lambda}\right)^2, \tag{5.6}$$

describes the relationship between stress-optic coefficient and wavelength of incident light. The parameter a gives the long-wavelength value of C. The decreasing relationship between a and $\langle d/N_c \rangle$ is consistent with the empirical model. The parameter c quantifies the type and amount of dispersion present for glass samples. It does not correlate linearly with $\langle d/N_c \rangle$, but there is again a transition from positive to negative values of c observed at ≈ 0.45 Å.

Interestingly, the parameters a, b and c are interdependent. We conclude that the stress-optic coefficient can be modelled as a function of λ and only one fitted parameter. Determining the relationship between glass composition and this parameter is central in developing a comprehensive theory of photoelasticity. The relationship between a, b, and c and material properties will be further discussed in Chapter 7.

Chapter 6

Individual Elasto-Optic Tensor Elements p_{ijkl}

Brillouin scattering spectra have been collected for binary lead and barium borate, phosphate and silicate glasses. The purpose of this research is to determine the effect of glass formers and of additives with both positive and negative stress-optic response on the elasto-optic tensor of glasses. The shear element p_{44} can be extracted from measurements of the stress-optic coefficient, but p_{11} and p_{12} have only been reported for a select number of glasses, typically with positive stress-optic response. For the glasses considered here, the values of p_{44} and p_{12} determined from Brillouin scattering are correlated with both glass composition and empirical parameter $\langle d/N_c \rangle$. The element p_{12} remains positive for all compositions considered, but p_{44} (like C) can have positive and negative values. The value p_{11} is independent of both glass composition and cation bonding environment.

6.1 Experimental Procedure

6.1.1 Glass Preparation

Lead and barium borate, phosphate and silicate glasses were prepared by conventional melt-quenching techniques. Stoichiometric amounts of commercial-grade lead(II) oxide (PbO, $\geq$ 99.9 %, Sigma-Aldrich), barium carbonate ($BaCO_3$, 99-101 %, Alfa Aesar), boron oxide (B_2O_3, 99 %, Sigma-Aldrich), ammonium phosphate monobasic ($NH_4H_2PO_4$, $\geq$ 98 %, Sigma-Aldrich), and/or silicon dioxide (SiO_2, purum p.a., Sigma-Aldrich) were weighed and mixed.

The lead-containing glasses were synthesized in platinum crucibles. Lead borates and silicates were placed in an oven directly at 1000-1100°C to melt and held at this temperature for 8-12 hrs. Lead phosphates, prepared by Leanne Chapman, were calcined at 550°C for 24 hrs before being melted at 1000°C for 1-2 hrs.

Barium borates and phosphates were prepared in alumina crucibles. The borates were melted directly at 1500°C for 1-2 hrs. The phosphates were calcined at 550°C for 22 hrs and 850°C for 24 hrs, and melted at 1100-1300°C for 12-36 hrs.

The liquids were quenched by pouring into a square metal mold on a brass plate. For the lead silicates, this mold was at room temperature (RT), while for the lead phosphates and borates, the mold was heated to 300°C and 400-500°C, respectively. Barium borates were poured at between RT and 200°C, while barium phosphates were poured at RT.

After being cast, the glasses were annealed for 12-24 hrs to remove residual stresses. Lead borates, silicates and phosphates were annealed at 350-500°C, 450°C and 150-350°C respectively, while the barium borates and phosphates tended to anneal at higher temperatures of 650°C and 450-550°C.

For all glasses, nominal compositions were confirmed by mass-loss and density measurements. The compositions of barium phosphates and lead borates and phosphates were also determined and confirmed from EMP. The barium glasses have 1-7 % Al contamination.

For Brillouin scattering measurements, it is very important for sample geometry to be consistent between samples so that all measured spectra come from equal scattering volume. To ensure this, all samples were cut with a low-speed saw (Buehler IsoMet, using a Lapcraft diamond saw blade) to have a square base of 10×10 mm^2 with a maximum variation of 1 mm on either length. The height of the sample cubes was cut to be > 4 mm to ensure that no scattered light was blocked by the edges of the sample holder.

Three faces of the glass cube perpendicular to the square base were polished to 1 μm optical transparency, beginning with 1200 grit silicon carbide paper and then diamond paste of decreasing particle size (30 μm, 15 μm, 9 μm, 6 μm, 3 μm and 1 μm MetaDi polishing compounds, Buehler).

6.1.2 Density, Elastic Moduli and Refractive Index Measurements

The procedure for measuring densities, sound velocities and refractive indices of the lead and barium borates, phosphates and silicates is described in Section 5.1.2. Values of n at 532 nm were taken from the wavelength-dependent refractive index measurements and used for the analysis of the Brillouin spectra.

6.1.3 Collection and Analysis of Brillouin Spectra

The Brillouin spectra of lead and barium borates, phosphates and silicates were collected at the University of Michigan with the help of Dr. Michael Aldridge using a Sandercock six-pass Tandem Fabry-Perot interferometer (TFPI), using 512-channel binning. Laser light with wavelength 532 nm and tunable power set to 145 mW was passed through a beam splitter to separate the light into two beams. The first reference beam was focused on the TFPI, while the second sample beam followed a path through the glass sample before being focused on the interferometer. The sample beam was initially linearly polarized, either in the vertical (V) or horizontal (H) plane, by passing through a half-wave plate. The polarized beam was focused on the glass sample, and light scattered at 90° relative to the incident light was collected. This light was focused, collimated, and passed through a polarizer such that either the V or H component could be selected. The sample beam was then focused on the TFPI and compared to the reference beam, resulting in Brillouin spectra similar to that in Figure 3.5 depending on polarizations selected and glass measured.

Longitudinal and transverse peaks for reference and sample Brillouin spectra were fit using Fityk [88]. Background noise was subtracted from the spectra where necessary. Spectral lines were fit with Voigt functions, which are convolutions of Gaussian and Lorentzian functions. Lorentzian line shapes often result from homogeneous line-broadening, which is primarily due to collisions of molecules with other molecules (for liquids or gases) or with phonons in the material (for solids). Gaussian line shapes result from inhomogeneous broadening, due to local electric field and frequency variations within a medium [89]. For glass, which has significant structural inhomogeneity, spectral line shapes tend toward Gaussian. The liquid toluene, on the other hand, has a near Lorentzian line shape since collision broadening is the predominant effect. The area under the curve gives the Brillouin intensity, which needs to be normalized by the number of counts or scans over which the data is collected. Each count represents a sweep over the frequency range of interest, and the resulting Brillouin intensity is summed over all counts. The position of the center of the Voigt peak relative to the Rayleigh peak gives the frequency shift, measured in GHz. The longitudinal or transverse frequency shift is then related to the sound velocity and elastic moduli by Equations 3.39 and 3.40. Each Brillouin spectra shows

Stokes and anti-Stokes scattering; both absolute frequencies and intensities are used to determine properties of interest.

Data collection for each glass sample began with VV measurements for both quartz and toluene, typically with 25-50 counts per measurement. The constant replacement of the references resulted in slight variations in the absolute longitudinal intensities. This is likely due to changes in the angle of incidence of light on the reference, or in the focusing of the scattered light on the TFPI. In order to minimize the effect of these variations on the measured elasto-optic coefficients, the reference intensities and frequency shifts were taken from the average (and standard deviations) of the day's measurements.

Data for p_{12} was then collected for glass samples. The intensity I_{VV} was measured at 5-10 spots along the height of the glass cube. Collection times were short for this relatively intense peak, with only 25-100 counts necessary to resolve the Brillouin peaks. After peaks were fit, the average longitudinal intensities and frequency shifts (sound velocities) were used to determine p_{12} through Equation 3.102. The uncertainty in this value is related to the standard deviation of the fitted values.

The values of p_{44} for the glass samples were determined relative to the sample p_{12} rather than the reference value. Data collection began with a measurement of the VV spectra. The glass sample was kept exactly in place, and the optics were adjusted to collect I_{VH}. Keeping the sample stationary in this way removes any variations due to changed angle of incidence or beam focus upon sample replacement. Since p_{44} is typically much smaller than p_{12}, a much larger number of scans were necessary to resolve the Brillouin peaks, ranging from 500 to 5000 counts. Depending on the magnitude of p_{44}, the spectra were collected for between 1 and 5 spots on the glass to determine the standard deviation of the transverse Brillouin intensity.

In order to determine the signs of the elasto-optic coefficients, the HH and VH spectra for glasses with non-zero p_{44} were measured at $\theta = 85°$, $90°$, and $95°$. Between 100-1000 scans were needed to resolve the Brillouin peaks. The sign of the slope of I_{HH}/I_{VH} gives information on the relative sign, and then the absolute sign of p_{44} is determined from independently measured stress-optic coefficients at 532 nm.

6.2 Results

6.2.1 Refractive Index, Density, Elastic Moduli and Stress-Optic Coefficient

Refractive indices measured at 532 nm by ellipsometry, densities and sound velocities as determined from the ultrasonic method are found in Table 6.1. As the amount of additive content, either barium or lead, is increased in the glass, the refractive indices and densities also increase. Longitudinal and transverse sound velocities are fairly constant for barium borates and phosphates. In the lead-based glass systems, v_L and v_T both decrease as x increases; this is most noticeable in the lead borates. For all glasses, the ratio $v_T/v_L \approx 0.55$ is independent of composition.

Table 6.1: Refractive indices, densities, and sound velocities (ultrasonic) of lead and barium borates, phosphates and silicates.

Family	x	n	ρ (g/cm^3)	v_L (km/s)	v_T (km/s)
xBaO -(1-x)B_2O_3	0.20	1.59(1)	2.89(1)	5.15(1)	2.834(5)
	0.25	1.60(1)	3.091(5)	5.24(1)	2.872(5)
	0.30	1.61(1)	3.375(5)	5.30(1)	2.908(5)
	0.35	1.62(1)	3.60(1)	5.27(1)	2.871(5)
xBaO -(1-x)P_2O_5	0.35	1.55(1)	3.26(1)	4.17(1)	2.287(5)
	0.40	1.56(1)	3.351(5)	4.49(1)	2.491(5)
	0.45	1.58(1)	3.482(5)	4.37(1)	2.387(5)
	0.50	1.59(1)	3.652(5)	4.28(1)	2.309(5)
	0.55	1.60(1)	3.84(1)	4.30(1)	2.287(5)
xPbO -(1-x)B_2O_3	0.35	1.78(1)	4.598(5)	4.33(1)	2.394(5)
	0.40	1.81(2)	5.037(5)	4.12(1)	2.281(5)
	0.45	1.86(1)	5.324(5)	3.99(1)	2.198(5)
	0.50	1.93(1)	5.67(1)	3.73(2)	2.046(5)
	0.55	1.99(3)	5.992(5)	3.57(3)	1.918(5)
	0.60	2.03(3)	6.278(5)	3.33(3)	1.779(5)
	0.65	2.04(2)	6.514(5)	3.16(3)	1.688(5)
xPbO -(1-x)P_2O_5	0.40	1.67(5)	4.036(5)	3.48(1)	1.895(5)
	0.45	1.69(1)	4.338(5)	3.44(1)	1.846(5)
	0.50	1.71(1)	4.65(1)	3.35(1)	1.774(5)
	0.55	1.76(1)	5.023(5)	3.29(1)	1.735(5)
	0.60	1.80(2)	5.422(5)	3.26(1)	1.680(5)
xPbO -(1-x)SiO_2	0.50	1.85(1)	5.649(5)	3.38(2)	1.901(5)
	0.55	1.92(1)	5.991(5)	3.26(1)	1.814(5)
	0.60	1.95(1)	6.392(5)	3.09(1)	1.704(5)

Elastic moduli calculated from the ultrasonic method and stress-optic coefficients and shear elasto-optic tensor elements determined from the Sénarmont compensator method are reproduced in Table 6.2. Barium borates and phosphates and lead phosphates show an increase in C_{11} and G as x increases; the opposite trend is seen in lead borates and silicates. As expected from the empirical model, barium and lead both decrease the stress-optic coefficients, while only lead induces negative stress-optic response.

Table 6.2: Elastic (ultrasonic) and photoelastic properties of lead and barium borates, phosphates and silicates

Family	x	C_{11} (Gpa)	G (Gpa)	C (B)	p_{44}
xBaO	0.20	76.7(3)	23.2(1)	4.02(15)	-0.0447(21)
-(1-x)B_2O_3	0.25	85.0(4)	25.5(2)	3.64(13)	-0.0453(21)
	0.30	94.8(4)	28.5(2)	2.38(21)	-0.032(3)
	0.35	100.1(4)	29.7(2)	1.90(17)	-0.0268(25)
xBaO	0.35	56.6(3)	17.1(1)	1.64(4)	-0.0150(7)
-(1-x)P_2O_5	0.40	67.5(3)	20.8(1)	1.54(4)	-0.0174(8)
	0.45	66.6(3)	19.8(1)	1.27(5)	-0.0129(7)
	0.50	67.0(3)	19.5(1)	0.96(6)	-0.0092(7)
	0.55	70.9(3)	20.1(1)	0.58(7)	-0.0056(7)
xPbO	0.35	86.1(3)	26.4(2)	2.20(5)	-0.0203(8)
-(1-x)B_2O_3	0.40	85.4(3)	26.2(2)	1.16(5)	-0.0100(6)
	0.45	84.7(3)	25.7(2)	0.71(2)	-0.0056(3)
	0.50	78.9(3)	23.7(2)	-0.02(2)	0.0001(1)
	0.55	76.2(3)	22.0(2)	-0.80(2)	0.0048(2)
	0.60	69.7(3)	19.9(2)	-1.52(4)	0.0070(4)
	0.65	65.0(3)	18.6(2)	-2.49(5)	0.0105(5)
xPbO	0.40	49.0(2)	14.5(1)	0.44(2)	-0.0041(3)
-(1-x)P_2O_5	0.45	51.2(2)	14.8(1)	0.03(1)	-0.0002(1)
	0.50	52.2(2)	14.6(1)	-0.48(5)	0.0029(3)
	0.55	54.4(3)	15.1(1)	-1.17(3)	0.0066(3)
	0.60	57.5(3)	15.3(1)	-2.38(4)	0.0128(1)
xPbO	0.50	64.6(3)	20.4(2)	-0.32(15)	0.002(1)
-(1-x)SiO_2	0.55	63.6(3)	19.7(2)	-1.83(33)	0.0098(18)
	0.60	61.1(3)	18.6(2)	-3.75(11)	0.0187(9)

6.2.2 Brillouin Results

The sound velocities, elastic moduli and elasto-optic tensor elements determined from Brillouin scattering spectra are compiled in Table 6.3. The values match well with those from the previous section. The values of the elasto-optic tensor elements p_{12} and p_{44} are shown in Table 6.3 as well as plotted versus mol % of additive in Figures 6.1, 6.2 and 6.3.

Table 6.3: Transverse and longitudinal sound velocities, elastic moduli and elasto-optic tensor elements (Brillouin scattering) for lead and barium borates, phosphates and silicates.

Family	x	v_L (km/s)	v_T (km/s)	C_{11} (Gpa)	G (Gpa)	p_{12}	p_{44}
xBaO -(1-x)B_2O_3	0.20	5.19(12)	2.84(9)	78(2)	23.3(8)	0.296(15)	-0.0459(80)
	0.25	5.30(11)	2.91(9)	87(2)	26.1(9)	0.279(15)	-0.0453(63)
	0.30	5.36(10)	2.93(8)	97(2)	29.0(9)	0.251(7)	-0.0376(63)
	0.35	5.32(9)	2.90(8)	102(2)	30.4(9)	0.251(4)	-0.0360(52)
xBaO -(1-x)P_2O_5	0.35	4.22(13)	2.31(11)	58(2)	17.4(9)	0.311(7)	-0.0134(9)
	0.40	4.50(6)	2.54(9)	68(1)	21.7(9)	0.307(4)	-0.0189(9)
	0.45	4.45(12)	2.44(10)	69(2)	20.8(9)	0.296(8)	-0.0141(11)
	0.50	4.32(11)	2.34(8)	68(2)	20.0(8)	0.285(8)	-0.0104(5)
	0.55	4.36(11)	2.34(8)	73(2)	21.1(8)	0.267(5)	-0.0080(3)
xPbO -(1-x)B_2O_3	0.35	4.37(9)	2.51(16)	88(2)	29(2)	0.211(13)	-0.0139(9)
	0.40	4.20(8)	2.29(3)	89(2)	26.4(4)	0.213(19)	-0.0109(11)
	0.45	4.00(8)	2.21(5)	85(2)	26.0(6)	0.196(19)	-0.0059(7)
	0.50	3.80(8)	1.94(25)	82(2)	21(3)	0.192(16)	0.0026(2)
	0.55	3.54(8)	1.92(2)	75(2)	22.2(3)	0.200(29)	0.0039(6)
	0.60	3.32(4)	1.82(5)	69(1)	20.8(6)	0.185(26)	0.0072(11)
	0.65	3.13(9)	1.71(7)	64(2)	19.0(9)	0.191(32)	0.0080(14)
xPbO -(1-x)P_2O_5	0.45	3.43(12)	1.94(11)	51(2)	16(1)	0.252(25)	-0.0053(7)
	0.50	3.38(6)	1.84(10)	53(1)	16(1)	0.245(19)	0.0017(5)
	0.55	3.34(11)	1.77(10)	56(2)	16(1)	0.215(18)	0.0057(5)
	0.60	3.27(5)	1.75(9)	58(1)	16.6(9)	0.220(21)	0.0078(10)
xPbO -(1-x)SiO_2	0.50	3.29(1)	1.90(17)	61(2)	20(2)	0.205(11)	0.0014(2)
	0.55	3.19(5)	1.79(6)	61(1)	19.2(7)	0.204(6)	0.0098(35)
	0.60	3.06(9)	1.72(7)	60(2)	18.9(8)	0.198(7)	0.0130(19)

There is good agreement between the values of p_{44} determined from stress-optic measurements and from Brillouin experiments; this is seen in Figure 6.1. The small inconsistencies likely come from difficulties in stressing the glass cubes homogeneously for stress-optic measurements. There is also a relationship between elasto-optic coefficient and molar % additive. This trend seems to be fairly linear, and does not strongly depend on glass former considered. Lead borates, phosphates and silicates have overlapping ranges, while there is some separation between the barium borates and phosphates. Also, lead-containing glasses have p_{44} that increases more rapidly with the addition of x than barium glasses. At $x = 0.30$, the value of p_{44} for the barium phosphates, is nearly equal to that of the lead borates. But, while the lead glasses transition from negative to positive p_{44} with increasing x, the elasto-optic coefficient of the barium glasses remains negative. This is consistent with the predictions of the empirical model of photoelasticity.

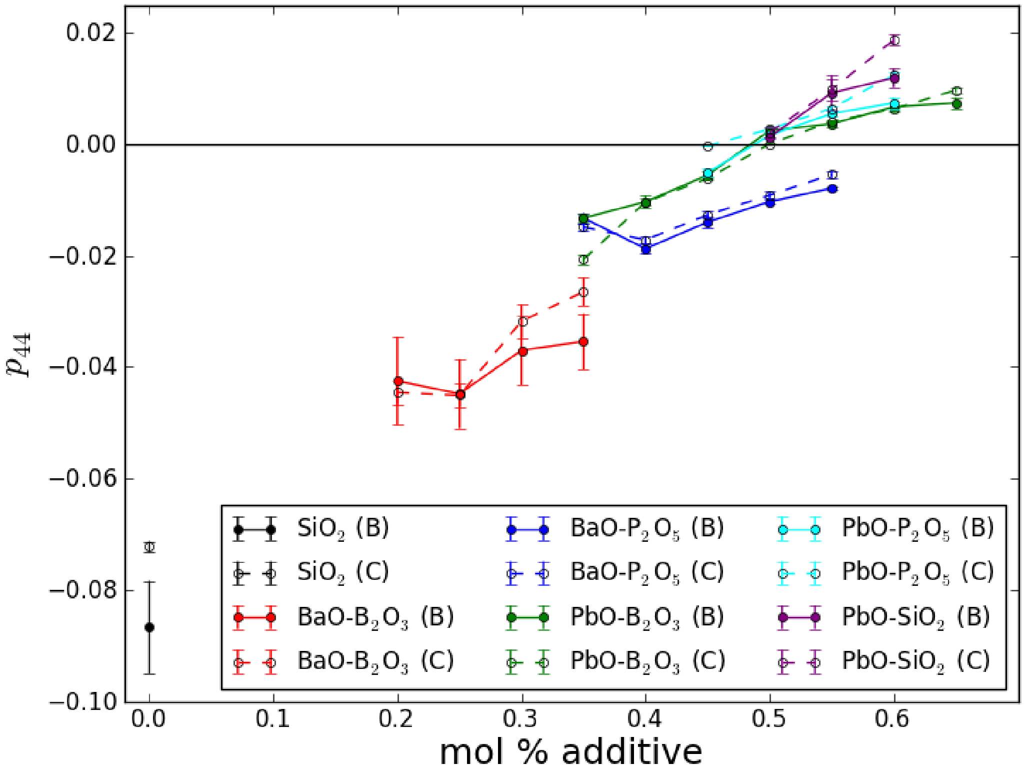

Figure 6.1: Elasto-optic coefficient p_{44} shown as a function of additive content. Values from Brillouin experiments (B) are given by solid lines and filled symbols, while those from stress-optic coefficients (C) are given by hollow symbols and dashed lines.

The values of p_{12}, seen in Figure 6.2, tend to decrease with increasing molar % of additive. This is opposite to the trend seen for p_{44}, and consistent with the results of previous experiments reproduced in Figure 2.5. Likewise, the values do seem to depend on both glass former and additive type. Barium phosphates have larger p_{12} than barium borates of the same additive content; the same is true of lead phosphates and lead borates. There also seems to be a difference in the elasto-optic constants between lead and barium phosphates with the same additive content x, as well as between lead and barium borates; typically, barium-containing glasses have larger p_{12}. Generally speaking, the values of p_{12} are between one and two orders of magnitude larger than those of p_{44}, and for all glasses measured, p_{12} remains positive.

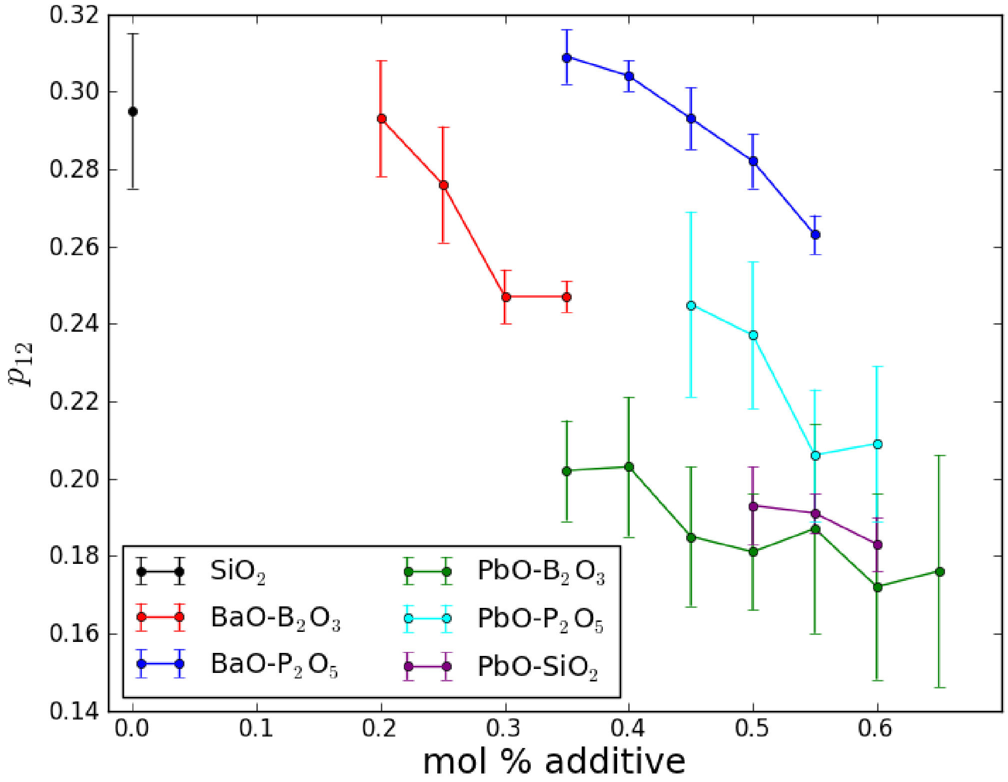

Figure 6.2: Elasto-optic coefficient p_{12} shown as a function of additive content.

The elasto-optic coefficient p_{11}, determined from the isotropy condition $p_{11} - p_{12} = 2p_{44}$, is plotted against additive content in Figure 6.3. The values of p_{11} do not seem to correlate with glass additive composition; its correlation coefficient is $R^2 \approx 0$. There are overlapping values for barium and lead borates with the same additive content, as well as for lead and barium silicates with the same x. The values for the phosphates are nominally larger than those for the borates, with the p_{11}s for lead silicates approximately equal to those of lead borates. Also, p_{11} is lower for pure silica than for the binary glass systems. If we consider the elasto-optic coefficients of the other pure glass formers seen in Figures 2.5 and 2.6, the p_{11} of B_2O_3 is about twice that of SiO_2 and GeO_2, which overlap. The magnitudes of p_{11} are of the same order as p_{12}, which is unsurprising for the small values of p_{44} measured.

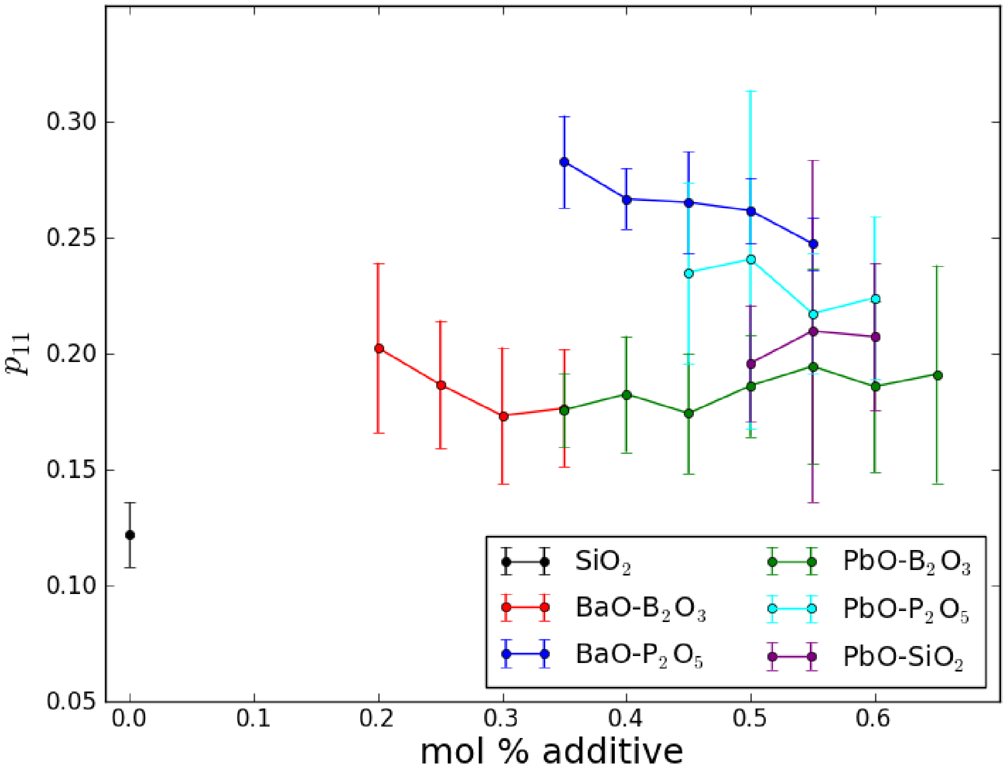

Figure 6.3: Elasto-optic coefficient p_{11} shown as a function of additive content. This value is not measured directly, but calculated from the experimental Brillouin and elasto-optic results using $p_{11} = p_{12} + 2p_{44}$.

6.2.3 Third Brillouin Peak

Typically, unpolarized Brillouin spectra of isotropic solids will have two peaks at frequencies corresponding to the transverse and longitudinal sound velocities within the material. Within the VH spectra of some of the glass samples, however, a third peak at higher frequencies became discernible for long scan times. An example for the glass with composition 40PbO-60B_2O_3 is seen in Figure 6.4, with the third peak highlighted in blue; the area of this peak per count is on the order of that of the transverse peak. The third peak was found in the VH spectra of lead borates, phosphates and silicates, while no convincing indication of this peak could be seen in barium phosphate or borate spectra. For the VV configuration, the peak was not visible, although scans were performed with less than 500 counts.

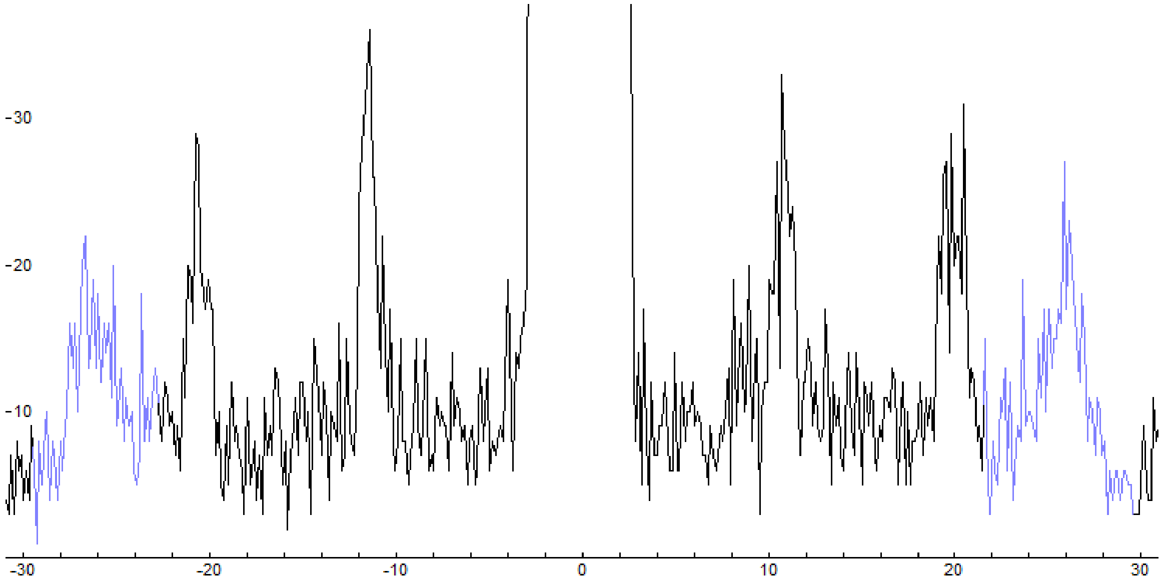

Figure 6.4: Brillouin spectra for 40PbO-60B_2O_3 glass taken over 3000 counts in VH polarization. The first peak at about ± 12 GHz is due to the transverse acoustic mode. The second peak at about ± 20 GHz is the bleedthrough of the longitudinal peak from the crossed polarizers; this accounts for less than 1 % of the longitudinal peak measured in VV configuration. A third, unexplained peak is visible between ± 20 and 30 GHz; it is highlighted in blue.

The Brillouin intensities per scan and frequency shifts of the third peak are plotted versus lead content in Figure 6.5. The intensity does not behave linearly with x, though it does tend to increase with additive with a possible local intensity maximum. It is important to remember that the intensity can vary slightly depending on how the sample is aligned, so these trends may be artificial. What is significant, however, is that the intensities of the third peak are all on the same order of magnitude. The frequency shift Δf of lead borates decreases with increasing lead content; the shifts of lead phosphates and lead silicates is fairly constant with x. Remembering that the sound velocities are related to their frequency shifts by $v = 2\pi\Delta f/q$, and that $q \propto n$, we can note that the velocities of the third wave from which the light is scattering, v_{3rd}, is larger than the transverse and longitudinal sound waves. Furthermore, this third wave shows the same trends as the other two sound velocities, with v_{3rd} greatly decreasing for lead borates and slightly decreasing for lead phosphates and silicates. Between glass samples, there is an approximately constant relationship, $v_L/v_{3rd} \approx 0.77$.

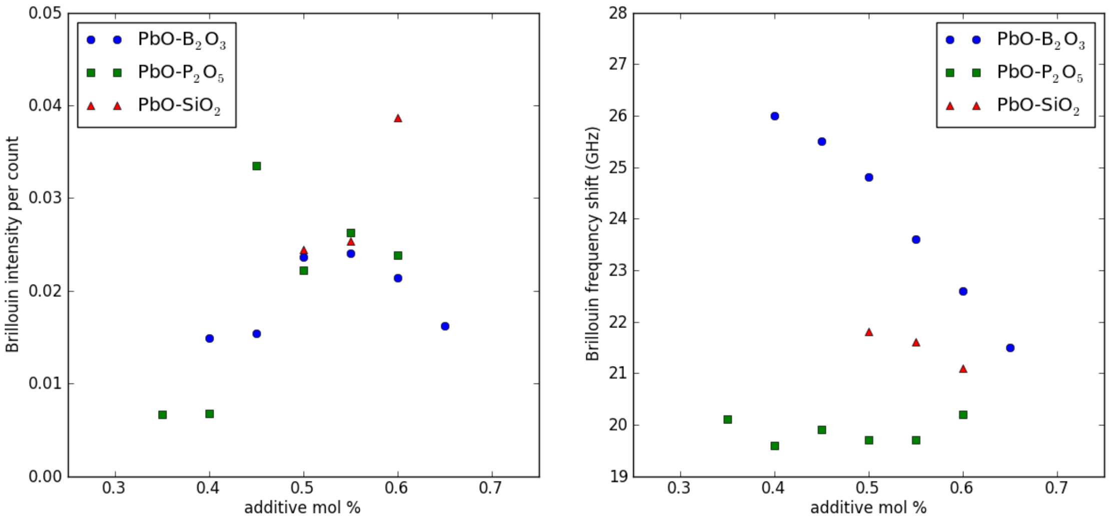

Figure 6.5: Measured normalized Brillouin intensities and frequency shifts of the third peak as a function of lead content.

We can conclude that the peak is not an artifact of the interferometer, since it is measurable in some glass compositions but not others. It is also not exclusive to one glass former or additive; the glass series xSnO-$(0.33 - x)$ZnO-0.67P_2O_5, which contains positive, negative and zero stress-optic glasses, also exhibits this peak. The frequency shift of the peak indicates that it is not due to back-scattering within the glass cube. Also, x-ray diffraction was performed on the two most lead-rich borate samples to exclude the possibility of scattering from a crystalline phase within the material; the glass samples were found to be fully amorphous.

6.3 Discussion

6.3.1 Elasto-Optic Coefficients and the Empirical Model

The empirical model of photoelasticity predicts that glasses will have positive stress-optic coefficient for compositions with $\langle d/N_c \rangle < 0.5$ Å and negative C with $\langle d/N_c \rangle > 0.5$ Å. Since $C = -n^3 p_{44}/(2G)$, this corresponds to the shear elasto-optic constant increasing with increasing $\langle d/N_c \rangle$, with values of $p_{44} = 0$ near $\langle d/N_c \rangle = 0.5$ Å.

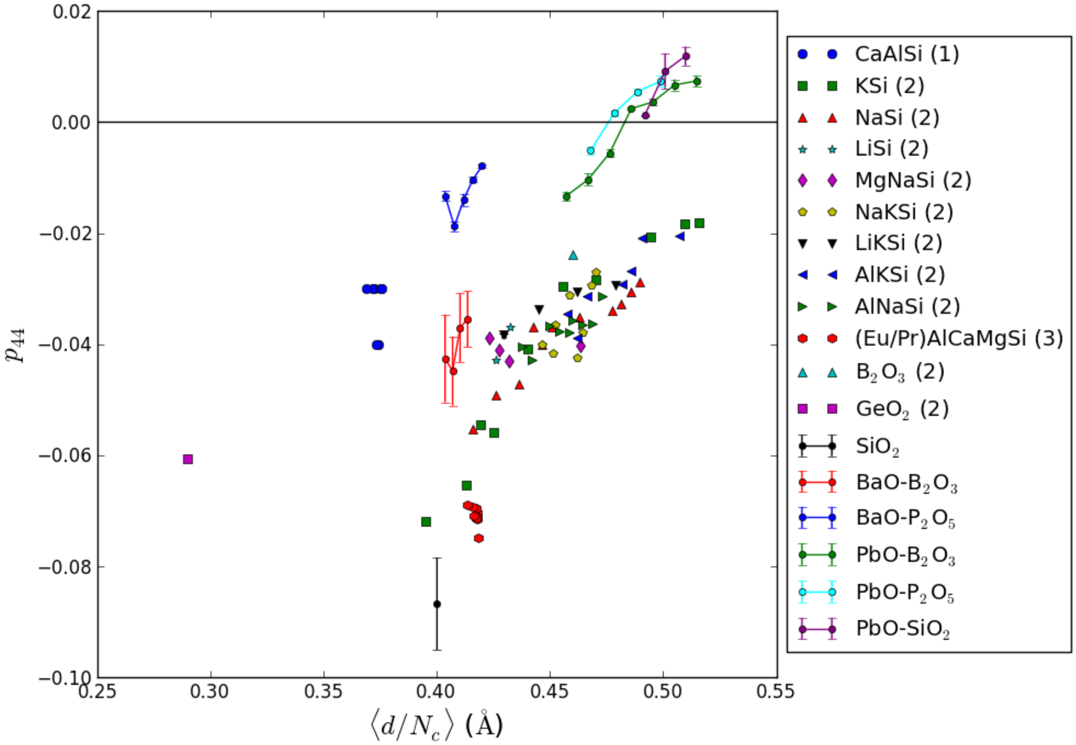

Figure 6.6: Elasto-optic coefficient p_{44} as a function of $\langle d/N_c \rangle$. The lead and barium borates, phosphates and silicates (plotted with lines connecting data points and error bars) were measured in this study. Glasses labelled (1) are from reference [66], (2) from [10], and (3) from [13].

Figure 6.6 shows the elasto-optic tensor element p_{44} plotted versus the $\langle d/N_c \rangle$ value for our lead and barium borate, phosphate and silicate glass systems and for previously measured glass systems with known compositions [10, 13, 66]. There is a correlation between p_{44} and $\langle d/N_c \rangle$ for the lead- and barium-based glasses, with an increasing trend as expected. The relationship is not perfectly linear, but it is neither predicted nor expected to be. The transition between negative and positive p_{44} occurs between 0.46 Å $\leq \langle d/N_c \rangle \leq 0.49$ Å, which is consistent with the empirical model for C.

There is more variation in the elasto-optic coefficient of previously measured glasses with $\langle d/N_c \rangle$. For glasses with $\langle d/N_c \rangle > 0.4$ Å, the elasto-optic coefficient increases with increasing ratio as one might expect when considering the empirical model. However, the rate of increase slows above $\langle d/N_c \rangle = 0.45$ Å. Zero-stress optic compositions are extrapolated for values of $\langle d/N_c \rangle > 0.5$ Å, which is larger than the empirical model predicts. It is likely in this case that the empirical model is overestimating the contribution of alkali oxides to the photoelastic response of a glass; all compositions with $\langle d/N_c \rangle > 0.45$ Å contain Na_2O, Li_2O, or K_2O.

Pure GeO_2 and the calcium aluminosilicates have similar values of p_{44} to the silicate, lead- and barium-based glasses, but have smaller $\langle d/N_c \rangle$ values. This decreased ratio could be due to an incorrect estimate of bond length and cation coordination. For example, GeO_2 is more likely to be 4-coordinated than 6-coordinated in its glass form [90]. The same might be true for Ca and Al in the calcium aluminosilicates. These glasses have < 20 mol % SiO_2, and the six-coordinated crystalline CaO and Al_2O_3 compounds used in the empirical model might have lower coordination in the glass structure.

It is also possible that the glass former type has a significant effect on p_{44} which is not currently described by the empirical model. In Figure 6.6, there appear be two regions of increasing p_{44}: the first region consisting of glass samples with primary glass former other than SiO_2, and the second region consisting of silicate glasses. Also, there is a difference in magnitude of p_{44} between barium phosphates and borates with the same $\langle d/N_c \rangle$ value. This too points to the importance of the glass former to the photoelastic response of a material. The lead-based glasses do not show the same variation in p_{44}, but this could be due to their overlapping near-zero values.

Interestingly, while typically C is larger for pure B_2O_3 than for binary borate systems, p_{44} of pure B_2O_3 is smaller in magnitude than the coefficients of barium borates. This is an effect of the much smaller shear elastic modulus of pure B_2O_3 relative to the mixed glasses.

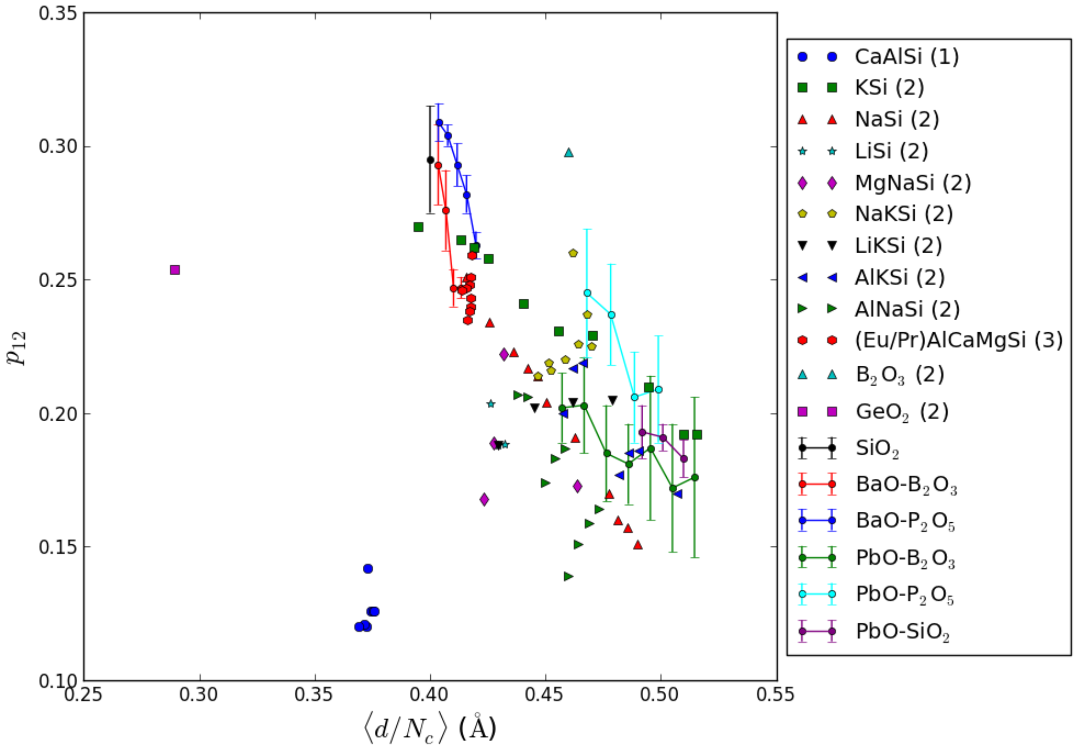

Figure 6.7: Elasto-optic coefficient p_{12} as a function of $\langle d/N_c \rangle$. The lead and barium borates, phosphates and silicates (plotted with lines connecting data points and error bars) were measured in this study. Glasses labelled (1) are from reference [66], (2) from [10], (3) from [13].

Figure 6.7 shows the elasto-optic coefficient p_{12} as a function of $\langle d/N_c \rangle$ for our barium and lead-based glasses and for the other previously measured glass systems [10, 13, 66]. The empirical model does not consider the individual contribution of p_{12}, so it is interesting to see that there does seem to be a correlation between this coefficient and $\langle d/N_c \rangle$. For all binary glass systems, p_{12} decreases almost linearly with increasing empirical ratio. However, the p_{12} of ternary systems deviate from this behaviour. Consider the Al_2O_3-Na_2O-SiO_2, Al_2O_3-K_2O-SiO_2 or Na_2O-K_2O-SiO_2 glasses. As the total amount of glass former decreases (and $\langle d/N_c \rangle$ increases), p_{12} also decreases. However, for constant amounts of glass former, as one additive is exchanged for another, the elasto-optic coefficient increases with decreasing $\langle d/N_c \rangle$. Still, this trend supports the idea that the d/N_c values for the alkali oxides (particularly K_2O) are currently overestimated in the empirical model.

Additionally, the values of p_{12} show a slight separation with glass former type. For example, in our binary glass systems, the barium phosphates have larger coefficients than barium borates with the same $\langle d/N_c \rangle$, and the same is true for lead phosphates and borates. The coefficients of pure GeO_2 and the calcium aluminosilicates are completely separate from those of borates, phosphates and silicates. As previously discussed, this could result from an underestimation of d/N_c for individual compounds, or it could be indicative of an aspect of the photoelastic response that is not considered by the empirical model.

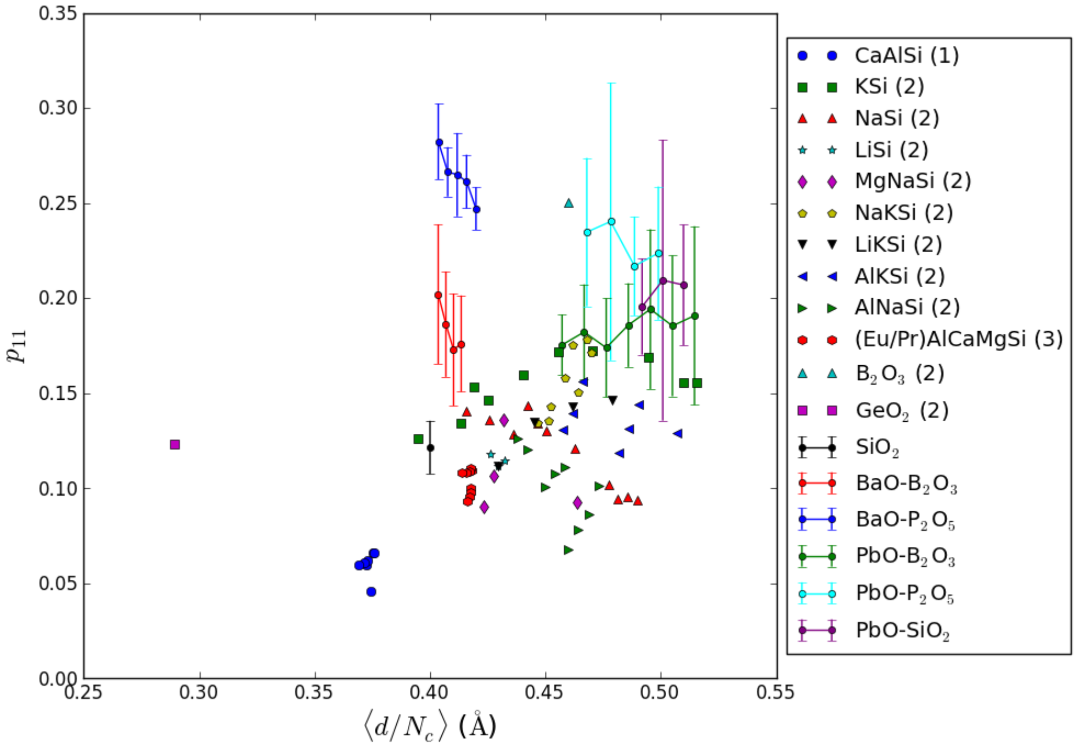

Figure 6.8: Elasto-optic coefficient p_{11} as a function of $\langle d/N_c \rangle$. The lead and barium borates, phosphates and silicates (plotted with lines connecting data points and error bars) were measured in this study. Glasses labelled (1) are from reference [66], (2) from [10], (3) from [13].

Figure 6.8 shows p_{11} as a function of $\langle d/N_c \rangle$ for our lead- and barium-based glasses, as well as for the previously measured glass systems [10, 13, 66]. There does not seem to be a definitive relationship between the two values. Some series have increasing trends between coefficient and ratio, others have decreasing, and some have fairly constant p_{11} across the glass system. Since the two independent elasto-optic coefficients p_{12} and p_{44} for these glass families do seem to show some dependence on $\langle d/N_c \rangle$, it is possible for the third, dependent coefficient $p_{11} = p_{12} + 2p_{44}$ to be uncorrelated with the empirical model.

The magnitudes of p_{11} seem to depend on the type of glass former and additive. Phosphates have the largest coefficients, followed by borates, silicates, GeO_2, and finally the calcium aluminosilicates. Likewise, glasses modified by barium oxide have the largest coefficients, followed by lead oxide, potassium oxide, and sodium and lithium oxides.

6.3.2 Comparison to Other Theories of Photoelasticity

While the theories of photoelasticity developed by Mueller, Carleton, Mazzacurati, Benassi, Harrison and Lines are all derived from varying models and theories (Lorentz-Lorenz, lattice and atomic strains, DID effects, bond-orbital energies) they all have one material property in common: the refractive index. While none of these theories shows universal correlation between prediction and experiment, and some also incorporate dependence on other material properties, it is still of interest to examine how p_{ij} depend on n.

Figure 6.9 shows p_{44} plotted as a function of n for our lead and barium borates, phosphates and silicates and for previously measured glass series [10, 13, 66]. Generally, as refractive index increases, the elasto-optic coefficient also increases. This is consistent with previous results, as additives which induce zero and negative stress-optic response (for example, PbO and SnO) also tend to increase the refractive index of a glass more than positive additives [42, 43, 53]. For lead borates, phosphates and silicates, the transition from positive to negative stress-optic response occurs in the range $1.7 \leq n \leq 1.9$, with exact value dependent on glass former.

For a given glass former, there does seem to be a fairly linear relationship between p_{44} and n regardless of modifier type. However, there are still slight separation of the coefficients with n depending on glass former. For example, barium borates have p_{44} with larger magnitude than the barium phosphates with the same refractive index. The $(Eu/Pr)_2O_3$-doped magnesium calcium aluminosilicate glasses also have larger

p_{44} than other silicates with similar refractive indices. Still, even with these minor deviations, the results do reinforce the idea that refractive index is an important descriptor of the photoelastic response of a glass.

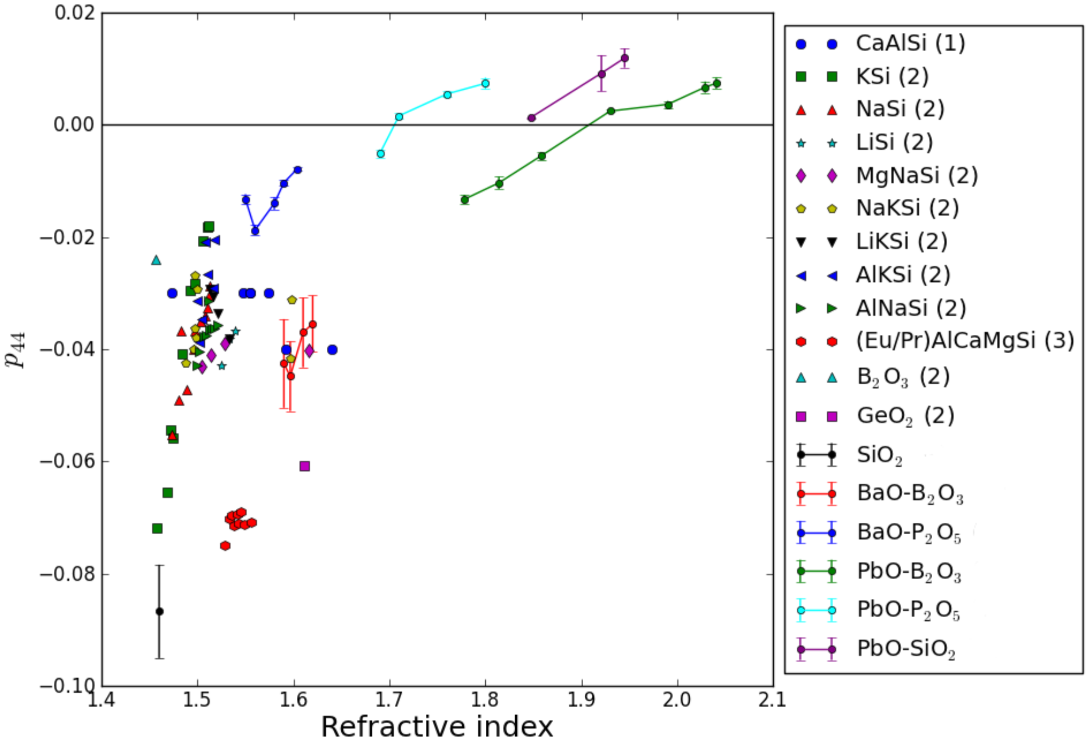

Figure 6.9: Elasto-optic coefficient p_{44} as a function of refractive index. The lead and barium borates, phosphates and silicates (plotted with lines connecting data points and error bars) were measured in this study. Glasses labelled (1) are from reference [66], (2) from [10], (3) from [13].

The relationship between p_{12} and n for our glass systems and previously measured glass systems [10, 13, 66] is shown in Figure 6.10. Generally, as n increases, the elasto-optic coefficient p_{12} decreases. However, the majority of the data falls into two categories: glass families with negative stress-optic additives and glasses with positive stress-optic additives. The former category follows a linear trend with p_{12} decreasing slowly with n, while the latter has a more rapidly decreasing linear trend between p_{12} and n.. Within these categories, there is little variation of p_{12} with additive type. The pure glass formers SiO_2 and B_2O_3 are at the apex of these lines, while GeO_2 has similar coefficient and refractive index as the negative additives. The dependency between elasto-optic coefficient and n would seem to suggest that p_{12} can be accounted for by a combination of the refractive index of the glass and the type of additives present in the composition.

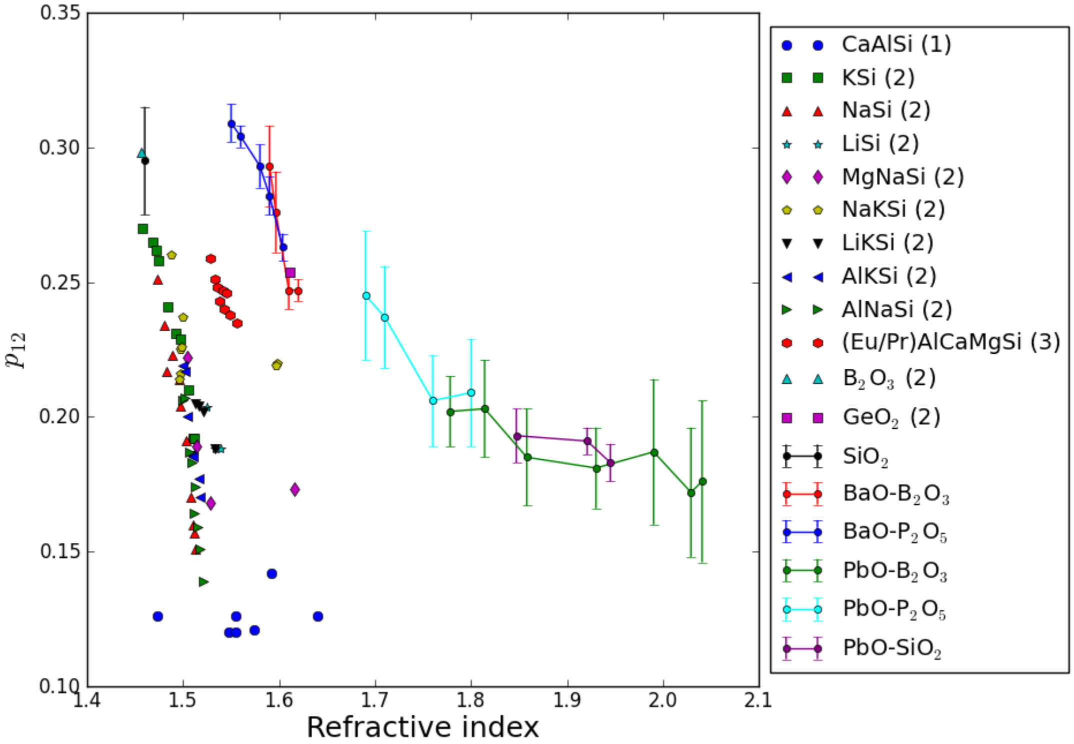

Figure 6.10: Elasto-optic coefficient p_{12} as a function of refractive index. The lead and barium borates, phosphates and silicates (plotted with lines connecting data points and error bars) were measured in this study. Glasses labelled (1) are from reference [66], (2) from [10], (3) from [13].

The values of p_{11} for the lead- and barium-based glasses and the previously measured glass series [10, 13, 66] are plotted in Figure 6.11 as a function of n. The elasto-optic values do not seem to strongly depend on refractive index, just as they did not depend on additive mol % or $\langle d/N_c \rangle$. However, as with p_{12}, there seem to be two regions of values for p_{11}. The first, with glass compositions containing negative modifiers, has $0.18 \lesssim p_{11} \lesssim 0.28$. The second region, composed of glass series with positive modifiers, has $0.05 \lesssim p_{11} \lesssim 0.18$. Typically, the positively modified glasses have $n < 1.6$, while negatively modified glasses have $n > 1.6$.

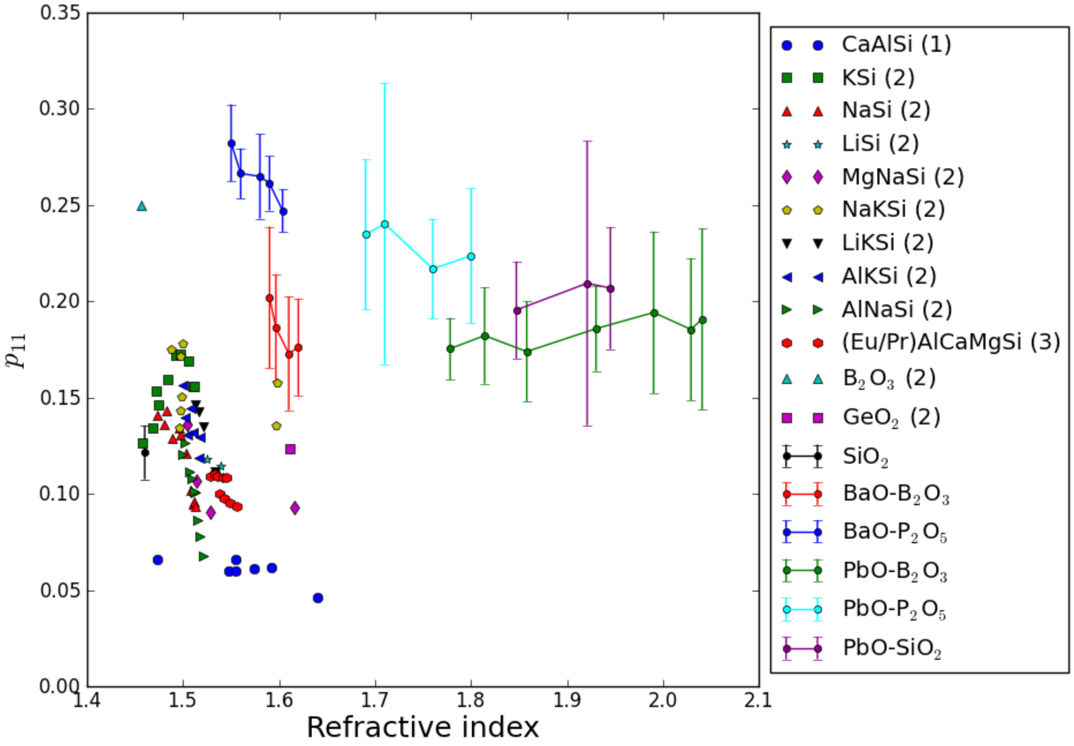

Figure 6.11: Elasto-optic coefficient p_{11} as a function of refractive index. The lead and barium borates, phosphates and silicates (plotted with lines connecting data points and error bars) were measured in this study. Glasses labelled (1) are from reference [66], (2) from [10], (3) from [13].

6.3.3 Appearance of the Third Brillouin Peak

The appearance of a third peak at larger frequencies in the Brillouin spectra of lead-containing glass samples is unexpected. Typical glass spectra contain peaks located only at frequencies corresponding to the velocities of longitudinal and transverse sound waves in the material. No other studies on the Brillouin scattering of glasses report the presence of a third peak in the VH/HV configuration.

The origin of this peak is ambiguous. It could be due to the scattering from higher order acoustic modes in the glass. It could also be indicative of a small amount of phase separation in the glass samples. This could be experimentally verified through small angle x-ray diffraction. There has been some evidence of Brillouin scattering from excitonic polaritons (coupled states of the light and excitations) in semiconductors, resulting in asymmetry and extra peaks in the Brillouin spectra [91–94]. Polaritons are most likely to occur for photon energies near to exciton absorption energies, and the coupling must occur at the surface of the material [91]. While these excitonic interactions are unlikely for pure glass surfaces, they could occur if small amounts of nanocrystals or microcrystals are present on the glass surface. It is interesting to note that the glasses with spectra exhibiting this peak all have large refractive indices relative to the pure glass formers and barium-based glasses.

6.4 Summary

The elasto-optic tensor elements p_{12} and p_{44} were measured using Brillouin spectroscopy for binary lead and barium borates, phosphates and silicates. The third element p_{11} was determined from the dependency $2p_{44} = p_{11} - p_{12}$. Generally, as the amount of modifier is increased in a binary glass system, p_{44} increases and p_{12} decreases. There was no compositional dependence for p_{11}.

The shear elasto-optic tensor element can be extracted from the stress-optic coefficient of a glass. As expected, values of p_{44} from taken from the stress-induced birefringence matched those determined through Brillouin scattering.

Just as the stress-optic coefficient C decreases with increasing empirical value $\langle d/N_c \rangle$, the shear elasto-optic coefficient p_{44} increases with increasing $\langle d/N_c \rangle$. This is expected from the relationship $C = -n^3 p_{44}/(2G)$. Interestingly , the tensor element p_{12} also seems to be described by the empirical model. For both p_{12} and p_{44}, there is some separation of values depending on the glass former and additive of the binary series. The element p_{11} is uncorrelated with $\langle d/N_c \rangle$.

The refractive index is also related to the photoelastic response of a glass: for binary glass series, as n increases, p_{44} increases and p_{12} decreases. The values of p_{12} and p_{44} are similarly separated depending on the different glass formers and modifiers present, and p_{11} again shows no correlated with refractive index.

The three elasto-optic tensor elements will be discussed further in Chapter 7.

Chapter 7

Discussion

7.1 Polarizability Model for Anions and Cations

The empirical model of photoelasticity has been very successful in predicting the sign of the stress-optic response and new zero-stress optic compositions, but it is unable to determine the magnitude of C. This is likely due to the structural differences in the individual glass former and modifier units between crystalline and glassy states. Indeed, predictions based on the compounds' d/N_c values are constantly improved when the glass structure is taken into account. Still, it would be valuable to develop a model of photoelasticity that is able to predict not only sign but also magnitude of the stress-optic response.

A model of photoelasticity similar to Mueller's was proposed by Weyl, focusing on the electrostatic interactions between anions and cations in the glass network rather than lattice or atomic effects [95]. The properties that are related to induced birefringence in the model are the electric density distribution and the polarizability of the ions, including both anions and cations. Polarizability has been used as a building block in many other photoelastic theories to relate individual elasto-optic tensor elements p_{ij} to material properties such as refractive index, bond lengths and optical deformabilities.

Weyl's model was developed for materials placed under tensile stress but can easily be adapted for compressive stress. According to the model, there will be three contributions to the photoelastic response for a compressive stress. First, the distance between anion and cation will decrease along the stress axis. This would result in an increased n_e, and thus positive contribution to C. Second, the electron cloud of oxygen will elongate in the direction of the stress, *i.e.* towards the closest cations. This also results in increased n_e, and positive C. Third, if the cation is polarizable, then its electrons will be repelled in the plane perpendicular to the applied stress. This would increase n_o and contribute negatively to C. The overall contribution to

C, then, would depend on the relative polarizabilities between oxygen (or anion) and the cation in the glass.

The model of photoelasticity proposed by Weyl is qualitative rather than quantitative. The principles described above correlated with the experimental results of Tashiro [34]. It was determined that the stress-optic coefficient decreased as "more polarizable" modifiers were added to a glass. However, the exact value of polarizability for each compound was not specified. It is worthwhile, then, to determine whether the magnitude of C can be related to the polarizability of a material.

The total polarizability α of a compound is defined in Section 2.2. It is related to the density, molar mass and refractive index of an isotropic material through the Clausius-Mossotti or Lorentz-Lorenz equation:

$$\alpha = \frac{3M}{4\pi N\rho}\frac{n^2-1}{n^2+2}. \tag{7.1}$$

Polarizability is an additive property; for a compound M_xO_y, the total polarizability is

$$\alpha = x\alpha_M + y\alpha_O, \tag{7.2}$$

where α_M is the polarizability of the cation and α_O is the polarizability of oxygen in the context of that compound. Dimitrov et al. assumed that cation polarizabilities are equal to the free ion polarizabilities, and used Equation 7.2 to estimate the oxide polarizabilities from the total polarizability of various compounds [96]. They found that the polarizability of oxygen varies from compound to compound.

In his doctoral dissertation, Martin defined a polarizability parameter,

$$\xi = \frac{x\alpha_M}{y\alpha_O}, \tag{7.3}$$

and related it to the stress-optic response of a glass [97]. He determined that as the value of ξ increased for different glass compositions, their stress-optic coefficient (or contribution to C) decreased, which is consistent with Weyl's model of photoelasticity. Martin characterized the total contribution of polarizability to the stress-optic response as $\sum_i x_i(e^{\xi})_i$, where x_i is the mol % of the ith compound in the glass composition, but found that e^{ξ} was not a better predictor of zero-stress optic compositions than $\langle d/N_c\rangle$.

However, polarizability is an additive property. Therefore it is more applicable to use an additive approach to determine the effect of polarizability on the stress-optic coefficient. For each compound, we will consider the relative polarizabilities between the anion and cation. Then, for a compound M_xO_y, the relative or normalized polarizability is

$$\alpha_n = \frac{x\alpha_M + y\alpha_O}{x+y} = \frac{\alpha}{x+y}. \tag{7.4}$$

The normalized polarizability α_n should be descriptive of the interation between anion and cation as their electron clouds are deformed under stress. Then, according to the principles of Weyl's polarizability model, the value α_n for a compound will give information on its contribution to the stress-optic coefficient of a glass.

The total polarizabilities of all glass formers and additives used in this study were determined using Equation 7.1 with the experimentally measured densities and long-wavelength refractive indices. Since n is an additive property, the refractive indices of individual compounds are estimated from the values for binary glass series measured in this report; density is similarly determined for the glass formers and additives. For glass systems considered in the literature with compounds not included in this study, α is taken from the literature [96, 98, 99]. Cation polarizabilities α_M were estimated to be equal to the free ion polarizabilities according to [96], and the anion polarizabilities were determined using Equation 7.2. The oxide polarizabilities were compared to the results of Dimitrov; our experimentally determined values for BaO, ZnO, PbO, Bi_2O_3 are all up to 1 Å^3 lower.

While the normalized bond polarizability α_n can be decomposed into the individual ionic polarizabilities α_M and α_O for each compound, these polarizabilities are not considered individually in the model. In fact, it is unlikely that α_M is a true representation of the cation polarizability, since it is estimated from the free ion value. While it is interesting to see the general evolution of α_O and α_M between glass compounds, only α_n (determined from experimental results) is needed to correlated polarizability with photoelasticity.

Table 7.1 shows the empirical parameter d/N_c and the oxide, cation and normalized polarizabilities for all oxide compounds considered in this thesis. The table is sorted by decreasing values of α_n. Note that the values d and N_c are determined from the crystal structure of compounds, and can often vary in the glass structure.

For example, the cation coordination of the alkali oxides typically increases to 6-8 in a glass. The polarizability α_n, on the other hand, is determined from experimental refractive indices and densities of glasses. As such, the polarizability of a compound is not expected to vary significantly depending on glass composition.

It is important to note that while the model is developed for the deformation of electron densities of anions and cations, it is not exclusive to ionic materials. In an SiO_2 glass, for example, the discussion is analagous to the deformation of electrons around silicon (cation) cores and oxygen (anion) cores under uniaxial stress. It is the polarizability of bonds between the so-called "anion" and "cation" in a glass which defines its photoelastic response.

Table 7.1: Empirical bonding and polarizability models for oxides. Values labelled (*a*) are from [96], (*b*) from [98], (*c*) from [99], and (*d*) from [100].

Compound	d (Å)	N_c	d/N_c (Å)	α_O (Å^3)	α_M (Å^3)	α_n (Å^3)
PbO	2.326	4	0.58	2.4	3.623	3.01
SnO	2.219	4	0.55	3.4	2.587	2.99
Bi_2O_3	1.918	4	0.48	2.6	1.508	2.46
$Sb_2O_3{}^{(a)}$	1.977	3	0.66	3.2	1.111	2.35
TeO_2	2.00	4	0.50	2.0	1.595	2.40
BaO	2.74	6	0.46	2.6	1.595	2.10
$K_2O^{(b)}$	2.787	4	0.70	2.3	1.98	2.09
$Pr_2O_3{}^{(c)}$	2.67	7	0.38	*	*	2.00
$SrO^{(a)}$	2.581	6	0.43	2.9	0.861	1.89
$Eu_2O_3{}^{(c)}$	2.3	7	0.33	*	*	1.80
$SnO_2{}^{(d)}$	2.055	6	0.34	1.15	2.587	1.63
Na_2O	2.403	4	0.60	2.3	1.14	1.53
CaO	2.408	6	0.40	2.3	0.469	1.38
P_2O_5	1.55	4	0.39	1.7	0.021	1.22
ZnO	1.98	4	0.50	1.8	0.283	1.04
SiO_2	1.58	4	0.40	1.4	0.033	0.94
$MgO^{(a)}$	2.108	6	0.35	1.7	0.094	0.90
$Al_2O_3{}^{(a)}$	1.852	6	0.31	1.46	0.054	0.90
B_2O_3	1.366	3 or 4	0.46 or 0.34	1.3	0.002	0.78
Li_2O	1.996	4	0.50	2.0	0.024	0.68

7.1.1 The Polarizability Model in Oxides

The stress-optic and elasto-optic coefficients of all oxide glasses measured by ellipsometry were determined away from the absorption edge, at λ_0 + 250 nm. For all glass samples, the empirical parameters

$$\left\langle \frac{d}{N_c} \right\rangle = \sum_i x_i \left(\frac{d}{N_c} \right)_i \tag{7.5}$$

and

$$\langle \alpha \rangle = \sum_i x_i (\alpha_n)_i \tag{7.6}$$

were determined from the individual compound values in Table 7.1 weighted by the mol % x_i of each component. For borates, a coordination number of $N_c = 3.5$ was used to estimate the value of d/N_c for B_2O_3; this is closer to the bonding environment of boron in glass [42].

Figure 7.1 shows the stress-optic coefficient plotted as a function of both $\langle d/N_c \rangle$ (left) and $\langle \alpha \rangle$ (right). The value $\langle d/N_c \rangle$ does a good job of predicting zero and negative stress-optic coefficients; however, it does not describe the stress-optic response of glasses with positive additives. The correlation between stress-optic coefficient and polarizability is much better for all compositions. There seems to be a strong linear trend between C and $\langle \alpha \rangle$. The fluctuations of positive phosphate and borate compositions from this trend are likely due to differences between actual and nominal compositions ($\langle \alpha \rangle$), and non-homogeneously stressed glasses (C). From these results, the stress-optic coefficient can be estimated from $C \approx -5\langle \alpha \rangle + 10$; zero-stress optic compositions are predicted when $\langle \alpha \rangle \approx 2$ Å^3.

Figure 7.2 shows literature values of the stress-optic coefficient as a function of $\langle d/N_c \rangle$ (left) and $\langle \alpha \rangle$ (right). For the majority of glass samples, predictions of the stress-optic coefficient are improved using $\langle \alpha \rangle$ rather than $\langle d/N_c \rangle$. However, the polarizability model does not provide a good correlation with C for all of the alkali borates. These values are shown in Figure 7.2; their polarizabilities are all below 1.0 Å^3. This could be due to a low estimate of the polarizability of pure B_2O_3; however, this is unlikely due to the overlap of zero-stress optic borates, phosphates and silicates. It is more likely that the polarizabilities of lithium, sodium and potassium oxide (see Table 7.1) are over- or underestimated. Also, the antimony borates have zero-stress

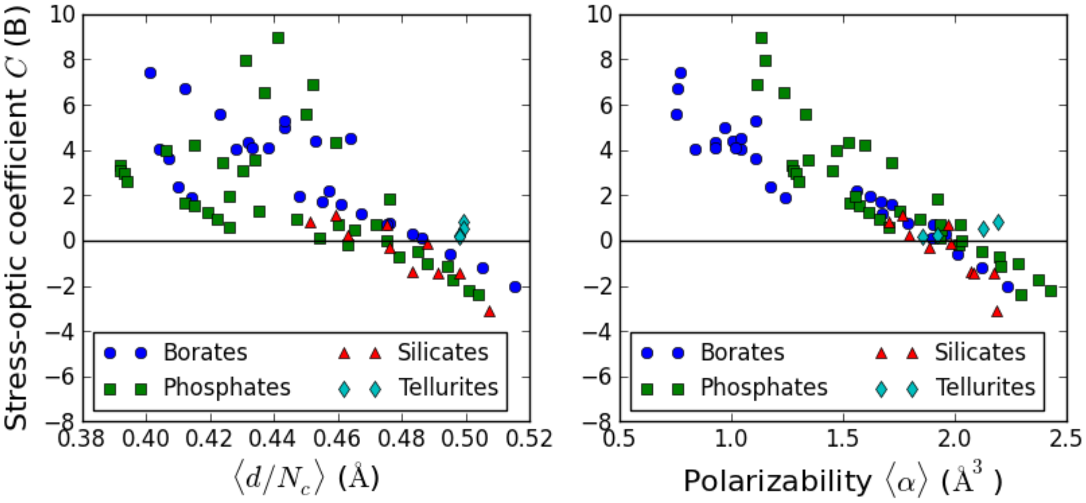

Figure 7.1: Stress-optic coefficient as a function of $\langle d/N_c \rangle$ (left) and polarizability $\langle \alpha \rangle$ (right).

optic coefficient at much lower polarizability than all other glass systems. Again, this could be due to a low estimate of the polarizability of Sb_2O_3. The values of the polarizabilities could be confirmed through calculations of the refractive index of pure glass additives, or by extrapolating the values of n and ρ from the measurements of many binary glasses.

Figure 7.3 shows the elasto-optic coefficient p_{44} (determined from C, G and n) plotted as a function of both $\langle d/N_c \rangle$ (left) and $\langle \alpha \rangle$ (right). Again, the parameter $\langle d/N_c \rangle$ correlates well with zero and positive values of p_{44}, but varies greatly for negative values of p_{44}. On the other hand, the polarizability parameter $\langle \alpha \rangle$ shows a strong correlation with the elasto-optic coefficient.

The reasoning behind the applicability of d/N_c to the stress-optic response of a glass is very similar to that of the polarizability. However, the bond lengths and coordinations are estimated from crystalline materials; for many compounds, including B_2O_3, ZnO, and GeO_2, this is not representative of the bonding environment of the cation in a glass. The polarizability model likely succeeds where d/N_c fails for a number of reasons. First, the total polarizability of the ions were calculated directly from the binary glass systems. Second, birefringence in a uniaxially stressed glass stems from changes in the ordinary and extraordinary refractive indices of

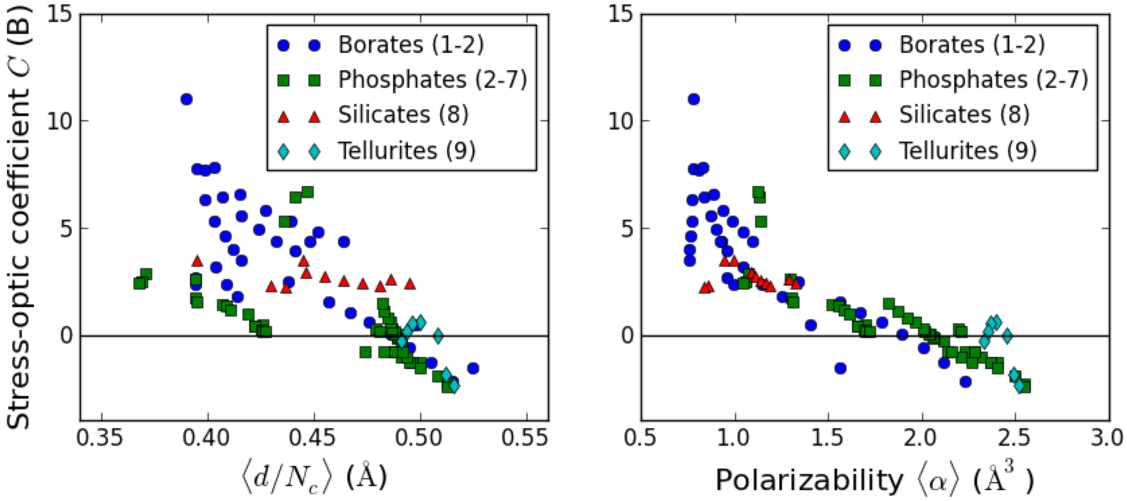

Figure 7.2: Stress-optic coefficient of glasses from the literature as a function of $\langle d/N_c \rangle$ (left) and polarizability $\langle \alpha \rangle$ (right). Label (1) is from [36], (2) from [1], (3) from [37], (4) from [53], (5) from [54], (6) from [43], (7) from [44], (8) from [38], and (9) from [41].

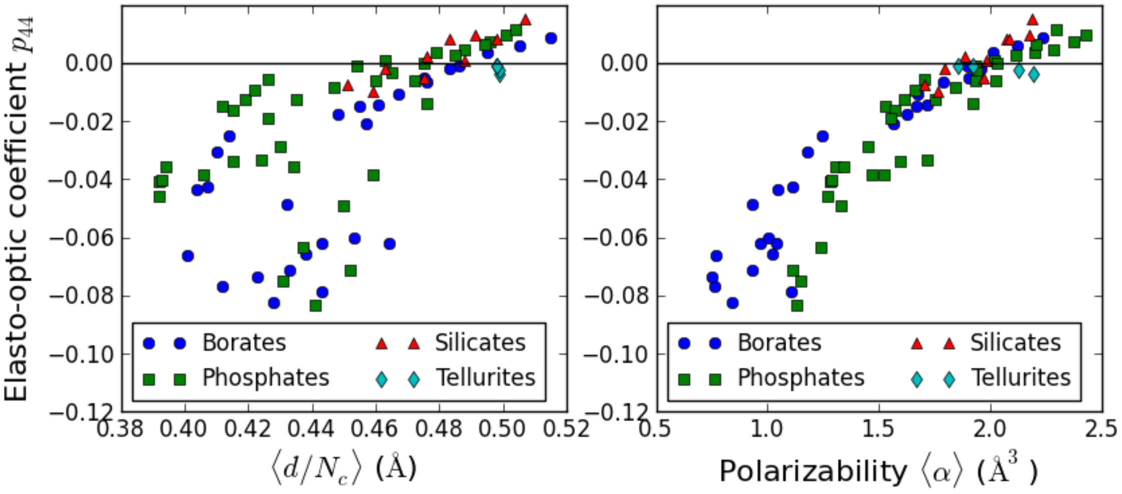

Figure 7.3: Elasto-optic coefficient p_{44} as a function of $\langle d/N_c \rangle$ (left) and polarizability $\langle \alpha \rangle$ (right).

the glass. The refractive index of a glass can be related to the bulk polarizability (Section 3.1.6), and so it is reasonable that differences in α_n could result in different stress-optic responses. Indeed, many theories of photoelasticity were derived using the Lorentz-Lorenz relationship (refer to Section 2.2).

7.1.2 The Polarizability Model in Sulfides

The polarizability model can also be applied to sulfide glasses. Table 7.2 shows the empirical parameter d/N_c as well as the oxide, cation and normalized polarizabilities for the sulfide compounds considered in this thesis. The two parameters are compared in Figure 7.4, where the stress-optic coefficients of stoichiometric Ge-P-S and Ge-Sb-S are plotted as a function of $\langle d/N_c \rangle$ (left) and $\langle \alpha \rangle$ (right). The empirical model of bonding shows the same trend between the two glass series (C decreasing as $\langle d/N_c \rangle$ increases), but has a different value of $\langle d/N_c \rangle$ for zero-stress optic glasses in the two series. Also, without structural information, the model underestimates the contribution of P_2S_5 as discussed in Section 4.3.1. The polarizability model, on the other hand, shows overlapping values for the two glass series. In fact, the Ge-P-S and Ge-Sb-S glasses with $C \approx -2.5$ B also both have the same $\langle \alpha \rangle$. The estimation of $\langle \alpha \rangle$ for the zero-stress optic coefficient ($\langle \alpha \rangle \approx 3.4$ Å^3) is consistent between the glass series; however, it is larger than the parameter predicting zero-stress optic oxide glasses. In this case, the empirical model (with dZ/N_c) does a better job at explaining the increased parameter.

Table 7.2: Empirical bond length/coordination and polarizability models for sulfides

Compound	d (AA)	N_c	d/N_c (Å)	α_S (Å^3)	α_c (Å^3)	α_n (Å^3)
GeS_2	2.20	4	0.55	4.40	0.137	2.81
P_2S_5	2.10	3 or 4	0.70 or 0.53	5.85	0.021	4.18
Sb_2S_3	2.54	3	0.89	6.657	1.111	4.44
S	*	*	*	0.63	0.000	0.63

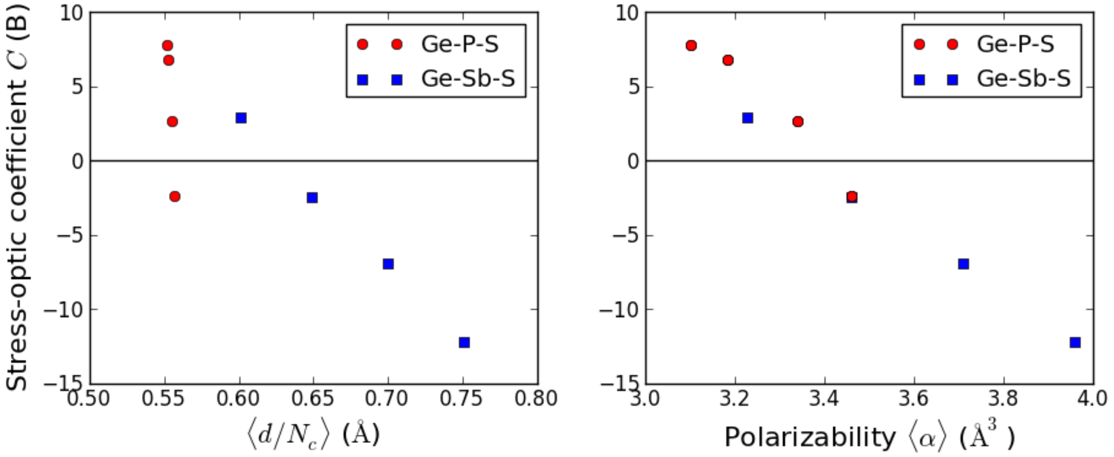

Figure 7.4: Stress optic coefficient of Ge-P-S and Ge-Sb-S glasses as a function of $\langle d/N_c \rangle$ (left) and polarizability $\langle \alpha \rangle$ (right).

7.2 Wavelength Dependence of the Stress-Optic Coefficient

7.2.1 Wavelength-Dependent Polarizabilities

To this point, the polarizabilities of compounds have been calculated using the long-wavelength refractive indices. However, the refractive index of a glass is dependent on the wavelength of incident light. It is expected, then, that the polarizability is also wavelength-dependent:

$$\alpha_\lambda = \frac{3M}{4\pi N\rho}\frac{n_\lambda^2 - 1}{n_\lambda^2 + 2}. \tag{7.7}$$

It is of interest to compute the wavelength-dependent polarizabilities for glass systems exhibiting positive and negative dispersion.

It is difficult to accurately determine the wavelength-dependent refractive index for all glass formers and additives. The estimation of n depends on two factors: first, that the refractive index is an additive property consistently from pure glass former to pure glass modifier. Second, the experimental values of n for binary glass systems are determined using a Cauchy fit of ellipsometric Ψ data. The collected Ψ values can be influenced by the surface roughness of the sample, and the alignment of the reflecting face with the light source and detector. This can result in an enhancement or reduction of n as λ approaches the absorption edge.

The glass series considered here are the positively dispersive barium borates and negatively dispersive lead borates. These glasses were cut to have very parallel sides and polished to 1 μm for Brillouin scattering measurements. Unlike the barium and lead phosphates, the borates are not strongly hygroscopic. As such, their reflection spectra are the most likely to be unaffected by alignment and surface roughness.

For the lead and barium borates, the polarizability is negatively correlated with wavelength: in the near-IR range, $\langle \alpha_\lambda \rangle$ is fairly constant with wavelength, and as λ decreases toward the absorption edge, $\langle \alpha_\lambda \rangle$ increases. Here, $\langle \alpha_\lambda \rangle = \sum_i x_i (\alpha_{n\lambda})_i$ as before, calculated for all wavelengths. The increase is more rapid in the lead borates. The relationship between stress-optic coefficient and wavelength-dependent polarizability for lead borates is shown in Figure 7.5. For all glass samples, C decreases as $\langle \alpha_\lambda \rangle$ increases. This trend is consistent with the polarizability model described in Section 7.1. The decrease in stress-optic coefficient is fairly continuous with $\langle \alpha_\lambda \rangle$ across many lead oxide contents, with a small amount of separation in C at the endpoints of the series. This separation could be the result of over- or under-estimated values of C due to an inhomogeneous application of stress to the glass. Or, more likely, it could be indicative of other properties contributing to the stress-optic response of a glass that are not fully described by the parameter α_n.

Figure 7.6 shows the stress-optic coefficients of barium borate glasses as a function of polarizability. For a given glass sample, the stress-optic coefficient increases as the wavelength-dependent polarizability increases, which is contrary to the polarizability model described in Section 7.1. This trend further suggests that the dispersion of the stress-optic coefficient is not entirely described by the polarizability $\langle \alpha_\lambda \rangle$. Still, between the glass samples, the average stress-optic coefficient does decrease as the average sample polarizability increases, which is consisted with the polarizability model.

It is clear from the results of the lead and barium borates that the stress-optic coefficient depends on wavelength in a way that is not fully described by the polarizability of a glass sample. To address the dependency of C on λ, we return to the pseudo-Cauchy fit described in Section 5.3.4.

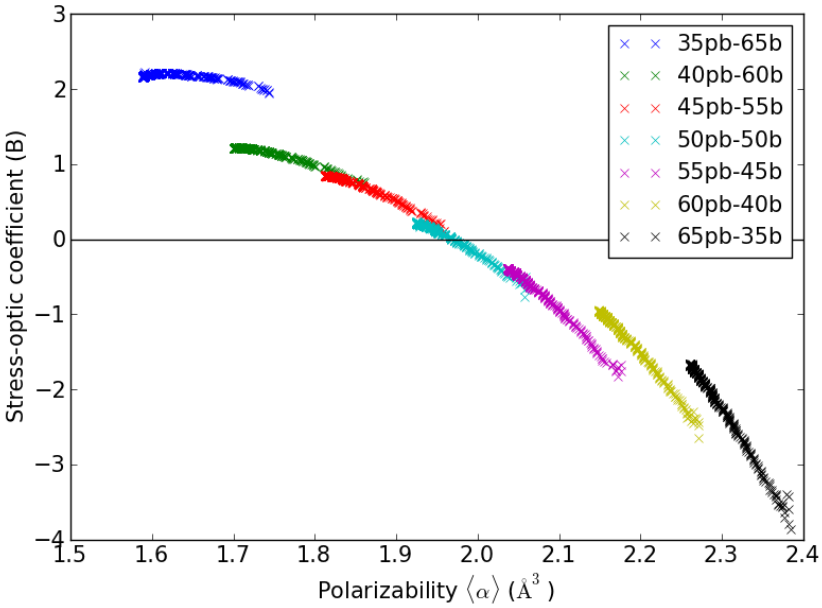

Figure 7.5: Stress-optic coefficients of lead borates as a function of wavelength-dependent polarizabilities $\langle \alpha \rangle$.

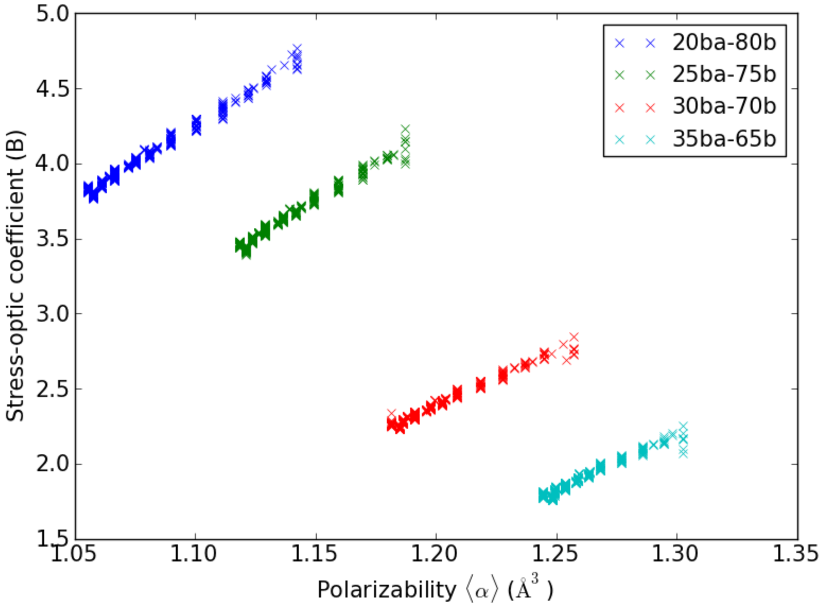

Figure 7.6: Stress-optic coefficients of barium borates as a function of wavelength-dependent polarizabilities $\langle \alpha \rangle$.

7.2.2 Polarizability and the Pseudo-Cauchy Model

The pseudo-Cauchy model applied to the stress-optic coefficient,

$$C(\lambda) = a + b\left(\frac{\lambda_0}{\lambda}\right) + c\left(\frac{\lambda_0}{\lambda}\right)^2. \tag{7.8}$$

allows the wavelength-dependent trends in C to be described by the fitted parameters a, b and c. The value a gives the long-wavelength stress-optic coefficient of a sample, while the sign and magnitude of c gives an indication of the type and amount of dispersion present for a glass sample. Positive (negative) values of c are indicative of positive (negative) dispersion, while larger magnitudes of c indicate stress-optic coefficients that increase or decrease more rapidly with wavelength.

Figure 7.7 shows the fitted parameter a as a function of the summed long-wavelength polarizability $\langle\alpha\rangle$ for borate, phosphate, silicate, and tellurite glasses. Compared to the empirical parameter $\langle d/N_c\rangle$, the polarizability shows a much better correlation with this parameter (the relationship between a and $\langle d/N_c\rangle$ is shown in Figure fig:a-dnc). Based on the discussion of $\langle\alpha\rangle$ and C in Section 7.1.1, this is expected.

Figure 7.8 shows the fitted parameter c as a function of the long-wavelength polarizability $\langle\alpha\rangle$ for borate, phosphate, silicate and tellurite glasses. The polarizability is only slightly better than $\langle d/N_c\rangle$ at indicating the amount of dispersion in glasses (the relationship between c and $\langle d/N_c\rangle$ is shown in Figure 5.26). While c does tend to decrease as $\langle\alpha\rangle$ increases, the polarizability does not correspond linearly with the amount of dispersion present in a glass. However, the type of dispersion can be modelled by $\langle\alpha\rangle$: when $\langle\alpha\rangle \leq 1.6$ Å^3, glasses exhibit positive dispersion in C, and for $\langle\alpha\rangle \geq 1.75$ Å^3, glasses typically have negative dispersion in C. From these results, non-dispersive values of the stress-optic coefficient are predicted for glass compositions with $\langle\alpha\rangle \approx 1.7$ Å^3.

At present, it is not clear whether the variations between the pseudo-Cauchy fitted parameters and the polarizability of a glass is caused by experimental variations from data collection and fitting, or whether α_n alone is not enough to describe the related parameters a, b and c. Still, the polarizability of a composition can be used to get a good estimate of the long-wavelength value of C, and also to obtain a decent estimate of the type and amount of dispersion that the glass will exhibit.

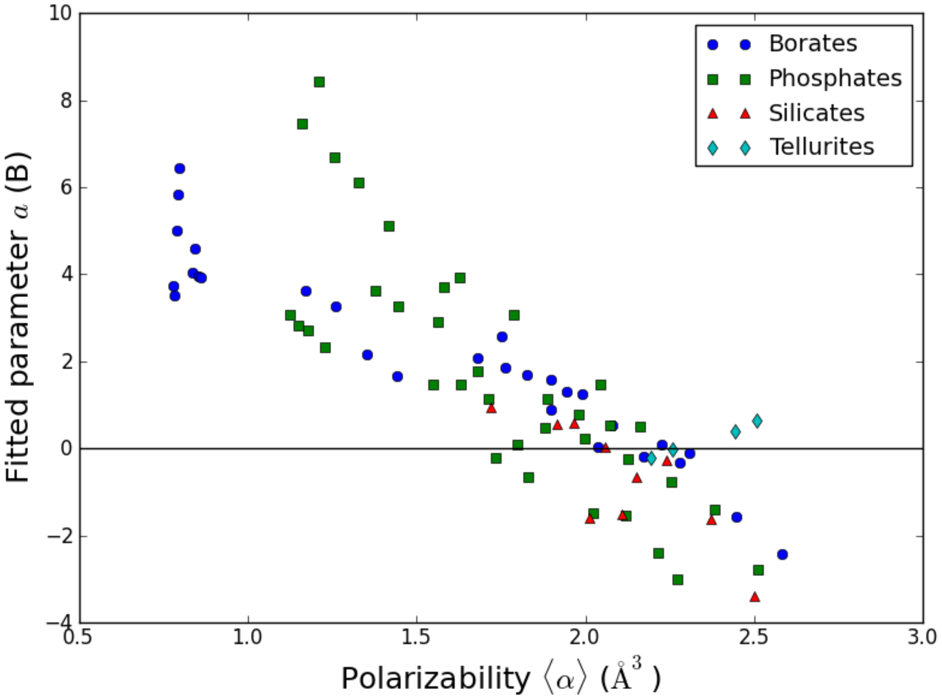

Figure 7.7: Fitted parameter a as a function of polarizability $\langle\alpha\rangle$.

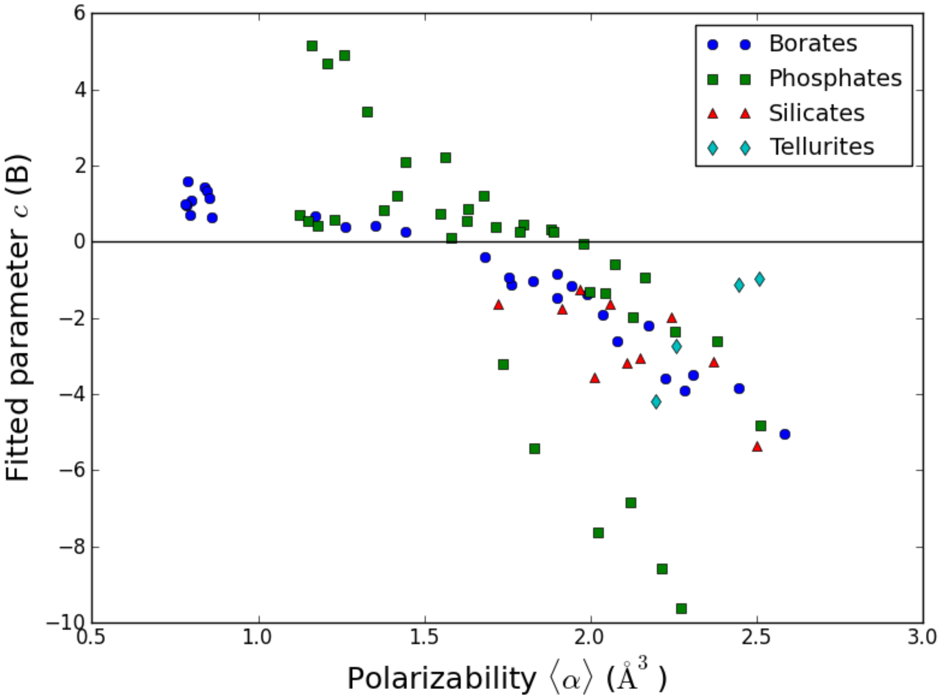

Figure 7.8: Fitted parameter c as a function of polarizability $\langle\alpha\rangle$.

7.3 The Polarizability Model for Individual Elasto-Optic Tensor Elements

The polarizability seems to describe both the sign and magnitude of the stress-optic coefficient, so it is of interest to compare the elasto-optic tensor elements p_{ij} to $\langle\alpha\rangle$ as well. Figure 7.9 shows the shear elasto-optic coefficient p_{44} as a function of polarizability for the lead and barium borates, phosphates and silicates, and for previously measured literature values. The elasto-optic tensor element increases nonlinearly as polarizability increases. This is consistent with the trends in the values of p_{44} determined from the stress-optic coefficients as discussed in Section 7.1.1. The lithium-containing silicates and pure B_2O_3 are slightly offset from the other values; this could be indicative of low estimates of α_n as previously discussed.

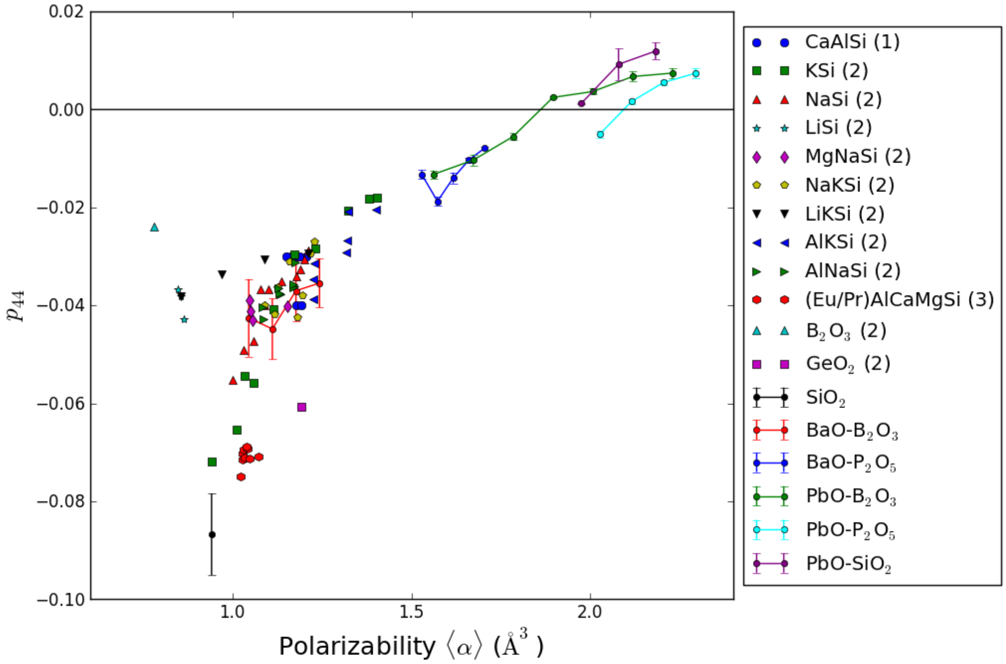

Figure 7.9: Elasto-optic coefficient p_{44} as a function of polarizability $\langle\alpha\rangle$. (1) from reference [66], (2) from [10], (3) from [13].

Figure 7.10 shows the tensor element p_{12} as a function of polarizability for the same glasses. For each binary or ternary glass series, p_{12} does decrease as $\langle\alpha\rangle$ increases. However, the values not overlap between different glass formers and modifiers. The empirical value $\langle d/N_c\rangle$ shows a better correlation with p_{12} for all glasses considered (see Figure 6.7). This might suggest that while the shear photoelastic response

(p_{44}, C) is described by the electronic interactions of anions and cations, the linear photoelastic response (p_{12}) is described by the chemical bonding environment of the cation.

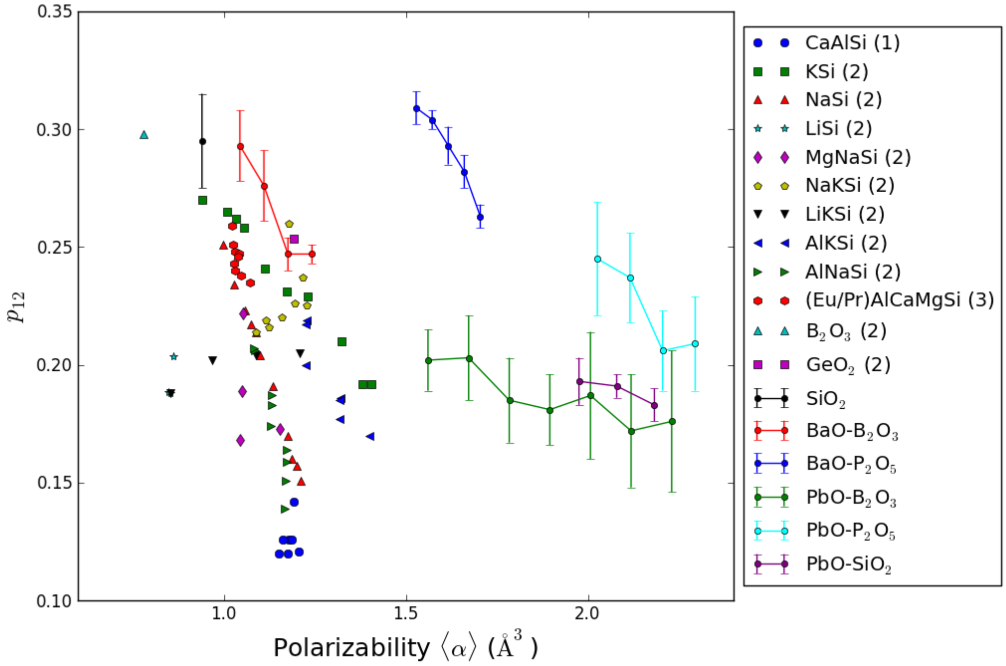

Figure 7.10: Elasto-optic coefficient p_{12} as a function of polarizability $\langle\alpha\rangle$. (1) from reference [66], (2) from [10], (3) from [13].

The elasto-optic coefficient p_{11} is plotted against polarizability in Figure 7.10. Just as there was no relationship between p_{11} and glass composition or $\langle d/N_c\rangle$, this tensor element is not described by $\langle\alpha\rangle$.

The shear elasto-optic response of a glass is described by the normalized sum of both anion and cation polarizabilities. The value of p_{44} can also be related to the other two tensor elements by $2p_{44} = p_{11} - p_{12}$. However, it is worth mentioning that the experimental trends in p_{12} and p_{11} are not predicted by individual anion or cation polarizabilities.

7.4 Predicting Other Material and Optical Properties

The polarizability and, to a certain extent, $\langle d/N_c\rangle$ are predictive of the photoelastic response of a glass. As such, the refractive index of a material could be described

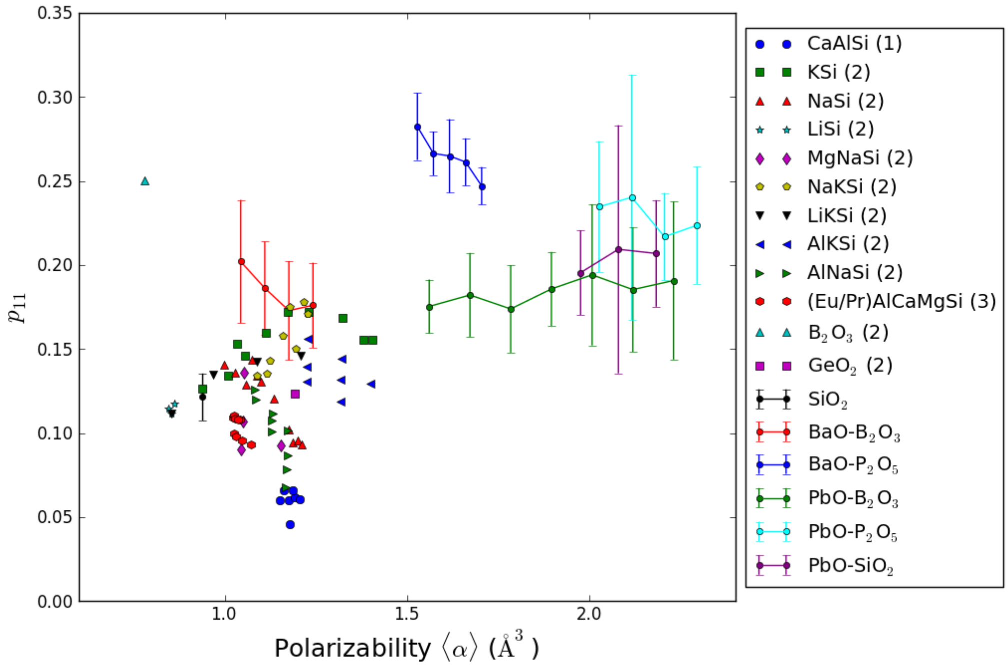

Figure 7.11: Elasto-optic coefficient p_{11} as a function of polarizability $\langle\alpha\rangle$. (1) from reference [66], (2) from [10], (3) from [13].

by $\langle\alpha\rangle$ or $\langle d/N_c\rangle$ as well. It can be seen in Figure 7.12 that the refractive index is correlated with both empirical parameters. As either $\langle d/N_c\rangle$ or $\langle\alpha\rangle$ increases, n also increases. There is some separation between the values of n for different glass formers and modifiers described by $\langle d/N_c\rangle$; this separation is less apparent between n and $\langle\alpha\rangle$, though the phosphate glasses are offset from the rest of the glasses. This might suggest that the experimentally extrapolated value of $\langle\alpha\rangle$ for P_2O_5 is overestimated. Or the phosphorus content in the glass could be higher or lower than the amount estimated by the nominal composition.

The refractive index is typically correlated with the density of a glass. As such, we expect a relationship between molar volume V_M (which is dependent on density) and the empirical models. Figure 7.13 shows the molar volume as a function of both $\langle d/N_c\rangle$ and $\langle\alpha\rangle$. For the borates, silicates and tellurites, molar volume is fairly constant with glass composition. Phosphate glasses have larger molar volumes that decrease as a function of $\langle d/N_c\rangle$ or $\langle\alpha\rangle$. The large separation between phosphates and other glass types is due to the much larger molar mass of P_2O_5 compared to B_2O_3, SiO_2 and TeO_2.

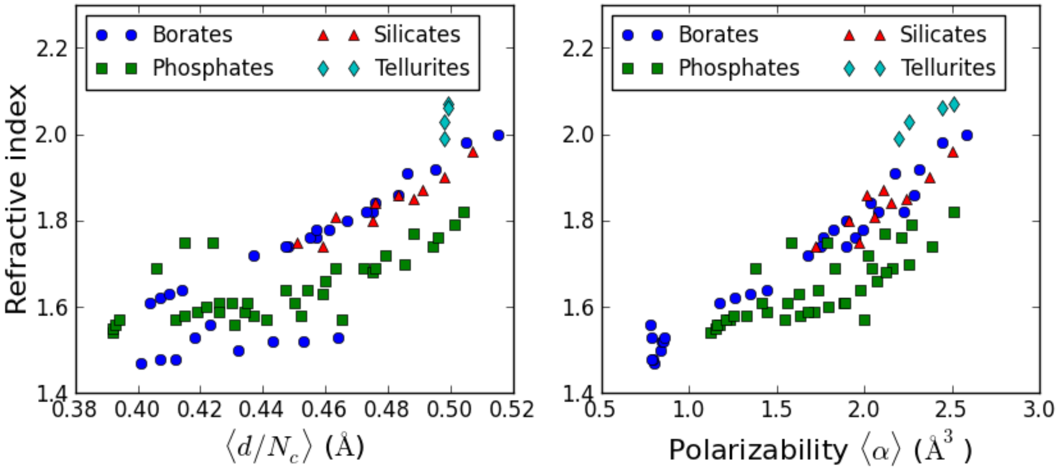

Figure 7.12: Refractive index as a function of $\langle d/N_c \rangle$ (left) and polarizability $\langle \alpha \rangle$ (right).

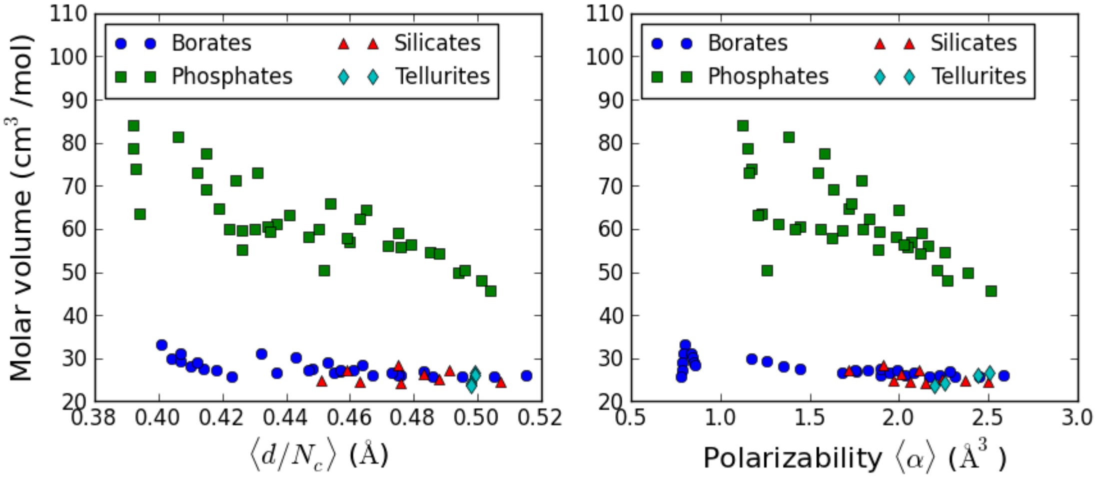

Figure 7.13: Molar volume as a function of $\langle d/N_c \rangle$ (left) and polarizability $\langle \alpha \rangle$ (right).

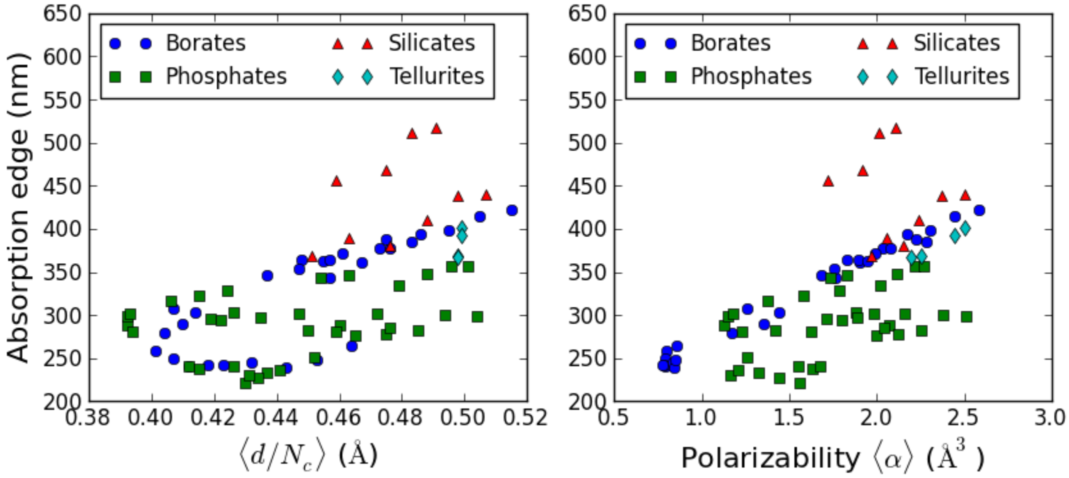

Figure 7.14: Absorption edge as a function of $\langle d/N_c \rangle$ (left) and polarizability $\langle \alpha \rangle$ (right).

The absorption edge of the borates, phosphates, silicates and tellurites also shows some dependence on both $\langle d/N_c \rangle$ and $\langle \alpha \rangle$; this relationship is shown in Figure 7.14. There is less variation in λ_0 with $\langle \alpha \rangle$. The absorption edge tends to shift to higher wavelengths as $\langle \alpha \rangle$ increases for the borates, silicates and tellurites. The values are more scattered for the phosphate glasses.

These results seem to suggest that important optical and material properties can be predicted by the empirical and polarizability models. The relationship between polarizability and n is somewhat expected from Weyl's model. Glasses with higher polarizabilities should have more attraction between cation units in the structure, which would result in a more densely packed structure. The correlation with absorption edge is more surprising. It is not clear at this point why the properties of the phosphate glass series are separate from the values for the other glass formers as a function of polarizability.

7.5 Summary

The polarizability model of photoelasticity appears to accurately describe the stress-optic response of oxide and non-oxide glasses. The polarizability of a material can be quantified by the sum of the normalized polarizabilities between the “anions” (*e.g.* O, S) and ”cations” (*e.g.* Si, Ba, Pb) in the structure.

The signs and magnitudes of the stress-optic coefficient C and elasto-optic coefficient p_{44} are correlated with the polarizability parameter $\langle\alpha\rangle$. The parameters of the pseudo-Cauchy model describing the wavelength dependence of C also appear to be related to the polarizability. Furthermore, $\langle\alpha\rangle$ can be used to estimate important material properties such as the refractive index and absorption edge wavelength.

Chapter 8

Conclusions

Understanding the origin of the photoelastic response in oxide and non-oxide glasses is a research topic that has received considerable attention for many years. Perhaps of equal interest industrially is the ability to design glasses with specific optical properties. The results of this research have contributed significantly both to the understanding of photoelasticity in glass and to the correlation of optical and photoelastic properties with glass composition.

The empirical model of photoelasticity developed by Guignard and Zwanziger has facilitated the prediction of new zero-stress optic glass compositions based on chemical bond lengths and coordinations. However, it is not able to predict the magnitude of the stress-optic response, likely due to the differences between the structure of the crystalline compounds used to estimate d and N_c, and the structure of individual units in a glass network. A model which considers the distortion of the electron clouds of "anions" and "cations" is more successful at describing the stress-optic response in a glass. A polarizability parameter $\langle\alpha\rangle$ is defined in this work as the contribution from the polarizabilities of individual anions and cations (or individual bonds). This value quantifies the response of individual bonds in the glass network to stress, and appears to correlate not only with the sign of the stress-optic coefficient of borates, phosphates and silicates but also with the magnitude.

The values of α_n for individual compounds were determined in this study by assuming additive relationships for n and ρ in binary systems, and extrapolating the refractive index and density for the pure glass former and additive. These values of α_n could be confirmed by extrapolating the values for many more binary borate, phosphate and silicate glass systems. Calculations of glassy compounds could also verify the experimentally determined polarizabilities.

We have determined that it is possible to relate the sign and perhaps also the magnitude of the stress-optic coefficient of non-oxide glasses to the compositionally dependent parameters $\langle d/N_c \rangle$ or $\langle \alpha \rangle$. Zero-stress optic non-oxide glass compositions are predicted for larger values of $\langle d/N_c \rangle$ or $\langle \alpha \rangle$ compared to oxide glasses. This has been attributed to non-stoichiometric sulfur-sulfur bonding in the glass network. The empirical model can accommodate for this by including the anion valence Z_a in the description of metallicity.

The results of Table 4.1 can be used to predict new binary and ternary glass systems containing zero-stress optic compositions. Values of $\langle d/N_c \rangle$ for glasses with $C = 0$ B could be used to estimate the amount of anion-anion bonding present in the network. The synthesis of selenide and telluride systems would confirm if $\langle d/N_c \rangle$ increases with decreasing electronegativity differences. It would also be beneficial to experimentally determine the polarizability parameters α_n for other sulfide, selenide and telluride compounds. In this way, the relationship between the magnitudes of C for stoichiometric non-oxide glass compositions and $\langle \alpha \rangle$ could be explored.

Perhaps the most interesting project remaining for non-oxide glasses is to map the dependence of the stress-optic coefficient of non-oxide glasses on amounts of excess and deficit chalcogen. The parameters described in Section 4.3.3 could be tested to determine whether there is in fact a correlation between stress-optic coefficient, structure and bonding environments.

The stress-optic coefficients of positively and negatively modified oxide glasses typically showed positive dispersion and negative dispersion, respectively. From these results, glass families containing non-dispersive values of C were predicted and synthesized. The type of dispersion was related to both $\langle d/N_c \rangle$ and $\langle \alpha \rangle$. With this knowledge, new non-dispersive glass compositions can be predicted. However, for oxide glasses, their stress-optic coefficients are expected to always be positive.

The wavelength dependence of the stress-optic coefficient was successfully modelled using a pseudo-Cauchy fit. The fitting coefficients a, b and c were found to be interdependent Then any theory of photoelasticity developed to describe C could be simplified to a function of λ_0/λ and one compositionally-dependent variable. The polarizability was partially correlated with a and c, but it is likely that other factors are at work. Following the work of Cardona, calculations of the band structure of glass systems could yield insight into the wavelength dependence of C.

Individual elasto-optic tensor elements p_{ij} have been measured for lead and barium borate, phosphate, and silicate glasses. Previous studies have only measured pure B_2O_3, GeO_2, SiO_2 and mixed silicate systems, and no compositions containing typically negative modifiers. The shear elasto-optic coefficient p_{44} behaved as expected from predictions of the empirical model and measurements of the stress-optic coefficient C. Interestingly, p_{12} was also correlated with $\langle d/N_c \rangle$. Comparing p_{44} with $\langle \alpha \rangle$ improved the correlation. For individual systems, p_{12} decreased as $\langle \alpha \rangle$ increased, but there was a separation of values between different glass formers and additives. The last, dependent element p_{11} varied randomly with composition, $\langle d/N_c \rangle$ and $\langle \alpha \rangle$.

The polarizability describes the response of a material to stress in both the stress direction and perpendicular to it, so it follows that p_{44} relates to $\langle \alpha \rangle$. But p_{11} and p_{12} depend on the response in the extraordinary and ordinary directions, respectively, so it is likely that they depend on different material properties. Indeed, many theories of photoelasticity, such as those developed by Mueller or Carleton, had p_{44}, p_{12} and p_{11} which all depended on different properties or on the same property but in different ways. Future work should examine p_{12} and p_{11} for more diverse binary and ternary glass families to determine if and how these elements are individually related to composition.

The normalized polarizability of a glass is a powerful new predictive parameter that can be used to estimate both the value of C and its wavelength dependence. Furthermore, the polarizability is a building block of many semi-successful theories of photoelasticity. From this, we conclude that $\langle \alpha \rangle$ does in fact describe a fundamental component of the stress-induced birefringence. It remains to be seen whether a comprehensive photoelastic theory can be developed which explains both the compositional and wavelength dependence of the elasto-optic tensor elements p_{ij} and stress-optic coefficient C. But it is certain that the results of this work have improved the understanding of many aspects of the stress-optic response of glass.

Bibliography

[1] M. Guignard, L. Albrecht, and J. Zwanziger, "Zero-stress optic glass without lead," *Chem. Mater.*, vol. 19, no. 2, pp. 286–290, 2007.

[2] W. H. Zachariasen, "The atomic arrangement in glass," *J. Am. Chem. Soc.*, vol. 54, no. 10, pp. 3841–3851, 1932.

[3] A. Varshneya, *Fundamentals of inorganic glasses.* San Diego: Academic Press, 1994.

[4] J. C. Mauro, C. S. Philip, D. J. Vaughn, and M. S. Pambianchi, "Glass science in the United States: Current status and future directions," *Int. J. Appl. Glass Sci.*, vol. 5, no. 1, pp. 2–15, 2014.

[5] H.-J. Hoffmann in *The Properties of Optical Glass* (H. Bach and N. Neuroth, eds.), pp. 96–123, Springer, 1998.

[6] F. Pockels, "Über die Änderung des optischen Verhaltens verschiedener Gläser durch elastische Deformation," *Ann. d. Phys.*, vol. 7, pp. 745–771, 1902.

[7] M. Born, E. Wolf, A. Bhatia, P. Clemmow, D. Gabor, A. Stokes, A. Taylor, P. Wayman, and W. Wilcock, *Principles of Optics: Electromagnetic Theory of Propagation, Interference and Diffraction of Light.* Cambridge University Press, 1999.

[8] H. Mueller, "Theory of photoelasticity in amorphous solids," *J. Appl. Phys.*, vol. 6, no. 6, pp. 179–184, 1935.

[9] H. Mueller, "The theory of photoelasticity*," *J. Am. Chem. Soc.*, vol. 21, no. 1, pp. 27–33, 1938.

[10] J. Schroeder, "Brillouin scattering and pockels coefficients in silicate glasses," *J. Non-Cryst. Solids*, vol. 40, no. 1, pp. 549–566, 1980.

[11] J. Smit, "On the signs of the elasto-optic coefficients," *J. Appl. Phys.*, vol. 49, no. 5, pp. 2935–2936, 1978.

[12] H. Carleton, "Amorphous materials: papers presented to the third international conference on the physics of non-crystalline solids held at Sheffield University, September, 1970," pp. 103–111, Wiley-Interscience, 1972.

[13] G.-Q. Shen, Z. Utegulov, J. P Wicksted, and S. Mian, "Effects of the rare earth modifier on the Brillouin scattering from soda magnesia alumina silicate glasses," *Phys. Chem. Glasses: Eur. J. Glass Sci. Technol., Part B*, vol. 43, no. 2, pp. 73–79, 2002.

[14] D. Biegelsen, J. Zesch, and C. Schwab, “Photoelasticity of the cuprous halides,” *Phys. Rev. B*, vol. 14, no. 8, p. 3578, 1976.

[15] W. A. Harrison, “Bond-orbital model and the properties of tetrahedrally coordinated solids,” *Phys. Rev. B*, vol. 8, no. 10, p. 4487, 1973.

[16] W. A. Harrison and S. Ciraci, “Bond-orbital model. II,” *Phys. Rev. B*, vol. 10, no. 4, p. 1516, 1974.

[17] S. Wemple, “Optical oscillator strengths and excitation energies in solids, liquids, and molecules,” *J. Chem. Phys.*, vol. 67, no. 5, pp. 2151–2168, 1977.

[18] M. Lines, “Photoelastic trends from halides to pnictides by a bond-orbital method,” *J. Appl. Phys.*, vol. 60, no. 4, pp. 1472–1478, 1986.

[19] V. Mazzacurati, M. Nardone, G. Ruocco, and G. Signorelli, “Brillouin scattering intensities in glasses: Theory and experiment,” *Philos. Mag. B*, vol. 59, no. 1, pp. 3–15, 1989.

[20] P. Benassi, A. Fontana, and P. Rodrigues, “Light scattering in superionic glasses $(\mathrm{AgI})_x(\mathrm{AgPO}_3)_{1-x}$: Brillouin and Raman scattering,” *Phys. Rev. B*, vol. 43, no. 2, p. 1756, 1991.

[21] P. Benassi, V. Mazzacurati, G. Ruocco, and G. Signorelli, “Elasto-optic constants in silicate glasses: Experiment and theory,” *Phys. Rev. B*, vol. 48, no. 9, p. 5987, 1993.

[22] D. Biegelsen, “Frequency dependence of the photoelastic coefficients of silicon,” *Phys. Rev. B*, vol. 12, no. 6, p. 2427, 1975.

[23] P. Etchegoin, J. Kircher, and M. Cardona, “Elasto-optical constants of Si,” *Phys. Rev. B*, vol. 47, no. 16, p. 10292, 1993.

[24] P. Etchegoin, J. Kircher, and M. Cardona, “Piezo-optical response of semiconductors,” *Thin Solid Films*, vol. 233, no. 1, pp. 141–144, 1993.

[25] P. Etchegoin, J. Kircher, M. Cardona, C. Grein, and E. Bustarret, “Piezo-optics of GaAs,” *Phys. Rev. B*, vol. 46, no. 23, p. 15139, 1992.

[26] P. Etchegoin, J. Kircher, M. Cardona, and C. Grein, “Piezo-optical response of Ge in the visible–uv range,” *Phys. Rev. B*, vol. 45, no. 20, p. 11721, 1992.

[27] F. Canal, M. Grimsditch, and M. Cardona, “Piezobirefringence in GaP and InP,” *Solid State Commun.*, vol. 29, no. 7, pp. 523–526, 1979.

[28] D. Rönnow, P. Santos, M. Cardona, E. Anastassakis, and M. Kuball, “Piezo-optics of InP in the visible-ultraviolet range,” *Phys. Rev. B*, vol. 57, no. 8, p. 4432, 1998.

[29] W. Kucharczyk, “Dispersion in the linear and second-order bond polarizabilities of alkali halides,” *Phys. Status Solidi B*, vol. 182, no. 2, pp. 477–484, 1994.

[30] D. K. Biegelsen and J. C. Zesch, “Optical frequency dependence of the photoelastic coefficients of fused silica,” *J. Appl. Phys.*, vol. 47, no. 9, pp. 4024–4025, 1976.

[31] S. Wemple and M. DiDomenico Jr, “Theory of the elasto-optic effect in nonmetallic crystals,” *Phys. Rev. B*, vol. 1, no. 1, p. 193, 1970.

[32] S. Wemple and M. DiDomenico Jr, “Optical dispersion and the structure of solids,” *Phys. Rev. Lett.*, vol. 23, no. 20, p. 1156, 1969.

[33] M. Cardona, D. Rönnow, and P. V. Santos, “Ellipsometric investigations of piezo-optical effects,” *Thin Solid Films*, vol. 313, pp. 10–17, 1998.

[34] M. Tashiro, “The effects of the polarisation of the constituent ions on the photoelastic birefringence of the glass,” *J. Soc. Glass Technol.*, vol. 40, pp. 353–362, 1956.

[35] A. Rabukhin and G. Belousova, “Photoelastic constants of bismuth-containing gallate glasses,” *Glass Ceram.*, vol. 49, no. 10, pp. 458–462, 1992.

[36] K. Matusita, R. Yokota, T. Kimijima, T. Komatsu, and C. Ihara, “Compositional trends in photoelastic constants of borate glasses,” *J. Am. Chem. Soc.*, vol. 67, no. 4, pp. 261–265, 1984.

[37] K. Matusita, C. Ihara, T. Komatsu, and R. Yokota, “Photoelastic effects in silicate glasses,” *J. Am. Chem. Soc.*, vol. 67, no. 10, pp. 700–704, 1984.

[38] K. Matusita, C. Ihara, T. Komatsu, and R. Yokota, “Photoelastic effects in phosphate glasses,” *J. Am. Chem. Soc.*, vol. 68, no. 7, pp. 389–391, 1985.

[39] A. Rabukhin, “Photoelastic constants of germanate glasses containing lead and bismuth oxides,” *Glass Ceram.*, vol. 51, no. 11-12, pp. 353–359, 1994.

[40] N. K. Sinha, “Normalised dispersion of birefringence of quartz and stress optical coefficient of fused silica and plate glass,” *Phys. Chem. Glasses*, vol. 19, no. 4, pp. 69–77, 1978.

[41] M. Guignard and J. Zwanziger, “Zero stress-optic barium tellurite glass,” *J. Non-Cryst. Solids*, vol. 353, no. 16, pp. 1662–1664, 2007.

[42] V. Martin, B. Wood, U. Werner-Zwanziger, and J. Zwanziger, “Structural aspects of the photoelastic response in lead borate glasses,” *J. Non-Cryst. Solids*, vol. 357, no. 10, pp. 2120–2125, 2011.

[43] V. Martin, U. Werner-Zwanziger, J. Zwanziger, and R. Dunlap, “Correlation of structure and photoelastic response in tin phosphate glass,” *Int. J. Appl. Glass Sci.*, vol. 2, pp. 282–289, 2011.

[44] N. Yamamoto, A. Saitoh, and H. Takebe, “Zero photoelastic zinc tin phosphate glass without lead oxide,” *Opt. Lett.*, vol. 37, no. 20, pp. 4203–4205, 2012.

[45] M. Smedskjaer, S. Saxton, A. Ellison, and J. Mauro, “Photoelastic response of alkaline earth aluminosilicate glasses,” *Opt. Lett.*, vol. 37, no. 3, pp. 293–295, 2012.

[46] M. M. Smedskjaer, M. Potuzak, X. Guo, and J. C. Mauro, “Compositional control of the photoelastic response of silicate glasses,” *Opt. Mater.*, vol. 35, no. 12, pp. 2435–2439, 2013.

[47] L. Filon and F. Harris, “The photo-elastic dispersion of vitreous silica,” *Proc. R. Soc. London, Ser. A*, vol. 130, no. 813, pp. 410–431, 1931.

[48] E. Jog and R. Krishnan, “Dispersion of the photoelastic constants of fused silica,” *Nature*, vol. 179, no. 4558, pp. 540–541, 1957.

[49] W. Primak and D. Post, “Photoelastic constants of vitreous silica and its elastic coefficient of refractive index,” *J. Appl. Phys.*, vol. 30, no. 5, pp. 779–788, 1959.

[50] T. Vasudevan and R. Krishnan, “Dispersion of the stress-optic coefficient in glasses,” *J. Phys. D: Appl. Phys.*, vol. 5, no. 12, pp. 2283–2287, 1972.

[51] S. Thomas, *Dispersive Effects of the Stress-optic Response in Oxide Glasses.* Master’s thesis, Dalhousie University, Halifax, Nova Scotia, Canada, 2010.

[52] T. Fukazawa, M. Korekawa, and Y. Fujita, “Spectroscopic photoelasticity of lead-silica glass analyzed by polarization modulated ellipsometry,” *J. Non-Cryst. Solids*, vol. 203, pp. 102–108, 1996.

[53] J. Cha, M. Kawano, H. Takebe, and M. Kuwabara, “Compositional dependence of photoelasticity of tin phosphate glasses,” *J. Ceram. Soc. Japan*, vol. 116, no. 1358, pp. 1100–1103, 2008.

[54] H. In, H. Takebe, and K. Morinaga, “Low photo-elastic characteristics of BaO-P_2O_5 glasses,” *J. Ceram. Soc. Japan*, vol. 111, no. 6, pp. 426–429, 2003.

[55] J. Thorbahn and J. Zwanziger, “Compositional dependence of the stress-optic response in zinc tellurite glasses,” *J. Non-Cryst. Solids*, vol. 381, pp. 48–53, 2013.

[56] L.-G. Hwa, C.-L. Lu, and L.-C. Liu, “Elastic moduli of calcium alumino-silicate glasses studied by Brillouin scattering,” *Mater. Res. Bull.*, vol. 35, no. 8, pp. 1285–1292, 2000.

[57] D. L. Sidebottom, P. F. Green, and R. K. Brow, “Brillouin scattering in alkali metaphosphate glasses and melts,” *J. Mol. Struct.*, vol. 479, no. 2, pp. 219–226, 1999.

[58] B. Champagnon, C. Chemarin, E. Duval, and R. Le Parc, “Glass structure and light scattering,” *J. Non-Cryst. Solids*, vol. 274, no. 1, pp. 81–86, 2000.

[59] M. Maczka, J. Hanuza, J. Baran, A. Hushur, and S. Kojima, “Heat capacity, Raman, and Brillouin scattering studies of M_2O-MgO-WO_3-P_2O_5 glasses (M = K, Rb),” *J. Chem. Phys.*, vol. 125, no. 24, p. 244503, 2006.

[60] J.-C. Sabadel, P. Armand, F. Terki, J. Pelous, D. Cachau-Herreillat, and E. Philippot, “Brillouin and low-frequency Raman studies of TeO_2-BaO-TiO_2 glasses,” *J. Phys. Chem. Solids*, vol. 61, no. 11, pp. 1745–1750, 2000.

[61] G. Hauret, Y. Vaills, T. Parot-Rajaona, F. Gervais, D. Mas, and Y. Luspin, “Dynamic behaviour of $(1-x)$ SiO_2-$0.5x$ M_2O glasses (M = Na, Li) investigated by infrared and Brillouin spectroscopies,” *J. Non-Cryst. Solids*, vol. 191, no. 1, pp. 85–93, 1995.

[62] C.-C. Lin, S.-F. Chen, L.-g. Liu, and C.-C. Li, “Anionic structure and elasticity of Na_2O-MgO-SiO_2 glasses,” *J. Non-Cryst. Solids*, vol. 353, no. 4, pp. 413–425, 2007.

[63] J. Schroeder, R. Mohr, P. Macedo, and C. Montrose, “Rayleigh and Brillouin scattering in K_2O-SiO_2 glasses,” *J. Am. Chem. Soc.*, vol. 56, no. 10, pp. 510–514, 1973.

[64] P. Benassi, V. Mazzacurati, G. Monaco, G. Ruocco, and G. Signorelli, “Brillouin and Raman cross sections in silicate glasses,” *Phys. Rev. B*, vol. 52, no. 2, p. 976, 1995.

[65] D. Heiman, D. Hamilton, and R. Hellwarth, “Brillouin scattering measurements on optical glasses,” *Phys. Rev. B*, vol. 19, no. 12, p. 6583, 1979.

[66] L.-G. Hwa, “Rayleigh–Brillouin scattering in calcium aluminosilicate glasses,” *J. Raman Spectrosc.*, vol. 29, no. 4, pp. 269–272, 1998.

[67] Z. D. Pan and J. P. Wicksted, “Rayleigh–Brillouin scattering studies of thoriated fluoride and fluorozirconate glasses,” *Optical Engineering*, vol. 31, no. 1, pp. 116–120, 1992.

[68] V. Martinez, C. Martinet, B. Champagnon, and R. Le Parc, “Light scattering in SiO_2-GeO_2 glasses: quantitative comparison of Rayleigh, Brillouin and Raman effects,” *J. Non-Cryst. Solids*, vol. 345, pp. 315–318, 2004.

[69] D. Linke, “Correlations between properties of chalcogenide glasses. X. photoelastic trends for infrared-transmitting chalcogenide glasses of differing network dimensionality,” *Z. Anorg. Allg. Chem.*, vol. 541, pp. 142–162, 1986.

[70] P. Anderson and A. Varshneya, "Stress-optic coefficient of Ge-As-Se chalcogenide glasses," *J. Non-Cryst. Solids*, vol. 168, no. 1, pp. 125–131, 1994.

[71] B. Cherry, J. W. Zwanziger, and B. G. Aitken, "The structure of GeS_2-P_2S_5 glasses," *J. Phys. Chem. B*, vol. 106, no. 43, pp. 11093–11101, 2002.

[72] B. R. Cherry, J. W. Zwanziger, and B. G. Aitken, "Structure and properties of $Ge_{2.5}PS_x$ glasses," *J. Non-Cryst. Solids*, vol. 333, no. 1, pp. 28–36, 2004.

[73] L. Petit, N. Carlie, F. Adamietz, M. Couzi, V. Rodriguez, and K. Richardson, "Correlation between physical, optical and structural properties of sulfide glasses in the system Ge-Sb-S," *Mater. Chem. Phys.*, vol. 97, no. 1, pp. 64–70, 2006.

[74] J. F. Nye, *Physical properties of crystals*, pp. 131–149. Clarendon Press, 2006.

[75] E. Hecht, *Optics (Fourth Edition).* Addison Wesley, 2002.

[76] F.-T. Lentes in *The Properties of Optical Glass* (H. Bach and N. Neuroth, eds.), pp. 19–58, Springer, 1998.

[77] J. Jackson, *Classical Electrodynamics (Third Edition)*, pp. 295–340. Wiley, 1998.

[78] M. McArthur, *An in-situ investigation of solid electrolyte interphase formation of electrode materials for lithium-ion batteries using spectroscopic ellipsometry.* Master's thesis, Dalhousie University, Halifax, Nova Scotia, Canada, 2011.

[79] J.A. Woollam Co., Inc., *Application note: Compensators*, 2009 (accessed October 13, 2014). `http://www.jawoollam.com/pdf/Compensators.pdf`.

[80] S.-M. Thomas, *Brillouin Spectroscopy*, 2014 (accessed October 13, 2014). `http://serc.carleton.edu/NAGTWorkshops/mineralogy/mineral_physics/brillouin.html`.

[81] S. Speziale, H. Marquardt, and T. S. Duffy, "Brillouin scattering and its application in geosciences," *Rev. Mineral. Geochem.*, vol. 78, no. 1, pp. 543–603, 2014.

[82] J. Sandercock, "Trends in Brillouin scattering: studies of opaque materials, supported films, and central modes," in *Light Scattering in solids III* (M. Cardona and G. Güntherodt, eds.), pp. 173–206, Springer, 1982.

[83] L. Landau and E. Lifshitz, *Electrodynamics of Continuous Media*, vol. 8. Pergamon Press, 1960.

[84] L. Landau and E. Lifshitz, *The classical theory of fields, 3rd edition*, vol. 2. Pergamon Press, 1971.

[85] T. Still, *High frequency acoustics in colloid-based meso-and nanostructures by spontaneous Brillouin light scattering*, pp. 9–34. Springer Theses, 2010.

[86] JRS Scientific Instruments, *Tandem Fabry-Perot Interferometer TFP-1 Operator Manual*, (accessed October 13, 2014). `http://tablestable.com/uploads/ckeditor/TFP-1/Manual_TFP_1.pdf`.

[87] J. Galbraith, J. Zwanziger, and B. Aitken, "Correlating structure with stress-optic response in non-oxide glasses," *J. Non-Cryst. Solids*, vol. 404, pp. 1–6, 2014.

[88] M. Wojdyr, "Fityk: a general-purpose peak fitting program," *J. Appl. Crystallogr.*, vol. 43, no. 5, pp. 1126–1128, 2010.

[89] O. Svelto, *Principles of Lasers.* Springer, 2010.

[90] S. Sugai and A. Onodera, "Medium-range order in permanently densified SiO_2 and GeO_2 glass," *Phys. Rev. Lett.*, vol. 77, no. 20, p. 4210, 1996.

[91] A. Fainstein and B. Jusserand, "Raman scattering in resonant cavities," in *Light Scattering in solids IX* (M. Cardona and R. Merlin, eds.), pp. 17–114, Springer, 2007.

[92] R. G. Ulbrich and C. Weisbuch, "Resonant Brillouin scattering of excitonic polaritons in gallium arsenide," *Phys. Rev. Lett.*, vol. 38, no. 15, p. 865, 1977.

[93] B. Sermage and G. Fishman, "Resonant Brillouin scattering of polaritons in ZnSe: Heavy and light excitons," *Phys. Rev. Lett.*, vol. 43, no. 14, p. 1043, 1979.

[94] P. Y. Yu and F. Evangelisti, "Brillouin scattering efficiencies of exciton polaritons and the additional boundary conditions in CdS," *Phys. Rev. Lett.*, vol. 42, no. 24, p. 1642, 1979.

[95] W. A. Weyl and E. C. Marboe, *The Constitution of Glasses: A Dynamic Interpretation (Volume II Part One).* Interscience Publishers, 1964.

[96] V. Dimitrov and T. Komatsu, "Classification of simple oxides: a polarizability approach," *J. Sol. St. Chem.*, vol. 163, no. 1, pp. 100–112, 2002.

[97] V. Martin, *Composition and structure dependence of the photoelastic response of oxide glass.* Phd thesis, Dalhousie University, Halifax, Nova Scotia, Canada, 2011.

[98] A. C. Lasaga and R. T. Cygan, "Electronic and ionic polarizabilities of silicate minerals," *Am. Mineral.*, vol. 67, no. 3, p. 328, 1982.

[99] O. Medenbach, D. Dettmar, R. Shannon, R. Fischer, and W. Yen, “Refractive index and optical dispersion of rare earth oxides using a small-prism technique,” *J. Opt. A: Pure Appl. Opt.*, vol. 3, no. 3, p. 174, 2001.

[100] Y. Ivanova and E. Gattef, “Phase diagram on the system SnO_2–V_2O_5–MoO_3,” *J. Mater. Sci. Lett.*, vol. 39, no. 12, pp. 4037–4038, 2004.

Appendix A

Refractive Indices as a Function of Wavelength

The results for the Cauchy-fit refractive indices as a function of wavelength for all oxide glass systems considered in this thesis are shown in Figures A.1-A.20.

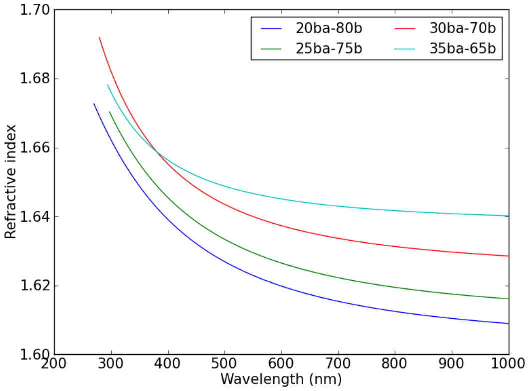

Figure A.1: Wavelength dependence of the refractive index for glasses with composition xBaO-(1-x)B_2O_3

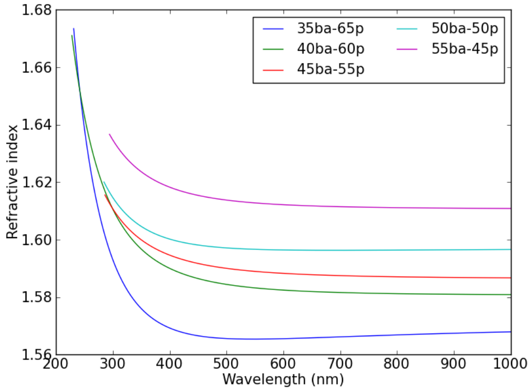

Figure A.2: Wavelength dependence of the refractive index for glasses with composition xBaO-(1-x)P_2O_5

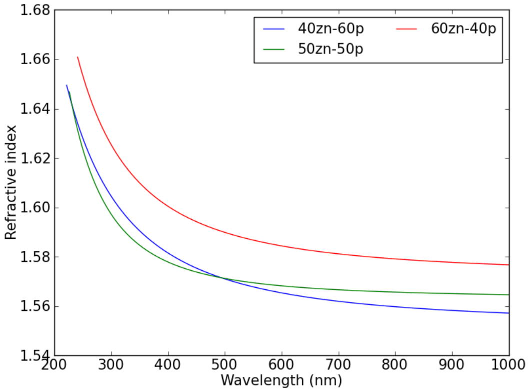

Figure A.3: Wavelength dependence of the refractive index for glasses with composition xZnO-(1-x)P_2O_5

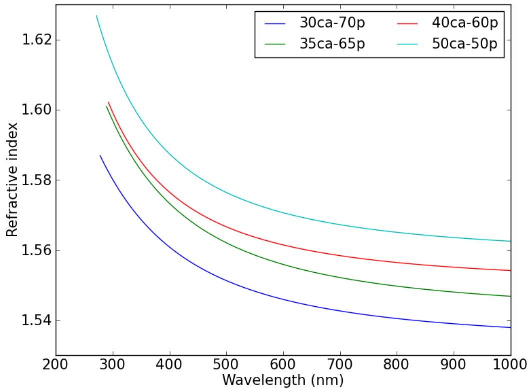

Figure A.4: Wavelength dependence of the refractive index for glasses with composition xCaO-(1-x)P_2O_5

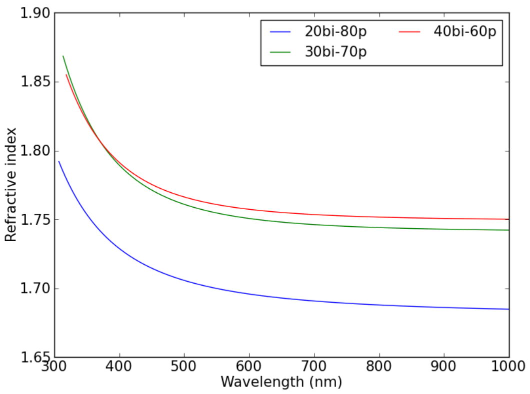

Figure A.5: Wavelength dependence of the refractive index for glasses with composition $x\mathrm{Bi_2O_3}$-(1-x)$\mathrm{P_2O_5}$

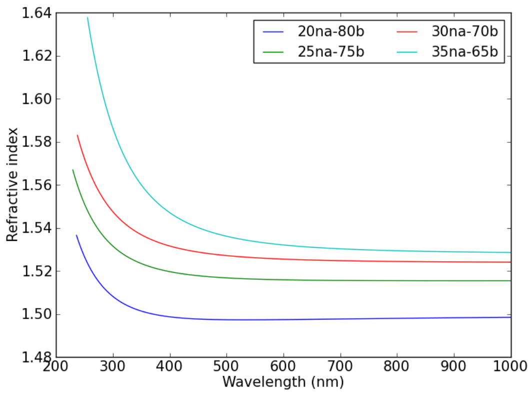

Figure A.6: Wavelength dependence of the refractive index for glasses with composition $x\mathrm{Na_2O}$-(1-x)$\mathrm{B_2O_3}$

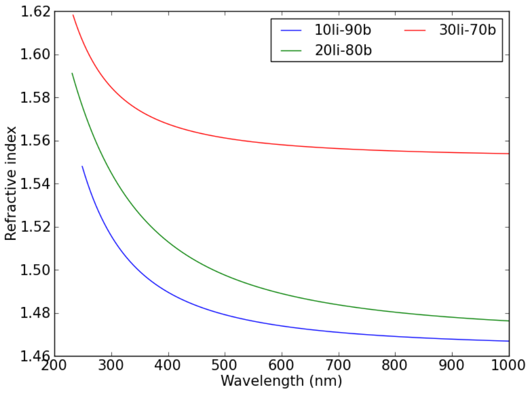

Figure A.7: Wavelength dependence of the refractive index for glasses with composition $x\mathrm{Li_2O}$-(1-x)$\mathrm{B_2O_3}$

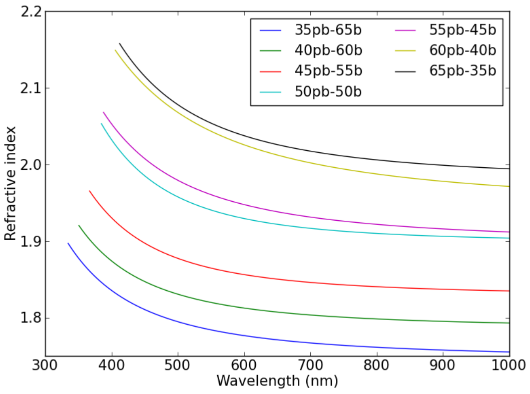

Figure A.8: Wavelength dependence of the refractive index for glasses with composition $x\mathrm{PbO}$-(1-x)$\mathrm{B_2O_3}$

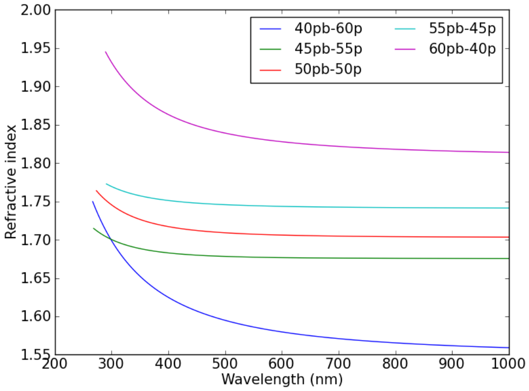

Figure A.9: Wavelength dependence of the refractive index for glasses with composition xPbO-(1-x)P_2O_5

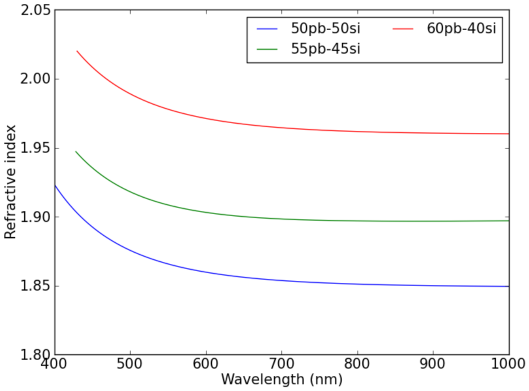

Figure A.10: Wavelength dependence of the refractive index for glasses with composition xPbO-(1-x)SiO_2

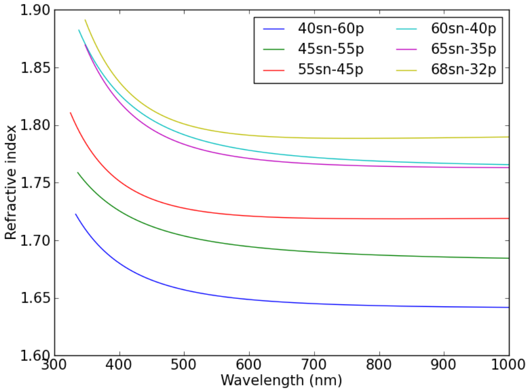

Figure A.11: Wavelength dependence of the refractive index for glasses with composition xSnO-(1-x)P_2O_5

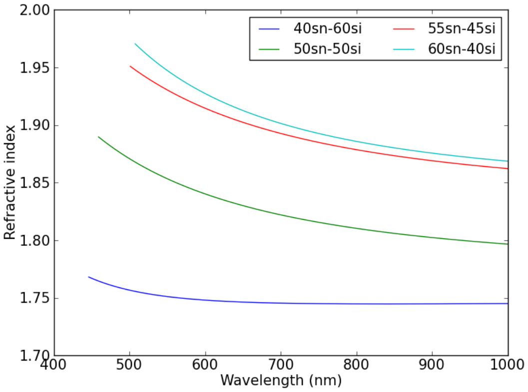

Figure A.12: Wavelength dependence of the refractive index for glasses with composition xSnO-(1-x)SiO_2

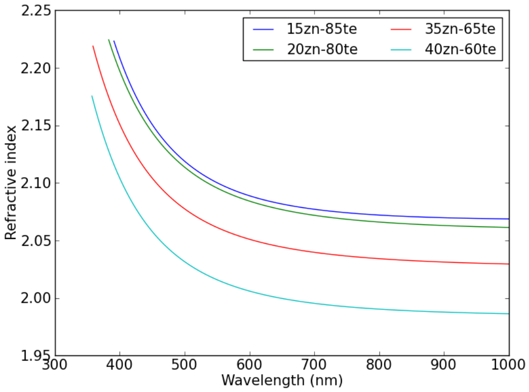

Figure A.13: Wavelength dependence of the refractive index for glasses with composition xZnO-(1-x)TeO$_2$

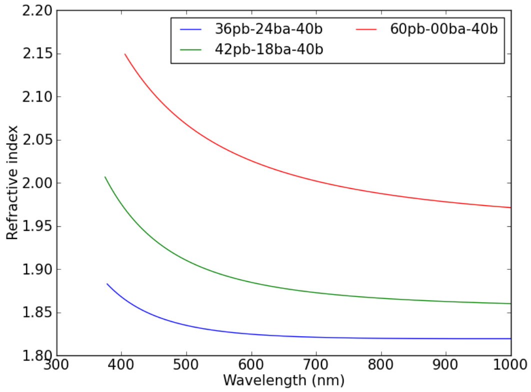

Figure A.14: Wavelength dependence of the refractive index for glasses with composition xPbO-(0.6-x)BaO-0.4B$_2$O$_3$

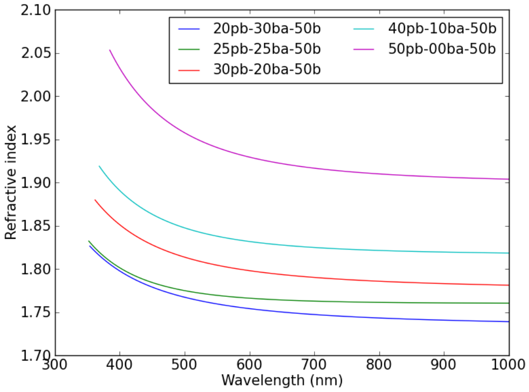

Figure A.15: Wavelength dependence of the refractive index for glasses with composition xPbO-(0.5-x)BaO-0.5B$_2$O$_3$

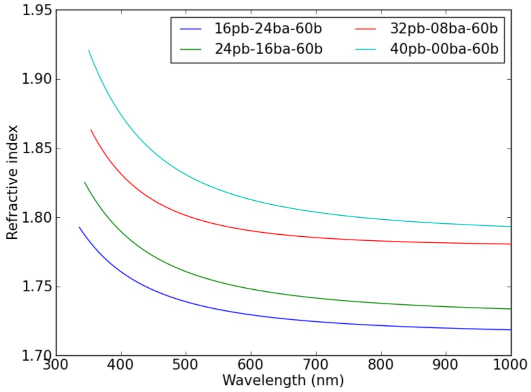

Figure A.16: Wavelength dependence of the refractive index for glasses with composition xPbO-(0.4-x)BaO-0.6B$_2$O$_3$

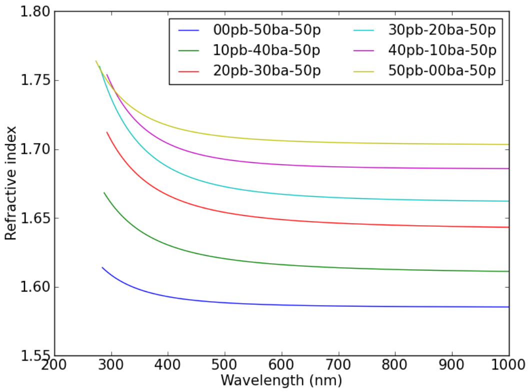

Figure A.17: Wavelength dependence of the refractive index for glasses with composition xPbO-(0.5-x)BaO-0.5P_2O_5

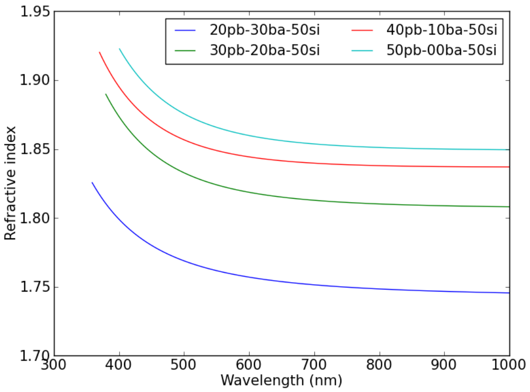

Figure A.18: Wavelength dependence of the refractive index for glasses with composition xPbO-(0.5-x)BaO-0.5SiO_2

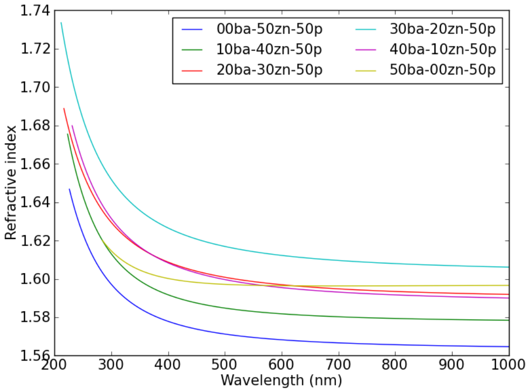

Figure A.19: Wavelength dependence of the refractive index for glasses with composition xBaO-(0.5-x)ZnO-0.5P_2O_5

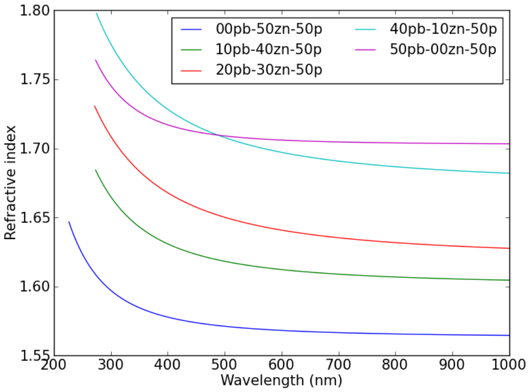

Figure A.20: Wavelength dependence of the refractive index for glasses with composition xPbO-(0.5-x)ZnO-0.5P_2O_5

Appendix B

Parameters of the Pseudo-Cauchy Fit

The fitting parameters a, b, and c of the pseudo-Cauchy fit stress-optic coefficient $C(\lambda)$ are included in Table B.1.

Table B.1: Parameters a, b, and c of the pseudo-Cauchy fit stress-optic coefficient for various glass types, as well as the quality of fit $\sum(C_\lambda - C(\lambda))^2$, where the sum is over all wavelengths.

Family	x	a	b	c	$\sum(C_\lambda - C(\lambda))^2$
xBaO-(1-x)B_2O_3	0.20	3.64	0.36	0.67	0.07
	0.25	3.26	0.42	0.40	0.05
	0.30	2.15	0.20	0.41	0.03
	0.35	1.67	0.26	0.25	0.03
xBaO-(1-x)P_2O_5	0.35	1.46	0.09	0.74	0.26
	0.40	1.47	-0.24	0.87	0.05
	0.45	1.15	0.01	0.39	0.01
	0.50	0.09	-0.06	0.45	0.01
	0.55	0.49	-0.03	0.34	0.01
xBaO-(0.5-x)ZnO-0.5P_2O_5	0.00	8.43	-1.47	4.69	5.20
	0.10	6.10	-0.09	3.42	2.00
	0.20	3.26	-0.42	2.09	0.10
	0.30	2.91	-0.73	2.22	0.23
	0.40	1.78	-0.31	1.22	0.03
	0.50	0.86	-0.06	0.45	0.01
$x$$Bi_2O_3$-(1-$x$)$P_2O_5$	0.20	3.62	0.16	0.82	0.11
	0.30	3.72	0.82	0.11	0.26
	0.40	3.08	0.46	0.25	0.06
xCaO-(1-x)P_2O_5	0.30	3.08	0.07	0.69	0.05
	0.35	2.83	0.11	0.56	0.03
	0.40	2.71	0.25	0.43	0.14
	0.50	2.33	0.19	0.57	0.05

Continued on Next Page...

Table B.1 – Continued

Family	x	a	b	c	$\sum(C_\lambda - C(\lambda))^2$
xLi$_2$O-(1-x)B$_2$O$_3$	0.10	6.44	1.34	1.08	0.88
	0.15	5.83	0.95	0.71	0.59
	0.20	5.02	0.07	1.59	3.10
	0.25	3.51	0.07	0.95	0.20
	0.30	3.75	0.21	1.00	0.21
xNa$_2$O-(1-x)B$_2$O$_3$	0.20	4.03	-0.06	1.42	0.24
	0.25	4.58	0.22	1.33	0.34
	0.30	3.97	0.25	1.16	0.21
	0.35	3.92	0.79	0.63	3.20
xPbO-(1-x)B$_2$O$_3$	0.35	1.85	1.30	-1.14	0.03
	0.40	0.89	1.40	-1.47	0.02
	0.45	0.05	1.70	-1.92	0.03
	0.50	-0.17	1.82	-2.19	0.05
	0.55	-0.10	2.78	-3.48	0.09
	0.60	-1.57	3.04	-3.85	0.10
	0.65	-2.43	3.88	-5.04	0.13
xPbO-(0.6-x)BaO-0.4B$_2$O$_3$	0.36	0.09	3.27	-3.59	0.16
	0.42	-0.31	3.43	-3.90	0.20
	0.60	-1.57	3.04	-3.85	0.10
xPbO-(0.5-x)BaO-0.5B$_2$O$_3$	0.20	1.59	1.16	-0.85	0.03
	0.25	1.31	1.35	-1.16	0.05
	0.30	1.25	1.48	-1.39	0.03
	0.40	0.54	2.34	-2.60	0.11
	0.50	-0.17	1.82	-2.19	0.05
xPbO-(0.5-x)BaO-0.5P$_2$O$_5$	0.00	0.86	-0.06	0.45	0.01
	0.10	1.13	0.17	0.26	0.02
	0.20	0.79	0.27	-0.05	0.02
	0.30	0.53	0.67	-0.59	0.08
	0.40	0.52	0.86	-0.94	0.12
	0.50	-0.75	1.78	-2.35	0.38
xPbO-(0.5-x)BaO-0.5SiO$_2$	0.20	0.58	1.20	-1.26	0.06
	0.30	0.04	1.35	-1.63	0.05
	0.40	-0.64	2.43	-3.06	0.15
	0.50	-0.26	1.44	-1.98	0.09

Continued on Next Page…

Table B.1 – Continued

Family	x	a	b	c	$\sum(C_\lambda - C(\lambda))^2$
xPbO-(0.4-x)BaO-0.6B_2O_3	0.16	2.09	0.80	-0.40	0.02
	0.24	2.57	1.32	-0.93	0.04
	0.32	1.69	1.20	-1.02	0.05
	0.40	0.89	1.40	-1.47	0.02
xPbO-(1-x)P_2O_5	0.40	0.24	1.16	-1.32	0.29
	0.45	-0.24	1.60	-1.99	0.30
	0.50	-0.75	1.78	-2.35	0.38
	0.55	-1.40	1.87	-2.60	0.42
	0.60	-2.77	3.47	-4.83	1.30
xPbO-(1-x)SiO_2	0.50	-0.26	1.44	-1.98	0.09
	0.55	-1.62	2.31	-3.15	0.11
	0.60	-3.39	3.91	-5.34	0.22
xPbO-(0.5-x)ZnO-0.5P_2O_5	0.00	8.43	-1.47	4.69	5.20
	0.10	5.11	0.22	1.20	0.09
	0.20	3.92	0.51	0.55	0.08
	0.40	1.46	1.44	-1.36	0.36
	0.50	-0.75	1.78	-2.35	0.38
xSnO-(1-x)P_2O_5	0.40	-0.20	2.37	-3.20	0.35
	0.45	-0.65	4.00	-5.41	0.54
	0.55	-1.47	5.76	-7.64	1.30
	0.60	-1.55	5.05	-6.85	1.10
	0.65	-2.39	6.32	-8.56	1.10
	0.68	-2.99	7.12	-9.63	2.20
xSnO-(1-x)SiO_2	0.40	0.94	1.33	-1.62	0.13
	0.50	0.55	1.38	-1.75	0.04
	0.55	-1.58	2.72	-3.54	0.05
	0.60	-1.51	2.24	-3.17	0.30
xZnO-(1-x)P_2O_5	0.40	7.47	-1.45	5.17	0.86
	0.50	8.43	-1.47	4.69	5.20
	0.60	6.70	-2.15	4.89	1.30
xZnO-(1-x)TeO_2	0.15	0.65	0.88	-0.96	0.02
	0.20	0.40	0.96	-1.11	0.16
	0.35	-0.03	2.10	-2.72	0.15
	0.40	-0.21	3.18	-4.18	0.34

Appendix C

Copyright Permission

The copyright permission for the manuscript reproduced in Chapter 4 is included in this appendix.

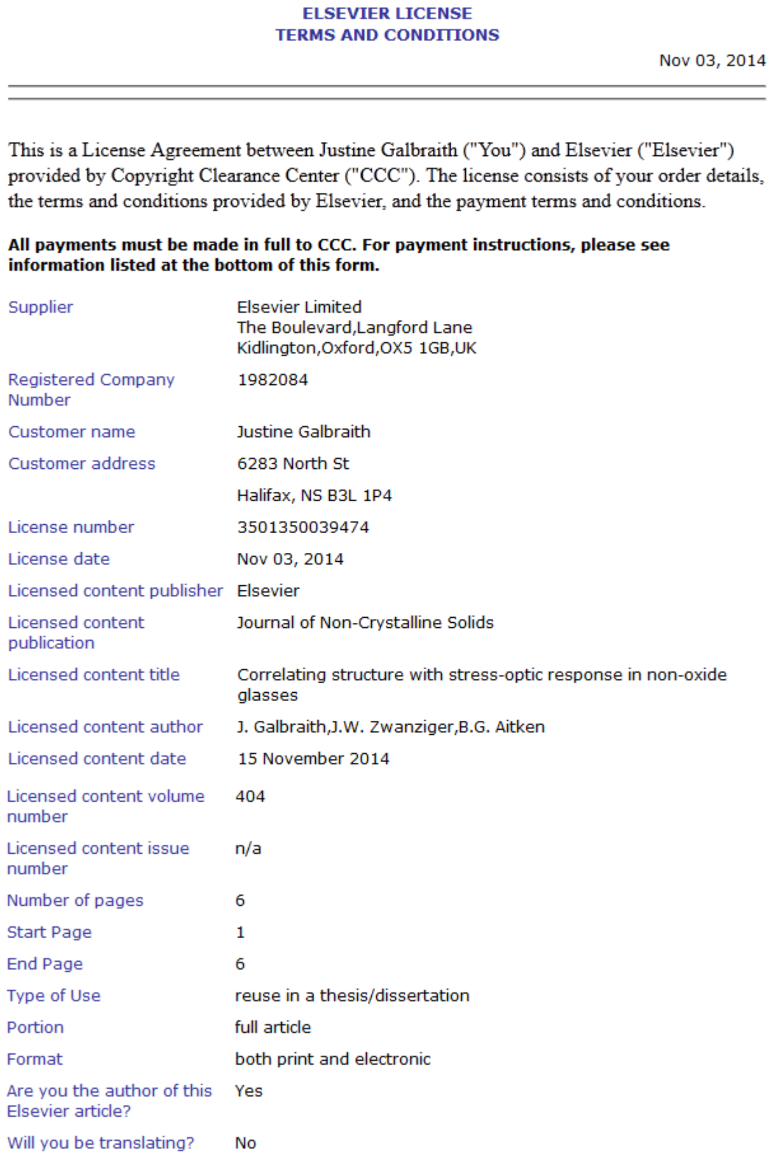

ELSEVIER LICENSE
TERMS AND CONDITIONS

Nov 03, 2014

This is a License Agreement between Justine Galbraith ("You") and Elsevier ("Elsevier") provided by Copyright Clearance Center ("CCC"). The license consists of your order details, the terms and conditions provided by Elsevier, and the payment terms and conditions.

All payments must be made in full to CCC. For payment instructions, please see information listed at the bottom of this form.

Supplier	Elsevier Limited The Boulevard,Langford Lane Kidlington,Oxford,OX5 1GB,UK
Registered Company Number	1982084
Customer name	Justine Galbraith
Customer address	6283 North St
	Halifax, NS B3L 1P4
License number	3501350039474
License date	Nov 03, 2014
Licensed content publisher	Elsevier
Licensed content publication	Journal of Non-Crystalline Solids
Licensed content title	Correlating structure with stress-optic response in non-oxide glasses
Licensed content author	J. Galbraith,J.W. Zwanziger,B.G. Aitken
Licensed content date	15 November 2014
Licensed content volume number	404
Licensed content issue number	n/a
Number of pages	6
Start Page	1
End Page	6
Type of Use	reuse in a thesis/dissertation
Portion	full article
Format	both print and electronic
Are you the author of this Elsevier article?	Yes
Will you be translating?	No

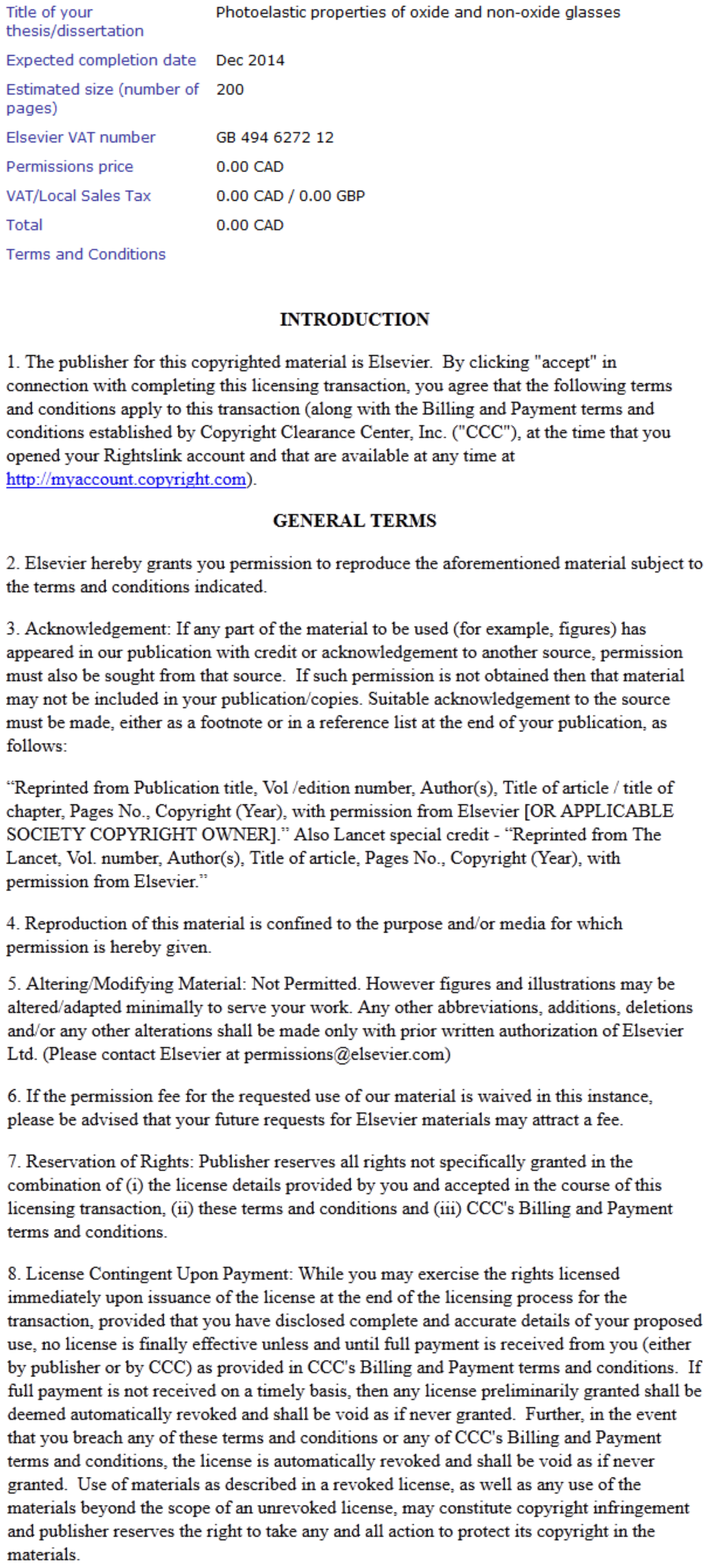

Title of your thesis/dissertation	Photoelastic properties of oxide and non-oxide glasses
Expected completion date	Dec 2014
Estimated size (number of pages)	200
Elsevier VAT number	GB 494 6272 12
Permissions price	0.00 CAD
VAT/Local Sales Tax	0.00 CAD / 0.00 GBP
Total	0.00 CAD
Terms and Conditions	

INTRODUCTION

1. The publisher for this copyrighted material is Elsevier. By clicking "accept" in connection with completing this licensing transaction, you agree that the following terms and conditions apply to this transaction (along with the Billing and Payment terms and conditions established by Copyright Clearance Center, Inc. ("CCC"), at the time that you opened your Rightslink account and that are available at any time at http://myaccount.copyright.com).

GENERAL TERMS

2. Elsevier hereby grants you permission to reproduce the aforementioned material subject to the terms and conditions indicated.

3. Acknowledgement: If any part of the material to be used (for example, figures) has appeared in our publication with credit or acknowledgement to another source, permission must also be sought from that source. If such permission is not obtained then that material may not be included in your publication/copies. Suitable acknowledgement to the source must be made, either as a footnote or in a reference list at the end of your publication, as follows:

“Reprinted from Publication title, Vol /edition number, Author(s), Title of article / title of chapter, Pages No., Copyright (Year), with permission from Elsevier [OR APPLICABLE SOCIETY COPYRIGHT OWNER].” Also Lancet special credit - “Reprinted from The Lancet, Vol. number, Author(s), Title of article, Pages No., Copyright (Year), with permission from Elsevier.”

4. Reproduction of this material is confined to the purpose and/or media for which permission is hereby given.

5. Altering/Modifying Material: Not Permitted. However figures and illustrations may be altered/adapted minimally to serve your work. Any other abbreviations, additions, deletions and/or any other alterations shall be made only with prior written authorization of Elsevier Ltd. (Please contact Elsevier at permissions@elsevier.com)

6. If the permission fee for the requested use of our material is waived in this instance, please be advised that your future requests for Elsevier materials may attract a fee.

7. Reservation of Rights: Publisher reserves all rights not specifically granted in the combination of (i) the license details provided by you and accepted in the course of this licensing transaction, (ii) these terms and conditions and (iii) CCC's Billing and Payment terms and conditions.

8. License Contingent Upon Payment: While you may exercise the rights licensed immediately upon issuance of the license at the end of the licensing process for the transaction, provided that you have disclosed complete and accurate details of your proposed use, no license is finally effective unless and until full payment is received from you (either by publisher or by CCC) as provided in CCC's Billing and Payment terms and conditions. If full payment is not received on a timely basis, then any license preliminarily granted shall be deemed automatically revoked and shall be void as if never granted. Further, in the event that you breach any of these terms and conditions or any of CCC's Billing and Payment terms and conditions, the license is automatically revoked and shall be void as if never granted. Use of materials as described in a revoked license, as well as any use of the materials beyond the scope of an unrevoked license, may constitute copyright infringement and publisher reserves the right to take any and all action to protect its copyright in the materials.

9. Warranties: Publisher makes no representations or warranties with respect to the licensed material.

10. Indemnity: You hereby indemnify and agree to hold harmless publisher and CCC, and their respective officers, directors, employees and agents, from and against any and all claims arising out of your use of the licensed material other than as specifically authorized pursuant to this license.

11. No Transfer of License: This license is personal to you and may not be sublicensed, assigned, or transferred by you to any other person without publisher's written permission.

12. No Amendment Except in Writing: This license may not be amended except in a writing signed by both parties (or, in the case of publisher, by CCC on publisher's behalf).

13. Objection to Contrary Terms: Publisher hereby objects to any terms contained in any purchase order, acknowledgment, check endorsement or other writing prepared by you, which terms are inconsistent with these terms and conditions or CCC's Billing and Payment terms and conditions. These terms and conditions, together with CCC's Billing and Payment terms and conditions (which are incorporated herein), comprise the entire agreement between you and publisher (and CCC) concerning this licensing transaction. In the event of any conflict between your obligations established by these terms and conditions and those established by CCC's Billing and Payment terms and conditions, these terms and conditions shall control.

14. Revocation: Elsevier or Copyright Clearance Center may deny the permissions described in this License at their sole discretion, for any reason or no reason, with a full refund payable to you. Notice of such denial will be made using the contact information provided by you. Failure to receive such notice will not alter or invalidate the denial. In no event will Elsevier or Copyright Clearance Center be responsible or liable for any costs, expenses or damage incurred by you as a result of a denial of your permission request, other than a refund of the amount(s) paid by you to Elsevier and/or Copyright Clearance Center for denied permissions.

LIMITED LICENSE

The following terms and conditions apply only to specific license types:

15. **Translation**: This permission is granted for non-exclusive world **English** rights only unless your license was granted for translation rights. If you licensed translation rights you may only translate this content into the languages you requested. A professional translator must perform all translations and reproduce the content word for word preserving the integrity of the article. If this license is to re-use 1 or 2 figures then permission is granted for non-exclusive world rights in all languages.

16. **Posting licensed content on any Website**: The following terms and conditions apply as follows: Licensing material from an Elsevier journal: All content posted to the web site must maintain the copyright information line on the bottom of each image; A hyper-text must be included to the Homepage of the journal from which you are licensing at http://www.sciencedirect.com/science/journal/xxxxx or the Elsevier homepage for books at http://www.elsevier.com; Central Storage: This license does not include permission for a scanned version of the material to be stored in a central repository such as that provided by Heron/XanEdu.

Licensing material from an Elsevier book: A hyper-text link must be included to the Elsevier homepage at http://www.elsevier.com . All content posted to the web site must maintain the copyright information line on the bottom of each image.

Posting licensed content on Electronic reserve: In addition to the above the following clauses are applicable: The web site must be password-protected and made available only to bona fide students registered on a relevant course. This permission is granted for 1 year only. You may obtain a new license for future website posting.

For journal authors: the following clauses are applicable in addition to the above: Permission granted is limited to the author accepted manuscript version* of your paper.

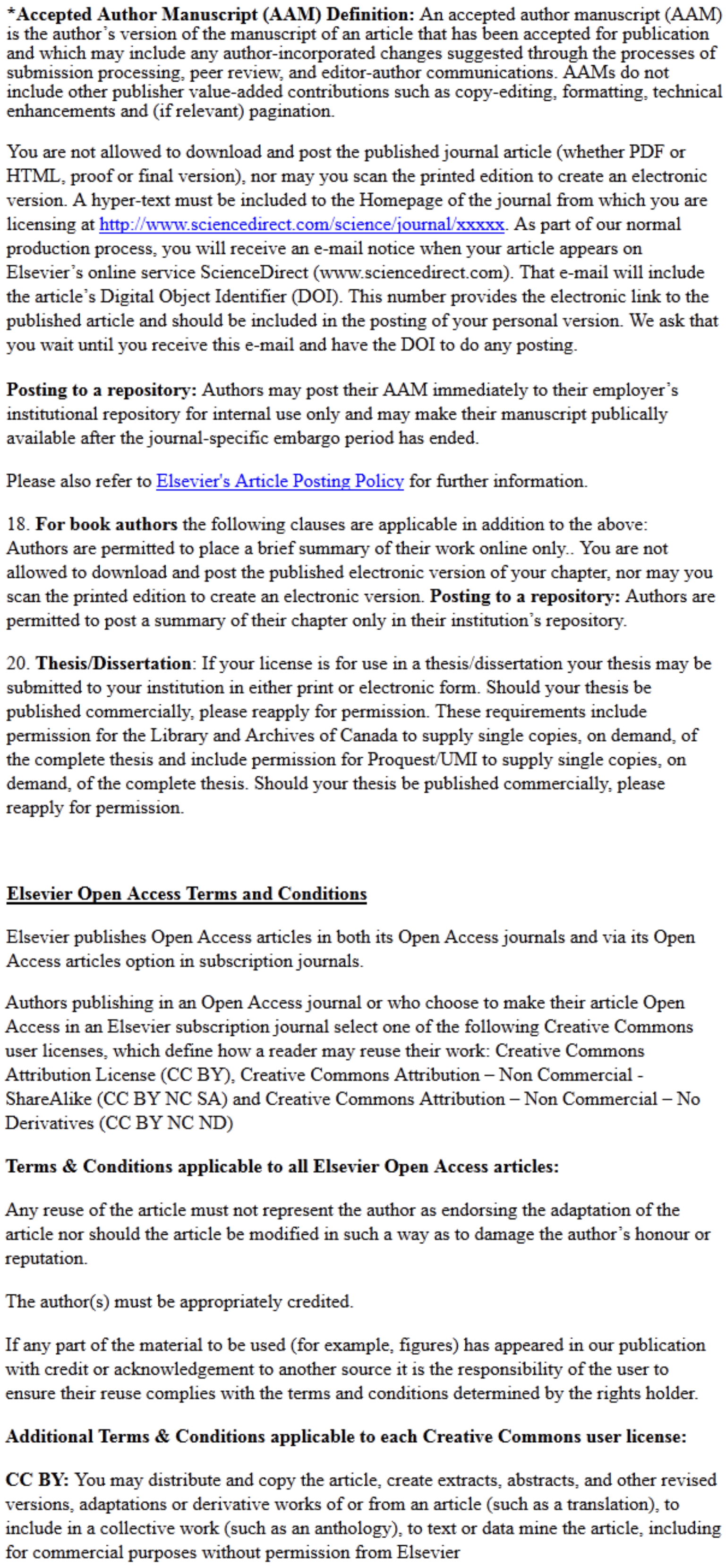

***Accepted Author Manuscript (AAM) Definition:** An accepted author manuscript (AAM) is the author's version of the manuscript of an article that has been accepted for publication and which may include any author-incorporated changes suggested through the processes of submission processing, peer review, and editor-author communications. AAMs do not include other publisher value-added contributions such as copy-editing, formatting, technical enhancements and (if relevant) pagination.

You are not allowed to download and post the published journal article (whether PDF or HTML, proof or final version), nor may you scan the printed edition to create an electronic version. A hyper-text must be included to the Homepage of the journal from which you are licensing at http://www.sciencedirect.com/science/journal/xxxxx. As part of our normal production process, you will receive an e-mail notice when your article appears on Elsevier's online service ScienceDirect (www.sciencedirect.com). That e-mail will include the article's Digital Object Identifier (DOI). This number provides the electronic link to the published article and should be included in the posting of your personal version. We ask that you wait until you receive this e-mail and have the DOI to do any posting.

Posting to a repository: Authors may post their AAM immediately to their employer's institutional repository for internal use only and may make their manuscript publically available after the journal-specific embargo period has ended.

Please also refer to Elsevier's Article Posting Policy for further information.

18. **For book authors** the following clauses are applicable in addition to the above: Authors are permitted to place a brief summary of their work online only.. You are not allowed to download and post the published electronic version of your chapter, nor may you scan the printed edition to create an electronic version. **Posting to a repository:** Authors are permitted to post a summary of their chapter only in their institution's repository.

20. **Thesis/Dissertation**: If your license is for use in a thesis/dissertation your thesis may be submitted to your institution in either print or electronic form. Should your thesis be published commercially, please reapply for permission. These requirements include permission for the Library and Archives of Canada to supply single copies, on demand, of the complete thesis and include permission for Proquest/UMI to supply single copies, on demand, of the complete thesis. Should your thesis be published commercially, please reapply for permission.

Elsevier Open Access Terms and Conditions

Elsevier publishes Open Access articles in both its Open Access journals and via its Open Access articles option in subscription journals.

Authors publishing in an Open Access journal or who choose to make their article Open Access in an Elsevier subscription journal select one of the following Creative Commons user licenses, which define how a reader may reuse their work: Creative Commons Attribution License (CC BY), Creative Commons Attribution – Non Commercial - ShareAlike (CC BY NC SA) and Creative Commons Attribution – Non Commercial – No Derivatives (CC BY NC ND)

Terms & Conditions applicable to all Elsevier Open Access articles:

Any reuse of the article must not represent the author as endorsing the adaptation of the article nor should the article be modified in such a way as to damage the author's honour or reputation.

The author(s) must be appropriately credited.

If any part of the material to be used (for example, figures) has appeared in our publication with credit or acknowledgement to another source it is the responsibility of the user to ensure their reuse complies with the terms and conditions determined by the rights holder.

Additional Terms & Conditions applicable to each Creative Commons user license:

CC BY: You may distribute and copy the article, create extracts, abstracts, and other revised versions, adaptations or derivative works of or from an article (such as a translation), to include in a collective work (such as an anthology), to text or data mine the article, including for commercial purposes without permission from Elsevier

CC BY NC SA: For non-commercial purposes you may distribute and copy the article, create extracts, abstracts and other revised versions, adaptations or derivative works of or from an article (such as a translation), to include in a collective work (such as an anthology), to text and data mine the article and license new adaptations or creations under identical terms without permission from Elsevier

CC BY NC ND: For non-commercial purposes you may distribute and copy the article and include it in a collective work (such as an anthology), provided you do not alter or modify the article, without permission from Elsevier

Any commercial reuse of Open Access articles published with a CC BY NC SA or CC BY NC ND license requires permission from Elsevier and will be subject to a fee.

Commercial reuse includes:

- Promotional purposes (advertising or marketing)
- Commercial exploitation (e.g. a product for sale or loan)
- Systematic distribution (for a fee or free of charge)

Please refer to Elsevier's Open Access Policy for further information.

21. **Other Conditions**:

v1.7

Questions? customercare@copyright.com or +1-855-239-3415 (toll free in the US) or +1-978-646-2777.

Gratis licenses (referencing $0 in the Total field) are free. Please retain this printable license for your reference. No payment is required.